Through Neutrino Eyes:
The Search for New Physics

Guest Editors: Abhijit Samanta, David Latimer, and Michael A. Schmidt

Through Neutrino Eyes: The Search for New Physics

Through Neutrino Eyes: The Search for New Physics

Guest Editors: Abhijit Samanta, David Latimer, and Michael A. Schmidt

Editorial Board

Contents

Editorial

Through Neutrino Eyes: The Search for New Physics

Abhijit Samanta,[1] David Latimer,[2] and Michael A. Schmidt[3]

[1]*Department of Physics, Heritage Institute of Technology, Kolkata 700 107, India*
[2]*Department of Physics, University of Puget Sound, Tacoma, WA, USA*
[3]*School of Physics A28, University of Sydney, Sydney, NSW 2006, Australia*

Correspondence should be addressed to Abhijit Samanta; abhijit.samanta@gmail.com

The year 2014 will mark the 60th anniversary since the neutrino detector of Frederick Reines and Clyde L. Cowan, Jr. was turned (neutrino detection in 1956). After many years, Super-Kamiokande [1] showed in 1998 that neutrinos are massive. Today, neutrino physics has become a very active research field: there is a plethora of different neutrino experiments and theoretical studies. Subsequent measurements [2–6] of the two neutrino mass squared differences and the leptonic mixing parameters lead to a phase of precision experiments in neutrino physics. Recently the last remaining mixing angle, the 1–3 mixing angle, has been measured by the Daya Bay [7, 8], Double Chooz [9, 10], and RENO [11] experiments after initial hints by T2K [12] and MINOS [13, 14]. Contrary to theoretical expectations from flavor symmetry considerations, it turned out to be large.

The next main goals of the experimental program are the measurement of the mass hierarchy and the Dirac CP phase, which is facilitated by the relatively large 1–3 mixing angles. These measurements will help to pin down the theoretical origin of neutrino mass and mixing, for example, confirming or refuting the idea of a flavor symmetry in the lepton sector. Additionally precision measurements of neutrino properties will also permit using neutrinos as a tool for probing new physics connected with neutrinos, like dark matter or dark energy. There are a huge number of ongoing and upcoming neutrino experiments worldwide studying these issues.

To celebrate the 60th anniversary of the first neutrino detector, we have collected original research articles as well as review articles for this special issue focusing mainly on physics at underground detectors and its complementary studies at the LHC to uncover the nature of neutrinos as well as physics beyond standard model.

The article *"The low-scale approach to neutrino masses"* by S. M. Boucenna et al. provides a short review on low-scale models of neutrino mass generation including the phenomenological potential signatures associated with direct neutrino mass messenger production at the LHC, messenger-induced lepton flavor violation processes, and the presence of WIMP cold dark matter candidates.

The article *"Beyond standard model searches in the Mini-BooNE experiment"* by Teppei Katori and Janet Conrad provides a review on the contribution of the MiniBooNE Experiment to beyond standard model searches in the neutrino sector. MiniBooNE observed excesses of ν_e and anti-ν_e candidate events in neutrino and antineutrino mode, respectively. To date, these excesses have not been explained within the neutrino Standard Model, the Standard Model extended by three massive neutrinos. The results set for the first time strict limits on Lorentz violating extensions of the Standard Model. Most recently, MiniBooNE is running with a beam tuned in beam-dump mode to search for dark sector particles.

The article *"Searching for neutrinoless double-beta decay of ^{130}Te with CUORE"* by D. R. Artusa et al. provides a review on the experimental techniques used in Cryogenic Underground Observatory for Rare Events (CUORE), its current status, and anticipated physics reach. CUORE is an upcoming experiment designed to search for neutrinoless double-beta decay of ^{130}Te using an array of 988 TeO_2 crystal bolometers operated at 10 mK. The detector will contain 206 kg of ^{130}Te and have an average energy resolution of 5 keV; the projected half-life sensitivity after five years of live time is 1.6×10^{26} y at 1σ (9.5×10^{25} y at the 90% confidence

level), which corresponds to an upper limit on the effective Majorana mass in the range 40–100 meV (50–130 meV).

The article *"Neutrinos as probes of Lorentz invariance"* by J. S. Díaz reviews generic experimental signatures of the breakdown of Lorentz symmetry in the neutrino sector. Neutrino oscillations are identified as an ideal experimental setup to search for breaking of Lorentz symmetry.

The article *"Constraints on light neutrino parameters derived from the study of neutrinoless double beta decay"* by S. Stoica and A. Neacsu revises the present constraints on the neutrino mass parameters derived from the decay analysis of the experimentally interesting nuclei using the latest results for the phase space factors and nuclear matrix elements (NMEs), as well as for the experimental lifetime limits. This restricts the range of spread of the NME values calculated with different methods and, hence, to reduce the uncertainty in deriving limits for the Majorana neutrino mass parameter. These results may be useful to have an updated image on the present neutrino mass sensitivities associated with measurements for different isotopes and to better estimate the range of values of the neutrino masses that can be explored in the future double beta decay experiments.

The article *"Theory of neutrino-atom collisions: the history, present status, and BSM physics"* by K. A. Kouzakov and Alexander I. Studenikin provides an overview of the current theoretical studies on neutrino-atom scattering processes. The ionization channel of these processes, which is studied in experiments searching for neutrino magnetic moments, is discussed. Recent developments in the theory of atomic ionization by the impact of reactor antineutrinos are also enlightened here.

The article *"Entanglement in a QFT model of neutrino oscillations"* by M. Blasone et al. uses the tools of quantum information theory to provide a convenient description of the phenomena of particle mixing and flavor oscillations in terms of entanglement using a suitable entanglement measure, the concurrence, that allows extracting the two-mode (flavor) entanglement from full multimode, multiparticle flavor neutrino states.

The article *"Gaseous detector with sub-keV threshold to study neutrino scattering at low recoil energies"* by A. V. Kopylov et al. discusses the construction of a gaseous detector with a sub-keV electron equivalent threshold, which allows a precision measurement of the neutrino magnetic moment and to observe coherent scattering of neutrinos on nuclei. The progress in the development of low noise electronics makes it possible to register rare events at the threshold less than 100 eV.

The article *"Performance of water-based liquid scintillator: an independent analysis"* by D. Beznosko et al. discusses a water-based liquid scintillator, which is based on the idea of dissolving an organic scintillator in water using special surfactants. The results show that a goal of 100 optical photons/MeV has been achieved. Simulations have indicated that this is an optimal light yield for observing both the Cerenkov ring and the scintillation light from proton decay in a large water detector.

The papers included in this special issue cover a small number of the diverse issues in neutrino physics. We are certain that the short reviews on different aspects in neutrino physics will help new researchers and the original research articles will have an impact on the future development of neutrino physics.

Abhijit Samanta
David Latimer
Michael A. Schmidt

References

[1] Y. Fukuda, T. Hayakawa, E. Ichihara et al., "Evidence for oscillation of atmospheric neutrinos," *Physical Review Letters*, vol. 81, no. 8, pp. 1562–1567, 1998.

[2] M. Apollonio, A. Baldini, C. Bemporad et al., "Limits on neutrino oscillations from the CHOOZ experiment," *Physics Letters B*, vol. 466, pp. 415–430, 1999.

[3] Q. Ahmad, R. C. Allen, T. C. Andersen et al., "Direct evidence for neutrino flavor transformation from neutral-current interactions in the Sudbury Neutrino Observatory," *Physical Review Letters*, vol. 89, Article ID 011301, 2002.

[4] S. N. Ahmed, A. E. Anthony, E. W. Beier et al., "Measurement of the total active ^{8}B solar neutrino flux at the sudbury neutrino observatory with enhanced neutral current sensitivity," *Physical Review Letters*, vol. 92, Article ID 181301, 2004.

[5] K. Eguchi, S. Enomoto, K. Furuno et al., "First results from KamLAND: evidence for reactor antineutrino disappearance," *Physical Review Letters*, vol. 90, Article ID 021802, 2003.

[6] M. Ahn, E. Aliu, S. Andringa et al., "Measurement of neutrino oscillation by the K2K experiment," *Physical Review D*, vol. 74, no. 7, Article ID 072003, 39 pages, 2006.

[7] F. An, J. Z. Bai, A. B. Balantekin et al., "Observation of electron-antineutrino disappearance at daya bay," *Physical Review Letters*, vol. 108, Article ID 171803, 2012.

[8] F. P. An, Q. An, J. Z. Bai et al., "Improved measurement of electron antineutrino disappearance at Daya Bay," *Chinese Physics C*, vol. 37, no. 1, Article ID 011001, 2013.

[9] Y. Abe, C. Aberle, T. Akiri et al., "Indication of reactor $\bar{\nu}_e$ disappearance in the double chooz experiment," *Physical Review Letters*, vol. 108, no. 13, Article ID 131801, 7 pages, 2012.

[10] Y. Abe, C. Aberle, J. C. dos Anjos et al., "Reactor $\bar{V}_e$ disappearance in the Double Chooz experiment," *Physical Review D*, Article ID 052008, 2012.

[11] J. Ahn, S. Chebotaryov, J. H. Choi et al., "Observation of reactor electron antineutrinos disappearance in the RENO experiment," *Physical Review Letters*, vol. 108, no. 19, 6 pages, 2012.

[12] K. Abe, N. Abgrall, Y. Ajima et al., "Indication of electron neutrino appearance from an accelerator-produced off-axis muon neutrino beam," *Physical Review Letters*, vol. 107, Article ID 041801, 2011.

[13] D. G. Michael, P. Adamson, T. Alexopoulos et al., "Observation of muon neutrino disappearance with the MINOS detectors in the NuMI neutrino beam," *Physical Review Letters*, vol. 97, Article ID 191801, 2006.

[14] P. Adamson, D. J. Auty, D. S. Ayres et al., "Improved search for Muon-neutrino to electron-neutrino oscillations in MINOS," *Physical Review Letters*, vol. 107, no. 18, Article ID 181802, 6 pages, 2011.

Review Article

Searching for Neutrinoless Double-Beta Decay of ^{130}Te with CUORE

D. R. Artusa,[1,2] **F. T. Avignone III,**[1] **O. Azzolini,**[3] **M. Balata,**[2] **T. I. Banks,**[2,4,5] **G. Bari,**[6]
J. Beeman,[7] **F. Bellini,**[8,9] **A. Bersani,**[10] **M. Biassoni,**[11,12] **C. Brofferio,**[11,12] **C. Bucci,**[2]
X. Z. Cai,[13] **A. Camacho,**[3] **L. Canonica,**[2] **X. G. Cao,**[13] **S. Capelli,**[11,12] **L. Carbone,**[12]
L. Cardani,[8,9] **M. Carrettoni,**[11,12] **N. Casali,**[2] **D. Chiesa,**[11,12] **N. Chott,**[1] **M. Clemenza,**[11,12]
S. Copello,[14] **C. Cosmelli,**[8,9] **O. Cremonesi,**[12] **R. J. Creswick,**[1] **I. Dafinei,**[9] **A. Dally,**[15]
V. Datskov,[12] **A. De Biasi,**[3] **M. M. Deninno,**[6] **S. Di Domizio,**[10,14] **M. L. di Vacri,**[2] **L. Ejzak,**[15]
D. Q. Fang,[13] **H. A. Farach,**[1] **M. Faverzani,**[11,12] **G. Fernandes,**[10,14] **E. Ferri,**[11,12] **F. Ferroni,**[8,9]
E. Fiorini,[11,12] **M. A. Franceschi,**[16] **S. J. Freedman,**[4,5] **B. K. Fujikawa,**[5] **A. Giachero,**[11,12]
L. Gironi,[11,12] **A. Giuliani,**[17] **J. Goett,**[2] **P. Gorla,**[2] **C. Gotti,**[11,12] **T. D. Gutierrez,**[18]
E. E. Haller,[7,19] **K. Han,**[5] **K. M. Heeger,**[20] **R. Hennings-Yeomans,**[4] **H. Z. Huang,**[21] **R. Kadel,**[22]
K. Kazkaz,[23] **G. Keppel,**[3] **Yu. G. Kolomensky,**[4,22] **Y. L. Li,**[13] **C. Ligi,**[16] **X. Liu,**[21] **Y. G. Ma,**[13]
C. Maiano,[11,12] **M. Maino,**[11,12] **M. Martinez,**[24] **R. H. Maruyama,**[20] **Y. Mei,**[5] **N. Moggi,**[6]
S. Morganti,[9] **T. Napolitano,**[16] **S. Nisi,**[2] **C. Nones,**[25] **E. B. Norman,**[23,26] **A. Nucciotti,**[11,12]
T. O'Donnell,[4] **F. Orio,**[9] **D. Orlandi,**[2] **J. L. Ouellet,**[4,5] **M. Pallavicini,**[10,14] **V. Palmieri,**[3]
L. Pattavina,[2] **M. Pavan,**[11,12] **M. Pedretti,**[23] **G. Pessina,**[12] **V. Pettinacci,**[9] **G. Piperno,**[8,9]
C. Pira,[3] **S. Pirro,**[2] **E. Previtali,**[12] **V. Rampazzo,**[3] **C. Rosenfeld,**[1] **C. Rusconi,**[12] **E. Sala,**[11,12]
S. Sangiorgio,[23] **N. D. Scielzo,**[23] **M. Sisti,**[11,12] **A. R. Smith,**[5] **L. Taffarello,**[27] **M. Tenconi,**[17]
F. Terranova,[11,12] **W. D. Tian,**[13] **C. Tomei,**[9] **S. Trentalange,**[21] **G. Ventura,**[28,29] **M. Vignati,**[9]
B. S. Wang,[23,26] **H. W. Wang,**[13] **L. Wielgus,**[15] **J. Wilson,**[1] **L. A. Winslow,**[21] **T. Wise,**[15,20]
A. Woodcraft,[30] **L. Zanotti,**[11,12] **C. Zarra,**[2] **B. X. Zhu,**[21] **and S. Zucchelli**[6,31]

[1] *Department of Physics and Astronomy, University of South Carolina, Columbia, SC 29208, USA*
[2] *INFN, Laboratori Nazionali del Gran Sasso, Assergi, 67010 L'Aquila, Italy*
[3] *INFN, Laboratori Nazionali di Legnaro, Legnaro, 35020 Padova, Italy*
[4] *Department of Physics, University of California, Berkeley, CA 94720, USA*
[5] *Nuclear Science Division, Lawrence Berkeley National Laboratory, Berkeley, CA 94720, USA*
[6] *INFN, Sezione di Bologna, 40127 Bologna, Italy*
[7] *Materials Science Division, Lawrence Berkeley National Laboratory, Berkeley, CA 94720, USA*
[8] *Dipartimento di Fisica, Sapienza Università di Roma, 00185 Roma, Italy*
[9] *INFN, Sezione di Roma, 00185 Roma, Italy*
[10] *INFN, Sezione di Genova, 16146 Genova, Italy*
[11] *Dipartimento di Fisica, Università di Milano-Bicocca, 20126 Milano, Italy*
[12] *INFN, Sezione di Milano Bicocca, 20126 Milano, Italy*
[13] *Shanghai Institute of Applied Physics, Chinese Academy of Sciences, Shanghai 201800, China*
[14] *Dipartimento di Fisica, Università di Genova, 16146 Genova, Italy*
[15] *Department of Physics, University of Wisconsin, Madison, WI 53706, USA*
[16] *INFN, Laboratori Nazionali di Frascati, Frascati, 00044 Roma, Italy*
[17] *Centre de Spectrométrie Nucléaire et de Spectrométrie de Masse, Orsay Campus, 91405 Orsay, France*
[18] *Physics Department, California Polytechnic State University, San Luis Obispo, CA 93407, USA*
[19] *Department of Materials Science and Engineering, University of California, Berkeley, CA 94720, USA*
[20] *Department of Physics, Yale University, New Haven, CT 06520, USA*

^{21}Department of Physics and Astronomy, University of California, Los Angeles, CA 90095, USA

^{22}Physics Division, Lawrence Berkeley National Laboratory, Berkeley, CA 94720, USA

^{23}Lawrence Livermore National Laboratory, Livermore, CA 94550, USA

^{24}Laboratorio de Fisica Nuclear y Astroparticulas, Universidad de Zaragoza, 50009 Zaragoza, Spain

^{25}Service de Physique des Particules, CEA/Saclay, 91191 Gif-sur-Yvette, France

^{26}Department of Nuclear Engineering, University of California, Berkeley, CA 94720, USA

^{27}INFN, Sezione di Padova, 35131 Padova, Italy

^{28}Dipartimento di Fisica, Università di Firenze, 50125 Firenze, Italy

^{29}INFN, Sezione di Firenze, 50125 Firenze, Italy

^{30}SUPA, Institute for Astronomy, University of Edinburgh, Blackford Hill, Edinburgh EH9 3HJ, UK

^{31}Dipartimento di Fisica, Università di Bologna, 40127 Bologna, Italy

Correspondence should be addressed to O. Cremonesi; cuore-spokesperson@lngs.infn.it

Neutrinoless double-beta ($0\nu\beta\beta$) decay is a hypothesized lepton-number-violating process that offers the only known means of asserting the possible Majorana nature of neutrino mass. The Cryogenic Underground Observatory for Rare Events (CUORE) is an upcoming experiment designed to search for $0\nu\beta\beta$ decay of ^{130}Te using an array of 988 TeO$_2$ crystal bolometers operated at 10 mK. The detector will contain 206 kg of ^{130}Te and have an average energy resolution of 5 keV; the projected $0\nu\beta\beta$ decay half-life sensitivity after five years of livetime is 1.6×10^{26} y at 1σ (9.5×10^{25} y at the 90% confidence level), which corresponds to an upper limit on the effective Majorana mass in the range 40–100 meV (50–130 meV). In this paper, we review the experimental techniques used in CUORE as well as its current status and anticipated physics reach.

1. Introduction

The discovery of neutrino oscillations revealed that neutrinos are massive particles and thereby provided the first evidence of physics beyond the Standard Model (cf. [1, 2]). This development resolved some longstanding mysteries but it also raised new questions about the fundamental nature of neutrinos: namely, What is the absolute mass scale of the neutrino? What is the hierarchy of its different mass states? Is the neutrino its own antiparticle?

Neutrinoless double-beta ($0\nu\beta\beta$) decay has attracted a great deal of attention in recent years because of its unique potential to provide insight into the above issues. This lepton-number-violating process,

$$(Z, A) \longrightarrow (Z + 2, A) + 2e^-, \tag{1}$$

can occur only if neutrinos are massive Majorana particles—that is, if they are their own antiparticles, a possibility first suggested by Majorana in 1937 [3]. Indeed, $0\nu\beta\beta$ decay offers the only feasible means of investigating this question at present (cf. [4, 5]). If $0\nu\beta\beta$ decay occurs, it is extremely rare, with a half-life greater than 10^{25} years. Observation of the process would unambiguously establish that neutrinos have Majorana mass and reveal them to be different from the other known fermions, which are Dirac particles. The scenario in which neutrinos are Majorana particles is widely viewed as more "natural" from a theoretical standpoint, and if true it would have profound implications for our understanding of how neutrinos acquire mass and possibly how the universe's matter-antimatter asymmetry arose [1]. Experimental searches for $0\nu\beta\beta$ decay also have the potential to provide information about the neutrino mass hierarchy and absolute mass scale, depending on whether $0\nu\beta\beta$ decay is observed and at what sensitivity.

To date there has been only one claim of observation of $0\nu\beta\beta$ decay [6, 7], which stands in tension with more recent null results from other experiments [8–10]. There are currently at least ten experiments aiming at searching for $0\nu\beta\beta$ decay in almost as many candidate isotopes. Among them is the Cryogenic Underground Observatory for Rare Events (CUORE) [11, 12], which will search for $0\nu\beta\beta$ decay of ^{130}Te by operating TeO$_2$ crystals as cryogenic bolometers at the underground Laboratori Nazionali del Gran Sasso (LNGS), Italy. The current lower limit on the half-life for $0\nu\beta\beta$ decay of ^{130}Te was established by a predecessor experiment, Cuoricino, at 2.8×10^{24} y (90% C.L.) [13]. CUORE aims to improve on this sensitivity by more than a factor of 30 by operating a larger, cleaner, better-shielded detector with enhanced energy resolution inside a new custom-built cryostat.

In this paper, we review the design, status, and physics outlook for CUORE. Section 2 describes the experimental techniques used, with a special focus on energy resolution (Section 2.1) and sources of background (Section 2.2). Section 3 describes the construction and operation of CUORE-0, a prototype detector which is now taking data. In Section 4, we discuss the status of CUORE, including the ongoing assembly of its detectors and commissioning of its

(a)

(b)

(c)
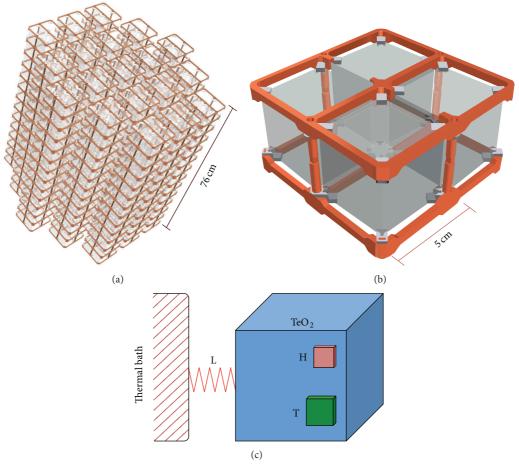
FIGURE 1: (a) Illustration of the planned 19-tower CUORE detector array. (b) Close-up of a single tower floor showing four TeO_2 crystals held inside their copper frame by PTFE spacers. (c) Schematic diagram of an individual TeO_2 crystal bolometer. Each crystal is instrumented with a heater (H) and a thermistor (T); the PTFE spacers and sensor readout wires act as weak thermal links (L) between the crystal and the thermal bath of the copper frame.

cryogenics, and in Section 5 we examine the potential physics reach of the experiment.

2. Bolometric Technique

The general strategy when searching for $0\nu\beta\beta$ decay is to look for a signature produced by the two final-state electrons, which would be emitted simultaneously and have a combined energy equal to the decay energy (a.k.a. Q-value) of the isotope under study. CUORE will use TeO_2 crystals as cryogenic bolometers to search for $0\nu\beta\beta$ decay of ^{130}Te. When a TeO_2 crystal is cooled to 10 mK, its heat capacity becomes so small that a single particle interaction depositing just a few keV inside the crystal will produce a measurable rise in its temperature—that is, the crystal functions as a highly sensitive calorimeter. The amplitude of the temperature increase is proportional to the energy deposited ($\Delta T/\Delta E \sim 10$–$20\,\mu$K/MeV), so the basic experimental method is to compile an energy spectrum from temperature pulses and look for an excess of events above background at ~2528 keV, the Q-value for $\beta\beta$ decay of ^{130}Te [14–16]. In this so-called "source = detector" approach, the TeO_2 crystal serves

a dual role: it contains the decay isotope and also acts as the detector. This method offers the advantages of high efficiency, scalability, and in our case excellent energy resolution, which is critical to discriminating any $0\nu\beta\beta$ decay peak in the measured energy spectrum.

The CUORE detector will consist of a close-packed array of 988 independent TeO_2 crystal bolometers arranged into 19 towers (Figure 1(a)). The basic detector element is a $5 \times 5 \times 5$ cm^3 crystal instrumented with a temperature sensor and a resistive heater. Each crystal weighs 750 g, giving a total detector mass of 741 kg. ^{130}Te has a natural isotopic abundance of 34.2%—the highest among the $0\nu\beta\beta$ decay candidate isotopes [17]—so the detector will contain 206 kg of source isotope.

The crystals were manufactured from 2009 to 2013 by the Shanghai Institute of Ceramics, Chinese Academy of Sciences (SICCAS). We worked in close conjunction with SICCAS to develop the rigorous quality and radiopurity controls followed during crystal production [18]. To guard against radioactive contamination of the crystal bulk and surfaces we performed high-sensitivity radiopurity checks (e.g., using ICP-MS) along the entire production chain, from

raw-material synthesis to crystal growth to the final surface treatment. Finished crystals were shipped to Italy by sea. Although this took longer than shipping by air, the increased transit time was more than compensated for by the reduced cosmogenic activation of the crystals from being exposed only to sea-level cosmic-ray flux.

Each TeO$_2$ bolometer is instrumented with a neutron-transmutation-doped (NTD) germanium thermistor that serves as a temperature sensor [19]. The device is glued to the crystal surface via a dot matrix of bicomponent epoxy. Previous work by the collaboration has demonstrated that epoxy dots provide a robust thermal coupling between the sensor and the crystal while also reducing the mechanical stresses that arise from differences in their thermal contraction rates during cryogenic cooldowns. (If a continuous veil of epoxy is used instead, the sensor will often detach with a fragment of the crystal during the cooldown step.) The thermistors were produced by neutron irradiation of pure Ge wafers in a research reactor for precise lengths of time and then dicing the wafers into $\sim 3 \times 3 \times 1\,\mathrm{mm}^3$ chips and sputtering gold contacts on the ends of each chip. Doped germanium just below the metal-insulator transition region functions as a sensitive, high-resistance thermal sensor with an exponential R-T curve, $R \approx R_0 \exp\left(\sqrt{T_0/T}\right)$ [20], where parameters R_0 and T_0 depend on the doping density and must be measured experimentally; typical values for the NTD thermistors produced for CUORE are $R_0 = 1\,\Omega$ and $T_0 = 4\,\mathrm{K}$. The NTD technique produces uniform doping density over an entire germanium wafer and thus guarantees uniform R-T properties and excellent performance for all sensors produced from it. The CUORE thermistors were characterized in multiple studies utilizing collaboration-managed dilution-refrigerator cryostats, and their bolometric performance was also evaluated in test runs (see Section 2.1).

The thermal response of a bolometer varies with its temperature, so each crystal is also instrumented with a Joule heater based on P-doped Si [21] for the purpose of monitoring the bolometer's performance over the natural temperature fluctuations ($\Delta T < 1\,\mathrm{mK}$) that occur in the course of normal cryostat operation [22]. A brief, precise pulse of current is sent through the heater at regular, known intervals, thereby injecting into the crystal a fixed amount of energy simulating a $\sim$3 MeV event. These reference signals are used later in the offline data analysis to correct for variations in the bolometer's thermal gain with time. Each heater consists of a resistive meander obtained by ion implantation on a Si chip. The device's resistance is $300 \pm 12\,\mathrm{k\Omega}$ at 10 mK and is stable to within 0.1% below 4.2 K.

A commonly used "figure of merit" expression for describing experimental sensitivity to $0\nu\beta\beta$ decay half-life is

$$T_{1/2}^{0\nu} \propto \eta \cdot a \cdot \sqrt{\frac{M \cdot t}{b \cdot \Delta E}}, \qquad (2)$$

where η is the physical detector efficiency, a is the isotopic abundance of the $0\nu\beta\beta$ decay candidate, M is the total detector mass, t is its livetime, b is the background rate per unit detector mass per energy interval, and ΔE is the detector's energy resolution [23]. For extremely rare processes like $0\nu\beta\beta$ decay, stringent requirements on energy resolution and background are critical.

2.1. Energy Resolution of CUORE Bolometers. Over the course of TeO$_2$ crystal production, the collaboration conducted ten CUORE crystal validation runs (CCVRs) in which we operated a small fraction of the newly manufactured crystals as bolometers in order to check their radiopurity and performance [25]. These month-long test runs also served as excellent R&D platforms for testing post-Cuoricino improvements to the PTFE and copper frame designs, for characterizing NTD thermistors, and for studying the energy resolutions of the bolometers at different working temperatures.

For each CCVR, we randomly selected four crystals from the latest production batch received at LNGS (typically consisting of ~100 crystals) and assembled them into a module equivalent to a single floor of a CUORE tower (Figure 1(b)). We used CUORE-type copper frames, which have less surface area facing the crystals than those used in Cuoricino in order to reduce α-related backgrounds, as well as new PTFE spacers which had been redesigned to reduce vibrational noise. The different thermal expansion coefficients of copper, PTFE, and TeO$_2$ have been exploited in such a way that the crystals are held increasingly tighter as the detector temperature decreases. Each crystal was instrumented with two NTD Ge thermistors, but the manual work of gluing thermistors to crystals and wiring them to the cryostat was delicate and labor-intensive and as a result we typically lost some channels during detector cooldown. In some CCVRs, each crystal was also instrumented with a heater, but in several runs they were omitted for expediency because the 5407 keV line from α decays of intrinsic, short-lived ^{210}Po contamination could be used instead to monitor fluctuations in the crystals' thermal gain.

Each CCVR bolometer module was mounted inside a copper canister and cooled down to cryogenic temperatures inside our R&D cryostat in Hall C at LNGS. We reached base working temperatures in the range 12–22 mK, as the dilution refrigerator's performance varied from run to run. The energy spectrum of background data from a single CCVR is shown in Figure 2 as an example. The energy resolution of CCVR bolometers was customarily characterized as the full width at half maximum (FWHM) of the most populated peak, which is the α line at 5407 keV from ^{210}Po decay. When the ^{40}K γ peak was sufficiently populated to permit evaluation, we found its energy resolution to be statistically consistent with the ^{210}Po α peak.

The distribution of measured energy resolutions at 5407 keV for all CCVR bolometers is shown in Figure 3(a). The average energy resolution of all 69 active channels is 5.1 keV, a result that is noticeably skewed by three noisy detectors with energy resolutions larger than 10 keV FWHM. In Figure 3(b), we plot the energy resolution versus bolometer working temperature for all except the three worst performing bolometers. When the bolometers were operated below 13 mK, close to the CUORE target temperature of 10 mK, we consistently achieved our target energy resolution of 5 keV. It is worth noting that the R&D cryostat in which the CCVRs were performed is a test facility subjected to frequent
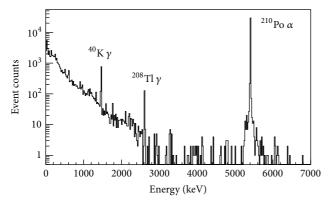
FIGURE 2: Energy spectrum of background events from one CCVR. The three prominent peaks are the 1461 keV γ-ray line from ^{40}K decay, the 2615 keV γ-ray line from ^{208}Tl decay, and the 5407 keV α peak at the Q-value for ^{210}Po decay. The ^{210}Po peak is accompanied by a less prominent peak at 5304 keV which arises because sometimes the decay α is detected but the corresponding nuclear recoil is not—namely, when the decay occurs on a copper surface facing the detectors. The livetime of this CCVR was 21.5 days, corresponding to 0.17 kg·y of detector exposure.

modifications that affect its performance and that its base-temperature rating is ~2 mK higher than that of the CUORE-0 cryostat and the future CUORE cryostat. We therefore expect bolometer performances in CUORE to be the same as or better than what was seen in the CCVRs.

2.2. Backgrounds. The paramount concern in $0\nu\beta\beta$ decay searches is suppressing backgrounds that could hide a decay signal. Common sources of background include cosmic-ray muons and their byproducts, such as cosmogenically activated detector materials; γ rays from natural uranium- and thorium-chain radioactivity in the detector, surrounding hardware, and the environment; α particles from surface contamination of materials facing the bolometers; and the irreducible tail from $2\nu\beta\beta$ decay at the end point of the $\beta\beta$ decay energy spectrum. For CUORE, the primary concerns are γ rays and α particles from radioactive decays inside the detector and the cryostat. The tail from $2\nu\beta\beta$ decay will be negligible, as it will be several orders of magnitude smaller than the other backgrounds due to the excellent energy resolution of the bolometers and the consequently narrow region of interest (ROI) in the energy spectrum.

Environmental backgrounds will be strongly suppressed in CUORE through a combination of location and shielding. The underground LNGS host facility is located at an average depth of ~3600 m water equivalent, which reduces the muon flux from its surface value by roughly six orders of magnitude to ~3×10^{-8} $\mu/cm^2/s$ [26–29] and thus dramatically limits background from cosmic muons and muon-induced neutrons and γ rays. The primary cosmogenic activation products in TeO$_2$ crystals and copper include ^{60}Co, ^{110}Ag, and ^{110m}Ag, and the estimated background rates in the ROI from those products are at least an order of magnitude smaller than backgrounds coming from surface contamination on the copper facing the crystals [30]. In order to limit cosmogenic

activation of the copper used in the experiment, we store the copper underground and bring it aboveground only when necessary for machining and cleaning [31].

The CUORE cryostat will be surrounded by a 73-ton octagonal external shield designed to screen the detector from environmental γ rays and neutrons. The shield has three layers: an outermost layer consisting of a floor of ~20 cm thick 5% borated polyethylene (PE) and sidewalls of an 18 cm thick pure PE to thermalize and absorb neutrons, a 2 cm thick side layer of boric-acid powder to absorb neutrons, and an innermost layer of lead bricks of minimum thickness of 25 cm to absorb γ rays.

Inside the cryostat two cold lead shields will provide additional protection: a 6 cm thick layer of ancient Roman lead [32], located between the 4 K and 600 mK copper vessels and thermally anchored to the 4 K vessel, will shield the detectors from radioactivity in the outer vessels and superinsulation, and a 30 cm thick disc of modern and Roman lead at 0.01 K below the mixing chamber plate will shield the detectors from radioactivity in the overhead cryostat apparatus. The close-packed detector array itself will also provide a measure of passive and active self-shielding, the latter via vetoing of simultaneous events in adjacent crystals.

From Monte Carlo simulations, we find the expected environmental muon, neutron, and γ background rates in the ROI to be $(1.04 \pm 0.22) \times 10^{-4}$, $(8.56 \pm 6.06) \times 10^{-6}$, and $<3.9 \times 10^{-4}$ counts/keV/kg/y (90% C.L. upper limit), respectively [33, 34]. These values are orders of magnitude smaller than the α and γ backgrounds expected to come from the experimental apparatus itself.

The 2528 keV Q-value for $0\nu\beta\beta$ decay of ^{130}Te lies above most naturally occurring γ backgrounds except the 2615 keV line from ^{208}Tl. Consequently, the γ background in the CUORE ROI should come almost entirely from ^{208}Tl present in the experimental setup. The upper limits on parent ^{238}U and ^{232}Th bulk contaminations in the TeO$_2$ crystals, as determined from CCVR measurements, are 6.7×10^{-7} and 8.4×10^{-7} Bq/kg, respectively, which translate to $<10^{-4}\gamma$ counts/keV/kg/y in the ROI [25]. The γ background due to bulk contamination in the experimental setup should be less than 6×10^{-3} counts/keV/kg/y (90% C.L.) [30].

The largest background in the ROI is expected to come from α particles emitted by contaminants on the surface of the copper in the detector towers and the innermost thermal shield. We tested four techniques for minimizing effects from copper surface contamination [31, 35]. Two of the techniques involved complex procedures for removing contamination by etching a thin layer off the copper surface, while the other two techniques involved covering the copper with a material (either polyethylene wrapping or a parylene conformal coating) to absorb emitted α particles and thereby prevent them from impinging on the crystal detectors. Based on the test results and practical concerns, we elected to subject all copper components facing the bolometers—that is, both the parts in the towers and the innermost thermal shield—to a surface-cleaning process consisting of abrasive tumbling, electropolishing, chemical etching, and magnetron plasma etching [31]. Recent results from the
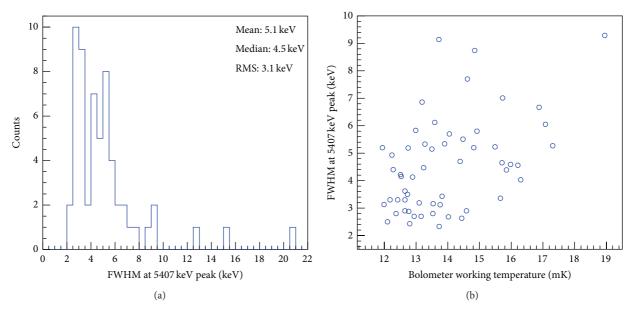
(a)

(b)

FIGURE 3: (a) Distribution of energy resolutions at 5407 keV for all CCVR bolometers. (b) Bolometer energy resolution versus detector working temperature for CCVRs 1–9.

currently running CUORE-0 detector (see Section 3) indicate that the copper surface cleaning has been effective. The expected upper limit on surface-related backgrounds in the ROI in CUORE, extrapolated from test results and the recent performance of CUORE-0, is 1-2 $\times 10^{-2}$ counts/keV/kg/y [30].

3. CUORE Prototype: CUORE-0

In order to commission the CUORE detector assembly line, confirm the effectiveness of our copper-surface-cleaning technique, and validate post-Cuoricino improvements to the tower design, we built CUORE-0, a single CUORE-type tower containing 52 TeO$_2$ bolometer modules (Figure 4(a)), and have been operating it since March 2013 [24]. CUORE-0 is the first tower produced using CUORE assembly techniques and materials, including surface-cleaned copper. The detector's total mass is 39 kg, with 11 kg of ^{130}Te isotope. In this section, we review the construction and commissioning of CUORE-0, its performance and background measurements, and its potential physics reach.

3.1. Construction and Commissioning. The CUORE-0 tower was constructed according to standard CUORE detector assembly procedures, described in Section 4.1. After being built, the tower was enclosed in a copper thermal shield and installed in the former Cuoricino cryostat. CUORE-0 therefore shares much of the same infrastructure used in Cuoricino, such as the external shielding, the Faraday cage, and the data acquisition (DAQ) hardware [36]. A Plexiglas shield surrounding the cryostat is continuously flushed with nitrogen gas to prevent ingress of radon. We operate CUORE-0 at ~13 mK due to the limitations of the aged cryostat.

The base temperature of each bolometer can be calculated from the measured resistance of its NTD thermistor

(Figure 4(b)). Of the 52-bolometer channels, one is not functional due to a failed wire bonding to its thermistor during assembly. In addition, one heater could not be bonded during assembly, and the connection to another heater was lost during the initial detector cooldown. We considered this situation acceptable and proceeded with data taking.

The DAQ hardware includes front-end preamplifiers, six-pole low-pass Bessel filters, and high-precision 18-bit National Instruments digitizers operating at 125 S/s [37, 38]. On the software side, we use the Apollo suite developed for CUORE. We record both the continuous data stream and software-triggered data samples; each bolometer module is triggered independently with a threshold in the range 50–100 keV. The detectors are calibrated using gamma lines from two thoriated tungsten strings which are lowered into guide tubes between the cryostat and external lead shield once per month. To calibrate the bolometers' response across the measured energy spectrum, we use a third-order polynomial to fit the locations of the source-generated gamma peaks in the range 511–2615 keV.

3.2. Detector Performance and Background Measurement. The offline analysis of CUORE-0 data follows a standard procedure [24] originally developed for the Cuoricino experiment [13, 36]. The heater pulses which periodically inject fixed amounts of energy into the bolometers are used to correct for small shifts in thermal gain due to temperature fluctuations. The amplitudes of the bolometer temperature pulses are extracted via optimum filtering [39] and then converted into energies using calibration data. Events occurring within ±100 ms of each other in multiple crystals are rejected to reduce background. Figure 4(c) shows the distribution of the full width half maximum (FWHM) values of the 2615 keV ^{208}Tl decay peak in calibration data for all 49 active channels

Temperature (mK)

FWHM @ 2615 keV
(keV)

(a)   (b)   (c)
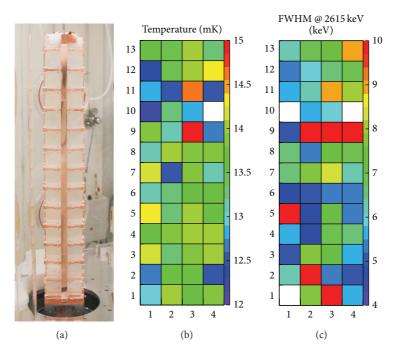
FIGURE 4: (a) The CUORE-0 tower inside a glove box during its assembly. (b) Base temperatures of the functioning CUORE-0 crystals, as calculated from the measured resistances of their thermistors in conjunction with R_0 and T_0 values previously determined in thermistor characterization studies (see Section 2). It should be mentioned that there is good evidence that a thermistor's R-T behavior can be modified by mechanical stresses caused by its glue-spot connections to the crystal, and this effect could be responsible in part for the seemingly erratic distribution of detector temperatures. (c) Energy resolution (FWHM) of each detector channel, determined from calibrations performed regularly during March–September 2013. The mean energy resolution in the calibration data is 6.8 keV, and the median is 6.0 keV.

with functional heaters used in the data analysis. At the conclusion of the first phase of data taking, the summed exposure of the individual detectors was 7.1 kg·y. We evaluate the overall detector energy resolution in the noncalibration data to be 5.7 keV, based on the FWHM of the 2615 keV peak in the energy spectrum created by summing the data for all active channels.

At present, the CUORE-0 data in the ROI for $0\nu\beta\beta$ decay of ^{130}Te is blinded while we accumulate more statistics and work on optimizing event selection. To perform the blinding, we exchange a random fraction of events within ±10 keV of the decay's Q-value with events within ±10 keV of the 2615 keV γ peak; the number and identity of the exchanged events are kept secret from the analyzers. Since the number of events in the γ peak is significantly larger than that in any possible $0\nu\beta\beta$ peak, this blinding procedure generates an artificial peak centered at the Q-value which hides any $0\nu\beta\beta$ decay signal. The ±10 keV exchange width was chosen because it is approximately twice the FWHM energy resolution of the detectors. Figure 5 shows the so-called "salted peak" and the nearby ^{60}Co γ peak.

To find the average background rate in the ROI, we use an unbinned maximum likelihood fit in which the likelihood function includes two Gaussians (for the ^{60}Co and $0\nu\beta\beta$ decay peaks) and a constant continuum which incorporates the α and γ backgrounds. The fitted background rate is 0.071 ± 0.011 counts/keV/kg/y. The main background contributions in the ROI are γ rays from decay of ^{208}Tl coming from ^{232}Th
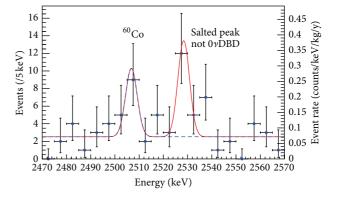
FIGURE 5: CUORE-0 background spectrum in the ROI, with a salted peak at the Q-value for $0\nu\beta\beta$ decay of ^{130}Te. The solid red line shows the result of an unbinned maximum-likelihood fit to the full spectrum, while the dotted blue line indicates the fit's background component, consisting of the ^{60}Co peak and a uniform continuum. The fit value for the continuum background is 0.071 ± 0.011 counts/keV/kg/y (from [24]).

in the cryostat and α particles from radioactive decays on the surface of the detector materials. The former is expected to be similar to the γ background measured in Cuoricino at 0.05-0.06 counts/keV/kg/y, while the latter can be extrapolated from the measured background rate at higher energies in the range 2.7–3.9 MeV. Any deviation from a constant (i.e., flat)
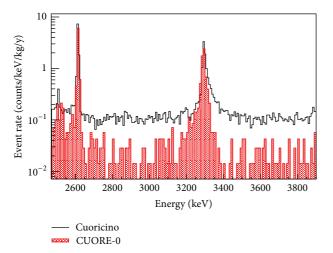
FIGURE 6: Background spectra from CUORE-0 (shaded, red) and Cuoricino (black) in the energy region dominated by degraded α particles [24]. The sixfold reduction in background achieved by CUORE-0 in the energy ranges 2.7–3.1 MeV and 3.4–3.9 MeV is clearly evident. The prominent peak at 3.3 MeV is from decay of ^{190}Pt, which is present in the TeO$_2$ crystals from their growth. The non-Gaussian shape of the peak is due to the fact that these spectra are made by summing the contributions from many detector channels having different (Gaussian) energy resolutions and positions, the variations in the latter arising because of calibration uncertainties.

continuum background is contained in the systematic error of the fitted background rate.

The α continuum from 2.7–3.9 MeV (excluding the peak in the range 3.1–3.4 MeV from decay of ^{190}Pt in the crystals) is above all naturally occurring γ lines, so the background in that region mainly comes from α particles whose energy has been degraded. In Figure 6, we compare CUORE-0 with Cuoricino in the α continuum region and find that the CUORE-0 background rate is 0.019 ± 0.002 counts/keV/kg/y, a factor of six less than in Cuoricino, 0.110 ± 0.001 counts/keV/kg/y.

3.3. Projected Sensitivity. CUORE-0 data taking is ongoing and expected to continue until CUORE comes online in early 2015. With its improved background compared to the previous generation of bolometer experiments, CUORE-0 has the potential to make a significant improvement on the limit for $0\nu\beta\beta$ of ^{130}Te. With roughly one year of livetime, CUORE-0 should surpass the half-life limit on $0\nu\beta\beta$ decay of ^{130}Te established by Cuoricino at 2.8×10^{24} y (90% C.L.) [24].

4. CUORE Status

In parallel with CUORE-0 data taking, we have also been building the CUORE detectors and experimental setup in Hall A at the LNGS underground facility. This work is scheduled to continue until the end of 2014, with the goal of turning on the experiment in early 2015.

4.1. Detector Assembly. Construction of the 19 detector towers is a lengthy, delicate activity that demands a sizable share of the collaboration's attention and resources. The assembly process is divided into four stages: gluing of thermistors and heaters to crystals, physical assembly of instrumented crystals into a tower, attachment of readout cables to the tower, and wire bonding of the crystals' chips to the readout cables. To minimize oxidization and contamination (especially by radon [40]), all of these operations are carried out using clean tools inside nitrogen-flushed glove boxes in a dedicated clean room on the first floor of the CUORE hut. Completed towers are stored in nitrogen-flushed canisters to await future installation in the cryostat all at once.

The gluing of semiconductor chips to crystals is performed inside a dedicated glove box by a semiautomated robotic system to achieve precise and uniform results. First, a cartesian robot equipped with a pneumatic gun dispenses matrices of uniformly sized dots of Araldite Rapid bicomponent epoxy on an upturned thermistor and heater placed atop a precision positioning device. Before the epoxy dots begin to cure, a robotic arm fetches a crystal and places it on a cradle above the chips; an actuator then immediately lowers the crystal to a position where it is separated from the chips by 50 μm. The crystal is left to cure undisturbed for a minimum of 50 minutes before being removed from the positioning device with its newly attached chips. For quality control purposes, we take pictures of the epoxy dots before and after the chips are attached to the crystal. Crystal gluing is a near-continuous activity and typical system throughput during normal operation is 6 crystals/day, or roughly one tower's worth of crystals every two weeks. Finished crystals are kept in vacuum-sealed containers inside nitrogen-flushed storage cabinets to await assembly into towers.

All subsequent tower-assembly operations are performed at a workstation containing a nitrogen-flushed storage garage and a work surface that can host a series of task-specific glove boxes and tools. In order to increase operational efficiency, we generally try to assemble towers in batches of 3-4 at a time.

The first task is to physically assemble chip-equipped crystals, specially treated ultraclean copper pieces [31], and PTFE spacers—almost 500 separate parts in all—into a tower. The tower is built one floor at a time, descending into the storage garage as it grows in size.

Once a tower is built, the next step is to install two sets of flexible printed circuit board (PCB) cables on opposite sides of it to provide the electrical connections to the cryostat wiring. The cables, which consist of wire traces etched from copper sheet on polyethylene naphthalate (PEN) substrate, are 2.4 m in length to run from the bottom floor of the tower up to the cryostat's mixing-chamber plate. The readout traces terminate in bonding pads located on horizontal arms extending from either side of the readout cables at each tower floor. We first glue the flexible PCB cables to a rigid copper backing using Araldite Standard bicomponent epoxy, and after curing overnight the cable assembly is affixed to the tower frame.

The last step is to connect the crystals' semiconductor chips to the PCB cable traces with 25 μm gold wires. This is accomplished using a modified Westbond 7700E manual wire bonder which has been oriented vertically and mounted on motor-driven rails to enable precise horizontal motion.

(a)

(b)
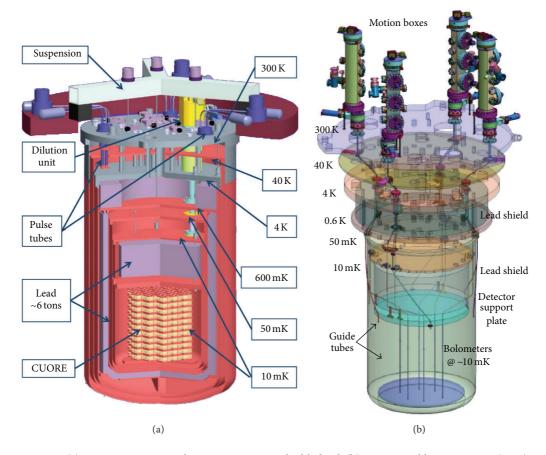
FIGURE 7: (a) CUORE cryostat, with major components highlighted. (b) Detector calibration system (DCS).

The 8 mm difference in depth between the chip pads and the copper-trace pads is beyond the wire bonder's reach, so the horizontal rails extend the access depth and make bonding possible. Each gold wire is first ball bonded to a chip pad and then wedge bonded to a copper pad, and then the wedge bond is reinforced with a security ball bond. Two wires are bonded for each electrical connection to provide redundancy. After bonding work on a tower is complete, protective copper covers are installed over the PCB cables and the finished tower is placed inside a nitrogen-flushed storage canister.

CUORE tower assembly began in January 2013, and the full complement of 19 towers was completed in Summer 2014.

4.2. Cryogenics and Calibration Systems. The other major challenges in building CUORE are constructing the cryogenics and calibration systems, which will comprise large, complex, interconnected parts packed close together and operating under extremely cold conditions. Given the relatively long time (~1 month) needed to close the cryostat and cool the detectors to base temperature, as well as the anticipated five-year running time for the experiment, it is essential that all cryostat systems be carefully designed for robust performance.

The cryogenics system (**Figure 7(a)**) encompasses the cryostat and a cryogen-free cooling system, the latter comprising five pulse-tube coolers and a dilution-refrigerator

unit [41]. The cryostat will consist of six nested copper vessels at 300 K (Outer Vacuum Chamber), 40 K, 4 K (Inner Vacuum Chamber), 0.6 K (Still), 0.05 K (Heat Exchanger), and 0.01 K (Mixing Chamber). Construction of all six vessels is complete. We are taking a phased approach to commissioning the cryostat, having started with the outer three vessels instrumented with three pulse tubes [42]. We cooled down this partial system twice, successfully reaching 3.5 K on the 4 K plate on the second attempt. The three inner vessels have been cleaned and delivered to LNGS and are presently being installed. To reduce vibrational noise, the detector will be suspended from a Y-beam whose supports are decoupled from the surrounding building structure and the cryostat.

In parallel with cryostat commissioning, the dilution unit (DU)—a custom-built, closed-cycle, high-power ^{3}He/^{4}He dilution refrigerator—was characterized in its own custom test cryostat. The DU was delivered to LNGS in Summer 2012 after passing in-house benchmarking at Leiden Cryogenics. It reached 5 mK base temperature at LNGS with a cooling power of 5 μW at 12 mK. During stable cryostat operation, the DU and a subset of the five pulse-tube coolers will provide enough cooling power to maintain the detector at base temperature. However, those devices do not have sufficient power to cool down the multiton apparatus from room temperature in a reasonable time. For this reason the DU and pulse tubes will be supplemented during cooldowns with

a fast-cooling system—namely, a forced He gas circulation system designed to improve the thermal exchange inside the cryostat and thereby reduce the cooling time to ~one month.

The detector calibration system (DCS) will be used to lower 12 radioactive source strings under their own weight through a set of guide tubes from the 300 K flange into the 10 mK detector region for the purpose of monthly energy calibrations. The DCS consists of a computer-controlled vacuum motion system above the 300 K flange, a thermalization mechanism at the 4 K flange, and guide tubes which snake through the cryostat's interior and run down between the detectors (Figure 7(b)). The sources are copper-covered capsules of thoriated tungsten crimped at intervals along a Kevlar string and coated with PTFE to minimize friction. A key challenge is developing a robust system that will not exceed the stringent heat-load constraints of the successive temperature stages inside the cryostat during the insertion and retrieval of source strings. During a test cooldown of the outer cryostat to 4 K, we successfully tested a complete calibration source deployment unit operating two strings.

All of the copper components that will be cooled to base temperature—the 10 mK plate and vessel, the tower frames, the tower-suspension plate, and the DCS tubes—are made of radiopure electrolytic tough pitch copper alloy [31, 41]. All other copper components in the cryostat are made of oxygen-free electrolytic (OFE) copper alloy [41, 42].

Electrical signals from the detectors will be carried up to the coldest stage of the cryostat by PCB wires and then to the outside world via NbTi wires running between the Mixing Chamber plate (0.01 K) and the top of the cryostat (300 K). The wires will be arranged in six bundles inserted through six 40 mm inner bore access ports placed between the 300 K and 4 K flanges. The wires will be cooled only by radiation inside the boreholes; below 4 K, the wires will be cooled by conduction through thermalization clamps connected to each cold stage of the refrigerator.

4.3. Electronics and Data Acquisition Hardware. The CUORE electronics will provide an effective low-noise system for reading and monitoring the detectors. The main boards consist of 8-layer 233×280 mm^2 PCBs which accommodate 6 channels each. Each channel consists of a preamplifier and a programmable-gain amplifier, load resistors, a detector biasing system, and a number of other circuits that enable the DC characterization of each thermistor and the monitoring of many voltage nodes. The antialiasing Bessel filter boards have programmable cutoff frequencies in the range 15–120 Hz, allowing for optimal analog filtering when used in conjunction with the new DAQ system that has higher sampling rates than the system that was used for Cuoricino and which is currently being used for CUORE-0. The production, characterization, and calibration of the electronics are in progress.

We are in the process of procuring all CUORE data acquisition (DAQ) hardware, including National Instruments NI-628x-series high-precision 18-bit digitizers. A small DAQ system, based on a single chassis, will be used for upcoming commissioning tests of the CUORE cryostat while we configure and test the full DAQ.

A Faraday cage will be needed to shield the signal links between the detectors and the front-end electronics from disturbances coming from the main power line (50 Hz), the cryogenic pumps, and any other electromagnetic interferences which could be injected from outside. The cage will be located atop the cryostat, on the second floor of the CUORE building, and have a volume of ~$6 \times 6 \times 3$ m^3 and a total surface area of ~150 m^2. The design specification is for a 60 dB attenuation at 50 Hz.

The CUORE slow control system will use LabVIEW for the instrumentation drivers, while the network layer will use one of the standard protocols available within LabVIEW and will store data in a schemaless database [43] as well as in the CUORE SQL analysis database. Custom packages will be used for high-level user interfaces, including web-based clients for monitoring and alarms. The slow control system is currently under development.

4.4. Data Acquisition and Analysis Software. CUORE will use a custom-built DAQ software package named Apollo that has been designed to read signals from ~1000 bolometers. Apollo will digitize the analog waveforms, run trigger algorithms, and store data for offline analysis. Data are saved in two formats: triggered bolometer pulses are saved to ROOT files [44] while the continuous waveforms are saved to compressed ASCII files. Detector parameters and run configurations are stored in an SQL database which is also used for offline data analysis. Apollo provides graphical user interfaces for run control and monitoring and a slow-control system for interacting with the front-end electronics. It also includes tools for the automated detector characterization to be performed in the start-up phase of the experiment. Apollo has been tested extensively in our experimental setups at Hall A and Hall C, most recently during CUORE-0 data taking.

For data analysis, we use a custom-built software framework named Diana, which was developed using a plugin architecture in C++. Diana has been used extensively as our standard tool for analyzing data from R&D runs, Cuoricino, and CUORE-0. As we analyze the CUORE-0 data, we are continuing to build upon the standard analysis procedure (see Section 3.2), developing new features such as noise decorrelation [45] and a web-based data quality monitoring system.

5. Conclusion and Outlook

With its large detector mass and an excellent anticipated energy resolution, CUORE is one of the most sensitive $0\nu\beta\beta$ decay experiments under construction. Figure 8(a) shows the experiment's projected half-life sensitivity to ^{130}Te $0\nu\beta\beta$ decay as a function of livetime, assuming the target background rate of 0.01 counts/keV/kg/y is achieved. After five years of livetime, CUORE should reach a 1σ (90% C.L.) sensitivity of 1.6×10^{26} y (9.5×10^{25} y) on the half-life of $0\nu\beta\beta$ decay of ^{130}Te.
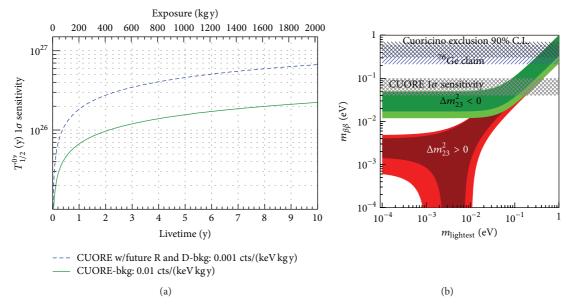
FIGURE 8: (a) Projected CUORE 1σ sensitivity to the half-life of $0\nu\beta\beta$ decay of ^{130}Te as a function of detector livetime. The solid green line shows the sensitivity for the target background rate of 0.01 counts/keV/kg/y, while the dashed blue line shows a speculative future scenario in which the background is ten times lower. (b) The corresponding 1σ sensitivity to effective Majorana mass versus the lightest neutrino mass after five years of detector livetime. The spread in the projected CUORE $m_{\beta\beta}$ bands arises from uncertainties in calculations of the nuclear matrix elements used to convert a measured half-life into an effective Majorana mass. The green band labeled $\Delta m_{23}^2 < 0$ denotes the inverted neutrino mass hierarchy while the red band labeled $\Delta m_{23}^2 > 0$ indicates the normal mass hierarchy. For both, the darker inner bands represent regions allowed by the best-fit neutrino oscillation parameters in the PMNS matrix, while the lighter outer bands extend to 3σ coverage. Both figures are from [23].

For $0\nu\beta\beta$ decay involving exchange of light Majorana neutrinos, the half-life $T_{1/2}^{0\nu}$ can be expressed as

$$\left(T_{1/2}^{0\nu}\right)^{-1} = G^{0\nu}(Q, Z) \left|M^{0\nu}\right|^2 \frac{\left|\langle m_{\beta\beta}\rangle\right|^2}{m_e^2}, \qquad (3)$$

where $G^{0\nu}(Q)$ is an accurately calculable phase-space factor which scales with the decay's Q-value as Q^5, $M^{0\nu}$ is the nuclear matrix element for the process, which carries a large uncertainty due to the range of results calculated from various models, and $|\langle m_{\beta\beta}\rangle|$ is the so-called effective Majorana neutrino mass which correlates $0\nu\beta\beta$ decay with neutrino mixing parameters [1]. This formula enables conversion of an experimentally measured $0\nu\beta\beta$ decay half-life (or lower limit thereof) into an effective Majorana mass (or upper limit thereof). For CUORE, five years of livetime should yield a 1σ (90% C.L.) sensitivity to an effective Majorana mass in the range 40–100 meV (50–130 meV), which overlaps the top edge of the allowed band for the inverted mass hierarchy (Figure 8(b)).

The successful commissioning of CUORE-0 and its promising background rates represent a significant milestone for CUORE. The average energy resolutions of the CUORE-0 bolometers are on par with Cuoricino and are among the best seen in large-mass bolometer arrays, even before optimization and while running at a suboptimal working temperature. We find that the background rates in the α continuum region and the ROI are lower by a factor of 6 and 2, respectively, with respect to Cuoricino. This success in

reducing the background has confirmed the efficacy of our copper-cleaning techniques and detector-assembly methods. We intend to continue operating CUORE-0 until CUORE begins data taking, by which time CUORE-0 should have become the most sensitive experiment searching for $0\nu\beta\beta$ decay of ^{130}Te.

CUORE is now in an advanced state of construction, making steady progress in all respects. Detector assembly was recently completed, and the phased commissioning of the cryostat and integration of its many interconnected systems, including the DCS and the dilution unit, is ongoing. We plan to complete the integration and commissioning of CUORE at the end of 2014 and commence data taking in the first half of 2015.

Conflict of Interests

The authors declare that there is no conflict of interests regarding the publication of this paper.

Acknowledgments

References

[1] J. Beringer, J. F. Arguin, R. M. Barnett et al., "Review of particle physics," *Physical Review D*, vol. 86, Article ID 010001, 2012.

[2] G. Bellini, L. Ludhova, G. Ranucci, and F. L. Villante, "Neutrino oscillations," *Advances in High Energy Physics*, vol. 2014, Article ID 191960, 28 pages, 2014.

[3] E. Majorana, "Teoria simmetrica dell'elettrone e del positrone," *Il Nuovo Cimento*, vol. 14, no. 4, pp. 171–184, 1937.

[4] F. T. Avignone, S. R. Elliott, and J. Engel, "Double beta decay, Majorana neutrinos, and neutrino mass," *Reviews of Modern Physics*, vol. 80, p. 481, 2008.

[5] S. M. Bilenky and C. Giunti, "Neutrinoless double-beta decay. A brief review," *Modern Physics Letters A*, vol. 27, Article ID 1230015, 2012.

[6] H. V. Klapdor-Kleingrothaus, I. V. Krivosheina, A. Dietz, and O. Chkvorets, "Search for neutrinoless double beta decay with enriched ^{76}Ge in Gran Sasso 1990–2003," *Physics Letters B: Nuclear, Elementary Particle and High-Energy Physics*, vol. 586, no. 3-4, pp. 198–212, 2004.

[7] H. V. Klapdor-Kleingrothaus and I. V. Krivosheina, "The evidence for the observation of $0\nu\beta\beta$ decay: the identification of $0\nu\beta\beta$ events from the full spectra," *Modern Physics Letters A*, vol. 21, no. 20, pp. 1547–1566, 2006.

[8] M. Auger, D. J. Auty, P. S. Barbeau et al., "Search for neutrinoless double-beta decay in ^{136}Xe with EXO-200," *Physical Review Letters*, vol. 109, Article ID 032505, 2012.

[9] A. Gando, Y. Gando, and H. Hanakago, "Limit on Neutrinoless $\beta\beta$ decay of ^{136}Xe from the first phase of KamLAND-Zen and comparison with the positive claim in ^{76}Ge," *Physical Review Letters*, vol. 110, Article ID 062502, 2013.

[10] M. Agostini, M. Allardt, E. Andreotti et al., "Results on neutrinoless double-β^{76}Ge decay of from phase I of the GERDA experiment," *Physical Review Letters*, vol. 111, Article ID 122503, 2013.

[11] C. Arnaboldi, F. T. Avignone III, and J. Beeman, "CUORE: a cryogenic underground observatory for rare events," *Nuclear Instruments and Methods in Physics Research A: Accelerators, Spectrometers, Detectors and Associated Equipment*, vol. 518, no. 3, pp. 775–798, 2004.

[12] R. Ardito, C. Arnaboldi, D. R. Artusa, and CUORE Collaboration, "CUORE: a cryogenic underground observatory for rare events," http://arxiv.org/abs/hepex/0501010.

[13] E. Andreotti, C. Arnaboldi, F. T. Avignone et al., "^{130}Te neutrinoless double-beta decay with CUORICINO," *Astroparticle Physics*, vol. 34, no. 11, pp. 822–831, 2011.

[14] M. Redshaw, B. J. Mount, E. G. Myers, and F. T. Avignone III, "Masses of ^{130}Te, ^{130}Xe and double-beta-decay Q-value of ^{130}Te," *Physical Review Letters*, vol. 102, no. 21, Article ID 212502, 2009.

[15] N. D. Scielzo, S. Caldwell, and G. Savard, "Double-β decay Q values of ^{130}Te, ^{128}Te, and ^{120}Te," *Physical Review C*, vol. 80, Article ID 025501, 2009.

[16] S. Rahaman, V.-V. Elomaa, T. Eronen et al., "Double-beta decay Q values of ^{116}Cd and ^{130}Te," *Physics Letters B*, vol. 703, no. 4, pp. 412–416, 2011.

[17] M. A. Fehr, M. Rehkämper, and A. N. Halliday, "Application of MC-ICPMS to the precise determination of tellurium isotope compositions in chondrites, iron meteorites and sulfides," *International Journal of Mass Spectrometry*, vol. 232, no. 1, pp. 83–94, 2004.

[18] C. Arnaboldi, "Production of high purity TeO$_2$ single crystals for the study of neutrinoless double beta decay," *Journal of Crystal Growth*, vol. 312, p. 2999, 2010.

[19] E. E. Haller, "Advanced far-infrared detectors," *Infrared Physics & Technology*, vol. 35, pp. 127–146, 1994.

[20] D. McCammon, "Semiconductor thermistors," *Applied Physics*, vol. 99, pp. 35–61, 2005.

[21] E. Andreotti, C. Brofferio, L. Foggetta et al., "Production, characterization, and selection of the heating elements for the response stabilization of the CUORE bolometers," *Nuclear Instruments and Methods in Physics Research A*, vol. 664, pp. 161–170, 2012.

[22] A. Alessandrello, C. Brofferio, C. Bucci et al., "Methods for response stabilization in bolome-ters for rare decays," *Nuclear Instruments and Methods in Physics Research A: Accelerators, Spectrometers, Detectors and Associated Equipment*, vol. 412, pp. 454–464, 1998.

[23] F. Alessandria, R. Ardito, D. R. Artusa (CUORE Collaboration), and CUORE Collaboration "Sensitivity and discovery potential of CUORE to neutrinoless double-beta decay," Submitted, http://arxiv.org/abs/1109.0494.

[24] D. R. Artusa, F. T. Avignone III, O. Azzolini et al., "Initial performance of the CUORE-0 experiment," *The European Physical Journal C*, vol. 74, article 2956, 2014.

[25] F. Alessandria, E. Andreotti, and R. Ardito, "CUORE crystal validation runs: results on radioactive contamination and extrapolation to CUORE background," *Astroparticle Physics*, vol. 35, pp. 839–849, 2012.

[26] M. Ambrosio, R. Antolini, G. Auriemma et al., "Vertical muon intensity measured with MACRO at the Gran Sasso laboratory," *Physical Review D*, vol. 52, no. 7, pp. 3793–3802, 1995.

[27] D. Mei and A. Hime, "Muon-induced background study for underground laboratories," *Physical Review D*, vol. 73, no. 5, Article ID 053004, 2006.

[28] M. Selvi, "Analysis of the seasonal modulation of the cosmic muon flux in the LVD detector during 2001–2008," in *Proceedings of the 31st International Cosmic Ray Conference (ICRC '09)*, 2009.

[29] G. Bellini, J. Benziger, D. Bick et al., "Cosmic-muon flux and annual modulation in Borexino at 3800 m water-equivalent depth," *Journal of Cosmology and Astroparticle Physics*, vol. 2012, article 015, 2012.

[30] D. R. Artusa et al., "Projected background budget of the CUORE experiment," to be submitted.

[31] F. Alessandria, R. Ardito, D. R. Artusa et al., "Validation of techniques to mitigate copper surface contamination in CUORE," *Astroparticle Physics*, vol. 45, pp. 13–22, 2013.

[32] A. Alessandrello, C. Arpesella, C. Brofferio et al., "Measurements of internal radioactive contamination in samples of Roman lead to be used in experiments on rare events," *Nuclear

Instruments and Methods in Physics Research B: Beam Interactions with Materials and Atoms, vol. 142, no. 1-2, pp. 163–172, 1998.

[33] E. Andreotti, C. Arnaboldi, F. T. Avignone III et al., "Muon-induced backgrounds in the CUORICINO experiment," *Astroparticle Physics*, vol. 34, no. 1, pp. 18–24, 2010.

[34] F. Bellini, C. Bucci, S. Capelli et al., "Monte Carlo evaluation of the external gamma, neutron and muon induced background sources in the CUORE experiment," *Astroparticle Physics*, vol. 33, no. 3, pp. 169–174, 2010.

[35] D. R. Artusa et al., "Validation of parylene coating technique to suppress copper surface contamination in CUORE," to be submitted.

[36] C. Arnaboldi, D. R. Artusa, and F. T. Avignone III, "Results from a search for the $0\nu\beta\beta$-decay of ^{130}Te," *Physical Review C*, vol. 78, Article ID 035502, 2008.

[37] C. Arnaboldi, C. Bucci, S. Capelli et al., "The front-end readout for CUORICINO, an array of macro-bolometers and MIBETA, an array of μ-bolometers," *Nuclear Instruments and Methods in Physics Research A*, vol. 520, no. 1–3, pp. 578–580, 2004.

[38] C. Arnaboldi, M. Cariello, S. Di Domizio, A. Giachero, and G. Pessina, "A programmable multichannel antialiasing filter for the CUORE experiment," *Nuclear Instruments and Methods in Physics Research A*, vol. 617, pp. 327–328, 2010.

[39] E. Gatti and P. F. Manfredi, "Processing the signals from solid-state detectors in elementary-particle physics," *La Rivista del Nuovo Cimento*, vol. 9, no. 1, pp. 1–146, 1986.

[40] M. Clemenza, C. Maiano, L. Pattavina, and E. Previtali, "Radon-induced surface contaminations in low background experiments," *The European Physical Journal C*, vol. 71, article 1805, 2011.

[41] A. Nucciotti, F. Alessandria, M. Ameri et al., "Status of the cryogen-free cryogenic system for the CUORE experiment," *Journal of Low Temperature Physics*, vol. 167, no. 3-4, pp. 528–534, 2012.

[42] E. Ferri, D. Bagliani, M. Biassotti et al., "Preliminary results of the MARE experiment," *Journal of Low Temperature Physics*, vol. 176, no. 5-6, pp. 885–890, 2014.

[43] K. Chodorow and M. Dirolf, *MongoDB—The Definitive Guide: Powerful and Scalable Data Storage*, O' Reilly, 2010.

[44] R. Brun and F. Rademakers, "ROOT: an object oriented data analysis framework," *Nuclear Instruments and Methods in Physics Research A*, vol. 389, no. 1-2, pp. 81–86, 1997.

[45] C. Mancini-Terracciano and M. Vignati, "Noise correlation and decorrelation in arrays of bolometric detectors," *Journal of Instrumentation*, vol. 7, Article ID P06013, 2012.

Review Article
Beyond Standard Model Searches in the MiniBooNE Experiment

Teppei Katori[1] and Janet M. Conrad[2]

[1]*Queen Mary University of London, London E1 4NS, UK*
[2]*Massachusetts Institute of Technology, Cambridge, MA 02139, USA*

Correspondence should be addressed to Teppei Katori; t.katori@qmul.ac.uk

The MiniBooNE experiment has contributed substantially to beyond standard model searches in the neutrino sector. The experiment was originally designed to test the $\Delta m^2 \sim 1\,\text{eV}^2$ region of the sterile neutrino hypothesis by observing $\nu_e(\bar{\nu}_e)$ charged current quasielastic signals from a $\nu_\mu(\bar{\nu}_\mu)$ beam. MiniBooNE observed excesses of ν_e and $\bar{\nu}_e$ candidate events in neutrino and antineutrino mode, respectively. To date, these excesses have not been explained within the neutrino standard model (νSM); the standard model extended for three massive neutrinos. Confirmation is required by future experiments such as MicroBooNE. MiniBooNE also provided an opportunity for precision studies of Lorentz violation. The results set strict limits for the first time on several parameters of the standard-model extension, the generic formalism for considering Lorentz violation. Most recently, an extension to MiniBooNE running, with a beam tuned in beam-dump mode, is being performed to search for dark sector particles. This review describes these studies, demonstrating that short baseline neutrino experiments are rich environments in new physics searches.

1. Introduction

Across the particle physics community, the mysterious periodic-table-like nature of the standard model (SM) is motivating searches for new particles, new forces, and new properties of the particles that are known. The neutrino sector is proving a rich environment for these searches. Having already found one beyond standard model (BSM) effect, neutrino mass [1], a series of experiments are pursuing other potential signals. Unlike the case of three-neutrino oscillation measurements within νSM, many of these searches are pursued over short baselines, from a few meters to approximately a kilometer. The Mini Booster Neutrino Experiment (MiniBooNE) at Fermi National Accelerator Laboratory (Fermilab) is an excellent example, having contributed substantially to BSM studies.

This review describes the MiniBooNE BSM program. We begin by describing the experiment. This is followed by a discussion of the MiniBooNE cross section studies, which have been essential input to both the BSM searches within this experiment and also to other experiments, including T2K

most recently [2]. We then describe three searches: the sterile neutrino search which motivated the experiment, Lorentz violation searches which set the first limits on five neutrino sector parameters, and the search for dark sector particles which is now being pursued with a reconfigured beam.

2. MiniBooNE Experiment

MiniBooNE (running from 2002 to 2012) was originally designed to test the LSND signal [3]. In the LSND experiment, low energy (0 to 53 MeV) muon antineutrinos were produced by pion decay-at-rest (DAR) and were detected by the liquid-scintillator-based LSND detector at 31 m from the target. The observed 3.8σ excess of $\bar{\nu}_e$ candidate events could be interpreted as oscillations in the $\Delta m^2 \sim 1\,\text{eV}^2$ region within a simple two massive neutrino oscillation hypothesis, where the oscillation probability is given by

$$P\left(\bar{\nu}_\mu \longrightarrow \bar{\nu}_e\right) = \sin^2 2\theta \sin^2\left(\frac{1.27\Delta m^2 L}{E}\right). \tag{1}$$

(a)

(b)

(c)
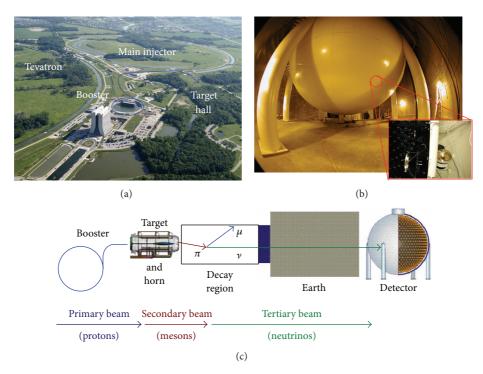
FIGURE 1: The MiniBooNE experiment layout [4]. (a) The Fermilab accelerator complex. (b) The MiniBooNE detector, with inset showing the black inner volume and the white outer volume. (c) Schematic layout of the beam and detector [18].

Here, θ and Δm^2 are oscillation parameters to control the amplitude and the period, respectively (further discussed in Section 4), L is the distance from neutrino production to interaction in meters, and E is the energy of the neutrino in MeV.

An experiment which maintains the same L/E ratio should observe an oscillation probability consistent with LSND if the simple two neutrino model is a good approximation of the underlying effect. However, by employing an average E which is an order of magnitude larger than LSND, the systematic errors associated with production and decay are quite different. If L is increased accordingly, and no signal is observed, this rules out the two-neutrino oscillation hypothesis of the LSND result.

MiniBooNE was designed with this in mind. The Mini-BooNE beam peaked at ~700 MeV and the Cherenkov detector was located at ~500 m baseline. Figure 1 shows an overview of the MiniBooNE design [4], and in the remainder of this section we provide more details.

2.1. Booster Neutrino Beam-Line. The Booster Neutrino Beam-line (BNB) extracts 8 GeV kinetic energy protons from the Fermilab Booster, a 149 m diameter synchrotron (Figure 1(a)). Eighty-one bunches, separated in time by $\sim$ 19 ns, are extracted by a fast kicker within a $\sim$1.6 μs pulse. Each pulse contains around 4×10^{12} protons. Typically, four to five pulses per second were sent to BNB to produce the neutrino beam.

This high intensity proton pulse collides with a beryllium target to produce a shower of mesons (Figure 1(c)). The target is located within a magnetic focusing horn. For neutrino mode running, the toroidal field generated by the horn focuses on positive mesons, with π^+ decay-in-flight (DIF) as the primary source of the ν_μ beam. In antineutrino mode running, the horn focuses on negative mesons to create the $\overline{\nu}_\mu$ dominant beam. The details of the BNB neutrino flux prediction can be found in [5].

MiniBooNE collected 6.46×10^{20} proton-on-target (POT) in neutrino mode and 11.27×10^{20} POT in antineutrino mode.

2.2. The MiniBooNE Detector. The MiniBooNE detector, located 541 m away from the target, is a mineral-oil-based Cherenkov detector. The 12.2 m spherical tank, filled with pure mineral oil, $(CH_2)_n$, has two optically separated regions. The interior region, lined by 1280 8-inch photomultiplier tubes (PMTs), contains the target volume. An outer volume, equipped with 240 8-inch PMTs, serves as the veto region [6]. The presence of a charged particle above threshold is detected through the Cherenkov radiation observed by PMTs. As seen from Figure 1(b), the inner volume is painted black to prevent scattering of the Cherenkov light, improving the reconstruction precision. On the other hand, the outer volume is painted white to enhance scattering of Cherenkov light, in order to achieve the 99.9% rejection of cosmic rays by the veto [7] even with fairly sparse PMT coverage. The charge and time information from all PMTs is used to reconstruct kinematics of charged-lepton and electromagnetic events. MiniBooNE mineral oil produces a small amount of scintillation light which can be used to reconstruct the total energy of the interaction via calorimetry, which is particularly important for particles below Cherenkov threshold.
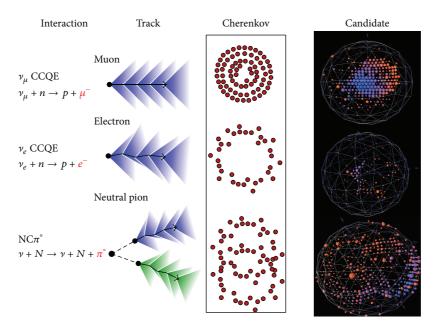
FIGURE 2: (Color online) MiniBooNE particle reconstruction [4]. From top to bottom, a muon neutrino charged-current quasielastic (CCQE) interaction, an electron neutrino CCQE interaction, and a neutral current, neutral pion production (NC1$\pi°$) interaction. The second and the third columns show the characteristics of tracks and Cherenkov rings [7], and the last column shows the event displays of candidate events.

For the $\nu_\mu \rightarrow \nu_e$ ($\overline{\nu}_\mu \rightarrow \overline{\nu}_e$) oscillation study, the following three particle reconstruction algorithms were the most important: single Cherenkov rings from (1) a muon and (2) an electron and the two-ring electromagnetic shower topology from (3) a neutral pion decay to two gammas. Figure 2 shows the different characteristics of these three signals, including examples of typical events in the detector [4].

The reconstruction algorithms can also reconstruct more complicated topologies important for constraining backgrounds and for cross section studies discussed below. The charged-current single charged pion (CC1π^+) interaction reconstruction algorithm [8] fit two Cherenkov rings from final state particles, a charged lepton, and a positive pion, to find their kinematics. The charged-current single neutral pion (CC1$\pi°$) interaction reconstruction algorithm [9] fit a charged lepton and a neutral pion (which consists of two electromagnetic showers, that is, the algorithm fits for three Cherenkov rings). Another algorithm identifies and reconstructs the neutral current elastic (NCE) interaction [10], where the total kinetic energy of final state nucleons is found using scintillation light.

Along with reconstruction of the light topology in the detector, event identification also relies upon "subevents." These are bursts of light separated in time which indicate a sequence of decay. For example, a muon which stops and then emits a decay ("Michel") electron will produce two subevents, one from the initial muon and the one from the Michel electron.

3. MiniBooNE Cross Section Results

All searches for BSM physics rely on a precise understanding of SM interactions. However, when MiniBooNE began

running, there was little neutrino cross section data in the 100 MeV to few GeV energy regime. In response, MiniBooNE developed a highly successful campaign of cross section measurements, some of which are described here. These results are interesting by themselves and also can be used as direct inputs to the BSM analyses, as described later in this paper.

MiniBooNE's beam is among the first high-statistics, high purity fluxes in the energy range from 100 to 1500 MeV. The observation of the resulting events in a large, isotropic detector with 4π coverage is unique. Within this detector it is relatively easy to achieve uniform angular acceptance. Also, the active veto makes it possible to measure NC interactions effectively. Insensitivity of hadronic details worked in positively. The hadron multiplicity often causes confusions for tracker detectors. Although the MiniBooNE detector cannot measure multiple hadron tracks, it measures total energy of low energy hadrons (such as protons below Cherenkov threshold from CCQE interactions) in calorimetric way, and, as a result, the details of final state interactions (FSIs), such as rescattering, absorption, and charge exchange, do not strongly affect reconstruction of kinematics.

Perhaps most importantly to the overall impact of the data, the MiniBooNE collaboration provided the cross section data in a form that is most useful to theorists. Traditionally, cross section data have been presented either as a function of neutrino energy (E_ν) or 4-momentum transfer (Q^2). This presentation is problematic in the MiniBooNE energy region, because of the importance of nuclear effects: Fermi motion smears the kinematics, binding energy shifts the energy spectrum, nucleon correlations affect both energy dependence and normalization of cross sections, and pions may be created, absorbed, and charge-exchanged within

the nuclear environment. These nuclear processes modify the features of primary neutrino-nucleon interactions, and so model dependent corrections are required to reconstruct E_ν and Q^2. This model dependence is problematic because there are a wide range of models available [11–15].

Instead, MiniBooNE chose to publish flux-integrated differential cross sections in terms of measured kinematic variables, which are essentially model-independent. These results have the detector efficiency unfolded but are presented without any other corrections. In particular, the neutrino flux is not unfolded. The result is data that is neutrino beam specific, and theoretical models are comparable only if those models are convoluted with the MiniBooNE predicted neutrino flux. However, this is trivial for all theorists to do, given that MiniBooNE published a first-principles flux prediction [16]. This isolates all model dependence in the data-to-prediction comparison entirely to the "prediction" side of the discussion. The data remains completely general. For this reason, the MiniBooNE cross section data are widely used to study and compare theoretical models. In this section, we describe each cross section measurement briefly.

3.1. Charged-Current Quasielastic (CCQE) Scattering. The CCQE interaction is the primary interaction at MiniBooNE energies. This interaction is used to detect $\nu_\mu(\bar{\nu}_\mu)$ and $\nu_e(\bar{\nu}_e)$ candidate events in the oscillation and Lorentz violation analyses:

$$\begin{aligned} \nu_\mu + n &\longrightarrow \mu^- + p, \\ \bar{\nu}_\mu + p &\longrightarrow \mu^+ + n, \\ \nu_e + n &\longrightarrow e^- + p, \\ \bar{\nu}_e + p &\longrightarrow e^+ + n. \end{aligned} \quad (2)$$

Therefore, a strong understanding of this channel is essential. High statistics $\nu_\mu(\bar{\nu}_\mu)$ interactions are used to study outgoing lepton kinematics [17]. The observable of this channel is the outgoing muon, with no pions in the final state; that is, the signal event topology is "1 muon + 0 pion + N protons." The main results were published in terms of flux-integrated double differential cross sections, as functions of the lepton kinetic energy and the scattering angle. Figure 3(a) shows the flux-integrated double differential cross section of ν_μ CCQE interactions [18]. The irreducible background from the pion production channel is subtracted based on a sideband study, but the subtracted background is also published so that readers can recover the irreducible background.

These data have revealed the importance of nucleon correlations [19, 20] in neutrino scattering, which had not been taken into account correctly in previous calculations. This led to models developed using electron scattering data that were tested against MiniBooNE data [21–26]. These models await being tested further by other experiments, such as MINERvA [27, 28] and T2K [29].

Another important test is CCQE antineutrino scattering, where a wide range of expectations were predicted prior to the run [30–34]. Before the data could be compared to the results,

however, the substantial contamination of neutrinos in the antineutrino beam had to be addressed. Three independent methods were used to constrain and tune the neutrino contamination prediction [35]. After subtracting the neutrino contamination, the flux-integrated double differential cross section for the muon antineutrino CCQE interaction was measured (Figure 3(b)) [36]. The comparison of models with data showed a preference for the high cross section models [37]. The rich shape information of the double differential data continues to provide additional tests, beyond the normalization.

The main result of the $\bar{\nu}_\mu$ CCQE cross section measurements is quoted as per CH_2 molecule. This is because the MiniBooNE target consists of CH_2, and the experiment cannot distinguish antineutrino interactions with bound protons in the carbon nuclei and free protons from hydrogen. As a separate study, however, MiniBooNE also presented an analysis that subtracted the hydrogen interactions, where the cross sections were then expressed per bound proton. This has also provided a useful handle for theorists.

3.2. Charged Single Pion Production. The understanding of charged-current single-pion channels is of great interest to the nuclear community, but also, there are significant implications for the neutrino oscillation studies. These interactions produce an irreducible background for CCQE events [38–41]. If the detector fails to tag outgoing pions, either because of detector effects or nuclear effects, pion production channels may be misclassified as CCQE. The distributions of irreducible backgrounds must be modelled, and those models rely on the pion production measurements, especially the MiniBooNE data described here. Therefore, understanding the kinematic distributions of pion production channels is a crucial task for neutrino oscillation physics.

There are three pion production channels for which MiniBooNE performed dedicated measurements: charged-current single π^+ (CC1π^+) production [8]; charged-current single π° (CC1π°) production [9]; and neutral current single π° (NC1π°) production [42]:

$$\begin{aligned} \nu_\mu + CH_2 &\longrightarrow \mu^- + \pi^+ + X, \\ \nu_\mu + CH_2 &\longrightarrow \mu^- + \pi^\circ + X, \\ \nu_\mu\left(\bar{\nu}_\mu\right) + CH_2+ &\longrightarrow \nu_\mu\left(\bar{\nu}_\mu\right) + \pi^\circ + X. \end{aligned} \quad (3)$$

Here, the topologies of each event are more complicated and are described as "1 muon + 1 positive pion + N protons" (CC1π^+), "1 muon + 1 neutral pion + N protons" (CC1π°), and "0 muon + 1 neutral pion + N protons" (NC1π°). Although the MiniBooNE detector is not magnetized and therefore cannot distinguish positive and negative pions based on their trajectories, separation is possible. Negative pions are absorbed by a nucleus almost 100% of the time, and in consequence, there is no emission of a Michel electron. This fact allows MiniBooNE to use the presence of a Michel electron to select positive pions.
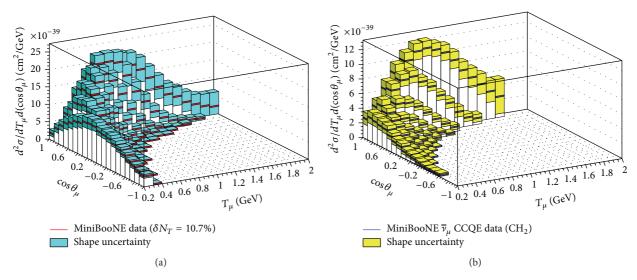
FIGURE 3: (Color online) MiniBooNE CCQE cross sections. (a) shows the muon neutrino flux-integrated CCQE double differential cross section on a neutron target. (b) shows muon antineutrino flux integrated CCQE double differential cross section on a CH_2 molecule.
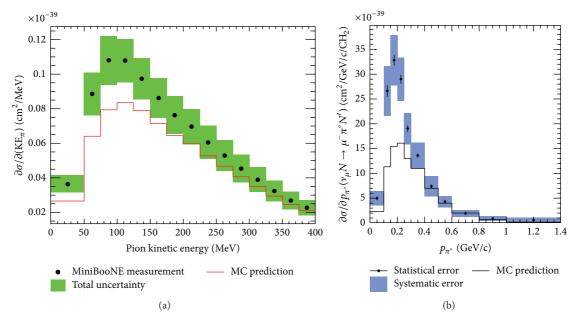
FIGURE 4: (Color online) MiniBooNE single pion production results. (a) is π^+ kinetic energy differential cross section from $CC1\pi^+$ interaction on CH_2 [8]. (b) is π° momentum differential cross section from $CC1\pi^\circ$ interaction in CH_2 [9]. As you see, predictions underestimate data for both channels and the shapes do not agree as well.

Because of the more complicated topologies, the differential cross sections for these data sets are presented in various variables. Among them, distributions in pion kinetic energy and momentum distributions exhibit the presence of nuclear effects, while we do not see this from the lepton distributions. Figure 4 shows differential cross sections, $CC1\pi^+$ pion kinetic energy, and $CC1\pi^\circ$ pion momentum, respectively. The shape and normalization are sensitive to nuclear effects, such as pion absorption, charge exchange, and rescattering. Therefore, the state-of-the-art nuclear models [43, 44] can be tested by these MiniBooNE data.

3.3. Neutral Current Elastic (NCE) Scattering. The NCE interaction can take place on both neutrons and protons, for both neutrino and antineutrinos. The results are relevant for dark matter searches in two ways: first through the measurement of Δs that we describe here, second as a background to a direct dark matter search by MiniBooNE, described in Section 6:

$$\nu_\mu\left(\bar{\nu}_\mu\right) + p \longrightarrow \nu_\mu\left(\bar{\nu}_\mu\right) + p,$$
$$\nu_\mu\left(\bar{\nu}_\mu\right) + n \longrightarrow \nu_\mu\left(\bar{\nu}_\mu\right) + n. \tag{4}$$

(a)

(b)
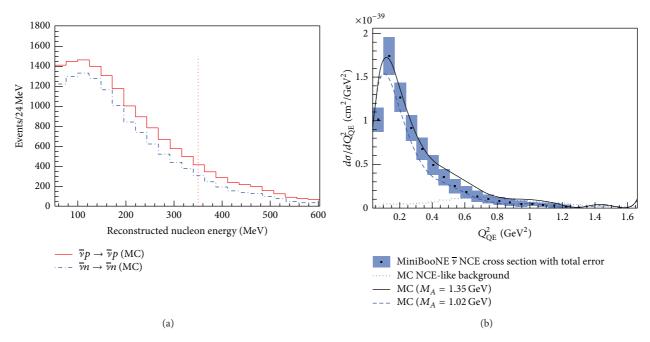
FIGURE 5: (Color online) MiniBooNE NCE results [45]. (a) shows simulated kinetic energy of protons and neutrons from NCE in MiniBooNE. The line denotes the Cherenkov threshold, that is, only protons which have higher energy from this line emit Cherenkov radiation. (b) shows the antineutrino NCE differential cross section. As you see, the data shows a "roll-over" in the low Q^2 region.

Since only protons with kinetic energy above ~350 MeV produce Cherenkov radiation (Figure 5(a)), the majority of these events only produce scintillation light and therefore necessitate a strictly calorimetric analysis. For neutrons, there is no Cherenkov radiation and the chance the secondary proton from the primary neutron exceeds this threshold is extremely low (in other words, if the proton exceeds Cherenkov threshold, this will most likely form the primary neutrino NC interaction). We call this topology "0 muon + 0 pion + N protons." However, when the kinetic energy exceeded the Cherenkov threshold, it is also possible to observe the direction of nucleons [10].

The calorimetric measurement causes the signal to be insensitive to the detailed final state interaction (FSI) process. Also, similar to the antineutrino CCQE analysis (Section 3.1), scattering on C and H cannot be distinguished, so the target may be a bound proton, a free proton, or a bound neutron. Hence, the cross section is presented per CH_2 target. Figure 5(b) shows the antineutrino mode NCE differential cross section [45].

The NCE data allows us to refine our understanding of nuclear effects at low Q^2. In NCE, the observable is the sum of all kinetic energies of outgoing protons, $\sum T_N$. Using this, the Q^2 can be reconstructed by assuming the target nucleon at rest:

$$Q^2_{QE} = 2M_N \sum T_N. \tag{5}$$

Note that irreducible backgrounds, such as NC pion production without an outgoing pion, are subtracted to make Q^2_{QE} physical.

The reconstructed data shows a roll-over at the low Q^2 region, due to the combination of Pauli blocking and the nuclear shadowing. Pauli blocking is a phenomenon where low momentum transfer interactions are forbidden due to occupied phase space, and the nuclear shadowing happens when the resolution (= low momentum transfer interaction) is insufficient to resolve a single nucleon wave function. Note that these nuclear effects do not appear if the signal of NCE is defined to be a single isolated proton, where strong FSI migrates all nucleons to low energy region [46]. However, because the MiniBooNE NCE data presents the sum of the total nucleon kinetic energy, the results preserve the feature of the primary neutrino interaction physics.

NCE interactions are connected to direct dark matter searches through the measurement of Δs, the spin of the strange quarks in the nucleon. It has been shown [47] that the uncertainty of Δs on the spin-dependent scattering between dark matter particles and target nuclei can be a large systematic error. Therefore, a Δs measurement is another way that neutrino cross section measurements contribute to BSM physics. We briefly consider how this information can be extracted from the NCE data here.

The spin structure of a nucleon is deeply fundamental and quite complicated. In the naive constituent quark model, the spin $-1/2$ of a nucleon can be derived by adding valence quark spins, where in the static limit ($Q^2 \rightarrow 0$) there are three valence quarks that make up all static properties of a nucleon, such as charge, magnetic moment, and spin. However, the spin contribution from up and down quarks deduced from inclusive deep inelastic scattering (DIS) measurements [48–50] indicates, in the static limit, that up and down quarks support only ~10% of the total spin of a proton. This so-called

"spin crisis" has triggered a world wide effort to look for other sources of spin in a nucleon. One of the interesting additional spin contributions is from the strange quarks, called Δs. Although recent measurements show the static limits of the strange quark charge and magnetic contributions are consistent with zero [51], the nonzero value of Δs is still under debate [52], because the weak coupling ($\propto (1 - 4\sin^2\theta_w)$) of Δs with parity violating electron asymmetry does not allow a clear measurement of Δs through electron scattering experiments.

However, Δs also contributes to neutrino NCE scattering, as an axial vector isoscalar term, increasing the cross section for neutrino-proton NCE and decreasing the cross section for neutrino-neutron NCE. Figure 6 shows the ratio of $\nu p \rightarrow \nu p$ to $\nu N \rightarrow \nu N$ candidates events, together with several predictions with nonzero Δs. Note MiniBooNE can only isolate neutrino-proton NCE in the case of high energy protons, and the denominator is chosen to be the total NCE events in order to cancel systematics. The fit to find Δs is performed on this plot. After the fit, the best fit value of $\Delta s = 0.08 \pm 0.26$ is found. Unfortunately, MiniBooNE does not have enough sensitivity to definitively determine nonzero Δs. This is due to the poor experimental proton-neutron separation which is only possible at high energy with large systematics. Therefore, a detector which has the ability to identify low energy protons, such as MicroBooNE [53], will have better sensitivity to Δs.

4. MiniBooNE Oscillation Results

The most well-known BSM search performed by the Mini-BooNE experiment was for neutrino oscillations consistent with LSND. These are also the most thoroughly reviewed results. Here, we briefly describe the studies. We recommend [54] for a more extended discussion.

MiniBooNE was conceived in 1998, shortly after the LSND results had reached 3.8σ significance and before the three massive neutrino model for active-flavor oscillations (νSM) had been well established. However, it was clear that if LSND was observing an oscillation signal, the associated squared mass splitting ($\Delta m_{\text{large}}^2$) was more than an order of magnitude larger than other evidence for oscillations. In this circumstance, a complicated three-neutrino appearance probability can reduce to a more simple two-neutrino case for designs with $(1.27L/E) \approx 1/\Delta m_{\text{large}}^2$, such as MiniBooNE.

This approach assumes no CP violation in the mixing matrix, and hence equal probabilities of neutrino and antineutrino oscillations. Leptonic CP violation in the mixing matrix had been discussed by Wolfenstein in 1978 [55] as a natural analogy to the quark sector. However, by extension of that analogy, the assumption was that this effect, if it existed, would be very small. As a result, theoretical interest in 1998 was largely isolated to CP violation. In retrospect, this approach was naive, but this made sense as the guiding principle for the MiniBooNE design at the time. The goal was to test a simple two-neutrino oscillation model with equal probabilities of neutrinos and antineutrinos, on the basis that this would be a good approximation if the underlying
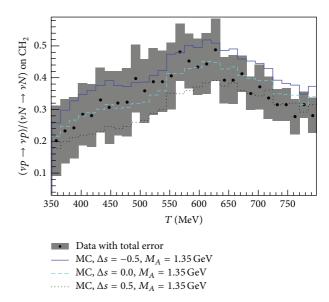
FIGURE 6: (Color online) The ratio of $\nu p \rightarrow \nu p$ to $\nu N \rightarrow \nu N$ as a function of the reconstructed total kinetic energy of nucleons [10].

reality was BSM physics. If a signal was not observed, the significantly different systematic errors were expected to result in a clear exclusion of the result. Thus, the MiniBooNE experiment began running in neutrino mode, which provided roughly ~6 times higher rate than antineutrino mode; a necessary choice since the MiniBooNE experiment was also relied on a significant Booster performance improvement. The results showed an anomalous excess of electron-like events in the ν_μ dominant neutrino mode beam [56] that was similar to, but not in good agreement with, LSND. The experiment then switched to running in antineutrino mode, where a result in agreement with LSND was observed.

Rather than considering these events historically, we present both results together in the next section, followed by a discussion of interpretations and considerations of follow-up experiments. There is a world-wide effort to probe the sterile neutrino in the region $\Delta m^2 \sim 1\,\text{eV}^2$ [57]. It is desirable for MiniBooNE to confirm this excess is electron-like, which is considered the sterile neutrino oscillation signal, not background gamma rays associated with $\nu_\mu(\overline{\nu}_\mu)$NC interactions. The MicroBooNE experiment [53] was proposed along this line. The MicroBooNE experiment features a large liquid argon (LAr) time projection chamber (TPC), and it has an ability to distinguish an electron (positron) and a gamma ray. The MicroBooNE experiment will start data taking in 2014. We will discuss more in a later section.

4.1. The Neutrino and Antineutrino Appearance Oscillation Results. After a decade of data collection, MiniBooNE's final appearance oscillation results have been published [58]. Figure 7 shows the electron candidate ($\nu_\mu \rightarrow \nu_e$ oscillation candidate) distribution in neutrino mode and positron ($\overline{\nu}_\mu \rightarrow \overline{\nu}_e$ oscillation candidate) distribution in antineutrino mode. Note that since the MiniBooNE detector is not magnetized, in general, it cannot distinguish between
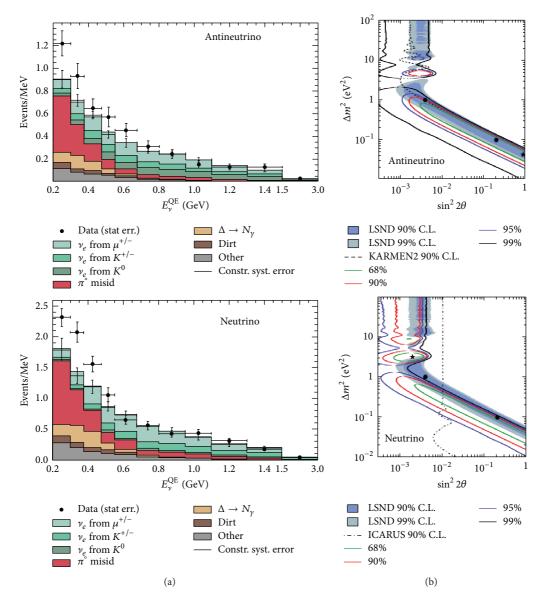
FIGURE 7: (Color online) The final MiniBooNE oscillation results [58]. (a) shows the reconstructed neutrino energy distribution of oscillation candidate events. The top is for antineutrino mode and the bottom is for neutrino mode. (b) shows the allowed region in $\Delta m^2 - \sin^2 2\theta$, where the best fit points are shown in black stars.

electrons and positrons, and so both are grouped into the "electron-like" category.

MiniBooNE observed event excesses in both modes of running, but the results have slight qualitative difference. In neutrino mode (left bottom plot), there is a statistically significant (3.8σ) event excess in the low energy region. Although the excess is significant, the shape of the spectrum leaves some tension with the oscillation hypothesis from LSND, which you can see from the right bottom plot where the MiniBooNE best fit region does not overlap well with the LSND best fit region. MiniBooNE uses a likelihood-ratio technique [59], to find the best fit values $(\Delta m^2, \sin^2 2\theta) = (3.14 \, \text{eV}^2, 0.002)$ in neutrino mode, with χ^2/dof of 13.2/6.8. In antineutrino mode (left top plot), the observed excess is not as statistically strong as neutrino mode (2.8σ). This is

expected when one compares the protons on target in each mode and considers the lower antineutrino flux and cross section. Although the statistical significance is lower, shape agreement with the LSND hypothesis is better. Again this can be seen from the right top plot where the parameter space selected by the MiniBooNE data agrees with the LSND best fit region. The best fit point in this mode was $(0.05 \, \text{eV}^2, 0.842)$ with χ^2/dof of 4.8/6.9.

The combined result significance is dominated by neutrino mode and is 3.8σ. It is possible to find compatible regions in a simple two-neutrino model between the two data sets [58]. However, we emphasize that considering MiniBooNE oscillations in the absence of other oscillation experiments leads to misunderstandings. We consider this point in a later section.

4.1.1. Potential Nonoscillation Explanations. The background-only χ^2-probability for the MiniBooNE oscillation search was 1.6% and 0.5% relative to the best oscillation fits for neutrino and antineutrino mode, respectively. Nevertheless, it is important to explore in detail the potential SM explanations of the MiniBooNE results. In particular, a Cherenkov detector, such as MiniBooNE, lacks the ability to distinguish electrons from single photons. Therefore any single photon production mechanism via neutral current interactions is a likely suspect as a background to this search.

The primary source of single photons is the NC1$\pi°$ reaction, followed by $\pi° \rightarrow \gamma\gamma$, where one photon is lost because it exits the detector or because the relativistic boost causes the energy to be too low to allow the Cherenkov signal to be identified. At the low energies of MiniBooNE, the background from two $\pi°$ rings that merge is less important than the case where a photon is lost. Fortunately, MiniBooNE has the largest sample of well reconstructed NC$\pi°$ events ever obtained. Keeping in mind that the largest uncertainties are in the production and not in the kinematics of the photons themselves, MiniBooNE was able to use this large data set to carefully evaluate this appearance background [60]. This study can constrain the variation of this largest misID background (red histogram in Figure 7(a)), and we have shown that if NC$\pi°$ was the source of the MiniBooNE excess, MiniBooNE's systematic error on the production would have to be underestimated by an order of magnitude [56]. This is not a likely solution to the problem, and so we turn to single photon production.

MiniBooNE also included the NC single photon process in their simulation. The process involves the single photon decay of a neutral current Δ resonance, which has a small but nonnegligible branching ratio (<1% of NC1$\pi°$). The rate of this process is strongly tied to the resonant production of pions; therefore MiniBooNE can utilize their *in situ* NC1$\pi°$ measurement to constrain this background. Therefore the variation of this second biggest misID background (light brown histograms in Figure 7(a)) is also constrained by the NC1$\pi°$ measurement, and we found this process was not large enough to explain the MiniBooNE excess [56].

After the first MiniBooNE oscillation result in 2007 [7], it was pointed out that there were additional single-photon-production channels missing from the NUANCE [11] event simulation used by experiments such as MiniBooNE [61]. Figure 8 shows the relevant underlying diagram. This source, triangular anomaly mediated photon production, features weak coupling via the neutrino neutral current and strong coupling with nucleons or nuclei. In fact, a similar type of interaction was suggested originally in the 1980s [62]; however, it was not widely noted or further investigated. This type of process can generate a single gamma ray from a NC interaction. The strength of the anomaly mediated diagram was evaluated [63], and the event rate in MiniBooNE, after convoluting the BNB neutrino flux, was, at the time, estimated to be high enough to explain a part of the MiniBooNE excesses [64].

The initially high estimate, which may have explained the MiniBooNE result, led nuclear theorists to reevaluate
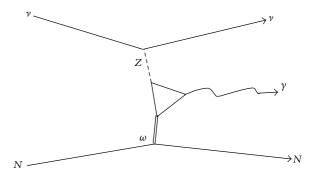
FIGURE 8: The triangular anomaly mediated photon production. The neutrino neutral current couples via Z-boson, and the target nucleon or nucleus couples with a strong force mediated vector meson, such as an omega meson.

this exotic "$Z - \gamma - \omega$ coupling," properly including nuclear effects, such as Pauli blocking and Δ resonance media width modification, as well as including careful calibrations of nuclear parameters from external data [65–67]. These are important to include since nuclear effects are sizable in this energy region. Note these nuclear effects tend to reduce the cross section.

Figure 9 shows our current knowledge of this channel [68]. The figure shows the total cross section of NC single photon production process per ^{12}C nucleus, which means the cross section includes all potential processes contributing to this final state topology ("0 muon + 0 pion + 1 photon + N protons"), both incoherently (neutrino-nucleon interaction) and coherently (neutrino-nucleus interaction). As you see, all neutrino interaction generators used by experimentalists (GENIE [13], NEUT [14], and NUANCE [11]) tend to predict lower cross sections than state-of-the-art theoretical models by Wang et al. [65], Zhang and Serot [69], and Hill [64].

The NC single photon prediction may explain part of the excess, but it is not likely to explain all of it [69, 70]. There was an active discussion on this channel at the recent INT workshop, and further experimental data on NC single photon production can help to guide more theoretical work [71].

Meanwhile, a BSM NC single photon model was proposed [72] where a decay of a heavy neutrino produces a single photon signal in the detector. Figure 10 shows the concept of such a model. The heavy neutrino is produced by the mixing with a muon neutrino; then the decay of the heavy neutrino leaves a photon signal in the detector. Interestingly, the required mass range of the heavy neutrino to produce such a signal in the MiniBooNE detector (40 MeV $< m_h <$ 80 MeV) is not constrained by other experiments. The beauty of this model is that it also explains the LSND signal, while evading the KARMEN null oscillation result [73].

At this time, NOMAD is the only experiment to have performed a dedicated NC single photon search [74]. The NOMAD result was consistent with its background prediction; thus, NOMAD set a limit on this channel. However, the limit was quoted with NOMAD's average energy ($< E > \sim$17 GeV) and is therefore not as relevant for lower energy experiments, such as MiniBooNE. Therefore, it is essential for
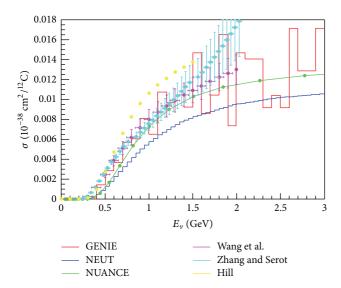
FIGURE 9: (Color online) A comparison of the total cross section of NC photon production per ^{12}C nucleus [68]. The neutrino interaction generators used by experimentalists (GENIE [13], NEUT [14], and NUANCE [11]) tend to predict lower cross sections than state-of-the-art theoretical models (Wang et al. [65], Zhang and Serot [69], Hill [64]).
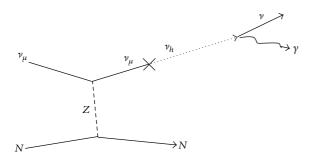
FIGURE 10: The concept of a heavy neutrino decay signal in the Mini-BooNE detector [73]. The mixing of a neutrino with a hypothetical heavy neutrino and its short life time allows for it to decay in the MiniBooNE detector to leave a photon signal.

new experiments that seek to check the MiniBooNE results to have an ability to distinguish between electrons and photons, such as MicroBooNE [53].

4.1.2. Potential Oscillation Explanations. Numerous articles have been written on the potential of oscillation models to explain the MiniBooNE signal. In particular, we recommend [75] as a pedagogical discussion of the issues of fitting the data. We excerpt the results from this reference here.

When MiniBooNE and LSND results are considered within the context of the world's oscillation data, νSM is excluded, because a third mass splitting must be introduced. Because the $Z \to \nu\bar{\nu}$ results from LEP and SLD [1] limit the number of low mass active neutrinos to three, sterile neutrinos are introduced to allow for these data sets. Sterile neutrinos are a consequence of many theories and could evade limits from cosmology, as discussed in [57]

(note recent Planck results [76] leave some tension with this interpretation).

If one sterile neutrino is added to the three active neutrinos, then the model is termed (3 + 1). Two additional sterile neutrinos lead to a (3 + 2) model and three result in a (3 + 3) model. The mass states are mixtures of flavor states, and in these models, fits to the data yield mass states that are either mostly active flavors or mostly sterile flavors. The splitting between the mostly active and mostly sterile flavors is large, and the splittings between the active flavors are, comparatively, negligible. So, in sterile neutrino fits, the short-baseline approximation where the mostly active flavors are regarded as degenerate in mass is used. In such a model, 3 + 1 models are simply two-neutrino models, such as what was initially proposed to explain LSND.

The disagreement between the MiniBooNE neutrino and antineutrino data leads to very poor fits for 3 + 1 models. In order to introduce a difference in the neutrino oscillation probabilities, *CP* violation must be included in the model. For the term which multiplies the *CP*-parameter to be significant, there must be two mass splittings that are within less than two orders of magnitude of each other. This can be accommodated in a 3 + 2 model.

Since the MiniBooNE and LSND results were published, two new anomalies consistent with high Δm^2 oscillations were brought forward. These are the reactor anomaly [77], which has been interpreted as $\bar{\nu}_e \to \bar{\nu}_s$, and the gallium source anomaly [78] which can be interpreted as $\nu_e \to \nu_s$ [57]. Both anomalies have weaker significance than Mini-BooNE and LSND, but they can be combined into a consistent model.

With this said, many experiments have searched for oscillations in the high Δm^2 region and found no evidence of oscillations. Reference [75] describes nine such results. The exclusion limits for electron-flavor disappearance and electron-flavor appearance can be shown to be compatible with the results of the four anomalous measurements. However, when muon-flavor disappearance is included, there is tension between the data sets which leads to low compatibility, except in the 3 + 3 picture (or more elaborated version of 3 + 2 model, called "1 + 3 + 1" model [79]).

4.1.3. Near-Future Experiment Addressing the MiniBooNE Results. To test MiniBooNE signals in a model-independent way, a new experiment is planned on the BNB. The Micro-BooNE experiment is a large liquid argon time projection chamber (LArTPC) experiment [53] at Fermilab, planning to start data taking from 2014. It is part of the US LArTPC program [80], with the eventual goal of an ultra-large LArTPC experiment, such as LBNE [81]. The experiments are motivated by the "bubble chamber level" LArTPC imaging quality.

Figure 11 shows a drawing [53] of MicroBooNE's 170 ton foam-insulated cryostat. The TPC volume is 89 tons. Ionized electrons along the neutrino-induced charged particle tracks are drifted via a high electric field in the TPC volume to the anode wires. The node wires are configured on three planes alternating by 60° orientation, to allow 3-dimensional reconstruction of the tracks. The first 2 wire planes record
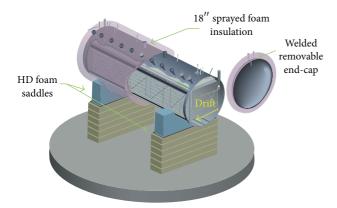
FIGURE 11: (Color online) A drawing of MicroBooNE cryostat [53]. The 170 ton cryostat contains the 89 ton TPC.

the signal from the induction on wires, and the last plane records the actual collection of ionization electrons.

An array of 8-inch PMTs is equipped behind the wire planes [82]. The main purpose of this photon collection system is to reject out-of-time cosmic rays and to trigger on in-time signals, since the scintillation light from the interaction arrives in ~ns whereas the time scale of ionization electron drift is of order ~ms. The detection of scintillation photons from LAr is not straightforward. First of all, the wavelength of Ar scintillation light is 128 nm, which requires careful R&D on potential wavelength shifters for use in LAr [83–85]. Second, the PMTs themselves behave differently in a cryogenic environment as compared to a warm environment, leading to the need for careful characterization [86].

The purity of the liquid argon must be kept very high to allow electrons to drift a long distance. Electronegative impurities (e.g., water and oxygen molecules) are removed through a custom made filter to achieve ≤ ppb level impurity [87, 88]. Such filtering is also effective for removing nitrogen molecules, which do not affect electron drift but do attenuate scintillation light [89].

A high resolution LArTPC detector will be a powerful tool in understanding the MiniBooNE signal, because the detector is expected to have the excellent electron-photon separation. Energetic electrons and photons both produce an electromagnetic shower in a LArTPC. However, the initial dE/dx of a single photon will be twice higher than in the single electron case in the first few centimeters before the track develops into the shower. Due to their high resolution capabilities, LArTPC detectors can distinguish this difference. Moreover, a displaced vertex, in the case of a photon conversion, can be distinguished from a track that is continuous from the vertex, indicative of an electron. The combination of these details can provide high efficiency background rejection for MicroBooNE.

5. Test of Lorentz and CPT Violation

Lorentz and CPT violation are scenarios motivated from Planck scale theories, such as string theory [90]. In the effective field theory framework, Lorentz violation contributes additional terms to the vacuum Lagrangian of neutrinos and hence modifies neutrino oscillations [91, 92]. Since Lorentz violating fields are of fixed direction in the universe, if Lorentz invariance is broken, the rotation of the Earth causes a sidereal time dependence of neutrino oscillation signals. There are number of phenomenological neutrino oscillation models based on Lorentz and CPT violation [93–95], some of which can explain the LSND excess [96]. In fact, a sidereal time dependence analysis of LSND data [97] failed to reject the Lorentz violation scenario. Therefore, it might be possible to reconcile LSND and MiniBooNE oscillation signals under Lorentz violation.

5.1. Analysis. Although Lorentz violation can be studied in any frame or coordinate system, it is convenient to choose one coordinate system to compare data sets. The standard choice is the Sun-centered celestial equatorial coordinates [98], where the origin of the coordinate is the center of the Sun. The orbital plane of the Earth is tilted so that the orbital axis and the rotation axis of the Earth align. This direction defineS the Z-axis. The X-axis points vernal equinox, and the Y-axis is chosen to complete the right handed system. Because the time scale of the rotation of the galaxy is too long for any terrestrial experiments, the Sun-centered frame is the better choice to test rotation symmetry (by using the rotation of the Earth) and Lorentz boost (by using the revolution of the Earth).

Having defined the coordinates, one uses the standard-model extension (SME) [99–101] as the framework for a general search for Lorentz violation. The SME can be considered a minimum extension of the SM, including the particle Lorentz and CPT violation. For the neutrino sector, the SME Lagrangian can be written as [91]

$$\mathscr{L} = \frac{1}{2} i \overline{\psi}_A \Gamma^\mu_{AB} \overleftrightarrow{D}_\mu \psi_B - \overline{\psi}_A M_{AB} \psi_B + h.c., \tag{6}$$

$$\Gamma^\nu_{AB} = \gamma^\nu \delta_{AB} + c^{\mu\nu}_{AB} \gamma_\mu + d^{\mu\nu}_{AB} \gamma_5 \gamma_\mu + e^\nu_{AB}$$
$$+ i f^\nu_{AB} \gamma_5 + \frac{1}{2} g^{\lambda\mu\nu}_{AB} \sigma_{\lambda\mu}, \tag{7}$$

$$M_{AB} = m_{AB} + i m_{5AB} \gamma_5 + a^\mu_{AB} \gamma_\mu + b^\mu_{AB} + \frac{1}{2} H^{\mu\nu}_{AB} \sigma_{\mu\nu}. \tag{8}$$

Here, the AB subscripts represent the flavor basis. The first term of (7) and the first and second terms of (8) are the only nonzero terms in the SM, and the rest of the terms are from Lorentz violation.

The physics consequences predicted by Lorentz violation are very rich. Among them, we are interested in Lorentz violating neutrino oscillations. Neutrino oscillations are natural interferometers and they are sensitive to small effects such as Lorentz violation. The smoking gun of Lorentz violation is the sidereal time dependence of physics observables. Therefore, we used the Lorentz violating $\nu_\mu \rightarrow \nu_e$ ($\overline{\nu}_\mu \rightarrow \overline{\nu}_e$) neutrino oscillation formula derived from above Lagrangian [102] to fit the sidereal time distribution of the $\nu_\mu \rightarrow \nu_e$ ($\overline{\nu}_\mu \rightarrow \overline{\nu}_e$) oscillation candidate data. Here, potentially, any day-night effect, either from the beam or from the detector, could mimic
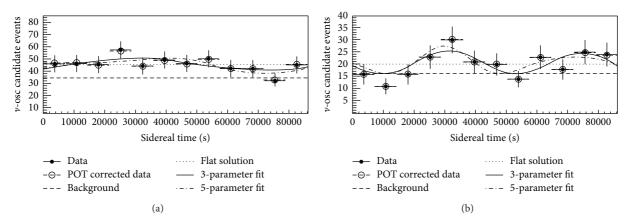
FIGURE 12: The MiniBooNE Lorentz violation results [103]. (a) shows the neutrino mode electron-like low energy excess sidereal time distribution, and (b) shows the antineutrino mode sidereal time distribution. Here, the data with a POT correction (open circle) show the size of the beam day-night variation. There are three fit curves based on different assumptions, a flat solution (dotted), a three-parameter fit (solid curve), and a full five-parameter fit (dash-dotted curve).

the sidereal time distribution. MiniBooNE studied effects versus the time distribution of the delivered POT and the high statistics $\nu_\mu (\bar{\nu}_\mu)$ CCQE sample [18, 36] and confirmed that day-night effects on both ν_e and $\bar{\nu}_e$ oscillation candidates are well below statistical errors.

5.2. Results. Figure 12 shows the neutrino and antineutrino mode electron-like events as a function of sidereal time [103]. Since background events are time-independent, we fit curves on the flat time-independent background (dashed lines). There are three curves fit to the data, depending on different hypotheses. A flat solution (dotted lines) assumes only time-independent Lorentz violating term, a 3-parameter fit (solid lines) includes all CPT-odd Lorentz violating terms, and a 5-parameter fit (dash-dotted lines) is the full parameter fit including both CPT-odd and CPT-even Lorentz violating terms. Although the antineutrino mode electron-like events show a rather interesting sidereal time dependence, the statistical significance is still low. Therefore, MiniBooNE found that the data are consistent with no Lorentz violation. This analysis provided the first limits on five time independent SME coefficients, at the level of 10^{-20} GeV (CPT-odd) and order 10^{-20} (CPT-even). Further analysis inferred limits on each SME coefficient, and, together with limits from the MINOS near detector [104, 105], it turns out these limits leave tension to reconcile the MiniBooNE and LSND data sets under a simple Lorentz violation motivated scenario [4].

In fact, existing limits from MiniBooNE [103], MINOS [104–107], IceCube [108], and Double Chooz [109, 110] set very tight limits on possible Lorentz violation in the neutrino sector at the terrestrial level. This was one of the reasons why the superluminal neutrino signal from OPERA [111] was suspicious from the beginning. Such a signal would have required very large Lorentz violation, while avoiding all these constraints when writing down the theory. Strictly speaking, limits on Lorentz violation from the oscillation experiments cannot be applied directly to the neutrino time of flight (TOF) measurement [112]. However, introducing
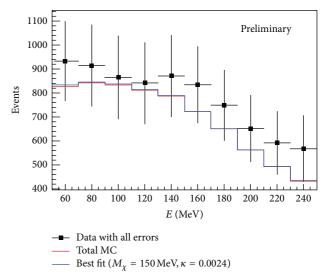
FIGURE 13: (Color online) The dark matter fit result to the NCE data [116].
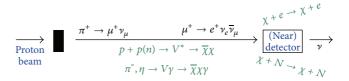
FIGURE 14: (Color online) The concept of the dark matter beam in MiniBooNE [116]. The dominant production mode of dark matter particles is decays of the mediator particles created by decays of neutral mesons. The dark matter particles can be also made through the direct collisions of protons on the beam dump.

large Lorentz violation in the neutrino TOF without other large parameters such as those associated with oscillations seems unnatural.
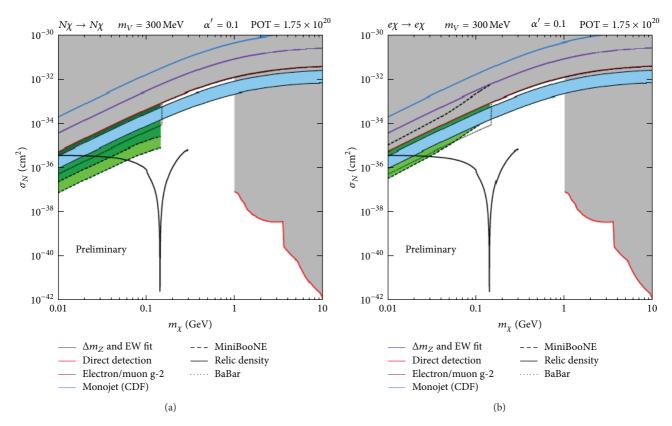
FIGURE 15: (color online) The MiniBooNE dark matter particles search phase space [116]. Here, the x-axis is the dark matter mass m_χ, and the y-axis is either the dark matter-nucleon or dark matter-electron cross section, assuming the vector mediator mass and the gauge coupling ($m_V = 300$ MeV and $\alpha = 0.1$). The MiniBooNE exclusion region can be seen in green.

6. Dark Matter Search

The proton collisions on target in the BNB line that produce a large flux of neutrinos could, potentially, produce sub-GeV scale dark matter particles that mimic NCE interactions in the MiniBooNE detector [113–115]. The most interesting scenario is that this light dark matter particle is the dark matter of the universe, which requires a light vector mediator particle (called a "dark photon"), in the model in order to obtain an efficient annihilation cross section. The minimum extension of the SM with the light dark matter particle and the vector mediator can be written in the following way [114]:

$$\mathscr{L} = \mathscr{L}_{SM} - \frac{1}{4}V_{\mu\nu}^2 + \frac{1}{2}m_V^2 V_\mu^2 + \kappa V_\nu \partial_\mu F^{\mu\nu}$$
$$+ \left|D_\mu\chi\right|^2 - m_\chi^2|\chi|^2 + \cdots.$$
(9)

The model has four free parameters: the mass of the light dark matter m_χ, the mass of the vector mediator m_V, kinetic mixing of the vector mediator and the photon κ, and the vector mediator's gauge coupling e' (or $\alpha' = e'^2/4\pi$). Nonzero κ leads to the decay of neutral mesons to a photon and a dark photon, and the dark photon in turn can decay to dark matter particles. This would be the dominant process to produce dark matter particles in the BNB. The second process is direct

production from the parton level annihilation by protons colliding in the target.

6.1. MiniBooNE Searches for Dark Matter Particles. MiniBooNE tested this model with the existing antineutrino NCE data set, taken during the oscillation studies. Figure 13 shows the fit result with a light dark matter particles hypothesis [116]. The plot shows the total energy distribution of the antineutrino NCE sample, and the red and blue histograms show before and after the fit. The best fit values are $M_\chi = 150$ MeV and $\kappa = 0.0024$. As can be seen, the current sensitivity to the light dark matter model is low.

The antineutrino mode data set is used because it has a lower neutrino interaction rate than the neutrino mode beam. Nevertheless, due to the antineutrino backgrounds, only weak limits are obtained on the kinetic mixing parameter κ.

This motivated a tuning of the proton beam that allowed MiniBooNE to run in a mode in which the protons are directed onto the beam dump instead of the target, eliminating the DIF neutrino flux. Figure 14 shows the schematic of this measurement [116]. The beam-dump mode is achieved by tuning the ~1 mm beam to aim 0.9 cm gap between the beryllium target rod and the inner conductor of the horn, to hit the beam dump located at the end of decay pipe
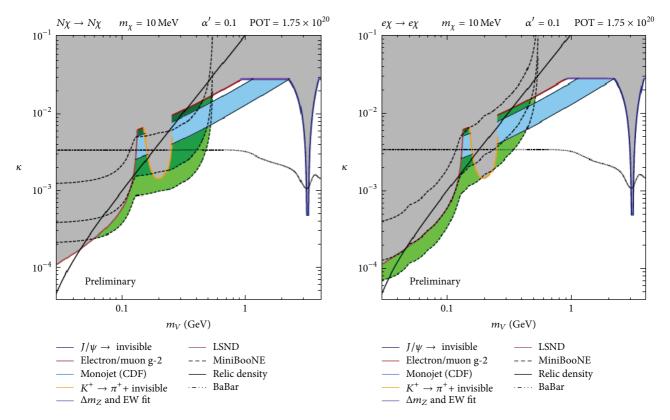
FIGURE 16: (Color online) The MiniBooNE dark matter search phase space [116]. Here, x-axis is the vector mediator mass m_V, and the y-axis is the kinetic mixing parameter κ, assuming the dark matter mass and the gauge coupling (m_χ = 10 MeV and α = 0.1). MiniBooNE exclusion region can be seen in green.

(50 m from the target) directly. This reduces the neutrino background by roughly a factor of 67. Dark matter production is largely unaffected in this run mode since it occurs through neutral meson decay. MiniBooNE is now running in this configuration. The goal is to accumulate 1.75×10^{20} POT data before MicroBooNE starts beam data taking in the neutrino mode, not the beam-dump mode.

6.2. Parameter Space of Light Dark Matter Particles and Vector Mediators.

Figure 15 shows the two-dimensional phase space of dark matter-nucleon and dark matter-electron scattering cross sections versus dark matter mass m_χ [116]. The limits from direct searches end up at the right side (m_χ ~1 GeV), and the left-side light dark matter region is explored by other techniques, such as rare decays and collider physics. MiniBooNE addresses direct light dark matter searches. In the case of either interaction, MiniBooNE is sensitive to the dark matter mass in the 10 to 200 MeV mass region.

There are many reasons why such a light dark matter search is interesting. First, recent data [117–120] from the direct WIMP (weakly interacting massive particle) searches suggest possible signals of dark matter particles in the lighter mass region. For example, SuperCDMS is also aiming the low mass dark matter search by utilizing the ionization signals [121]. Second, the muon g-2 anomaly can be explained by the presence of a vector mediator [122, 123]. Although the interesting phase space of muon g-2 was already excluded by

other experiments, MiniBooNE can further push the limits in this region.

The sensitivity that is obtained from the dark matter-electron scattering looks weaker than dark matter-nucleon in the $\sigma - m_\chi$ phase space (Figure 15(b)); however, as Figure 16 shows, the limit from the dark matter-electron interaction can be stronger in the low vector mass region in $\kappa - m_V$ phase space [116]. Therefore, both channels are complimentary and MiniBooNE should strive to measure both. There was a little interest in ν-e elastic scattering because of its small cross section, but this electron channel is as important as the nucleon channel for the dark matter search.

6.3. Dark Matter Time of Flight (TOF).

MiniBooNE's sensitivity to dark matter particles can be further improved by combining event topology and kinematics with the timing information. Figure 17 shows the "dark matter TOF" concept. The dark matter particles are most likely produced at the beam dump after prompt decays of neutral pions or etas ($< 10^{-16}$ sec), so the dark matter production is localized in both time and space. This would result in a dark matter beam that has a well-defined timing and allows us to perform the TOF-based searches. The heavier dark matter particles should be slower than the neutrinos (as well as the speed of light). Thus the dark matter particles would lag behind the bunch center and separate from the neutrino background.
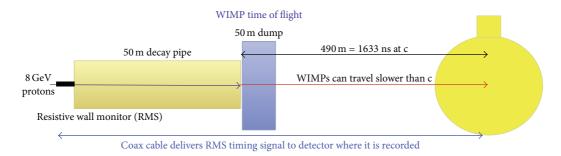
FIGURE 17: (Color online) The concept of dark matter particles TOF. Because of the localization of the dark matter particle production in time and in space, the dark matter beam has well-defined timing structure.

In the Fermilab Booster, the 81 bunches have 19 ns separations (Section 2.1). MiniBooNE defines events within 4 ns < T < 16 ns from the bunch center as the in-time events, and the T < 4 ns and T > 16 ns events are out-time. The absolute timing information of all bunches is recorded by the resistive wall monitor (RWM) which is located just before the target. Using the previous MiniBooNE antineutrino run to test this idea, Figure 18 shows the overlaid profile of all bunches of antineutrino NCE candidate events [116]. As expected, the data shows the peak in in-time region, because the data is dominated by antineutrino NCE interactions.

A beam-dump test run was performed for one week during 2012 running. During the beam-dump mode test run, the timing of neutrinos was tested using CC interaction. Since the CC interaction is detected through the prompt Cherenkov light from the muons, timing resolution is better than NCE events. Using the new system installed for the beam-dump run, MiniBooNE achieved 1.5 ns resolution [116]. The resolution will be worse for NCE because of the nature of the exponential decay of scintillation light, but MiniBooNE, nevertheless, still expects ~4 ns resolutions. This gives full confidence for MiniBooNE to perform a full beam-dump run.

7. Conclusion

Since beginning its run in 2002, MiniBooNE has been searching for new physics in a wide variety of ways. The most important results have been those related to oscillations of sterile neutrinos, which has pushed the community toward new and exciting experiments in the future [53, 57, 124–126]. MiniBooNE also tested for possible signals from the Planck scales, and set very strong constraints on Lorentz violation. MiniBooNE's light dark matter search with a beam-dump configuration run is a unique opportunity that can provide the best limit on the dark matter mass in the 10 to 200 MeV range. All of these searches have been grounded in the revolutionary set of cross section measurements performed with MiniBooNE. This experiment demonstrates the rich possibilities to go beyond the standard model in low cost short-baseline venues and encourages a strong investment in future programs.
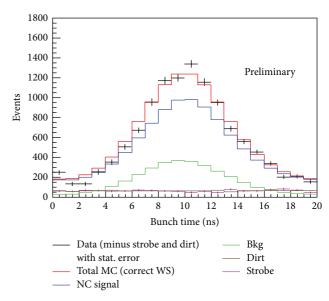
FIGURE 18: (Color online) The reconstructed NCE event time profile for the antineutrino mode beam. The events are overlaid relative to the bunch center. As expected, the data peaks in the bunch center, which means these are dominated with antineutrino interactions and there is no delay of events.

Conflict of Interests

The authors declare that there is no conflict of interests regarding the publication of this paper.

Acknowledgments

References

[1] J. Beringer, J.-F. Arguin, R. M. Barnett et al., "Review of particle physics," *Physical Review D*, vol. 86, Article ID 010001, 2012.

[2] K. Abe, J. Adam, H. Aihara et al., "Observation of electron neutrino appearance in a muon neutrino beam," *Physical Review Letters*, vol. 112, no. 6, Article ID 061802, 8 pages, 2014.

[3] A. Aguilar-Arevalo, L. B. Auerbach, R. L. Burman et al., "Evidence for neutrino oscillations from the observation of electron anti-neutrinos in a muon anti-neutrino beam," *Physical Review D*, vol. 64, Article ID 112007, 2001.

[4] T. Katori, "Tests of Lorentz and CPT violation with MiniBooNE neutrino oscillation excesses," *Modern Physics Letters A*, vol. 27, no. 25, Article ID 1230024, 2012.

[5] A. Aguilar-Arevalo, C. E. Anderson, A. O. Bazarko et al., "Neutrino flux prediction at MiniBooNE," *Physical Review D*, vol. 79, Article ID 072002, 2009.

[6] A. Aguilar-Arevalo, C. E. Andersonp, L. M. Bartoszekg et al., "The MiniBooNE detector," *Nuclear Instruments and Methods in Physics Research Section A*, vol. 599, pp. 28–46, 2009.

[7] A. Aguilar-Arevalo, A. O. Bazarko, S. J. Brice et al., "Search for electron neutrino appearance at the $\triangle m^2 \sim 1$ eV^2 scale," *Physical Review Letters*, vol. 98, Article ID 231801, 2007.

[8] A. A. Aguilar-Arevalo, C. E. Anderson, A. O. Bazarko et al., "Measurement of neutrino-induced charged-current charged pion production cross sections on mineral oil at $E_\nu \sim 1$ GeV," *Physical Review D*, vol. 83, no. 5, Article ID 052007, 2011.

[9] A. Aguilar-Arevalo, C. E. Anderson, A. O. Bazarko et al., "Measurement of ν_μ-induced charged-current neutral pion production cross sections on mineral oil at $\mathbf{E_\nu} \in 0.5 - 2.0$ GeV," *Physical Review D*, vol. 83, Article ID 052009, 2011.

[10] A. Aguilar-Arevalo, B. G. Tice, [MiniBooNE collaboration] et al., "Measurement of the neutrino neutral-current elastic differential cross section on mineral oil at $E_\nu \sim 1$ GeV," *Physical Review D*, vol. 82, Article ID 092005, 2010.

[11] D. Casper, "The nuance neutrino simulation, and the future," *Nuclear Physics B*, vol. 112, no. 1–3, pp. 161–170, 2002.

[12] C. Juszczak, "Running nuwro," *Acta Physica Polonica B*, vol. 40, pp. 2507–2512, 2009.

[13] C. Andreopoulos, A. Bell, D. Bhattacharya et al., "The GENIE neutrino Monte Carlo generator," *Nuclear Instruments and Methods in Physics Research Section A*, vol. 614, pp. 87–104, 2010.

[14] Y. Hayato, "A neutrino interaction simulation program library NEUT," *Acta Physica Polonica B*, vol. 40, pp. 2477–2489, 2009.

[15] O. Buss, T. Gaitanos, K. Gallmeister et al., "Transport-theoretical description of nuclear reactions," *Physics Reports*, vol. 512, no. 1-2, pp. 1–124, 2012.

[16] C. Juszczak, J. T. Sobczyk, and J. Zmuda, "Extraction of the axial mass parameter from MiniBooNE neutrino quasielastic double differential cross-section data," *Physical Review C*, vol. 82, Article ID 045502, 2010.

[17] A. Aguilar-Arevalo, A. O. Bazarko, S. J. Brice et al., "Measurement of muon neutrino quasielastic scattering on carbon," *Physical Review Letters*, vol. 100, Article ID 032301, 2008.

[18] A. Aguilar-Arevalo, C. E. Anderson, A. O. Bazarko et al., "First measurement of the muon neutrino charged current quasielastic double differential cross section," *Physical Review D*, vol. 81, no. 9, Article ID 092005, 22 pages, 2010.

[19] M. Martini, M. Ericson, G. Chanfray, and J. Marteau, "A unified approach for nucleon knock-out, coherent and incoherent pion production in neutrino interactions with nuclei," *Physical Review C*, vol. 80, Article ID 065501, 2009.

[20] J. Nieves, I. R. Simo, and M. V. Vacas, "Inclusive charged-current neutrino-nucleus reactions," *Physical Review C*, vol. 83, no. 4, Article ID 045501, 2011.

[21] M. Martini, M. Ericson, and G. Chanfray, "Neutrino quasielastic interaction and nuclear dynamics," *Physical Review C*, vol. 84, no. 5, Article ID 055502, 2011.

[22] J. Nieves, I. R. Simo, and M. V. Vacas, "The nucleon axial mass and the MiniBooNE quasielastic neutrino–nucleus scattering problem," *Physics Letters B*, vol. 707, no. 1, pp. 72–75, 2012.

[23] J. Amaro, M. Barbaro, J. Caballero, T. Donnelly, and C. Williamson, "Meson-exchange currents and quasielastic neutrino cross sections in the superscaling approximation model," *Physics Letters B*, vol. 696, pp. 151–155, 2011.

[24] A. Bodek, H. Budd, and M. Christy, "Neutrino quasielastic scattering on nuclear targets," *The European Physical Journal C*, vol. 71, article 1726, 2011.

[25] A. Meucci, C. Giusti, and F. D. Pacati, "Relativistic descriptions of final-state interactions in neutral-current neutrino-nucleus scattering at MiniBooNE kinematicsc," *Physical Review D*, vol. 84, Article ID 113003, 2011.

[26] O. Lalakulich, K. Gallmeister, and U. Mosel, "Complete set of polarization transfer observables for the $^{16}\text{O}(\underset{p}{\rightarrow}, \underset{p}{\rightarrow})^{16}\text{F}$ reaction at 296 MeV and 0," *Physical Review C*, vol. 84, no. 1, Article ID 014614, 8 pages, 2012.

[27] G. Fiorentini, D. W. Schmitz, and P. A. Rodrigues, "Measurement of muon neutrino quasielastic scattering on a hydrocarbon target at $E_\nu \sim 3.5$ GeV," *Physical Review Letters*, vol. 111, Article ID 022502, 2013.

[28] L. Fields, J. Chvojka, L. Aliaga et al., "Measurement of muon antineutrino Quasi-elastic scattering on a hydrocarbon target at E_$\nu \sim 3.5$ GeV," *Physical Review Letters*, vol. 111, Article ID 022501, 2013.

[29] K. Abe, N. Abgrall, H. Aihara et al., "Measurement of the inclusive ν_μ charged current cross section on carbon in the near detector of the T2K experiment," *Physical Review D*, vol. 87, Article ID 092003, 2013.

[30] M. Martini, M. Ericson, G. Chanfray, and J. Marteau, "Neutrino and antineutrino quasielastic interactions with nuclei," *Physical Review C*, vol. 81, Article ID 045502, 2010.

[31] M. Martini and M. Ericson, "Quasielastic and multinucleon excitations in antineutrino-nucleus interactions," *Physical Review C*, vol. 87, no. 6, Article ID 065501, 2013.

[32] J. Nieves, I. Ruiz Simo, and M. Vicente Vacas, "Two particle-hole excitations in charged current quasielastic antineutrino-nucleus scattering," *Physics Letters B*, vol. 721, pp. 90–93, 2013.

[33] A. Meucci and C. Giusti, "Relativistic descriptions of final-state interactions in charged-current quasielastic antineutrino-nucleus scattering at MiniBooNE kinematics," *Physical Review D*, vol. 85, Article ID 093002, 2010.

[34] J. Amaro, M. Barbaro, J. Caballero, and T. Donnelly, "Meson-exchange currents and quasielastic antineutrino cross sections in the superscaling approximation," *Physical Review Letters*, vol. 108, Article ID 152501, 2012.

[35] A. A. Aguilar-Arevalo, C. E. Anderson, S. J. Brice et al., "Measurement of the neutrino component of an antineutrino beam observed by a nonmagnetized detector," *Physical Review D*, vol. 84, no. 7, Article ID 072005, 2011.

[36] A. Aguilar-Arevalo, B. C. Brown, L. Bugel et al., "First measurement of the muon antineutrino double-differential charged-current quasielastic cross section," *Physical Review D*, vol. 88, Article ID 032001, 2013.

[37] J. Grange and R. Dharmapalan, "New anti-neutrino cross-section results from MiniBooNE," http://arxiv.org/abs/1304.7395.

[38] M. Martini, M. Ericson, and G. Chanfray, "Neutrino energy reconstruction problems and neutrino oscillations," *Physical Review D*, vol. 85, Article ID 093012, 2012.

[39] D. Meloni and M. Martini, "Revisiting the T2K data using different models for the neutrino-nucleus cross sections," *Physics Letters B*, vol. 716, no. 1, pp. 186–192, 2012.

[40] J. Nieves, F. Sanchez, I. Ruiz Simo, and M. Vicente Vacas, "Neutrino energy reconstruction and the shape of the CCQE-like total cross section," *Physical Review D*, vol. 85, Article ID 113008, 2012.

[41] O. Lalakulich, U. Mosel, and K. Gallmeister, "Neutrino energy reconstruction in quasielastic-like scattering in the MiniBooNE and T2K experiments," *Physical Review C*, vol. 86, Article ID 054606, 2012.

[42] A. A. Aguilar-Arevalo, C. E. Anderson, A. O. Bazarko et al., "Measurement of ν_μ and $\bar{\nu}_\mu$ induced neutral current single π^0 production cross sections on mineral oil at $E_\nu \sim \mathcal{O}$ (1 GeV)," *Physical Review D*, vol. 81, Article ID 013005, 2010.

[43] O. Lalakulich and U. Mosel, "Pion production in the Mini-BooNE experiment," *Physical Review C*, vol. 87, no. 1, Article ID 014602, 2013.

[44] E. Hernndez, J. Nieves, and M. J. V. Vacas, "Single pion production in neutrino nucleus scattering," *Physical Review D*, vol. 87, Article ID 113009, 2013.

[45] A. Aguilar-Arevalo, B. C. Brown, L. Bugel et al., "Measurement of the antineutrino neutral-current elastic differential cross section," http://arxiv.org/abs/arXiv:1309.7257.

[46] T. Leitner, L. Alvarez-Ruso, and U. Mosel, "Neutral current neutrino-nucleus interactions at intermediate energies," *Physical Review C*, vol. 74, Article ID 065502, 2006.

[47] J. R. Ellis, K. A. Olive, and C. Savage, "Hadronic uncertainties in the elastic scattering of supersymmetric dark matter," *Physical Review D*, vol. 77, Article ID 065026, 2008.

[48] J. Ashmana, B. Badelekb, G. Baum et al., "A measurement of the spin asymmetry and determination of the structure function g_1 in deep inelastic muon-proton scattering," *Physics Letters B*, vol. 206, no. 2, pp. 364–370, 1988.

[49] D. Adams, B. Adeva, E. Arik et al., "Measurement of the spin-dependent structure function $g_1(x)$ of the proton," *Physics Letters B*, vol. 329, pp. 399–406, 1994.

[50] V. W. Hughes, V. Papavassiliou, R. Piegaia, K. P. Schüler, and G. Baum, "The integral of the spin-dependent structure function g1p and the Ellis-Jaffe sum rule," *Physics Letters B*, vol. 212, no. 4, pp. 511–514, 1988.

[51] D. Andrić, D. S. Armstrong, J. Arvieux et al., "Strange quark contributions to parity-violating asymmetries in the backward angle G0 electron scattering experiment," *Physical Review Letters*, vol. 104, Article ID 012001, 2010.

[52] S. F. Pate, D. W. McKee, and V. Papavassiliou, "Strange quark contribution to the vector and axial form factors of the nucleon: combined analysis of data from the G0, HAPPEx, and Brookhaven E734 experiments," *Physical Review C*, vol. 78, Article ID 015207, 2008.

[53] L. Camilleri, "MicroBooNE," *Nuclear Physics B—Proceedings Supplements*, vol. 237-238, pp. 181–183, 2013.

[54] J. M. Conrad, W. C. Louis, and M. H. Shaevitz, "The LSND and MiniBooNE oscillation searches at high Δm^2," *Annual Review of Nuclear and Particle Science*, vol. 63, pp. 45–67, 2013.

[55] L. Wolfenstein, "Oscillations among three neutrino types and CP violation," *Physical Review D*, vol. 18, no. 3, pp. 958–960, 1978.

[56] A. Aguilar-Arevalo, B. C. Brown, L. Bugel et al., "Unexplained excess of electronlike events from a 1-GeV neutrino beam," *Physical Review Letters*, vol. 102, Article ID 101802, 2009.

[57] K. N. Abazajian, M. A. Acero, S. K. Agarwalla et al., "Light sterile neutrinos: a white paper," http://arxiv.org/abs/1204.5379.

[58] A. Aguilar-Arevalo, B. C. Brown, L. Bugel et al., "Improved search for $\bar{\nu}_\mu \rightarrow \bar{\nu}_e$ oscillations in the MiniBooNE experiment," *Physical Review Letters*, vol. 110, no. 16, Article ID 161801, 2013.

[59] A. Aguilar-Arevalo, C. Anderson, S. Brice et al., "Event excess in the MiniBooNE search for $\bar{\nu}_\mu \rightarrow \bar{\nu}_e$ oscillations," *Physical Review Letters*, vol. 105, Article ID 181801, 2010.

[60] A. Aguilar-Arevalo, C. E. Anderson, A. O. Bazarko et al., "First observation of coherent π^0 production in neutrino–nucleus interactions with $E_\nu < 2$ GeV," *Physics Letters B*, vol. 664, pp. 41–46, 2008.

[61] J. A. Harvey, C. T. Hill, and R. J. Hill, "Anomaly mediated neutrino-photon interactions at finite baryon density," *Physical Review Letters*, vol. 99, Article ID 261601, 2007.

[62] S. Gershtein, Y. Y. Komachenko, and M. Y. A. Khlopov, "Production of single photons in the exclusive neutrino process $\nu N \rightarrow \nu \gamma N$," *Soviet Journal of Nuclear Physics*, vol. 33, p. 860, 1981.

[63] R. J. Hill, "Low energy analysis of $\nu N \rightarrow \nu N_\gamma$ in the standard model," *Physical Review D*, vol. 81, Article ID 013008, 2010.

[64] R. J. Hill, "Single photon background to ν_e appearance at MiniBooNE," *Physical Review D*, vol. 84, Article ID 017501, 2011.

[65] E. Wang, L. Alvarez-Ruso, and J. Nieves, "Photon emission in neutral-current interactions at intermediate energies," *Physical Review C*, vol. 89, Article ID 015503, 2014.

[66] X. Zhang and B. D. Serot, "Coherent neutrinoproduction of photons and pions in a chiral effective field theory for nuclei," *Physical Review C*, vol. 86, Article ID 035504, 2012.

[67] X. Zhang and B. D. Serot, "Incoherent neutrinoproduction of photons and pions in a chiral effective field theory for nuclei," *Physical Review C*, vol. 86, Article ID 035502, 2012.

[68] R. Dharmapalan, I. Stancu, Z. Djurcic et al., "A Proposal for MiniBooNE+: a new investigation of muon neutrino to electron neutrino oscillations with improved sensitivity in an enhanced MiniBooNE experiment," FERMILAB-PROPOSAL-1033, 2013.

[69] X. Zhang and B. D. Serot, "Can neutrino-induced photon production explain the low energy excess in MiniBooNE?" *Physics Letters B*, vol. 719, pp. 409–414, 2013.

[70] E. Wang, L. Alvarez-Ruso, and J. Nieves, "Single photon events from neutral current interactions at MiniBooNE," http://arxiv.org/abs/1407.6060.

[71] "Neutrino-Nucleus Interactions for Current and Next Generation Neutrino Oscillation Experiments," 2013, http://www.int.washington.edu/PROGRAMS/13-54w.

[72] S. Gninenko, "MiniBooNE anomaly and heavy neutrino decay," *Physical Review Letters*, vol. 103, Article ID 241802, 2009.

[73] S. N. Gninenko, "Resolution of puzzles from the LSND, KARMEN, and MiniBooNE experiments," *Physical Review D*, vol. 83, Article ID 015015, 2011.

[74] C. Kullenberg, G. Bassompierre, J. M. Gaillard et al., "A Search for Single Photon Events in Neutrino Interactions," *Physics Letters B*, vol. 706, pp. 268–275, 2012.

[75] J. Conrad, C. Ignarra, G. Karagiorgi, M. Shaevitz, and J. Spitz, "Sterile neutrino fits to short-baseline neutrino oscillation measurements," *Advances in High Energy Physics*, vol. 2013, Article ID 163897, 26 pages, 2013.

[76] P. Ade, N. Aghanim, C. Armitage-Caplan et al., "Planck 2013 results. XVI. Cosmological parameters," 2013, http://arxiv.org/abs/1303.5076.

[77] G. Mention, M. Fechner, T. Lasserre et al., "The reactor antineutrino anomaly," *Physical Review D*, vol. 83, Article ID 073006, 2011.

[78] C. Giunti and M. Laveder, "Statistical significance of the gallium anomaly," *Physical Review C*, vol. 83, Article ID 065504, 2011.

[79] J. Kopp, P. A. N. Machado, M. Maltoni, and T. Schwetz, "Sterile neutrino oscillations: the global picture," *Journal of High Energy Physics*, vol. 50, 2013.

[80] G. Karagiorgi, "Current and future liquid argon neutrino experiment," http://arxiv.org/abs/1304.2083.

[81] C. Adams, D. Adams, T. Akiri et al., "The long-baseline neutrino experiment: exploring fundamental symmetries of the universe," 2013, http://arxiv.org/abs/1307.7335.

[82] T. Katori, "MicroBooNE light collection system," *Journal of Instrumentation*, vol. 8, Article ID C10011, 2013.

[83] B. Baptista, L. Bugel, C. Chiu, J. Conrad, and C. Ignarra, "Benchmarking TPB-coated light guides for liquid argon TPC light detection systems," 2012, http://arxiv.org/abs/1210.3793.

[84] C. Chiu, C. Ignarra, L. Bugel et al., "Environmental efects on TPB wavelength-shifting coatings," http://arxiv.org/abs/1204.5762.

[85] B. Jones, J. Van Gemert, J. Conrad, and A. Pla-Dalmau, "Photodegradation mechanisms of tetraphenyl butadiene coatings for liquid argon detectors," *Journal of Instrumentation*, vol. 8, Article ID P01013, 2013.

[86] T. Briese, L. Bugel, J. Conrad et al., "Testing of cryogenic photomultiplier tubes for the MicroBooNE experiment," *Journal of Instrumentation*, vol. 8, Article ID T07005, 2013.

[87] A. Curioni, B. Fleming, W. Jaskierny et al., "A regenerable filter for liquid argon purification," *Nuclear Instruments and Methods in Physics Research A*, vol. 605, pp. 306–311, 2009.

[88] R. Andrews, W. Jaskierny, H. Jostlein, C. Kendziora, and S. Pordes, "A system to test the effects of materials on the electron drift lifetime in liquid argon and observations on the effect of water," *Nuclear Instruments and Methods in Physics Research A*, vol. 608, pp. 251–258, 2009.

[89] B. Baptista, L. Bugel, C. Chiu et al., "Benchmarking TPB-coated light guides for liquid argon TPC light detection systems," http://arxiv.org/abs/arXiv:1210.3793.

[90] V. A. Kostelecky and S. Samuel, "Spontaneous breaking of Lorentz symmetry in string theory," *Physical Review D*, vol. 39, article 683, 1989.

[91] V. A. Kostelecky and M. Mewes, "Lorentz and *CPT* violation in neutrinos," *Physical Review D*, vol. 69, no. 1, Article ID 016005, 25 pages, 2004.

[92] J. S. Diaz, V. A. Kostelecky, and M. Mewes, "Perturbative Lorentz and *CPT* violation for neutrino and antineutrino oscillations," *Physical Review D*, vol. 80, Article ID 076007, 2009.

[93] V. A. Kostelecky and M. Mewes, "Lorentz and *CPT* violation in the neutrino sector," *Physical Review D*, vol. 70, Article ID 031902(R), 2004.

[94] J. S. Diaz and V. A. Kostelecky, "Three-parameter Lorentz-violating texture for neutrino mixing," *Physics Letters B*, vol. 700, no. 1, pp. 25–28, 2011.

[95] J. S. Díaz and A. Kostelecký, "Lorentz- and CPT-violating models for neutrino oscillations," *Physical Review D*, vol. 85, no. 1, Article ID 016013, 17 pages, 2012.

[96] T. Katori, V. A. Kostelecky, and R. Tayloe, "Global three-parameter model for neutrino oscillations using Lorentz violation," *Physical Review D*, vol. 74, Article ID 105009, 2006.

[97] L. Auerbach, R. L. Burman, D. O. Caldwell et al., "Tests of Lorentz violation in $\bar{\nu}_\mu \rightarrow \bar{\nu}_e$ oscillations," *Physical Review D*, vol. 72, Article ID 0506067, 2005.

[98] V. A. Kostelecky and N. Russell, "Data tables for Lorentz and CPT violation," *Reviews of Modern Physics*, vol. 83, no. 1, pp. 11–31, 2011.

[99] D. Colladay and V. A. Kostelecky, "Lorentz-violating extension of the standard model," *Physical Review D*, vol. 58, Article ID 9809521, 1998.

[100] D. Colladay and V. A. Kostelecky, "CPT violation and the standard model," *Physical Review D*, vol. 55, pp. 6760–6774, 1997.

[101] V. A. Kostelecký, "Gravity, Lorentz violation, and the standard model," *Physical Review D*, vol. 69, no. 10, Article ID 105009, 2004.

[102] V. A. Kostelecký and M. Mewes, "Lorentz violation and short-baseline neutrino experiments," *Physical Review D*, vol. 70, Article ID 076002, 2004.

[103] A. Aguilar-Arevalo, C. E. Anderson, A. O. Bazarko et al., "Test of Lorentz and CPT violation with short baseline neutrino oscillation excesses," *Physics Letters B*, vol. 718, no. 4-5, pp. 1303–1308, 2013.

[104] P. Adamson, C. Andreopoulos, K. E. Arms et al., "Testing Lorentz invariance and CPT conservation with NuMI neutrinos in the MINOS near detector," *Physical Review Letters*, vol. 101, no. 15, Article ID 151601, 2008.

[105] P. Adamson, D. S. Ayres, G. Barr et al., "Search for Lorentz invariance and CPT violation with muon antineutrinos in the MINOS near detector," *Physical Review D*, vol. 85, Article ID 031101, 2012.

[106] P. Adamson, D. J. Auty, and D. S. Ayres, "Search for Lorentz invariance and CPT violation with the MINOS far detector," *Physical Review Letters*, vol. 105, no. 15, Article ID 151601, 2010.

[107] B. Rebel and S. Mufson, "The search for neutrino—antineutrino mixing resulting from Lorentz invariance violation using neutrino interactions in MINOS," *Astroparticle Physics*, vol. 48, pp. 78–81, 2013.

[108] R. Abbasi, Y. Abdou, and T. Abu-Zayyad, "Search for a Lorentz-violating sidereal signal with atmospheric neutrinos in IceCube," *Physical Review D*, vol. 82, Article ID 112003, 2010.

[109] Y. Abe, C. Aberle, J. C. dos Anjos et al., "First test of Lorentz violation with a reactor-based antineutrino experiment," *Physical Review D*, vol. 86, Article ID 112009, 2012.

[110] J. Díaz, T. Katori, J. Spitz, and J. Conrad, "Search for neutrino-antineutrino oscillations with a reactor experiment," *Physics Letters B*, vol. 727, no. 4-5, pp. 412–416, 2013.

[111] T. Adam, N. Agafonova, A. Aleksandrov et al., "Measurement of the neutrino velocity with the OPERA detector in the CNGS beam," *Journal of High Energy Physics*, vol. 1210, article 093, 2012.

[112] A. Kostelecký and M. Mewes, "Neutrinos with Lorentz-violating operators of arbitrary dimension," *Physical Review D*, vol. 85, Article ID 096005, 2012.

[113] B. Batell, M. Pospelov, and A. Ritz, "Exploring portals to a hidden sector through fixed targets," *Physical Review D*, vol. 80, Article ID 095024, 2009.

[114] P. de Niverville, M. Pospelov, and A. Ritz, "Observing a light dark matter beam with neutrino experiments," *Physical Review D*, vol. 84, Article ID 075020, 2011.

[115] P. de Niverville, D. McKeen, and A. Ritz, "Signatures of sub-GeV dark matter beams at neutrino experiments," *Physical Review D*, vol. 86, Article ID 035022, 2012.

[116] R. Dharmapalan, I. Stancu, R. A. Johnson et al., "A proposal to search for dark matter with MiniBooNE," Fermilab Proposal 1032, 2012.

[117] R. Bernabei, P. Belli, F. Cappella et al., "New results from DAMA/LIBRA," *The European Physical Journal C*, vol. 67, no. 1-2, pp. 39–49, 2010.

[118] C. Aalseth, P. S. Barbeau, N. S. Bowden et al., "Results from a search for light-mass dark matter with a P-type point contact germaniumdetector," *Physical Review Letters*, vol. 106, Article ID 131301, 2011.

[119] G. Angloher, M. Bauer, I. Bavykina et al., "Results from 730 kg days of the CRESST-II dark matter search," *The European Physical Journal C*, vol. 72, p. 1971, 2012.

[120] R. Agnese, Z. Ahmed, A. J. Anderson et al., "Silicon detector dark matter results from the final exposure of CDMS II," *Physical Review Letters*, vol. 111, Article ID 251301, 2013.

[121] R. Agnese, A. J. Anderson, M. Asai et al., "Search for low-mass weakly interacting massive particles using voltage-assisted calorimetric ionization detection in the SuperCDMS experiment," *Physical Review Letters*, vol. 112, no. 4, Article ID 041302, 2014.

[122] G. Bennett, B. Bousquet, H. N. Brown et al., "Final report of the E821 muon anomalous magnetic moment measurement at BNL," *Physical Review D*, vol. 73, Article ID 072003, 2006.

[123] M. Pospelov, "Secluded U(1) below the weak scale," *Physical Review D*, vol. 80, Article ID 095002, 2009.

[124] A. Adelmann, J. R. Alonso, W. Barletta et al., "Cost-effective design options for IsoDAR," 2012, http://arxiv.org/abs/1210.4454.

[125] D. Adey, S. K. Agarwalla, C. M. Ankenbrandt et al., "nuSTORM-neutrinos from STORed muons: proposal to the fermilab PAC," 2013, http://arxiv.org/abs/1308.6822.

[126] Y.-F. Li, J. Cao, Y. Wang, and L. Zhan, "Unambiguous determination of the neutrino mass hierarchy using reactor neutrinos," *Physical Review D*, vol. 88, Article ID 013008, 2013.

Review Article
The Low-Scale Approach to Neutrino Masses

Sofiane M. Boucenna,[1] Stefano Morisi,[2] and José W. F. Valle[1]

[1] *AHEP Group, Instituto de Física Corpuscular-Parque Científico (IFIC), Universitat de València,*
  C/Catedrático José Beltrán 2, 46980 Paterna, València, Spain
[2] *DESY, Platanenallee 6, 15735 Zeuthen, Germany*

Correspondence should be addressed to Stefano Morisi; stefano.morisi@gmail.com

In this short review we revisit the broad landscape of low-scale $SU(3)_c \otimes SU(2)_L \otimes U(1)_Y$ models of neutrino mass generation, with view on their phenomenological potential. This includes signatures associated to direct neutrino mass messenger production at the LHC, as well as messenger-induced lepton flavor violation processes. We also briefly comment on the presence of WIMP cold dark matter candidates.

1. Introduction

The flavor problem, namely, why we have three families of fermions with the same standard model quantum numbers, but with very hierarchical masses and a puzzling pattern of mixing parameters, constitutes one of the most challenging open problems in particle physics. In this regard neutrinos are probably the most mysterious particles. Indeed, while the discovery of the Higgs boson by the ATLAS and CMS experiments at the Large Hadron Collider (LHC) at CERN [1–3] has clarified to some extent the nature of electroweak symmetry breaking, the origin of neutrino masses remains elusive. With standard model fields one can induce Majorana neutrino masses through the nonrenormalizable dimension-5 operator

$$\mathcal{O}_{\text{dim}=5} = \frac{\lambda}{\Lambda} LLHH \qquad (1)$$

or higher order ones, for example, $LLHH(H^\dagger H)^m$ [4–9], where λ is a dimensionless coupling and Λ denotes some unknown effective scale. However, strictly speaking, we still do not know whether neutrinos are Dirac or Majorana fermions, and many issues remain open regarding the nature of the associated mass-giving operator, for example,

  (i) its underlying symmetries, such as total lepton number,

  (ii) its flavor structure which should account for the observed oscillation pattern,

  (iii) its dimensionality,

  (iv) its characteristic scale, and

  (v) its underlying mechanism.

This leads to considerable theoretical freedom which makes model building an especially hard task, a difficulty which to a large extent persists despite the tremendous experimental progress of the last fifteen years [10, 11].

Indeed the origin of neutrino mass remains so far a mystery. From oscillation studies we can not know the absolute neutrino mass scale. Still we know for certain that neutrinos are the lightest known fermions. Their mass must be below the few eV scale from tritium beta decay studies at the Katrin experiment [12], with somewhat stronger, though more model dependent limits coming from cosmology [13] and from negative neutrinoless double beta decay searches [14]. Unfortunately this vast body of information is far from sufficient to underpin the nature of the neutrino mass generation mechanism.

Mechanisms inducing neutrino mass may be broadly divided on the basis of whether the associated messengers lie at the high energy scale, related say, to some unification scheme or, in contrast, they involve new physics at the TeV scale, potentially accessible at the LHC.

For simplicity here we tacitly assume neutrino masses to come from Weinberg's operator in (1). This operator can arise in a rich variety of different pathways [15]. For instance in the case of the standard type-I seesaw mechanism [16–21] the right-handed neutrino messengers have a Majorana mass at some large scale, fitting naturally in Grand Unified Theories (GUTs). There are, however, many alternative realizations of the dimension-5 operator, such as the type-II [19, 22–25] and type-III seesaw [26] constructions, in which the messengers have nontrivial gauge quantum numbers. Such schemes are *bona fide* high-scale seesaw in the sense that, to account for the observed neutrino masses with reasonable strength for the relevant neutrino Yukawa couplings, one needs very large scales for the messenger mass, hence inaccessible to collider experiments. Of course within such scenarios one may artificially take TeV scales for the messenger mass by assuming tiny Yukawas, so as to account for the smallness of neutrino mass (One can avoid this in schemes where *ad hoc* cancellations [27] or symmetries [28, 29] prevent seesaw-produced masses. We do not consider such a special case in this review. Similarly we will not assume any family symmetry restricting the flavor structure of models.). However by doing so one erases a number of potential phenomenological implications. Hence we call such standard seesaw varieties as *high-scale seesaw*. It has long ago been realized [19] that, carrying no anomalies, singlets can be added in an arbitrary number to any gauge theory. Within the framework of the standard model $SU(3)_c \otimes SU(2)_L \otimes U(1)_Y$ gauge structure, the models can be labeled by an integer, m, the number of singlets. For example, to account for current neutrino oscillation data, a type-I seesaw model with two right-handed neutrinos is sufficient ($m = 2$). Likewise for models with $m = 1$ in which another mechanism such as radiative corrections (see below) generates the remaining scale. Models with $m > 3$ are especially interesting, where one can exploit the extra freedom to realize symmetries, such as lepton number L, so as to avoid seesaw-induced neutrino masses, naturally allowing for TeV-scale messengers. This is the idea behind the inverse [30] and linear seesaw schemes [31–33] described in the next section. We call such schemes as genuine *low-scale seesaw* constructions. A phenomenologically attractive alternative to low-scale seesaw are models where neutrino masses arise radiatively [34].

In principle one can assume the presence of supersymmetry in any such scheme, though in most cases it does not play an essential role for neutrino mass generation, *per se*. However we give an example where it could, namely, when the origin of neutrino mass is strictly supersymmetric because *R*-parity breaks. Indeed, neither gauge invariance nor supersymmetry requires *R*-parity conservation. There

are viable models where *R*-parity is an exact symmetry of the Lagrangian but breaks spontaneously through the Higgs mechanism [35, 36] by an $L = 1$ vacuum expectation value. As we will explain in the next section this scheme is hybrid in the sense that it combines seesaw and radiative contributions. In all of the above one can assume that the neutrino mass messengers lie at the TeV mass scale and hence have potentially detectable consequences.

In this review we consider the low-scale approach to neutrino masses. We choose to map out the possible schemes taking their potential phenomenological implications as guiding criteria, focusing on possible signatures at the LHC and lepton flavor violation (LFV) processes (Figure 1). The paper is organized as follows: in Section 2 we review low energy seesaw schemes; in Section 3 we discuss one-, two-, and three-loop radiative models. In Section 4 we discuss the supersymmetric mechanism and we sum up in Section 5.

2. Seesaw Mechanism

2.1. High-Scale Seesaw. Within minimal unified models such as SO(10), without gauge singlets, one automatically encounters the presence of new scalar or fermion states that can act as neutrino mass mediators inducing Weinberg's operator in (1). This leads to different variants of the so-called seesaw mechanism. One possibility is to employ the right-handed neutrinos present in the **16** of SO(10) and broadly called type-I seesaw schemes [16–21] (see Figure 2). Similar unified constructions can also be made substituting the right-handed neutrino exchange by that of an exotic hypercharge-neutral isotriplet lepton [26]

$$\Sigma = \left(\Sigma^+, \Sigma^0, \Sigma^- \right), \tag{2}$$

which is called type-III seesaw [26]. An alternative mediator is provided by a hypercharge-carrying isotriplet coming from the **126** of SO(10) and goes by the name type-II seesaw mechanism [19, 22, 23, 25] (see Figure 2).

The three options all involve new physics at high scale, typically close to the unification scale. While being model dependent, the expected magnitude of the mass of such messengers is typically expected to be high, say, associated to the breaking of extra gauge symmetries, such as the *B-L* generator.

Within standard type-I or type-III seesaw mechanism with three right-handed neutrinos the isodoublet neutrinos get mixed with the new messenger fermions by a 6×6 seesaw block diagonalization matrix that can be determined perturbatively using the general method in [21]. For example in the conventional type-I seesaw case the 6×6 matrix U that diagonalizes the neutrino mass is unitary and is given by

$$U = \begin{pmatrix} \left(I - \dfrac{1}{2} m_D^* (M_R^*)^{-1} M_R^{-1} m_D^T \right) V_1 & m_D^* (M_R^*)^{-1} V_2 \\[2ex] -M_R^{-1} m_D^T V_1 & \left(I - \dfrac{1}{2} M_R^{-1} m_D^T m_D^* (M_R^*)^{-1} \right) V_2 \end{pmatrix} + O\left(\epsilon^3 \right), \tag{3}$$
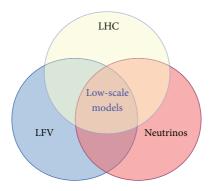
FIGURE 1: Low-scale neutrino mass models at the crossroad of high and low energy experiments.

(a)   (b)
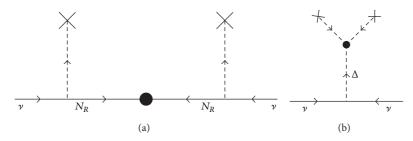
FIGURE 2: Neutrino mass generation in the type-I seesaw (a) and type-II seesaw (b). The black disks show where lepton number violation takes place.

where V_1 and V_2 are the unitary matrices that diagonalizes the light and heavy subblock, respectively. From (3) one sees that the active 3×3 subblock is no longer unitary and the deviation from unitary is of the order of $\epsilon^2 \sim (m_D/M_R)^2$. The expansion parameter ϵ is very small if the scale of new physics is at the GUT scale so the induced lepton flavor violation processes are suppressed. In this case there are no detectable direct production signatures at colliders nor LFV processes. This follows from the well know type-I seesaw relation

$$m_\nu \sim \frac{m_D^2}{M_{\text{messenger}}}, \tag{4}$$

where $M_{\text{messenger}} = M_R$ implying that

$$\epsilon^2 \sim \frac{m_\nu}{M_R}, \tag{5}$$

is suppressed by the neutrino mass, hence negligible regardless of whether the messenger scale M_R lies in the TeV scale (Weak universality tests as well as searches at LEP and previous colliders rule out lower messenger mass scales [37, 38].). As a result there is a decoupling of the effects of the messengers at low energy other than providing neutrino masses. This includes, for example, lepton flavor violation effects in both type-I and type-III seesaw mechanisms. Regarding direct signatures at collider experiments these require TeV-scale messengers which can be artificially implemented in both type-I and type-III cases by assuming the Dirac-type Yukawa couplings to be tiny. This makes messenger production at colliders totally hopeless in type-I seesaw but does not affect

the production rate in type-III seesaw mechanism, since it proceeds with gauge strength [39].

Coming to the type-II scheme, neutrino masses are proportional to the vev of the neutral component of a scalar electroweak triplet Δ^0 and we have

$$m_\nu = y_\nu v_T, \quad \text{where } v_T = \frac{\mu_T v^2}{M_T^2}, \tag{6}$$

where v is the vev of the standard model Higgs, M_T is the mass of the scalar triplet Δ, y_ν is the coupling of the neutrino with the scalar triplet, and μ_T is the coupling (with mass dimension) of the trilinear term between the standard model Higgs boson and the scalar triplet $H^T \Delta H$. Assuming y_ν of order one, in order to have light neutrino mass, there are two possibilities: either M_T is large or μ_T is small. The first case is the standard type-II seesaw where all the parameters of the model are naturally of order one.

In such high-scale type-I and type-III seesaw varieties neutrino mass messengers are above the energy reach of any conceivable accelerator, while lepton flavor violation effects arising from messenger exchange are also highly suppressed. Should lepton flavor violation ever be observed in nature, such schemes would suggest the existence of an alternative lepton flavor violation mechanism. A celebrated example of the latter is provided the exchange of scalar leptons in supersymmetric models [40–42].

In contrast, if type-II seesaw schemes are chosen to lie at the TeV scale, then lepton flavor violation effects as well as same-sign dilepton signatures at colliders remain [43];
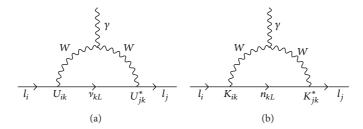
FIGURE 3: Radiative decays $\ell_i \rightarrow \ell_j \gamma$ in the standard model with massive light neutrinos (a) and heavy neutrinos (b).

see below. Obviously supersymmetrized "low-scale" type-II seesaw has an even richer phenomenology [44, 45].

2.2. Low-Scale Type-I Seesaw. The most general approach to the seesaw mechanism is that provided by the standard $SU(3)_c \otimes SU(2)_L \otimes U(1)_Y$ gauge group structure which holds at low energies. Within this framework one can construct seesaw theories with an arbitrary number of right-handed neutrinos, m [19], since gauge singlets carry no anomalies. In fact the same trick can be upgraded to other extended gauge groups, such as $SU(3) \otimes SU(2)_L \otimes SU(2)_R \otimes U(1)_{B-L}$ or Pati-Salam and also unified groups such as SO(10) [46, 47] or E_6. This opens the door to genuine low-scale realizations of the seesaw mechanism.

Before turning to the description of specific low-scale type-I seesaw schemes let us briefly note their basic phenomenological feature; namely, that in genuine low-scale seesaw schemes, (5) does not hold so that, for light enough messengers, one can have lepton flavor violation processes [48–50]. For example, radiative decays $\ell_i \rightarrow \ell_j \gamma$ proceed through the exchange of light Figure 3(a) as well as heavy neutrinos Figure 3(b). Clearly expected lepton flavor violation rates such as that for the $\mu \rightarrow e\gamma$ process are too small to be of interest. Another important conceptual feature of phenomenological importance is that lepton flavor violation survives even in the limit of strictly massless neutrinos (i.e., $\mu \rightarrow 0$; see text below) [51, 52].

2.2.1. Inverse Type-I Seesaw. In its simplest realization the inverse seesaw extends the standard model by means of two sets of electroweak two-component singlet fermions N_{Ri} and S_{Lj} [30]. The lepton number L of the two sets of fields N_R and S_L can be assigned as $L(N_R) = +1$ and $L(S_L) = +1$. One assumes that the fermion pairs are added sequentially; that is, $i, j = 1, 2, 3$, though other variants are possible. After electroweak symmetry breaking the Lagrangian is given by

$$\mathcal{L} = m_D \bar{\nu}_L N_R + M \overline{N}_R S_L + \mu \widetilde{S}_L S_L + \text{h.c.} \qquad (7)$$

We define $\widetilde{S}_L \equiv S_L^T C^{-1}$, where C is the charge conjugation matrix, m_D and M are arbitrary 3×3 Dirac mass matrices, and μ is a Majorana 3×3 matrix. We note that the lepton number is violated by the μ mass term here. The full neutrino mass matrix can be written as a 9×9 matrix instead of 6×6

as in the typical type-I seesaw and is given by (in the basis ν_L, N_R, and S_L)

$$M_\nu = \begin{pmatrix} 0 & m_D^T & 0 \\ m_D & 0 & M^T \\ 0 & M & \mu \end{pmatrix}. \qquad (8)$$

The entry μ may be generated from the spontaneous breaking of lepton number through the vacuum expectation value of a gauge singlet scalar boson carrying $L = 2$ [53].

It is easy to see that in the limit, where $\mu \rightarrow 0$ the exact $U(1)$ symmetry associated to total lepton number conservation holds, the light neutrinos are strictly massless. However individual symmetries are broken; hence flavor is violated, despite neutrinos being massless [51, 52]. For complex couplings, one can also show that CP is violated despite the fact that light neutrinos are strictly degenerate [54, 55]. The fact that flavor and CP are violated in the massless limit implies that the attainable rates for the corresponding processes are unconstrained by the observed smallness of neutrino masses and are potentially large.

This feature makes this scenario conceptually and phenomenologically interesting and is a consequence of the fact that the lepton number is conserved. However when $\mu \neq 0$ light neutrino masses are generated; see Figure 4. In particular in the limit where $\mu, m_D \lesssim M$ (on the other hand, the opposite limit $\mu \gg M$ is called double seesaw. In contrast to the inverse seesaw, the double seesaw brings no qualitative differences with respect to standard seesaw and will not be considered here) the light neutrino 3×3 mass matrix is given by

$$m_\nu \simeq m_D \frac{1}{M} \mu \frac{1}{M^T} m_D^T. \qquad (9)$$

It is clear from this formula that for "reasonable" Yukawa strength or m_D values, M of the order of TeV, and suitably small μ values one can account for the required light neutrino mass scale at the eV scale. There are two new physics scales, M and μ, the last of which is very small. Therefore it constitutes an extension of the standard model from below rather than from above. For this reason, it has been called inverse seesaw: in contrast with the standard type-I seesaw mechanism, neutrino masses are suppressed by a small parameter, instead of the inverse of a large one. The smallness of the scale μ is *natural* in t'Hooft's sense, namely, in the limit $\mu \rightarrow 0$; the symmetry is enhanced since lepton number is recovered (There are realizations where the low scale of μ is radiatively
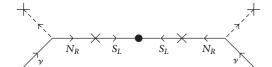
FIGURE 4: Neutrino mass generation in the type-I inverse seesaw.

calculable. As examples see the supersymmetry framework given in [56] or the standard model extension suggested in [57].).

In this case the seesaw expansion parameter $\epsilon \sim m_D/M$ also characterizes the strength of unitarity and universality violation and can be of order of percent or so [50, 58], leading to sizable lepton flavor violation rates, close to future experimental sensitivities. For example, with $m_D = 30$ GeV, $M = 300$ GeV, and $\mu = 10$ eV we have that $\epsilon^2 \sim 10^{-2}$. The deviation from the unitary is typically of order ϵ^2. As mentioned above, typical expected lepton flavor violation rates in the inverse seesaw model can be potentially large. For example, the rates for the classic $\mu \to e\gamma$ process are illustrated in Figure 5. The figure gives the predicted branching ratios $\mathrm{Br}(\mu \to e\gamma)$ in terms of the small neutrino mixing angle θ_{13}, for different values of the remaining oscillation parameters, with the solar mixing parameter $\sin^2\theta_{12}$ within its 3σ allowed range and fixing the inverse seesaw parameters as $M = 1$ TeV and $\mu = 3$ KeV. The vertical band corresponds to the 3σ allowed θ_{13} range.

Regarding direct production at colliders, although kinematically possible, the associated signatures are not easy to catch given the low rates as the right-handed neutrinos are gauge singlets and due to the expected backgrounds (see, e.g., [59]).

The way out is by embedding the model within an extended gauge structure that can hold at TeV energies, such as an extra $U(1)$ coupled to B-L which may arise from SO(10) [33]. Viable scenarios may also have TeV-scale $SU(3) \otimes SU(2)_L \otimes SU(2)_R \otimes U(1)_{B-L}$ or Pati-Salam intermediate symmetries [60]. In this case the right-handed messengers can be produced through a new charged [61–63] or neutral gauge boson [64]. In fact one has the fascinating additional possibility of detectable lepton flavor violation taking place at the large energies now accessible at the LHC [64].

2.2.2. Linear Type-I Seesaw. This variant of low-scale seesaw was first studied in the context of $SU(3) \otimes SU(2)_L \otimes SU(2)_R \otimes U(1)_{B-L}$ theories [31, 32] and subsequently demonstrated to arise naturally within the SO(10) framework in the presence of gauge singlets [33]. The lepton number assignment is as follows: $L(\nu_{Li}) = +1$, $L(N_{Ri}) = 1$, and $L(S_{Li}) = +1$ so that after electroweak symmetry breaking the Lagrangian is given by

$$\mathcal{L} = m_D \bar{\nu}_L N_R + M_R \overline{N}_R S_L + M_L \nu_L \widetilde{S}_L + \text{h.c.} \quad (10)$$
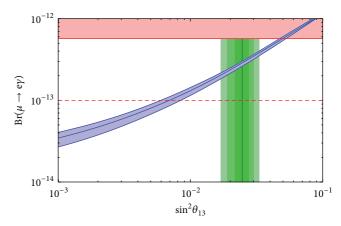
FIGURE 5: Branching ratios $\mathrm{Br}(\mu \to e\gamma)$ in the inverse seesaw model of neutrino mass [49].

Notice that the lepton number is broken by the mass term proportional to M_L. This corresponds to the neutrino mass matrix in the basis ν_L, N_R, and S_L given as

$$M_\nu = \begin{pmatrix} 0 & m_D^T & M_L \\ m_D & 0 & M_R \\ M_L & M_R & 0 \end{pmatrix}. \quad (11)$$

If $m_D \ll M_{L,R}$ then the effective light neutrino mass matrix is given by

$$m_\nu = m_D M_L \frac{1}{M_R} + \text{Transpose}. \quad (12)$$

Note that, in contrast with other seesaw varieties which lead to $m_\nu \propto m_D^2$, this relation is linear in the Dirac mass entry, hence the origin of the name "linear seesaw." Clearly neutrino masses will be suppressed by the small value of M_L irrespective of how low is the M_R scale characterizing the heavy messengers. For example, if one takes the SO(10) unification framework [33], natural in this context, one finds that the scale of M_L, that is, ν_L, is related to the scale of M_R, that is, ν_R, through

$$\nu_L \sim \frac{\nu_R \nu}{M_{\mathrm{GUT}}}, \quad (13)$$

where M_{GUT} is the unification scale of the order of $\mathcal{O}(10^{16}$ GeV$)$ and ν is the electroweak breaking scale of the order of $\mathcal{O}(100$ GeV$)$. Replacing the relation (13) in (12) the new physics scale drops out and can be very light, of the order of TeV.

Neutrino mass messengers are naturally accessible at colliders, like the LHC, since the right-handed neutrinos can be produced through the Z' "portal," as light as few TeV. The scenario has been shown to be fully consistent with the required smallness of neutrino mass as well as with the requirement of gauge coupling unification [33]. Other $SU(3) \otimes SU(2)_L \otimes SU(2)_R \otimes U(1)_{B-L}$ and Pati-Salam implementations have also been studied in [60].

Similarly to the inverse type-I seesaw scheme, we also have here potentially large unitarity violation in the effective

lepton mixing matrix governing the couplings of the light neutrinos. This gives rise to lepton flavor violation effects similar to the inverse seesaw case. Finally we note that, in general, a left-right symmetric linear seesaw construction also contains the lepton number violating Majorana mass term $\widetilde{S}_L S_L$ considered previously.

2.3. Low-Scale Type-III Seesaw. Here we consider a variant of the low-scale type-III seesaw model introduced in [65] based on the inverse seesaw mechanism [30] but replacing the N_R lepton field with the neutral component Σ^0 of a fermion triplet under $SU(2)_L$ with hypercharge zero [66]

$$\Sigma = \left(\Sigma^+, \Sigma^0, \Sigma^-\right). \tag{14}$$

As in the the inverse type-I seesaw one introduces an extra set of gauge singlet fermions S_L with lepton number $L(S_L) = +1$ and $L(\Sigma^0) = +1$. The mass Lagrangian is given by

$$\mathscr{L} = m_D \bar{\nu}_L \Sigma^0 + M\overline{\Sigma^0}S_L + \mu \widetilde{S}_L S_L - \frac{1}{2} m_\Sigma \operatorname{Tr}\left(\overline{\Sigma}\Sigma^c\right) + \text{h.c.} \tag{15}$$

In the basis (ν, Σ^0, S_L) the neutrino mass matrix is given by

$$M_\nu = \begin{pmatrix} 0 & m_D^T & 0 \\ m_D & m_\Sigma & M^T \\ 0 & M & \mu \end{pmatrix}. \tag{16}$$

As in the inverse seesaw case, in the limit $\mu = 0$, the light neutrinos are massless at tree level even if the mass term m_Σ breaks lepton number. And for a small $\mu \neq 0$ neutrinos get mass. Again, the scale of new physics is naturally small leading to sizable lepton flavor violation rates (Table 1).

On the other hand the charged component of the fermion triplet $\Sigma^\pm$ gives also a contribution to the charged lepton mass matrix

$$M_{\text{ch.lep}} = \begin{pmatrix} M_l & m_D \\ 0 & m_\Sigma \end{pmatrix}, \tag{17}$$

leading to a violation of the Glashow-Iliopoulos-Maiani mechanism [67] in the charged lepton sector, leading to tree-level contributions to $\mu \to eee$ and similar tau decay processes.

As in the standard type-III seesaw mechanism [26], universality violation is also present here. However, in contrast to the standard case, here its amplitude is of the order

$$\epsilon^2 \sim \left(\frac{m_D}{m_\Sigma}\right)^2, \tag{18}$$

which need not be neutrino mass suppressed. Indeed, in the inverse type-III seesaw scheme neutrino masses are proportional to the parameter μ. As a result there are sizeable lepton flavor violation processes such as $\mu \to e\gamma$ and $\mu \to eee$, whose attainable branching ratios are shown in **Figure 6**.

Finally, to conclude this discussion, we stress that, in contrast with the inverse type-I seesaw mechanism, here

TABLE 1: Phenomenological implications of low-scale $SU(3)_c \otimes SU(2)_L \otimes U(1)_Y$ seesaw models together with their particle content.

Model	Scalars	Fermions	LFV	LHC
Type-I		$(\mathbf{1},\mathbf{1},0)_{+1}$	✗	✗
Type-II	$(\mathbf{1},\mathbf{3},2)_{+2}$		✓	✓
Type-III		$(\mathbf{1},\mathbf{3},0)_{+1}$	✗	✓
Inverse		$(\mathbf{1},\mathbf{1},0)_{+1}$	✓	✗
Linear		$(\mathbf{1},\mathbf{1},0)_{+1}$	✓	✗
Inverse type-III		$(\mathbf{1},\mathbf{3},0)_{+1}, (\mathbf{1},\mathbf{1},0)_{+1}$	✓	✓

The subscript in the representations is lepton number. "✗" would change to "✓" in the presence of new gauge bosons or supersymmetry, as explained in the text.
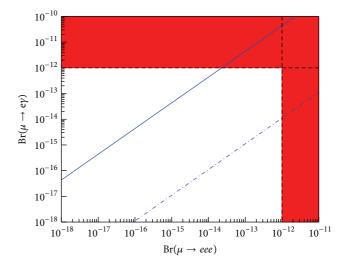
FIGURE 6: Branching of μ decay into $3e$ versus the branching of $\mu \to e\gamma$ varying the parameter μ parameter for different values of the mixing between the Σ^0 and S fields, 0.5 (continuous) and 0.1 (dashed) and with M is fixed at 1 TeV.

the neutrino mass messenger Σ^0, being an isotriplet member, has gauge interactions. Hence, if kinematically allowed it will be copiously produced in collider experiments like the LHC [39].

In short this scheme is a very interesting one from both the points of view of the detectability of collider signatures at the LHC as well as lepton flavor violation phenomenology.

2.4. Low-Scale Type-II Seesaw. We now turn to the so-called type-II seesaw mechanism [19, 22, 23, 25] which, though normally assumed to involve new physics at high energy scales, typically close to the unification scale, may also be considered (perhaps articially) as a low-scale construction, provided one adopts a tiny value for the trilinear mass parameter

$$\mu_T \sim 10^{-8}\,\text{GeV}, \tag{19}$$

in the scalar potential; then the triplet mass M_T can be assumed to lie around the TeV scale. Barring naturalness issues, such a scheme could be a possibility giving rise to very interesting phenomenological implications. In fact, in

this case, if kinematically allowed, the scalar triplet Δ will be copiously produced at the LHC because it interacts with gauge bosons.

Moreover the couplings y_ν that mediate lepton flavor violation processes are of order one and therefore such processes are not neutrino mass suppressed, as in the standard type-I seesaw. Indeed, from the upper limit $\mathrm{Br}(\mu \rightarrow 3e) < 10^{-12}$ it follows that (see [68])

$$y_\nu^2 < 1.4 \times 10^{-5} \left(\frac{m_\Delta}{1\,\mathrm{TeV}} \right), \qquad (20)$$

implying a sizeable triplet Yukawa coupling. With $y_\nu \sim 10^{-2}$, in order to get adequate neutrino mass values, one needs

$$v_T \sim 10^{-7}\,\mathrm{GeV}, \qquad (21)$$

which restricts the scalar triplet vacuum expectation value (vev). For such small value of the vev, the decay of the Δ^{++} is mainly into a pair of leptons with the same charge; while for $v_T > 10^{-4}\,\mathrm{GeV}$, the Δ^{++} decays mainly into a sam-sign WW pair; see [68].

Note that the tiny parameter μ_T controls the neutrino mass scale but does not enter in the couplings with fermions. This is why the lepton flavor violation rates can be sizable in this case. For detailed phenomenological studies of low energy type-II seesaw see, for example, [61, 68, 69].

Before reviewing the models based on radiative generation mechanisms for neutrino masses, we summarize the phenomenological implications of low scale seesaw models, together with their particle content, in Table 1.

3. Radiative Neutrino Masses

In the previous sections we reviewed mechanisms ascribing the smallness of neutrino masses to the small coefficient in front of Weinberg's dimension-five operator. This was generated through either tree-level exchange of superheavy messengers, with mass associated to high-scale symmetry breaking, or conversely, because of symmetry breaking at low scale. In what follows we turn to radiatively induced neutrino masses, a phenomenologically attractive way to account for neutrino masses. In such scenarios the smallness of the neutrino mass follows from loop factor(s) suppression. From a purely phenomenological perspective, radiative models are perhaps quite interesting as they rely on new particles that typically lie around the TeV scale, hence accessible to collider searches.

Unlike seesaw models, radiative mechanisms can go beyond the effective $\Delta L = 2$ dimension-five operator in (1) and generate the neutrino masses at higher order. This leads to new operators and to further mass suppression. Such an approach has been reviewed in [7, 70–73]. In what follows we will survey some representative underlying models up to the third loop level.

3.1. One-Loop Schemes. A general survey of one-loop neutrino mass operators leading to neutrino mass has been performed in [6]. Neutrino mass models in extensions of the SM
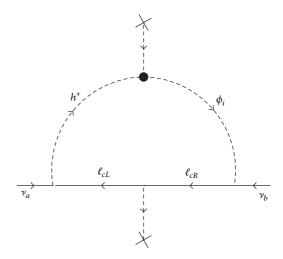
FIGURE 7: Neutrino mass generation in the Zee model.

with singlet right-handed neutrinos have been systematically analyzed in [74, 75] and for higher representations in [76]. Here we review the most representative model realizations.

3.1.1. Zee Model. The Zee Model [77] extends the standard $SU(3)_c \otimes SU(2)_L \otimes U(1)_Y$ model with the following fields:

$$h^+ \sim (\mathbf{1}, \mathbf{1}, +1)_{-2}, \qquad \phi_{1,2} \sim \left(\mathbf{1}, \mathbf{2}, +\frac{1}{2} \right)_0, \qquad (22)$$

where the subscript denotes lepton number. Given this particle content neutrino masses are one-loop calculable. The relevant terms are given by

$$\mathscr{L} = y_i^{ab} \overline{L}_a \phi_i \ell_{bR} + f^{ab} \widetilde{L}_a i\tau_2 L_b h^+ - \mu \phi_1^\dagger i\tau_2 \phi_2^* h^+ + \mathrm{h.c.}, \quad (23)$$

where a, b indicate the flavor indices; that is, $a, b = e, \mu, \tau$, $\widetilde{L} \equiv L^T C^{-1}$, and τ_2 is the second Pauli matrix. Notice that the matrix f must be antisymmetric in generation indices. The violation of lepton number, required to generate a Majorana mass term for neutrinos, resides in the coexistence of the two Higgs doublets in the μ term. The one-loop radiative diagram is shown in Figure 7. The model has been extensively studied in the literature [78–101], particularly in the Zee-Wolfenstein limit where only ϕ_1 couples to leptons due to a $\mathbb{Z}_2$ symmetry [102].

This particular simplification forbids tree-level Higgs-mediated flavor-changing neutral currents (FCNC), although it is now disfavored by neutrino oscillation data [90, 103]. However the general Zee model is still valid phenomenologically [87] and is in testable with FCNC experiments. For instance the exchange of the Higgs bosons leads to tree-level decays of the form $\ell_i \rightarrow \ell_j \ell_k \overline{\ell}_k$, in particular $\tau \rightarrow \mu\mu\overline{\mu}, \mu e\overline{e}$ (see, e.g., [104]). Collider phenomenology has been studied in [105, 106].

Recently, a variant of the Zee model has been considered in [107] by imposing a family-dependent $\mathbb{Z}_4$ symmetry acting on the leptons, thereby reducing the number of effective free parameters to four. The model predicts inverse hierarchy spectrum in addition to correlations among the mixing angles.

3.1.2. Radiative Seesaw Model. Another one-loop scenario was suggested by Ma [108]. Besides the standard model fields, three right-handed Majorana fermions N_i ($i = 1, 2, 3$) and a Higgs doublet are added to the $SU(3)_c \bigotimes SU(2)_L \otimes U(1)_Y$ model:

$$N_i \sim (\mathbf{1}, \mathbf{1}, 0)_{+1}, \qquad \eta \sim \left(\mathbf{1}, \mathbf{2}, +\frac{1}{2}\right)_0. \tag{24}$$

In addition, a parity symmetry acting only on the new fields is postulated. This $\mathbb{Z}_2$ is imposed in order to forbid Dirac neutrino mass terms. The relevant interactions of this model are given by

$$\mathcal{L} = y_{ab}\overline{L}_a i\tau_2 \eta^* N_b - M_{N_i}\widetilde{N}_i N_i + \text{h.c.} \tag{25}$$

In the scalar potential a quartic scalar term of the form $(H^\dagger \eta)^2$ is allowed. The one-loop radiative diagram is shown in Figure 8 and generates calculable $\mathcal{M}_\nu$ if $\langle \eta \rangle = 0$, which follows from the assumed symmetry. The neutrino masses are given by

$$(M_\nu)_{ab} = \sum_i \frac{y_{ai}y_{bi}M_{N_i}}{16\pi^2}$$
$$\times \left[\frac{m_R^2}{m_R^2 - M_{N_i}^2} \ln \frac{m_R^2}{M_{N_i}^2} - \frac{m_I^2}{m_I^2 - M_{N_i}^2} \ln \frac{m_I^2}{M_i^2} \right], \tag{26}$$

where m_R (m_I) is the mass of the real (imaginary) part of the neutral component of η.

Thanks to its simplicity and rich array of predictions, the model has become very popular and an extensive literature has been devoted to its phenomenological consequences. As is generally the case with multi-Higgs standard model extensions, the induced lepton flavor violation effects such as $\mu \rightarrow e\gamma$ provide a way to probe the model parameters. In particular the lepton flavor violation phenomenology has been studied in [109–114]. The effect of corrections induced by renormalization group running has also been considered [115], showing that highly symmetric patterns such as the bimaximal lepton mixing structure can still be valid at high energy but modified by the running to correctly account for the parameters required by the neutrino oscillation measurements [11]. Collider signatures have also been investigated in [116–119].

A remarkable feature of this model is the natural inclusion of a WIMP (weakly interacting massive particle) dark matter candidate. Indeed, the same parity that makes the neutrino mass calculable also stabilizes N_i and the neutral component of η. The lightest $\mathbb{Z}_2$-odd particle, either a boson or a fermion, can play the role of WIMP cold dark matter candidate [109, 111, 114, 120–124]. There is also the interesting possibility of the dark matter being warm in this setup [110, 125]. Various extensions of the model have also been considered, for example, [126, 127]. For a review on models with one-loop radiative neutrino masses and viable dark matter candidates we refer the reader to the complete classification given in [128, 129].
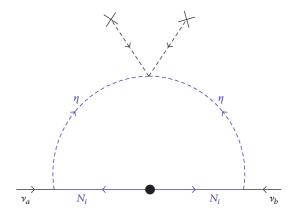
FIGURE 8: Neutrino mass generation in the radiative seesaw model. The blue color represents the potential dark matter candidates.
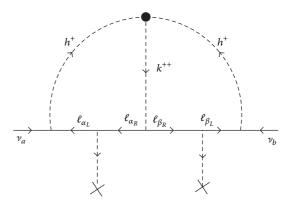
FIGURE 9: Neutrino mass generation in the Zee-Babu model.

3.2. Two-Loop Schemes. As a prototype two-loop scheme we consider the model proposed by Zee [130] and Babu [34] (which first appeared in [22]) that leads to neutrino masses at two-loop level by extending the standard model with two complex singly and doubly [131] charged $SU(2)_L$ singlet scalars

$$h^+ \sim (\mathbf{1}, \mathbf{1}, +1)_{-2}, \qquad k^{++} \sim (\mathbf{1}, \mathbf{1}, +2)_{-2}. \tag{27}$$

The relevant terms in the Lagrangian are therefore

$$\mathcal{L} = f_{ab}\widetilde{L}_a i\tau_2 L_b h^+ + g_{ab}\widetilde{\ell}_{aR}\ell_{bR}k^{++} - \mu h^- h^- k^{++} + \text{h.c.} \tag{28}$$

The trilinear μ term in the scalar potential (this term can arise spontaneously through the vev of an extra gauge singlet scalar boson [132]) provides lepton number violation and leads to a calculable Majorana neutrino mass generated at the second loop order, as shown in Figure 9 and given by

$$(M_\nu)_{ab} \sim \mu \frac{1}{(16\pi)^2} \frac{1}{M} \frac{16\pi^2}{3} f_{ac}m_c g_{cd}^* m_d f_{bd}, \tag{29}$$

where $M = \max(M_{k^{++}}, M_{h^+})$ and m_a are charged lepton masses [133]. As in the Zee model, the matrix f is antisymmetric. Therefore the determinant of m_ν vanishes and, as a result, one of the light neutrinos must be massless.

TABLE 2: Phenomenological implications of radiative $SU(3)_c \otimes SU(2)_L \otimes U(1)_Y$ neutrino mass models discussed in this review. Representations are labelled as in the rest of the paper.

	Model	Scalars	Fermions	LFV	DM	LHC
1-Loop	Zee	$(\mathbf{1}, \mathbf{1}, +1)_{-2}$, $(\mathbf{1}, \mathbf{2}, -1/2)_0$		✓	✗	✓
	Ma	$(\mathbf{1}, \mathbf{2}, +1/2)_0$	$(\mathbf{1}, \mathbf{1}, 0)_{+1}$	✓	✓	✓
2-Loops	Zee-Babu	$(\mathbf{1}, \mathbf{1}, +1)_{-2}$, $(\mathbf{1}, \mathbf{1}, +2)_{-2}$		✓	✗	✓
3-Loops	KNT	$(\mathbf{1}, \mathbf{1}, +1)_{-2}$	$(\mathbf{1}, \mathbf{1}, 0)_{+1}$	✓	✓	✗

The Zee-Babu model is constrained by a variety of lepton flavor violation processes among which the tree-level lepton flavor violation $\ell_i \rightarrow \ell_j \ell_k \bar{\ell}_l$ decays induced by k^{++} exchange and the radiative decays $\ell_i \rightarrow \ell_j \gamma$ mediated by the charged scalars h^+ and k^{++}. Weak universality is also violated since the h^+ exchange induces new contributions for muon decay [133–136]. Both lepton flavor violation and weak universality tests constrain the model parameters. Combining lepton flavor violation and universality constraints [134] pushes the mass of h^+ and k^{++} above the TeV scale, for both inverted and normal hierarchies, making it a challenge to probe the model at the LHC. The collider phenomenology of the model has been considered in [133, 134, 137].

3.3. Three-Loop Schemes. Of the possible three-loop schemes we will focus on the one suggested by Krauss-Nasri-Trodden (KNT) [138]. These authors considered an extension of the standard model with two charged scalar singlets h_1 and h_2 and one right-handed neutrino N. Consider the following:

$$h_{1,2}^+ \sim (\mathbf{1}, \mathbf{1}, +1)_{-2}, \qquad N \sim (\mathbf{1}, \mathbf{1}, 0)_{+1}. \tag{30}$$

As usual in radiative neutrino mass models that include gauge singlet Majorana fermions, an additional $\mathbb{Z}_2$ symmetry is imposed, under which the standard model fields as well as h_1 transform trivially, while N and h_2 are odd. The most general renormalizable terms that may be added to the standard model fermion Lagrangian are

$$\mathscr{L} = f_{ab}\widetilde{L}_a i\tau_2 L_b h_1^+ + g_a N h_2^+ \ell_{a_R} + M_N \widetilde{N} N + \text{h.c.} \tag{31}$$

Note that the scalar potential contains a term of the form $(h_1 h_2^*)^2$, which makes the diagram of Figure 10 possible. Hence neutrinos acquire Majorana masses induced only at the 3-loop level. Such strong suppression allows for sizable couplings of the TeV-scale singlet messenger states.

In addition to neutrino masses, the model also includes a WIMP dark matter candidate. Indeed for the choice of parameters $M_{h_2} > M_N$, N is stable and can be thermally produced in the early universe, leading naturally to the correct dark matter abundance.

A very similar model with the same loop topology has been proposed in [139], replacing the neutral gauge singlets by new colored fields and the charged leptons by quarks and in [140] the triplet variant of the model has been introduced. These variations make the model potentially testable at hadron colliders. Other three loop mass models have also been considered more recently, for instance, in [140–143]. A systematic study generalizing the KNT model was presented in [144] (Table 2).
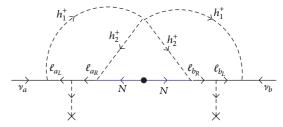
FIGURE 10: Neutrino mass generation in the KNT model.

We summarize the models discussed in this section and their phenomenological implications in Table 2.

4. Supersymmetry as the Origin of Neutrino Masses

The standard formulation of supersymmetry assumes the conservation of a discrete symmetry called R-parity (R_p), under which all the standard model states are R-even, while their superpartners are R-odd [145]. R_p is related to the spin (S), total lepton (L), and baryon (B) number as

$$R_p = (-1)^{(3B+L+2S)}. \tag{32}$$

Hence requiring baryon and lepton number conservation implies R_p conservation. In this case the supersymmetric states must be produced in pairs, while the lightest of them is absolutely stable.

On general grounds, however, neither gauge invariance nor supersymmetry requires R_p conservation and many implications can be associated to R-parity violation [146]. The most general supersymmetric standard model extension contains explicit R_p violating interactions. Constraints on the relevant parameters and their possible signals have been analysed [147, 148]. In general, there are too many independent couplings, some of which must be set to zero in order to avoid too fast the proton decay. For these reasons we focus our attention to the possibility that R_p can be an exact symmetry of the Lagrangian, broken spontaneously through the Higgs mechanism [35, 149]. This may occur via nonzero vacuum expectation values for scalar neutrinos, such as

$$v_R = \langle \widetilde{\nu}_{R\tau} \rangle ; \qquad v_L = \langle \widetilde{\nu}_{L\tau} \rangle . \tag{33}$$

Here we consider the simplest prototype scheme where supersymmetry seeds neutrino masses in an essential way. The idea is to take the simplest effective description of the above picture, namely, bilinear R-parity violation [150–152].

TABLE 3: Neutrino mass models in terms of their phenomenological potential at the LHC and/or the sizable presence of lepton flavor violation phenomena where we use the same labeling convention as in the text.

	Type-I	Type-II	Type-III	Inverse	Linear	Invers type-III	Radiative
LHC	✗	✓	✓	✗	✗	✓	✓
LFV	✗	✓	✗	✓	✓	✓	✓

As we have explained in the text, "✗" could change to "✓" in the presence of new gauge bosons or supersymmetry.

This is the minimal way to incorporate lepton number and R-parity violation to the minimal supersymmetric standard model (MSSM), providing a simple way to accommodate neutrino masses in supersymmetry. The superpotential is

$$W = W^{\text{MSSM}} + \epsilon_a \widehat{L}_a \widehat{H}_u. \qquad (34)$$

The three $\epsilon_a = (\epsilon_e, \epsilon_\mu, \epsilon_\tau)$ parameters have dimensions of mass and explicitly break lepton number by $\Delta L = 1$. Their size and origin can be naturally explained in extended models where the breaking of lepton number is spontaneous [35, 149, 152]. These parameters are constrained to be small ($\epsilon_a \ll m_W$) so as to account for the small neutrino masses. Furthermore, the presence of the new superpotential terms implies new soft supersymmetry breaking terms as well

$$V_{\text{soft}} = V_{\text{soft}}^{\text{MSSM}} + B_a \epsilon_a \widetilde{L}_a H_u, \qquad (35)$$

where the B_a are parameters with units of mass.

In this scheme, neutrinos get tree-level mass by mixing with the neutralino sector [153–155]. In the basis $(\psi^0)^T = (-i\widetilde{B}^0, -i\widetilde{W}_3^0, \widetilde{H}_d^0, \widetilde{H}_u^0, \nu_e, \nu_\mu, \nu_\tau)$ the neutral fermion mass matrix M_N this matrix is given by

$$M_{N\chi} = \begin{pmatrix} \mathcal{M}_{\chi^0} & m^T \\ m & 0 \end{pmatrix}, \qquad (36)$$

where $\mathcal{M}_{\chi^0}$ is the usual neutralino mass matrix and

$$m = \begin{pmatrix} -\dfrac{1}{2}g'\nu_{L_e} & \dfrac{1}{2}g\nu_{L_e} & 0 & \epsilon_e \\[2mm] -\dfrac{1}{2}g'\nu_{L_\mu} & \dfrac{1}{2}g\nu_{L_\mu} & 0 & \epsilon_\mu \\[2mm] -\dfrac{1}{2}g'\nu_{L_\tau} & \dfrac{1}{2}g\nu_{L_\tau} & 0 & \epsilon_\tau \end{pmatrix} \qquad (37)$$

is the matrix describing R-parity violation. Here ν_{L_a} are the vevs of sneutrinos induced by the presence of ϵ_i and B_i. The smallness of the R-parity violating parameters implies that the components of m are suppressed with respect to those in $\mathcal{M}_{\chi^0}$. Hence the resulting M_N matrix has a type-I seesaw structure so the effective light neutrino mass matrix can be obtained from the usual formula $m_\nu^0 = -m \cdot \mathcal{M}_{\chi^0}^{-1} \cdot m^T$, which can be expanded to give

$$(M_\nu)_{ab} = \alpha \Lambda_a \Lambda_b, \qquad (38)$$

where α is a combination of SUSY parameters, while $\Lambda_a = \mu\nu_{L_a} + \nu_d \epsilon_a$ are known as the *alignment parameters*. The above matrix is projective and has two zero eigenvalues; therefore

only one neutrino is massive at tree level. A natural choice is to ascribe this eigenvalue to the atmospheric scale whereas the solar mass scale, $\Delta m_{\text{sol}}^2 \ll \Delta m_{\text{atm}}^2$, arises from quantum corrections calculable at the one-loop level of the neutrino mass matrix in (38). Detailed computations of the one-loop contributions to the neutrino mass matrix are given in [153, 154]. The corrections are of the type

$$\left(m_\nu^{\text{rad}}\right)_{ab} \approx \alpha^{(\text{rad})}\Lambda_a\Lambda_b + \beta^{(\text{rad})}\left(\Lambda_a\epsilon_b + \Lambda_a\epsilon_b\right) + \gamma^{(\text{rad})}\epsilon_a\epsilon_b, \qquad (39)$$

where the coefficients $\alpha^{(\text{rad})}$, $\beta^{(\text{rad})}$, and $\gamma^{(\text{rad})}$ are complicated functions of the SUSY parameters. These corrections generate a second nonzero mass eigenstate associated with the solar scale and the corresponding mixing angle (the neutrino mixing angles are determined as ratios of R-parity violating parameters ϵ_i and Λ_i) θ_{12}.

The bilinear R-parity breaking model offers a hybrid mechanism combining seesaw-type and radiative contributions, thereby providing an explanation for the observed smallness of the solar squared mass splitting with respect to the atmospheric one.

The above scheme is both well motivated and testable at colliders. Indeed in the absence of R-parity, the lightest supersymmetric particle (LSP) is no longer protected and decays to standard model particles. The smallness of the breaking strength, required to account for neutrino masses, makes the lifetime of the LSP long enough so that it may decay within the detector with displaced vertices. Since LSP decays and neutrino masses have a common origin, one can show that ratios of LSP decay branching ratios correlate with the neutrino mixing angles measured at low energies [156]. This provides a remarkable connection which allows one to use neutrino oscillation data to test the model at the LHC; see, for example, [157, 158].

5. Summary and Outlook

We have given a brief overview of the low-scale $SU(3)_c \otimes SU(2)_L \otimes U(1)_Y$ approach to neutrino mass generation. To chart out directions within such a broad neutrino landscape we used their possible phenomenological potential as a guide. We analyzed signatures associated to direct neutrino mass messenger production at the LHC, as well as messenger-induced lepton flavor violation processes. We have considered seesaw-based schemes as well as those with radiative or supersymmetric origin for the neutrino mass. We summarize our conclusions in Table 3. We stressed the phenomenological interest on radiative models and low-scale seesaw schemes as well as the type-II seesaw "tuned" to lie

at the low scale. We also briefly comment on the presence of WIMP cold dark matter candidates.

In conclusion if the messengers responsible for the light neutrino masses lie at a very high scale, like in type-I seesaw, it will be very difficult if not impossible to have any detectable signal within the nonsupersymmetric $SU(3)_c \otimes SU(2)_L \otimes U(1)_Y$ seesaw framework. In contrast, within the low-scale approach to neutrino mass we can have very interesting phenomenological implications. They can give rise to signatures at high energy collider experiments, as well as lepton flavor violation rates close to the sensitivity of planned experiments. In some of the schemes there is a natural WIMP dark matter candidate. In short, these scenarios may help reconstructing the neutrino mass from a variety of potentially overconstrained set of observables.

Conflict of Interests

The authors declare that there is no conflict of interests regarding the publication of this paper.

Acknowledgments

References

[1] ATLAS and CMS Collaboration, "Birth of a Higgs boson," *CERN Courier*, vol. 53, no. 4, pp. 21–23, 2013.

[2] G. Aad, T. Abajyan, B. Abbott et al., "Observation of a new particle in the search for the Standard Model Higgs boson with the ATLAS detector at the LHC," *Physics Letters B*, vol. 716, no. 1, pp. 1–29, 2012.

[3] S. Chatrchyan, V. Khachatryan, A. M. Sirunyan et al., "Observation of a new boson at a mass of 125 GeV with the CMS experiment at the LHC," *Physics Letters B*, vol. 716, no. 1, pp. 30–61, 2012.

[4] S. Weinberg, "Baryon- and lepton-nonconserving processes," *Physical Review Letters*, vol. 43, article 1566, 1979.

[5] F. Bonnet, M. Hirsch, T. Ota, and W. Winter, "Systematic decomposition of the neutrinoless double beta decay operator," *Journal of High Energy Physics*, vol. 2013, article 55, 2013.

[6] F. Bonnet, M. Hirsch, T. Ota, and W. Winter, "Systematic study of the $d = 5$ Weinberg operator at one-loop order," *Journal of High Energy Physics*, vol. 2012, no. 153, 2012.

[7] A. de Gouvea and J. Jenkins, "A survey of lepton number violation via effective operators," *Physical Review D*, vol. 77, Article ID 013008, 2008.

[8] F. Bonnet, D. Hernandez, T. Ota, and W. Winter, "Neutrino masses from higher than d = 5 effective operators," *Journal of High Energy Physics*, vol. 10, article 076, 2009.

[9] M. B. Krauss, D. Meloni, W. Porod, and W. Winter, "Neutrino mass from a $d = 7$ effective operator in a SUSY-GUT framework," *Journal of High Energy Physics*, vol. 2013, no. 5, article 121, 2013.

[10] H. Nunokawa, S. J. Parke, and J. W. F. Valle, "CP violation and neutrino oscillations," *Progress in Particle and Nuclear Physics*, vol. 60, pp. 338–402, 2008.

[11] D. Forero, M. Tortola, and J. W. F. Valle, "Global status of neutrino oscillation parameters after Neutrino-2012," *Physical Review D*, vol. 86, Article ID 073012, 2012.

[12] A. Osipowicz, H. Blumer, G. Drexlin et al., "KATRIN: a next generation tritium beta decay experiment with sub-eV sensitivity for the electron neutrino mass. Letter of intent," http://arxiv.org/abs/hep-ex/0109033.

[13] J. Lesgourgues, G. Mangano, G. Miele, and S. Pastor, *Neutrino Cosmology*, Cambridge University Press, Cambridge, UK, 2013.

[14] A. Barabash, "75 years of double beta decay: yesterday, today and tomorrow," http://arxiv.org/abs/1101.4502.

[15] E. Ma, "Pathways to naturally small neutrino masses," *Physical Review Letters*, vol. 81, p. 1171, 1998.

[16] P. Minkowski, "$\mu \rightarrow e\gamma$ at a rate of one out of 10^9 muon decays?" *Physics Letters B*, vol. 67, no. 4, pp. 421–428, 1977.

[17] T. Yanagida, "Horizontal symmetry and masses of neutrinos," *Conference Proceedings C*, Article ID 7902131, pp. 95–99, 1979.

[18] M. Gell-Mann, P. Ramond, and R. Slansky, "Complex spinors and unified theories," in *Proceedings of the Supergravity Workshop C790927*, pp. 315–321, 1979.

[19] J. Schechter and J. W. F. Valle, "Neutrino masses in SU(2) ⊗ U(1) theories," *Physical Review D*, vol. 22, p. 2227, 1980.

[20] R. N. Mohapatra and G. Senjanovic, "Neutrino mass and spontaneous parity nonconservation," *Physical Review Letters*, vol. 44, p. 912, 1980.

[21] J. Schechter and J. W. F. Valle, "Neutrino decay and spontaneous violation of lepton number," *Physical Review D*, vol. 25, p. 774, 1982.

[22] T. P. Cheng and L.-F. Li, "Neutrino masses, mixings, and oscillations in SU(2)×U(1) models of electroweak interactions," *Physical Review D*, vol. 22, no. 11, p. 2860, 1980.

[23] M. Magg, C. Wetterich, and B. Phys. Lett, "Neutrino mass problem and gauge hierarchy," *Physics Letters B*, vol. 94, pp. 61–64, 1980.

[24] C. Wetterich, "Neutrino masses and the scale of *B-L* violation," *Nuclear Physics B*, vol. 187, no. 2, pp. 343–375, 1981.

[25] R. N. Mohapatra and G. Senjanovic, "Neutrino masses and mixings in gauge models with spontaneous parity violation," *Physical Review D*, vol. 23, p. 165, 1981.

[26] R. Foot, H. Lew, X. G. He, and G. C. Joshi, "See-saw neutrino masses induced by a triplet of leptons," *Zeitschrift für Physik C: Particles and Fields*, vol. 44, no. 3, pp. 441–444, 1989.

[27] J. Kersten and A. Y. Smirnov, "Right-handed neutrinos at LHC and the mechanism of neutrino mass generation," *Physical Review D*, vol. 76, Article ID 073005, 2007.

[28] P.-H. Gu, M. Hirsch, U. Sarkar, and J. W. F. Valle, "Neutrino masses, leptogenesis, and dark matter in a hybrid seesaw model," *Physical Review D*, vol. 79, Article ID 033010, 2009.

[29] P. S. B. Dev, A. Pilaftsis, and U.-K. Yang, "New production mechanism for heavy neutrinos at the LHC," *Physical Review Letters*, vol. 112, Article ID 081801, 2014.

[30] R. N. Mohapatra and J. W. F. Valle, "Neutrino mass and baryon-number nonconservation in superstring models," *Physical Review D*, vol. 34, p. 1642, 1986.

[31] E. Akhmedova, M. Lindnerb, E. Schnapkab, and J. Vallec, "Left-right symmetry breaking in NJL approach," *Physics Letters B*, vol. 368, no. 4, pp. 270–280, 1996.

[32] E. Akhmedov, M. Lindner, E. Schnapka, and J. W. F. Valle, "Dynamical left-right symmetry breaking," *Physical Review D*, vol. 53, p. 2752, 1996.

[33] M. Malinsky, J. C. Romao, and J. W. F. Valle, "Supersymmetric SO(10) seesaw mechanism with low B-L scale," *Physical Review Letters*, vol. 95, Article ID 161801, 2005.

[34] K. S. Babu, "Model of "calculable" Majorana neutrino masses," *Physics Letters B*, vol. 203, pp. 132–136, 1988.

[35] A. Masiero and J. Valle, "A model for spontaneous *R* parity breaking," *Physics Letters B*, vol. 251, no. 2, pp. 273–278, 1990.

[36] J. C. Romao, C. A. Santos, and J. W. F. Valle, "How to spontaneously break R parity?" *Physics Letters B*, vol. 288, pp. 311–320, 1992.

[37] P. Abreu, W. Adam, T. Adye et al., "Search for neutral heavy leptons produced in Z decays," *Zeitschrift für Physik C*, vol. 74, no. 1, pp. 57–71, 1997.

[38] J. Beringer, J.-F. Arguin, R. M. Barnett et al., "Review of particle physics," *Physical Review D*, vol. 86, Article ID 010001, 2012.

[39] R. Franceschini, T. Hambye, and A. Strumia, "Type-III seesaw mechanism at CERN LHC," *Physical Review D*, vol. 78, Article ID 033002, 2008.

[40] F. Borzumati and A. Masiero, "Large muon- and electron-number nonconservation in supergravity theories," *Physical Review Letters*, vol. 57, no. 8, pp. 961–964, 1986.

[41] M. Hirsch, J. W. F. Valle, W. Porod, J. C. Romao, and A. Villanova del Moral, "Probing minimal supergravity in the type-I seesaw mechanism with lepton flavor violation at the CERN LHC," *Physical Review D*, vol. 78, Article ID 013006, 2008.

[42] J. Esteves, J. Romao, M. Hirsch et al., "LHC and lepton flavour violation phenomenology of a left-right extension of the MSSM," *Journal of High Energy Physics*, vol. 1012, article 077, 2010.

[43] P. F. Perez, "Type III seesaw and left-right symmetry," *Journal of High Energy Physics*, vol. 142, no. 3, 2009.

[44] D. Aristizabal Sierra, M. Hirsch, J. W. F. Valle et al., "Reconstructing neutrino properties from collider experiments in a Higgs triplet neutrino mass model," *Physical Review D*, vol. 68, Article ID 033006, 2003.

[45] J. N. Esteves, J. C. Romao, A. V. del Moral et al., " Flavour violation at the LHC: type-I versus type-II seesaw in minimal supergravity," *Journal of High Energy Physics*, vol. 05, article 003, 2009.

[46] P. S. B. Dev and R. N. Mohapatra, "TeV scale inverse seesaw model in SO(10) and leptonic nonunitarity effects," *Physical Review D*, vol. 81, Article ID 013001, 2010.

[47] C.-H. Lee, P. Bhupal Dev, and R. Mohapatra, "Natural TeV-scale left-right seesaw mechanism for neutrinos and experimental tests," *Physical Review D*, vol. 88, Article ID 093010, 2013.

[48] F. Deppisch, T. S. Kosmas, and J. W. F. Valle, "Enhanced μ^--e^- conversion in nuclei in the inverse seesaw model," *Nuclear Physics B*, vol. 752, pp. 80–92, 2006.

[49] F. Deppisch and J. W. F. Valle, "Enhanced lepton flavour violation in the supersymmetric inverse seesaw model," *Physical Review D*, vol. 72, Article ID 036001, 2005.

[50] D. Forero, S. Morisi, M. Tortola, and J. W. F. Valle, "Lepton flavor violation and non-unitary lepton mixing in low-scale type-I seesaw," *Journal of High Energy Physics*, vol. 2011, no. 9, article 142, 2011.

[51] J. Bernabeu, A. Santamaria, and J. Vidal, "Lepton flavour non-conservation at high energies in a superstring inspired standard model," *Physics Letters B*, vol. 187, pp. 303–308, 1987.

[52] M. C. Gonzalez-Garcia and J. W. F. Valle, "Enhanced lepton flavor violation with massless neutrinos: a Study of muon and tau decays," *Modern Physics Letters A*, vol. 7, p. 477, 1992.

[53] M. Gonzalez-Garcia and J. Valle, "Fast decaying neutrinos and observable flavour violation in a new class of majoron models," *Physics Letters B*, vol. 216, no. 3-4, pp. 360–366, 1989.

[54] G. C. Branco, M. N. Rebelo, and J. W. F. Valle, "Leptonic CP violation with massless neutrinos," *Physics Letters B*, vol. 225, no. 4, pp. 385–392, 1989.

[55] N. Rius and J. W. F. Valle, "Leptonic *CP* violating asymmetries in Z^0 decays," *Physics Letters B*, vol. 246, pp. 249–255, 1990.

[56] F. Bazzocchi, D. Cerdeno, C. Munoz, and J. W. F. Valle, "Calculable inverse-seesaw neutrino masses in supersymmetry," *Physical Review D*, vol. 81, Article ID 051701(R), 2010.

[57] F. Bazzocchi, "Minimal dynamical inverse seesaw mechanism," *Physical Review D*, vol. 83, Article ID 093009, 2011.

[58] H. Hettmansperger, M. Lindner, and W. Rodejohann, "Phenomenological consequences of sub-leading terms in see-saw formulas," *Journal of High Energy Physics*, vol. 2011, article 123, 2011.

[59] A. Das and N. Okada, "Inverse seesaw neutrino signatures at LHC and ILC," *Physical Review D*, vol. 88, Article ID 113001, 2013.

[60] V. de Romeri, M. Hirsch, and M. Malinský, "Soft masses in supersymmetric SO(10) GUTs with low intermediate scales," *Physical Review D*, vol. 84, Article ID 053012, 2011.

[61] P. Nath, B. D. Nelson, H. Davoudiasl et al., "The hunt for new physics at the large hadron collider," *Nuclear Physics B: Proceedings Supplements*, vol. 200–202, pp. 185–417, 2010.

[62] S. Das, F. Deppisch, O. Kittel, and J. Valle, "Heavy neutrinos and lepton flavor violation in left-right symmetric models at the LHC," *Physical Review D*, vol. 86, Article ID 055006, 2012.

[63] J. Aguilar-Saavedra, F. Deppisch, O. Kittel, and J. Valle, "Flavor in heavy neutrino searches at the LHC," *Physical Review D*, vol. 85, Article ID 091301, 2012.

[64] F. F. Deppisch, N. Desai, and J. W. F. Valle, "Is charged lepton flavour violation a high energy phenomenon?" *Physical Review D*, vol. 89, Article ID 051302, 2014.

[65] E. Ma, "Inverse seesaw neutrino mass from lepton triplets in the U(1)_sigma model," *Modern Physics Letters A*, vol. 24, no. 31, p. 2491, 2009.

[66] D. Ibanez, S. Morisi, and J. W. F. Valle, "Inverse tribimaximal type-III seesaw mechanism and lepton flavor violation," *Physical Review D*, vol. 80, Article ID 053015, 2009.

[67] S. L. Glashow, J. Iliopoulos, and L. Maiani, "Weak interactions with lepton-hadron symmetry," *Physical Review D*, vol. 2, no. 7, pp. 1285–1292, 1970.

[68] P. Fileviez Perez, T. Han, G.-Y. Huang, T. Li, and K. Wang, "Neutrino masses and the CERN LHC: testing the type II seesaw mechanism," *Physical Review D*, vol. 78, Article ID 015018, 2008.

[69] F. del Aguila and J. A. Aguilar-Saavedra, "Distinguishing seesaw models at LHC with multi-lepton signals," *Nuclear Physics B*, vol. 813, pp. 22–90, 2009.

[70] K. Babu and C. N. Leung, "Classification of effective neutrino mass operators," *Nuclear Physics B*, vol. 619, pp. 667–689, 2001.

[71] P. W. Angel, N. L. Rodd, and R. R. Volkas, "Origin of neutrino masses at the LHC: $\Delta L = 2$ effective operators and their ultraviolet completions," *Physical Review D*, vol. 87, Article ID 073007, 2013.

[72] Y. Farzan, S. Pascoli, and M. A. Schmidt, "Recipes and ingredients for neutrino mass at loop level," *Journal of High Energy Physics*, vol. 2013, article 107, 2013.

[73] S. S. Law and K. L. McDonald, "The simplest models of radiative neutrino mass," *International Journal of Modern Physics A*, vol. 29, no. 10, Article ID 1450064, 18 pages, 2014.

[74] A. Pilaftsis, "Radiatively induced neutrino masses and large Higgs-neutrino couplings in the Standard Model with Majorana fields," *Zeitschrift für Physik C*, vol. 55, no. 2, pp. 275–282, 1992.

[75] P. B. Dev and A. Pilaftsis, "Minimal radiative neutrino mass mechanism for inverse seesaw models," *Physical Review D*, vol. 86, Article ID 113001, 2012.

[76] P. Fileviez Perez and M. B. Wise, "On the origin of neutrino masses," *Physical Review D*, vol. 80, Article ID 053006, 2009.

[77] A. Zee, "A theory of lepton number violation and neutrino Majorana masses," *Physics Letters B*, vol. 93, pp. 389–393, 1980.

[78] D. Aristizabal Sierra and D. Restrepo, "Leptonic charged Higgs decays in the Zee model," *Journal of High Energy Physics*, vol. 2006, no. 8, article 036, 2006.

[79] A. Y. Smirnov and M. Tanimoto, "Is the Zee model the model of neutrino masses?" *Physical Review D*, vol. 55, pp. 1665–1671, 1997.

[80] C. Jarlskog, M. Matsuda, S. Skadhauge, and M. Tanimoto, "Zee mass matrix and bi-maximal neutrino mixing," *Physics Letters B*, vol. 449, pp. 240–252, 1999.

[81] P. H. Frampton and S. L. Glashow, "Can the Zee ansatz for neutrino masses be correct?" *Physics Letters B*, vol. 461, no. 1-2, pp. 95–98, 1999.

[82] A. S. Joshipura and S. D. Rindani, "Q-Ising neural network dynamics: a comparative review of various architectures," *Physics Letters B*, vol. 464, p. 239, 1999.

[83] G. McLaughlin and J. Ng, "Partitioning of a polymer chain between two confining cavities: the roles of excluded volume and finite size conduits," *Chemical Physics Letters*, vol. 327, no. 3-4, pp. 238–244, 1999.

[84] K.-M. Cheung and O. C. Kong, "Zee neutrino mass model in a SUSY framework," *Physical Review D*, vol. 61, Article ID 113012, 2000.

[85] D. Chang and A. Zee, "Radiatively induced neutrino Majorana masses and oscillation," *Physical Review D*, vol. 61, Article ID 071303(R), 2000.

[86] D. A. Dicus, H.-J. He, and J. N. Ng, "Neutrino-lepton masses, Zee scalars, and muon *g-2*," *Physical Review Letters*, vol. 87, Article ID 111803, 2001.

[87] K. Balaji, W. Grimus, and T. Schwetz, "The solar LMA neutrino oscillation solution in the Zee model," *Physics Letters B*, vol. 508, no. 3-4, pp. 301–310, 2001.

[88] E. Mitsuda and K. Sasaki, "Zee model and phenomenology of lepton sector," *Physics Letters B*, vol. 516, pp. 47–53, 2001.

[89] A. Ghosal, Y. Koide, and H. Fusaoka, "Lepton flavor violating Z decays in the Zee model," *Physical Review D*, vol. 64, Article ID 053012, 2001.

[90] Y. Koide, "Can the Zee model explain the observed neutrino data?" *Physical Review D*, vol. 64, Article ID 077301, 2001.

[91] B. Brahmachari and S. Choubey, "Viability of bi-maximal solution of the Zee mass matrix," *Physics Letters B*, vol. 531, pp. 99–104, 2002.

[92] T. Kitabayashi and M. Yasue, "Large solar neutrino mixing in an extended zee model," *International Journal of Modern Physics A*, vol. 17, no. 19, pp. 2519–2534, 2002.

[93] Y. Koide, "Prospect of the Zee model," *Nuclear Physics B—Proceedings Supplements*, vol. 111, no. 1–3, pp. 294–296, 2002.

[94] M.-Y. Cheng and K.-M. Cheung, "Zee model and Neutrinoless double beta decay," http://arxiv.org/abs/hep-ph/0203051.

[95] X. G. He and A. Zee, "Some simple mixing and mass matrices for neutrinos," *Physics Letters B*, vol. 560, no. 1-2, pp. 87–90, 2003.

[96] K. Hasegawa, C. Lim, and K. Ogure, "Escape from washing out of baryon number in a two-zero-texture general Zee model compatible with the large mixing angle MSW solution," *Physical Review D*, vol. 68, Article ID 053006, 2003.

[97] S. Kanemura, T. Ota, and K. Tsumura, "Lepton flavor violation in Higgs boson decays under the rare tau decay results," *Physical Review D*, vol. 73, Article ID 016006, 2006.

[98] B. Brahmachari and S. Choubey, "Modified Zee mass matrix with zero-sum condition," *Physics Letters B*, vol. 642, pp. 495–502, 2006.

[99] N. Sahu and U. Sarkar, "Extended Zee model for neutrino mass, leptogenesis, and sterile-neutrino-like dark matter," *Physical Review D*, vol. 78, Article ID 115013, 2008.

[100] T. Fukuyama, H. Sugiyama, and K. Tsumura, "Phenomenology in the Zee model with the A_4 symmetry," *Physical Review D*, vol. 83, no. 5, Article ID 056016, 2011.

[101] F. del Aguila, A. Aparici, S. Bhattacharya, A. Santamaria, and J. Wudka, "Effective Lagrangian approach to neutrinoless double beta decay and neutrino masses," *Journal of High Energy Physics*, vol. 2012, no. 6, article 146, 2012.

[102] L. Wolfenstein, "A theoretical pattern for neutrino oscillations," *Nuclear Physics B*, vol. 175, pp. 93–96, 1980.

[103] P. H. Frampton, M. C. Oh, and T. Yoshikawa, "Zee model confronts SNO data," *Physical Review D*, vol. 65, Article ID 073014, 2002.

[104] X.-G. He, "Is the Zee model neutrino mass matrix ruled out?" *The European Physical Journal C*, vol. 34, no. 3, pp. 371–376, 2004.

[105] S. Kanemura, T. Kasai, G.-L. Lin et al., "Phenomenology of Higgs bosons in the Zee model," *Physical Review D*, vol. 64, Article ID 053007, 2001.

[106] K. A. Assamagan, A. Deandrea, and P.-A. Delsart, "Search for the lepton flavor violating decay $A^0/H^0 \rightarrow \tau^\pm \mu^\mp$ at hadron colliders," *Physical Review D*, vol. 67, Article ID 035001, 2003.

[107] K. Babu and J. Julio, "Predictive model of radiative neutrino masses," http://arxiv.org/abs/1310.0303.

[108] E. Ma, "Verifiable radiative seesaw mechanism of neutrino mass and dark matter," *Physical Review D*, vol. 73, Article ID 077301, 2006.

[109] J. Kubo, E. Ma, and D. Suematsu, "Cold dark matter, radiative neutrino mass, mu to e gamma, and neutrinoless double beta decay," *Physics Letters B*, vol. 642, pp. 18–23, 2006.

[110] D. Aristizabal Sierra, J. Kubo, D. Restrepo, D. Suematsu, and O. Zapata, "Radiative seesaw model: warm dark matter, collider signatures, and lepton flavor violating signals," *Physical Review D*, vol. 79, Article ID 013011, 2009.

[111] D. Suematsu, T. Toma, and T. Yoshida, "Reconciliation of CDM abundance and $\mu \rightarrow e\gamma$ in a radiative seesaw model," *Physical Review D*, vol. 79, no. 4, Article ID 093004, 2009.

[112] A. Adulpravitchai, M. Lindner, and A. Merle, "Confronting flavor symmetries and extended scalar sectors with lepton flavor violation bounds," *Physical Review D*, vol. 80, Article ID 055031, 2009.

[113] T. Toma and A. Vicente, "Lepton flavor violation in the scotogenic model," *Journal of High Energy Physics*, vol. 1401, article 160, 2014.

[114] D. Schmidt, T. Schwetz, and T. Toma, "Direct detection of leptophilic dark matter in a model with radiative neutrino masses," *Physical Review D*, vol. 85, Article ID 073009, 2012.

[115] R. Bouchand and A. Merle, "Running of radiative neutrino masses: the scotogenic model," *Journal of High Energy Physics*, vol. 2012, no. 7, article 84, 2012.

[116] M. Aoki and S. Kanemura, "Probing the Majorana nature of TeV-scale radiative seesaw models at collider experiments," *Physics Letters B*, vol. 689, pp. 28–35, 2010.

[117] M. Aoki, S. Kanemura, and H. Yokoya, "Reconstruction of inert doublet scalars at the international linear collider," *Physics Letters B*, vol. 725, no. 4-5, pp. 302–309, 2013.

[118] S.-Y. Ho and J. Tandean, "Probing scotogenic effects in e^+e^- colliders," *Physical Review D*, vol. 89, Article ID 114025, 2014.

[119] S.-Y. Ho and J. Tandean, "Probing scotogenic effects in Higgs boson decays," *Physical Review D*, vol. 87, Article ID 095015, 2013.

[120] Y. Kajiyama, J. Kubo, and H. Okada, "D_6 family symmetry and cold dark matter at CERN LHC," *Physical Review D*, vol. 75, Article ID 033001, 2007.

[121] D. Suematsu, T. Toma, and T. Yoshida, "Enhancement of the annihilation of dark matter in a radiative seesaw model," *Physical Review D*, vol. 82, Article ID 013012, 2010.

[122] Y. Kajiyama, H. Okada, T. Toma, and J. C, "Direct and indirect detection of dark matter in D_6 flavor symmetric model," *The European Physical Journal C*, vol. 71, p. 1688, 2011.

[123] Y. Kajiyama, H. Okada, and T. Toma, "A light scalar dark matter for CoGeNT and DAMA in D_6 flavor symmetric model," http://arxiv.org/abs/1109.2722.

[124] M. Klasen, C. E. Yaguna, J. D. Ruiz-Alvarez, D. Restrepo, and O. Zapata, "Scalar dark matter and fermion coannihilations in the radiative seesaw model," *Journal of Cosmology and Astroparticle Physics*, vol. 1304, article 044, 2013.

[125] P.-K. Hu, "Radiative seesaw model with non-zero θ_{13} and warm dark matter scenario," http://arxiv.org/abs/1208.2613.

[126] M. Hirsch, R. Lineros, S. Morisi, J. Palacio, N. Rojas, and J. W. F. Valle, "WIMP dark matter as radiative neutrino mass messenger," *Journal of High Energy Physics*, vol. 2013, article 149, 2013.

[127] V. Brdar, I. Picek, and B. Radovcic, "Radiative neutrino mass with scotogenic scalar triplet," *Physics Letters B*, vol. 728, pp. 198–201, 2014.

[128] D. Restrepo, O. Zapata, and C. E. Yaguna, "Models with radiative neutrino masses and viable dark matter candidates," *Journal of High Energy Physics*, vol. 2013, article 11, 2013.

[129] S. S. Law and K. L. McDonald, "A class of inert N-tuplet models with radiative neutrino mass and dark matter," *Journal of High Energy Physics*, vol. 2013, no. 9, article 92, 2013.

[130] A. Zee, "Quantum numbers of Majorana neutrino masses," *Nuclear Physics B*, vol. 264, pp. 99–110, 1986.

[131] J. Schechter and J. W. F. Valle, "Neutrinoless double-β decay in SU(2)×U(1) theories," *Physical Review D*, vol. 25, p. 2951, 1982.

[132] J. T. Peltoniemi and J. W. F. Valle, "Massive neutrinos and electroweak baryogenesis," *Physics Letters B*, vol. 304, no. 1-2, pp. 147–151, 1993.

[133] M. Nebot, J. F. Oliver, D. Palao, and A. Santamaria, "Prospects for the Zee-Babu Model at the LHC and low energy experiments," *Physical Review D*, vol. 77, Article ID 093013, 2008.

[134] D. Schmidt, T. Schwetz, and H. Zhang, "Status of the Zee–Babu model for neutrino mass and possible tests at a like-sign linear collide," vol. 885, pp. 524–541, 2014.

[135] K. S. Babu and C. Macesanu, "Two-loop neutrino mass generation and its experimental consequences," *Physical Review D*, vol. 67, no. 7, Article ID 073010, 2003.

[136] D. Aristizabal Sierra and M. Hirsch, "Experimental tests for the Babu-Zee two-loop model of Majorana neutrino masses," *Journal of High Energy Physics*, vol. 2006, no. 12, article 052, 2006.

[137] J. Herrero-Garcia, M. Nebot, N. Rius, and A. Santamaria, "The Zee-Babu Model revisited in the light of new data," http://arxiv.org/abs/1402.4491.

[138] L. M. Krauss, S. Nasri, and M. Trodden, "Model for neutrino masses and dark matter," *Physical Review D*, vol. 67, Article ID 085002, 2003.

[139] J. N. Ng and A. de la Puente, "Top quark as a dark portal and neutrino mass generation," *Physics Letters B*, vol. 727, no. 1–3, pp. 204–210, 2013.

[140] A. Ahriche, C.-S. Chen, K. L. McDonald, and S. Nasri, "A three-loop model of neutrino mass with dark matter," http://arxiv.org/abs/1404.2696.

[141] M. Aoki, S. Kanemura, and O. Seto, "Neutrino mass, dark matter, and Baryon asymmetry via TeV-scale physics without fine-tuning," *Physical Review Letters*, vol. 102, no. 5, Article ID 051805, 2009.

[142] M. Aoki, S. Kanemura, and O. Seto, "Model of TeV scale physics for neutrino mass, dark matter, and baryon asymmetry and its phenomenology," *Physical Review D*, vol. 80, Article ID 033007, 2009.

[143] M. Gustafsson, J. M. No, and M. A. Rivera, "Predictive model for radiatively induced neutrino masses and mixings with dark matter," *Physical Review Letters*, vol. 110, Article ID 211802, 2013.

[144] C.-S. Chen, K. L. McDonald, and S. Nasri, "A class of three-loop models with neutrino mass and dark matter," *Physics Letters B*, vol. 734, pp. 388–393, 2014.

[145] S. P. Martin, *A Supersymmetry Primer*, vol. 21 of *Advanced Series on Directions in High Energy Physics*, 2010, http://arxiv.org/abs/hepph/9709356.

[146] R. Barbier, "R-parity violating supersymmetry," *Physics Reports*, vol. 420, no. 1–6, pp. 1–195, 2005.

[147] V. Barger, G. F. Giudice, and T. Han, "Some new aspects of supersymmetry R-parity violating interactions," *Physical Review D*, vol. 40, no. 9, pp. 2987–2996, 1989.

[148] H. Baer and X. Tata, *Weak Scale Supersymmetry: From Superfields to Scattering Events*, Cambridge University Press, Cambridge, UK, 2006.

[149] P. Nogueira, J. Romao, and J. Valle, "Supersymmetry phenomenology with spontaneous R parity breaking in Z^0 decays," *Physics Letters B*, vol. 251, pp. 142–149, 1990.

[150] L. J. Hall and M. Suzuki, "Explicit R-parity breaking in supersymmetric models," *Nuclear Physics B*, vol. 231, no. 3, pp. 419–444, 1984.

[151] M. A. Díaz, J. C. Romão, and J. W. F. Valle, "Minimal supergravity with R-parity breaking," *Nuclear Physics B*, vol. 524, no. 1-2, pp. 23–40, 1998.

[152] J. C. Romao, A. Ioannisian, and J. W. F. Valle, "Supersymmetric unification with radiative breaking of R parity," *Physical Review D*, vol. 55, no. 1, pp. 427–430, 1997.

[153] M. Hirsch, M. A. Díaz, W. Porod, J. C. Romão, and J. W. F. Valle, "Neutrino masses and mixings from supersymmetry with

bilinear R-parity violation: a theory for solar and atmospheric neutrino oscillations," *Physical Review D*, vol. 62, Article ID 113008, 2000.

[154] M. A. Diaz, M. Hirsch, W. Porod, J. C. Romão, and J. W. F. Valle, "Solar neutrino masses and mixing from bilinear *R*-parity broken supersymmetry: analytical versus numerical results," *Physical Review D*, vol. 68, Article ID 013009, 2003.

[155] E. J. Chun and S. K. Kang, "One-loop corrected neutrino masses and mixing in the supersymmetric standard model without *R* parity," *Physical Review D*, vol. 61, Article ID 075012, 2000.

[156] B. Mukhopadhyaya, S. Roy, and F. Vissani, "Correlation between neutrino oscillations and collider signals of supersymmetry in an R-parity violating model," *Physics Letters B*, vol. 443, no. 1–4, pp. 191–195, 1998.

[157] F. de Campos, O. Eboli, M. Magro et al., "Probing neutralino properties in minimal supergravity with bilinear *R*-parity violation," *Physical Review D*, vol. 86, Article ID 075001, 2012.

[158] F. de Campos, O. J. P. Éboli, M. Hirsch et al., "Probing neutrino oscillations in supersymmetric models at the Large Hadron Collider," *Physical Review D*, vol. 82, no. 7, Article ID 075002, 2010.

Research Article

Performance of Water-Based Liquid Scintillator: An Independent Analysis

D. Beznosko, A. Batyrkhanov, A. Duspayev, A. Iakovlev, and M. Yessenov

Department of Physics, Nazarbayev University, Astana 010000, Kazakhstan

Correspondence should be addressed to D. Beznosko; dima@hitecht.us

The water-based liquid scintillator (WbLS) is a new material currently under development. It is based on the idea of dissolving the organic scintillator in water using special surfactants. This material strives to achieve the novel detection techniques by combining the Cerenkov rings and scintillation light, as well as the total cost reduction compared to pure liquid scintillator (LS). The independent light yield measurement analysis for the light yield measurements using three different proton beam energies (210 MeV, 475 MeV, and 2000 MeV) for water, two different WbLS formulations (0.4% and 0.99%), and pure LS conducted at Brookhaven National Laboratory, USA, is presented. The results show that a goal of ~100 optical photons/MeV, indicated by the simulation to be an optimal light yield for observing both the Cerenkov ring and the scintillation light from the proton decay in a large water detector, has been achieved.

1. Motivation

In large water detectors, the Cerenkov radiation produced by a charged particle above the threshold can be used for particle identification and the reconstruction of its direction and energy [1]. However, all charged particles below the Cerenkov threshold are missed. Detecting these below-threshold particles is important for various applications, for example, in the search of the proton decay, in the $p^+ \rightarrow K^+ \bar{\nu}$ channel, where K^+ is mostly below Cerenkov threshold and is invisible in a water detector. The use of the WbLS makes the kaon visible and allows for the separation of K^+, μ^+, and e^+ signals using timing and thus reducing the background for this decay channel. The same goes for the quasielastic collisions in the large water-based neutrino detectors such as Super Kamiokande detector [1] with proton often being below the Cerenkov threshold and thus not visible.

In either LS or WbLS, the isotropic scintillation light is produced by the charged particle energy deposition via ionization, but the scintillator components may interfere with the Cerenkov ring detection. To detect K^+ and preserve the Cerenkov ring, MC studies indicate that the light yield (LY)

from the scintillator component in the WbLS should be 100 optical photons/MeV [2].

Thus, WbLS potentially combines both the Cerenkov ring and scintillation light capabilities. It can preserve the particle identification for the particles above the Cerenkov threshold and detect the charged particles below the threshold via the scintillation light. In addition, WbLS features the lower cost than pure LS and it is safer to handle [3].

The ability to reach the desired LY can be checked using the monoenergetic proton beam with different WbLS concentrations. For the test, the two different WbLS formulations (0.4% and 0.99%), pure water and pure LS samples, were chosen. Three different proton beam energies were used with each sample. The choice of the energies comes from the following considerations:

(i) 2000 MeV protons behave as minimum ionizing particle (MIP);

(ii) 475 MeV protons are just below the Cerenkov limit in water;

(iii) 210 MeV protons have ~same energy deposition as K^+ from the proton decay channel mentioned above.
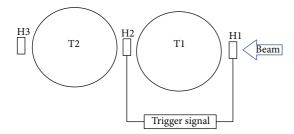
FIGURE 1: Proton beam test experimental setup.

2. Experimental Setup

The experimental setup used for the proton beam test is shown in Figure 1. Two tubs with the samples were used (T1 and T2). Three 2 cm × 2 cm and 5 mm thick plastic scintillator hodoscopes were used (H1 to H3) with the beam trigger being formed by the coincidence of the H1 and H2 only. H3 was intended to verify whether particles exit T2.

2.1. Tub and Signal Readout Description. Two tubs were used in the experiment:

   (i) T1 from polytetrafluoroethylene (PTFE) (white, highly reflective),

   (ii) T2 from aluminum, coated with black PTFE (very low reflectivity).

The T1 allows the capture of most of the light produced in the tub (~75% of the total light produces in the tub), whereas T2 allows for the observation of the light coming directly from the scintillation without the multiple wall reflections (~10%) as it was coated with black material on the inside. An image of a tub is in Figure 2. Both T1 and T2 have the same dimensions:

   (i) lid is 19.05 mm thick;

   (ii) walls and bottom are 6.35 mm thick;

   (iii) inner height and diameter are 150 mm.

A detailed setup readout scheme is shown in Figure 3. Both tubs (and hodoscopes) were read out by Hamamatsu Photonics [4] R7723 $2''$ Photomultiplier tubes (PMT). A transparent to the ultraviolet light acrylic window was used as a partition between the PMT and the liquid in the tub. The window was protruding through the lid and into the liquid by several millimeters to ensure that there are no air bubbles on its surface.

A readout was performed by the 4-channel 14-bit CAEN [5] V1729A flash analog-to-digital converter (FADC). All tubs signals were connected to the FADC via a variable attenuation unit (Phillips Scientific [6] 804) and a variable amplifier unit (Phillips Scientific 778) with two equal outputs. For the T1 and the T2 readouts, the gain was set to the value of ~2x. The first output from the amplifier goes to the FADC, with a dedicated channel for each tub. The second output from each amplifier channel was used for the single photoelectron (PE) calibration. The gain for the second amplification stage was set at ~10x.

FIGURE 2: PTFE tub detector with a PMT.

All hodoscopes were also connected via ~2x gain amplifiers that allowed output signal splitting into two. H1 and H3 share the same FADC channel with the latter signal being delayed by 200 ns. H2 was connected to the last remaining channel of the FADC.

2.2. Triggering Scheme. Triggering schema was realized using three 2 cm × 2 cm, 5 mm thick plastic scintillator counters that were readout by $2''$ PMTs via an air waveguide in order to remove the PMTs from direct beam exposure. The signals from the front-most and the middle counters (H1 and H2) were used to form a beam trigger, as indicated in Figure 3.

2.3. Proton Beamline Description. A proton test beam was conducted at NASA Space Radiation Laboratory (NSRL) facility at BNL [7]. As described above, the three following proton beam energies were used: 210 MeV, 475 MeV, and 2 GeV. The beam had the following main characteristics:

   (i) intensity was ~$1p^+$/bunch;

   (ii) beam size was 1 cm × 1 cm at 2 GeV and 5.4 cm × 5.4 cm at 210 MeV;

   (iii) 0.4 s long spills every ~4 sec.

3. Data Analysis

3.1. Liquids Measured. A surfactant (linear alkylbenzene sulfonic acid, LAS) is used to dissolve the 1,2,4-trimethyl-benzene, or pseudocumene (PC), which is a common LS material, in water. The PPO (2,5-diphenyloxazole) and MSB (1,4-Bis(2-methylstyryl) benzene) are used as a fluor and a wavelength shifter to downshift the ultraviolet light from the LS to the blue region of the spectrum where water has higher transparency. Further details can be found in [3].
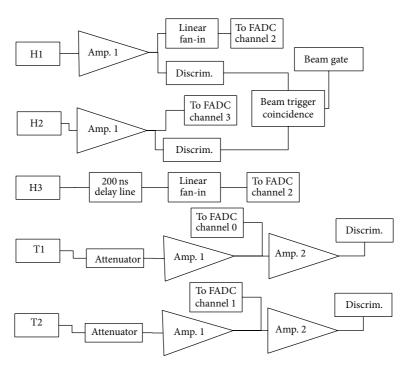
FIGURE 3: Proton beam test electronics readout setup.
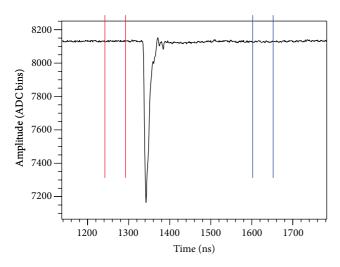
FIGURE 4: Typical PMT waveform with baseline check windows.

FIGURE 5: Typical baseline value for a single channel.

The composition of the 4 samples tested in this experiment are as follows:

(i) water (purified);

(ii) WbLS1: 0.4%PC + 0.4 g/L PPO + 3 mg/L MSB + surfactant in water;

(iii) WbLS2: 0.99%PC + 1.36 g/L PPO + 7.48 mg/L MSB + surfactant in water;

(iv) LS: LAB + 2 g/L PPO + 15 mg/L MSB.

3.2. Waveform Analysis. The PMT signal is acquired as a waveform with a sample shown in Figure 4. Total acquisition window is 2560 bins per event with each bin being 1 ns wide; the approximate position of the signal is known beforehand. A 300 ns window (central one in the figure, between the red and blue lines) is used to obtain the integrated signal area by summation. Each point is subtracted from the average baseline to achieve a positive sum. A typical signal is smaller than the chosen window width; however, there is a small spread in the timing of the signals and we want to be sure that signal's entire area has been integrated. The size of the chosen window is the same for all samples and measurements.

A baseline is defined as the average value of all the points in the first integration window (between the two red lines) that is 50 ns wide. A typical baseline is shown in Figure 5. To check the baseline quality, its averaged value is compared with the average of the postsignal window (between the two
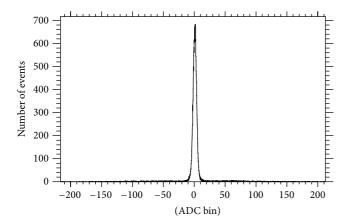
FIGURE 6: Difference between the baseline and the average of the postsignal window.

FIGURE 7: A sample fit of a tub signal.

blue lines). This difference is illustrated in Figure 6. Events with this difference larger than ~20 ADC bins are flagged as bad. This allows for the removal of the noise events or events with the bad baseline due to the shifted signal or multiparticle events. Additionally, a comparison of the baseline with an average of a window at the very beginning of the waveform (between 10 ns and 40 ns, not shown because the figure is zoomed around the signal area) is used for general baseline quality check using the above criterion.

The integrated area is a measure of total charge that can be converted to the PE yield using the single PE calibration of the PMTs. This allows the description of the measured signals independent of the hardware differences between the channels.

The trigger information is saved with the data. This allows the offline trigger requirements to be used later during the analysis stage.

3.3. Single Photoelectron Calibration. A single PE calibration was conducted for both T1 and T2 signal channels at the end of the test beam run. The trigger for this calibration is produced by the discriminator that is connected to the second amplifier for the T1 and T2 signals (separately, for each channel, see Figure 3). The discriminator is set to ~1/10th of the single PE amplitude so as to allow for better PE signal detection efficiency than using purely random trigger. Additionally, this forces the PE signal into the signal window region of the FADC output for the simplified analysis and elimination of the partially captured signals. Note that a PE signal is much narrower and lower in amplitude/area than the beam signals as they are typically many PEs that arrive according to some time distribution; thus a smaller integration window is used to reduce noise for cleaner calibration (50 ns instead of 300 ns).

The calibration signal area is 168.0 ± 1.2 ADC bins and 132.9 ± 1.6 ADC bins for T1 and T2, respectively (the PE signal is summed within the window, so the unit of ADC bin is still used). A special care was taken to verify that this method yields the same calibration values as using the light-emitting diode (LED) scheme. For that, calibration runs using
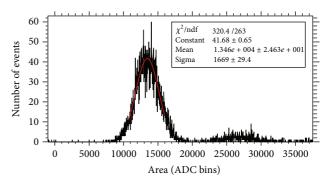
the scheme described above and using the dim LED pulses were compared to each other. The LED light level is chosen such that only ~1/10th of the events has the single PE signal to ensure that these are indeed the single photon detection responses.

3.4. Data Quality Selection. The data quality check is done as a single step before the data is analyzed. The care was taken to choose the criteria that do not introduce a bias into the selection. These are

  (i) offline double trigger requirement for H1 and H2 to be above ~50 mV and within the expected time window;

  (ii) baseline quality check as outlined in Section 3.2;

  (iii) ADC saturation check for H1 and H2.

Each check is intended to remove potential noise or multiple particles in an event. The saturation check indicates that several particles have passed through the hodoscopes in a same beam spill, which happens very rarely at the beam intensity used.

3.5. Light Yield Results. For each sample and energy, a histogram of the signal areas is computed. A Gaussian fit using a bin likelihood method is then performed. The fitting is done in two steps. First, a Gaussian is fitted in the range between the half of the maximum peak values to obtain the first approximation for the peak position. Then, the fits around the found mean with 1, 1.5, and 2σ are carried. This is done to estimate the uncertainty that the fitted signal width limitation is added to the mean. This is because there is the second peak to the right of the main one, from the second particle, rarely passing through the tub during the same trigger time. Figure 7 shows the 1.5σ fit of the first particle peak, and the second particle peak is visible on it as well. This plot is in the ADC bins for clarity; single PE calibration will be applied to all further plots.

The data for all the samples and all energies is then processed in the same way. Plots in Figures 8 and 9 show that the light yield results in PE for the different samples and beam energies for T1 and T2, respectively. Note that the light yield values for LS are reduced by a factor of 30 on these plots. In addition, the data point for the LS at 210 MeV for T1 is not going to be shown on further plots because of the readout

TABLE 1: Energy deposition in samples.

Beam energy (MeV)	Sample	T1 energy deposit (MeV)	T2 energy deposit (MeV)
210	Water, WbLS	72.7 ± 3.1	107.5 ± 6.1
	LS	59.2 ± 2.5	124.1 ± 7.0
475	Water, WbLS	40.4 ± 2.0	43.7 ± 2.2
	LS	34.4 ± 1.7	36.3 ± 1.9
2000	Water, WbLS	28.6 ± 2.6	28.7 ± 3.1
	LS	24.1 ± 2.3	24.2 ± 2.7
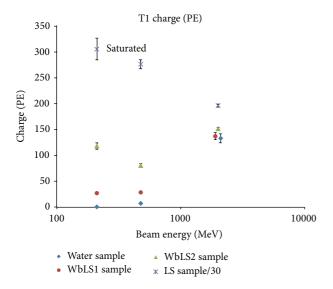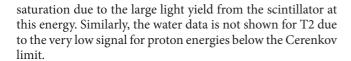
FIGURE 8: The light yield in PE for T1. At 2 GeV beam energy, some points are offset for clarity.

FIGURE 9: The light yield in PE for T2.

saturation due to the large light yield from the scintillator at this energy. Similarly, the water data is not shown for T2 due to the very low signal for proton energies below the Cerenkov limit.

3.6. Energy Deposition. In order to assess the PE/MeV light yield of each sample, the energy deposition in each sample is needed. Two methods were used for this purpose. The first one uses a GEANT4 simulation of the proton beam with the most likely deposition being the mean of the 1000 runs at each energy. Second one is a simplified code [8] that would calculate the proton energy loss along a straight line path through the tubs and hodoscopes with small steps, using the proton stopping power and range (PSTAR) tables from the National Institute of Standards and Technology (NIST). The WbLS was modeled as water and LS as toluene.

The resulting energy depositions are listed in Table 1. The values are taken from the GEANT4 simulation results, and the difference between two methods is taken as the uncertainty for the values obtained. The light yield from the data that is converted into the PE/MeV is shown in Figure 10 for the T1 and in Figure 11 for the T2.

We see that the PE/MeV light yield is the same for LS at proton energies of 2 GeV and 475 MeV on both tubs,

indicating that the Cerenkov light contribution is negligible for LS. It is not the same for the WbLS as there is a significant LY change between these two energies. However, at 475 MeV, there is virtually no Cerenkov light contribution to the total LY (as indicated by the very small amount of light at this energy in water in T1). Thus, we can use the data at this energy for LS to WbLS comparison and for obtaining the LY of the scintillator components of the WbLS. From the data, Figures 12 and 13 show the ratio of the WfbLS signal to the LS signal for the T1 and T2 at the proton energy of 475 MeV, and the same ratio for the T2 only for the 210 MeV (due to the saturation of the LS signal in T1 at this energy, it is not used in the analysis).

3.7. Light Yield in Photons/MeV. An estimate of the LY in photons/MeV is also possible. The calibration is needed here to estimate the efficiency of the PMT readouts from the T1 and T2. Typically, this is a difficult task to carry out precisely, so two simple methods have been used to do this estimate.

The first method is based on the fact that the LY in photons for the LS is known to be 10 k photons/MeV for a MIP signal [9]. Since the proton at 2 GeV has the ~same dE/dx as MIP, this LY value can be used to get the approximate efficiency for each tub (e.g., PE to photon conversion) for the WbLS data. The second one can be used for T1 only to check
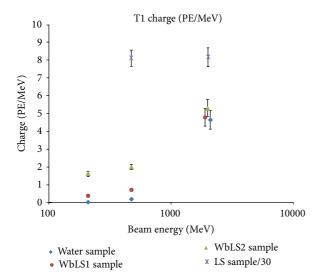
FIGURE 10: The light yield in PE/MeV for T1. At 2 GeV beam energy, some points are offset for clarity.
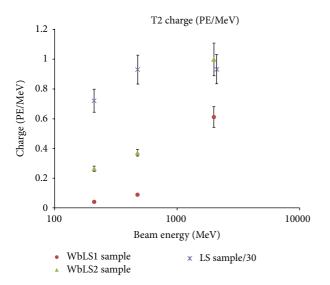
FIGURE 11: The light yield in PE/MeV for T2. At 2 GeV beam energy, some points are offset for clarity.

FIGURE 12: The WbLS light yield ratio to LS at 475 MeV. Some points are offset for clarity.
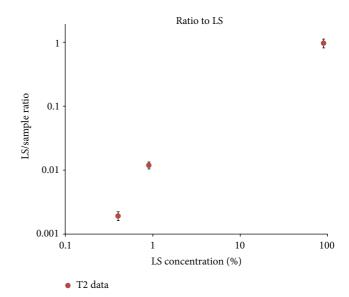
FIGURE 13: The WbLS light yield ratio to LS at 210 MeV. Only data for T2 is shown.

the validity of the first method. The difference between the methods was added to the total uncertainty of the result.

As mentioned above, a second method for the efficiency check was done for T1. We can use the 2 GeV proton data on water to get the readout efficiency; first we need to try and estimate the number of the protons produced in water using (1) that is commonly used to estimate the photon LY for the Cerenkov radiation in water as follows:

$$\frac{dN}{dx} \approx 370z^2 \left(E_{\max} - E_{\min} - \frac{1}{\beta^2} \frac{E_{\max} - E_{\min}}{n_{\text{ave}}^2} \right). \quad (1)$$

The average index of refraction for the optical range was used, and the $E_{\max}$ and $E_{\min}$ have been taken from the PMT sensitivity data. To get a better estimate, the sensitivity range for the T1 PMT was divided into a number of small subranges with ~constant sensitivity. The results for each subrange were weighted by the sensitivity at that range and combined together for a better estimate. Then, an efficiency calibration is obtained.

Using the resulting calibration of PE to photon conversion, now the 2 GeV proton LS data was used to compare the number of PE produced by the second method to the value taken as a base in the first method (which was 10000 photons/MeV). The result came very close to be 9713 photons/MeV for the LS using the efficiency from the Cerenkov light for T1.

The final estimate results for the WbLS data are presented in Figures 14 and 15 for the T1 and T2, respectively.
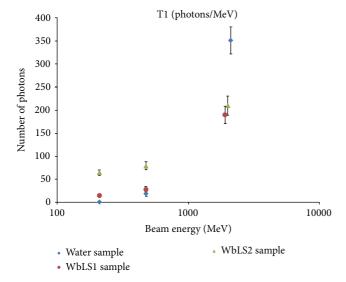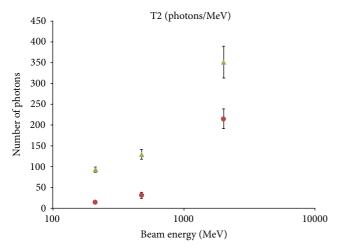
FIGURE 14: The light yield in photons/MeV for T1. At 2 GeV beam energy; some points are offset for clarity.

FIGURE 15: The light yield in photons/MeV for T2.

As it can be seen from these figures, the estimate shows that the goal of about 100 photons/MeV has been reached using the WbLS2 sample, and different LY are possible by adjusting the concentrations.

3.8. Systematics. A number of the systematic effects have been identified. Their effects have been accounted for in all the results presented.

During the experiment, the tubs with samples had to be disconnected and samples changed. An effect on the PMT of turning biasing on and off and exposing the PMT to ambient light during the disconnects was tested. There is some minor variation in PMT noise and gain for less than 2 minutes after bias is turned on before a steady state is reached. Typically, there was at least a 5- to 10-minute interval between installing the new sample in the beamline and data taking (the time was needed for the beam tuning process), thus greatly diminishing the influence of this effect on the data. In addition, a very small variation in gain between each steady state was noted; this variation has been added into the single PE calibration uncertainty.

A long-term stability of the single PE calibration was studied separately using the data taking run that was 450 hours. The LED calibration was collected during the entire run in 2 h periods and the resulting calibration variation (~1%) was added into the single PE calibration uncertainty.

The effects on the result due to the fitting procedure have been described in Section 3.5.

Another systematic effect arises from the window size selection process during the waveform analysis described in Section 3.2. The integration window size had to be optimized to fit all signal widths from all the data samples collected. If the window is too narrow then some signal may be lost in the integration, and if it is too large, too much noise will be integrated together with the signal and may add a nonzero contribution due to some of the noise not being random. A comprehensive study was carried out to determine the window size (300 ns) and the effect of this choice on the fitted means for each sample. The effect turned out to be small (the largest contribution of this effect is being less than ~0.5% for one of the samples, while it is being even smaller for all others) and it is accounted for in the total fit uncertainty together with the uncertainties estimated due to the fitting procedure.

4. Conclusion

The LY for the water, pure LS, and two formulations of the WbLS have been measured successfully. The 0.99% WbLS sample yields ~1% light of the pure LS, implying that the goal of 100 photons/MeV has been achieved and assuming that typical LY of LS is 10000 optical photons per MeV. Therefore, the WbLS that satisfies the requirements for the K^+, μ^+, and e^+ detection can be fabricated. The result also illustrates that different LY can be easily achieved by adjusting the WbLS components concentration.

The next experiment that will allow for the separation of the Cerenkov and scintillation light in WbLS has been conducted and the data is being analyzed. In addition, the work is planned at Nazarbayev University to carry out the optimization of the composition of the WbLS formulation.

Conflict of Interests

The authors declare that there is no conflict of interests regarding the publication of this paper.

Acknowledgments

References

[1] M. Fechner, K. Abe, Y. Hayato et al., "'Kinematic reconstruction of atmospheric neutrino events in a large water Cherenkov detector with proton identification," *Physical Review D*, vol. 79, Article ID 112010, 2009.

[2] C. Zhang, "A large water-based liquid scintillation detector in search for proton decay $p \rightarrow K^+ \bar{\nu}$ and Other Physics," in *Proceedings of the American Physical Society Meeting*, abstract #L12.005, April 2013.

[3] M. Yeh, S. Hans, W. Beriguete et al., "A new water-based liquid scintillator and potential applications," *Nuclear Instruments and Methods in Physics Research A*, vol. 660, pp. 51–56, 2011.

[4] Hamamatsu Photonics, Shizuoka, Japan, http://www.hamamatsu.com/.

[5] CAEN (Costruzioni Apparecch iature Elettroniche Nucleari S.p.A.), Via della Vetraia 11, 55049 Viareggio, Province of Lucca, Italy, 0584 388398.

[6] Phillips Scientific, "31 Industrial Ave. Suite 1," Mahwah, NJ, USA.

[7] Brookhaven National Lab, PO Box 5000, Upton, NY 11973-5000.

[8] D. Jaffe, "Preliminary results on water-based liquid scintillator in a proton beam," in *2nd Open Meeting for Hyper-Kamiokande Project*, January 2013.

[9] C. Aberle, A. Elagin, H. J. Frisch, M. Wetstein, and L. Winslow, "Measuring directionality in double-beta decay and neutrino interactions with kiloton-scale scintillation detectors," *Journal of Instrumentation*, vol. 9, 2014.

Research Article

Gaseous Detector with Sub-keV Threshold to Study Neutrino Scattering at Low Recoil Energies

A. V. Kopylov, I. V. Orekhov, V. V. Petukhov, and A. E. Solomatin

Institute of Nuclear Research of Russian Academy of Sciences, Prospect of 60th Anniversary of October Revolution 7A, Moscow 117312, Russia

Correspondence should be addressed to A. V. Kopylov; beril@inr.ru

Gaseous detector with a sub-keV electron equivalent threshold is a very perspective tool for the precision measurement of the neutrino magnetic moment and for observing coherent scattering of neutrinos on nuclei. The progress in the development of low noise electronics makes it possible to register the rare events at the threshold less than 100 eV. The construction of the gaseous detector is given and the typical pulses with amplitudes of a few eV observed on a bench scale installation are presented. The possible implications for future experiments are discussed.

1. Introduction

First neutrino detector made by F. Reines and C. L. Cowan 60 years ago opened a new field of a fascinating research with neutrino which seemed to be nearly undetectable object, as it was noted by W. Pauli himself. Since that time tremendous success in this field has been achieved. But till now neutrino continues intriguing the researchers and promises new discoveries. Development of the detectors with a threshold below 1 keV electron equivalent for experiments with reactor antineutrinos may, indeed, lead to new discoveries in neutrino physics. So far the lowest threshold achieved in these experiments is 3 keV; see, for example, GEMMA experiment [1] where the upper limit for the neutrino magnetic moment $2.9 \cdot 10^{-11}\,\mu_B$ has been set. For the Dirac neutrino magnetic moment with standard model interactions $\mu_\nu \sim 3 \times 10^{-19}\,\mu_B$ ($m_\nu/1\,\mathrm{eV}$) which is far below the sensitivity of the experiment. However, in the extension of MSSM which, for example, includes a vector-like leptonic generation which contains a fourth leptonic generation along with its mirrors a magnetic moment for the neutrinos as large as $10^{-12}\,\mu_B$ can be obtained [2]. This is a basic motivation for experimentalists to refine the technique of its measurements. In the dark matter experiment CoGeNT [3] the germanium detector has been developed with a threshold of about 0.3 keV

electron equivalent. Any further substantial reduction of the threshold for the semiconducting devices would be hardly possible. To progress in this field of research one highly demands the development of the detectors with a threshold of about 100 eV electron equivalent and may be even lower. This is a crucial point especially for the discovery of a coherent scattering of neutrinos on atomic nuclei (CNNS). The process of neutral current neutrino-nucleus elastic scattering has been described long ago [4, 5] but till now it remains to be a challenge for experimentalists. In CNNS the amplitude is a superposition of the individual amplitudes of scattering off each nucleon with relative phase factors:

$$
\begin{aligned}
\left(\frac{d\sigma}{dT}\right)_c = \frac{G_F^2 M_A}{2\pi} & \left(2 - \frac{2T}{E_\nu} + \left(\frac{T}{E_\nu}\right)^2 - \frac{M_A T}{E_\nu^2}\right) \\
& \times \frac{Q_W^2}{4} F^2\left(Q^2\right),
\end{aligned}
\tag{1}
$$

where $Q_W = N - Z(1 - 4\sin^2\theta_W)$ is a weak charge of a nucleus, G_F is the Fermi coupling constant, M_A is the mass of the nucleus, and $F^2(Q^2)$ is the nuclear form factor [6]. Due to a coherence the cross section is proportional to the square of a number of nucleons and may be so high that even a detector with 1 kg of a target material placed near
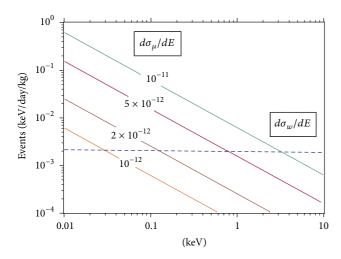
FIGURE 1: The count rate for antineutrino-electron elastic scattering as a function of energy in keV for different values of magnetic moment. By dashed line is indicated the count rate by standard electroweak model. The flux of antineutrinos is taken here 10^{13} $\nu/cm^2/s$.

FIGURE 2: The count rate from CNNS as a function of energy of the recoiled nucleus for different gases. By dashed lines are indicated the count rates from neutrons generated by cosmic rays. The flux of antineutrinos is taken here 10^{13} $\nu/cm^2/s$.

the core of a commercial nuclear reactor may have a count rate from CNNS on the level of 1000 events per year for the flux of reactor antineutrinos of about 10^{13} $\nu/cm^2/s$. In the GEMMA experiment at the Kalinin Nuclear Power Plant (KNPP), where a high-purity germanium detector of 1.5 kg has been placed 13.9 m from the 3 GW reactor core, the flux of antineutrinos was 2.7×10^{13} $\nu/cm^2/s$. Just for comparison, to get a similar count rate on the beam of neutrinos from a spallation neutron source [7] one needs a detector of a few tons scale. In Figure 1 is shown the contribution of the effect from magnetic moment of neutrino to the total cross section of νe^- scattering [8]:

$$\frac{d\sigma}{dT} = \left(\frac{d\sigma}{dT}\right)_W + \left(\frac{d\sigma}{dT}\right)_\mu, \tag{2a}$$

$$\left(\frac{d\sigma}{dT}\right)_W = \frac{2G_F m_e}{\pi} \left[g_R^2 + g_L^2 \left(1 - \frac{T}{E_\nu}\right) - g_R g_L \frac{m_e T}{E_\nu^2} \right], \tag{2b}$$

$$\left(\frac{d\sigma}{dT}\right)_\mu = \frac{\pi\alpha^2}{m_e^2} \left(\frac{1}{T} - \frac{1}{E_\nu}\right) \left(\frac{\mu_\nu}{\mu_B}\right)^2, \tag{2c}$$

where $g_L = \sin^2\theta_W$, $g_R = g_L + 1$.

One can see that to observe the effect from magnetic moment less than 10^{-11} μ_B the detector should have a threshold below 0.1 keV electron equivalent. With a threshold of a few tens of eV it will be possible to reach a limit $2 \cdot 10^{-12}$ μ_B. The notable feature of this scattering is that the cross section does not depend on the target because it is a pure νe^- elastic scattering. The situation is drastically different at coherent scattering of neutrinos on nuclei. CNNS can be observed only at small recoil energies when neutrino scatters on a nucleus as a wave on a grid; here the "grid" is composed of the nucleons tied by strong force with the rest of a nucleus. The energy of the recoiled nucleus depends on a mass of a nucleus; the heavier the nucleus the smaller

the energy of the recoils. This constitutes the "signature" of this process and may be used for events identification to determine what is responsible for the effect: νe^- elastic scattering or coherent scattering. Thus it would be useful to make measurements with different targets. High cross section makes it very attractive for experimentalists but low (less than 1 keV electron equivalent) recoil energy of a nucleus makes it very difficult for practical implementation. In Figure 2 is shown the simulated effect for different nuclei.

One can see that for heavy nuclei the cross section is higher, but the energy of the recoils of the nuclei is smaller. This demands a detector with a very low threshold. The heavier are the nuclei, the more severe are these demands. By dashed lines is indicated the background from neutrons generated by cosmic rays at the site of KNPP. It was shown in [1] that background from fast neutrons of the reactor by adequate shielding is lower than from neutrons generated by cosmic rays. The precise (with the uncertainty of about 1-2%) measurement of CNNS will be useful for the study of neutron form factor $F^2(Q^2)$ of a nucleus and may be even $\sin^2\theta_W$ presented in a weak charge of a nucleus (see expression (1)). What is also crucial is the possibility of verifying the discovery of this process by an independent way. Thus it is very important to develop not one, but several techniques to search for CNNS. In Figure 3 the rates for xenon (a) and argon (b) from coherent scattering on nuclei and from νe^- scattering are shown.

Here we should take into account that only a small fraction of the nuclear recoil energy is used in the ionizing process. This fraction is called a quenching factor (QF) and for the recoil energy of the nuclei less than a few hundred eV it may be very different for different gases. To measure this factor for some specific gas used in experiment is a very crucial point and actually not an easy task. It demands the special efforts which may be very rewarding because it may give a very interesting result. Here is taken as a very probable value $QF = 0.1$ for recoiled nuclei. One can see that

(a)

(b)
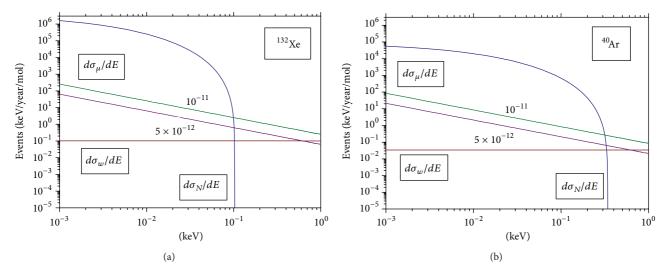
FIGURE 3: The count rates in xenon (a) and argon (b) for coherent scattering on nuclei and from νe^- scattering at magnetic moment $5 \cdot 10^{-12}\ \mu_B$ and $10^{-11}\ \mu_B$.

the effect from coherent scattering is absolutely predominant in the lower range of energy. The result of this is that for xenon it would be possible to extract the effect from magnetic moment if it is higher than or equal to $5 \cdot 10^{-12}\ \mu_B$ while for argon the lower limit is somewhere around $10^{-11}\ \mu_B$. If $QF < 0.1$ this will shift the spectrum from coherent scattering to lower energies and this will be more appropriate for registration of the effect from magnetic moment of neutrino. From this point of view the most perspective gas to search for magnetic moment would be xenon. It has also advantage of having high Z which is very important for measuring the effect from νe^- elastic scattering. If the gas amplification can be as high as 10^5 the threshold can be as low as 10 eV and then xenon is also good for detection of coherent scattering. The very promising aspect is also the possibility of using isotopically enriched xenon which will enable reducing the background from internal radioactivity. At present several groups are working in this field. Both antineutrinos generated at nuclear reactors with the energy of several MeV and neutrinos of higher energies (of several tens of MeV) produced in the decays of pions and muons in the high intensity proton beams are planned to be used. For the first ones the mass of a target material should be of several kilograms, for the second ones several tons to see the effect from CNNS. The recoil of a nucleus for the first case is expected to be less than 1 keV, for the second case tens of keV. Obviously, each approach has strong and weak points. Here we discuss the possibility of using a special construction of a gaseous detector of ionizing eradiation as a detector of CNNS. By choosing the gaseous proportional counter the emphasis is done on the following advantages of this technique.

(1) Very high factor of the gas amplification ($>10^4$).

(2) Possibility of using gas at relatively high pressure about 1 MPa to obtain the mass sufficient for count rate of about 1 event per day.

(3) Good signature of the events by a pulse shape (very characteristic front and tail of the pulses).

(4) The possibility of discriminating noise from electromagnetic disturbances and microphonic effect.

(5) Availability of the efficient methods of gas purification.

(6) Detector that can be fabricated only from very pure materials without PMTs as a possible source of ionizing eradiation, and so forth.

(7) The possibility of changing easily the working gas (CO_2–CF_4-argon-xenon) not changing the configuration, which is important to perform the comparative measurements at the same site.

The crucial point will be the background observed at very low recoil energy of nucleus. This is the main factor limiting the accuracy which can be achieved in experiment.

2. Materials and Methods

2.1. The Design of the Detector. The count rate from CNNS of reactor antineutrinos is predicted to be about 100 events per year per kg of a target material in the energy range from 20 eV to 200 eV of produced ionization. To collect a mass of about 1 kg in gas phase one needs a detector with a volume of about 50 liters even at pressure of about 1 MPa. But to get the gas amplification higher 10^4 at High Voltage 3 kV the diameter of the cathode should be 40 mm, not more. To reconcile these conflicting demands we should use an array of counters and each one apart from a central, avalanche region with a small diameter of a cathode should have also external, drift region, separated from avalanche region by a grid. The diameter of the drift region is taken to be 140 mm. Apart from this, there should be external cylindrical layer of counters working as an active shielding and also as a passive one of the fluorescence from the walls of the counter. All assembly is placed in

FIGURE 4: The counter before assembling.

FIGURE 5: A schematic of the detection concept.

FIGURE 6: The energy spectrum from ^{55}Fe calibration source.

a cylindrical body made of titanium as a material relatively pure on ^{226}Ra, as our previous measurements have shown [9]. In Figure 4 we show the general view of this counter.

We plan to use an array of 16 similar counters, each working on separate charge sensitive preamplifier and digitizing board. The counters will be assembled in 4 planes, each one having 4 counters. The size of the assembly will be approximately $100 \times 100 \times 100$ cm. To reduce the background from cosmic rays, neutrons and gamma-rays the assembly will be placed in the box made of slabs of iron 30 cm thick; internal surfaces will be lined by borated polyethylene 40 cm thick. To shield from fast neutrons from the reactor we plan to use additional external layer of water 50 cm thick and on the outside-plastic scintillator as an active veto shield from ionizing particles of cosmic rays penetrating to the depth of about 16 m of water equivalent. The water shield reduces the background from fast neutrons by an order of magnitude; thus, it will be possible by comparing the data collected with and without water to prove that the contribution of reactor neutrons to the effect is negligible. All this assembly will be placed in a hermetically sealed housing filled by argon purified of radon. We select this design of shielding to reduce at most the background from gamma-quanta from external radioactivity and from neutrons, generated in iron by cosmic rays. Borated polyethylene 40 cm thick decreases approximately 100-fold the flux of fast neutrons from iron. The slabs of iron 30 cm thick effectively absorb gamma-radiation from the walls. In Figure 2 we show the calculated effect from CNNS and the background from neutrons, generated by cosmic rays at 16 meters of water equivalent for different working mediums of the detector.

2.2. The Technique of the Pulse Shape Discrimination. We performed the measurements of the energy spectra of the pulses in argon using a small bench scale assembly. Proportional counter had 37 mm, the central wire of 20 mm in diameter, and it was filled by argon and methane (10%) mixture by 100 and 300 kPa. A schematic of the detection concept is presented in Figure 5.
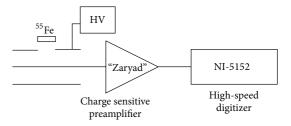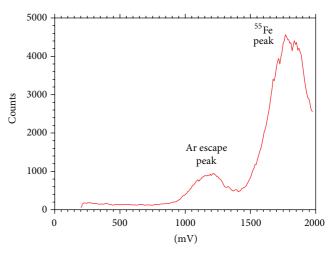
The calibration has been done using ^{55}Fe as a source of X-ray eradiation of 5.9 keV. The energy spectrum of the pulses from ^{55}Fe is presented in Figure 6.

One can see two peaks: 5.9 keV from ^{55}Fe and 2.95 keV escape peak of argon. The resolution of the peak 5.9 keV of ^{55}Fe was 20% at 0.3 MPa of Ar + 10% CH_4 mixture. To get a high gas amplification of order 10^5 we have increased High Voltage to 2760 V till the beginning of a regime of limited proportionality. Two peaks from ^{55}Fe source can be used for identification of the resulting nonlinearity. One can see this in Figure 7 where the amplitude in mV is presented as a function of the energy of the peak in keV.

The shapes of the pulses from output of charge sensitive preamplifier of the sensitivity of about 0.5 V/pC have been recorded by 8-bit digitizer. The shapes recorded during certain time were analysed off-line. The aim was to see how efficient the pulse shape discrimination of the noise pulses from electromagnetic disturbances and microphonic effect in the region below 100 eV could be, that is, where the main effect is expected from CNNS of reactor antineutrinos. In Figure 8 we show the pulses observed during time interval 400 μs. For small amplitudes less than 100 mV the conversion factor was 0.6 mV/eV; see Figure 7.

Figures 8(a) and 8(b) are "true" pulses with correct signature from ionization process. One can see from these two pictures that the noise level somewhat varies in time and this influences the shapes of the pulses but still it is possible to reliably select the pulses with amplitudes even as low as a few eV.
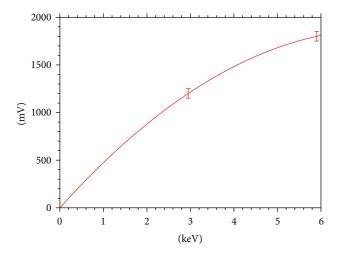
FIGURE 7: An observed amplitude of the pulse as a function of energy.

Figures 8(c), 8(d), 8(e), and 8(f) show the "bad" pulses which are due to electromagnetic disturbances and microphonics. One can see the difference just by naked eye. The pulses from the point ionization in gas have typically a relatively short front edge (a few microseconds) corresponding to the time drift of positive ions to cathode and long (hundreds of microseconds) tail corresponding to the time of the base line restoration of the charge sensitive preamplifier. These events might be produced by internal radioactivity of the materials of the counter, by electronic emission from the walls of the counter, and also by ionizing particles produced by cosmic rays. The amplitude of these events may be even smaller than an average energy to produce a single electron pulse because of the relatively broad energy distribution in this case (Polya distribution). In the range from 5 eV to 100 eV, where main effect from coherent scattering of reactor antineutrinos should be observed, the pulse shape discrimination enabled reducing the noise by a factor of about 10^3. The lower cut of 5 eV corresponds to the loss of efficiency of the detection of single electron events by approximately 5% which is quite appropriate for this experiment. Thus we show that this range can be effectively used for counting of the events from CNNS. Similar problem of counting the events from very small energy release has been solved in a number of experiments with cryogenic detectors. In 1997 we together with the staff of the laboratory of Professor S. Vitale at University of Genoa in Italy were the first who succeeded in counting the pulses from peaks 57 eV and 112 eV from the decay of ^{7}Be [10]. The energy threshold in this work was 40 eV. This was achieved thanks to effective pulse shape discrimination of the noise pulses from electromagnetic disturbances and "microphonic effect."

2.3. The Expected Uncertainty of Measurements. The rate of counting for different gases for antineutrinos from reactor depends on the threshold of counting. The background count rate depends on the counting interval: the less is an interval, the less is the background. The optimal counting interval can

be found from the calculated integral efficiency of counting presented in Figure 9.

The crossing of the dashed line with curves for some specific gas indicates the interval which contains ≈90% of the total count rate higher than a threshold 300 eV at $QF = 1$. From this point of view the most advantages would be to use xenon and the least advantages would be to use CO_2. In the real experiment QF is expected to be on the level of 0.1; thus the real threshold will be around ≈30 eV, that is, equal to an average energy of ionizing eradiation to produce an electron-ion pair in argon. However, QF may be very different for different gases and for low nuclear recoil energies less than 1 keV there is no valid approximation for QF. The measurement of this factor is very challenging and important task, but it is out of the scope of this paper. Here we consider two cases: when the background B is equal to the rate R and when it is 10 times higher: $B = 10R$. We take a relative uncertainty δ equal to 10%, 5%, and 2%. The first one is what we need to prove that we really observe the effect. The last one is what is necessary for the precise measurements to search for new physics. Having these R and X one writes for the time of measurements needed to achieve these uncertainties as $t_1 = 3/R \cdot (0.01\delta)^2$ for the first case and $t_1 = 21/R \cdot (0.01\delta)^2$ for the second case. Table 1 shows the times needed for both cases for different gases. The flux of antineutrinos was taken $2.7 \cdot 10^{13}$ n/cm^2/sec, that is, equal to the one at the site of KNPP in GEMMA experiment. One can see that for the vast majority of cases these times are quite reasonable and can be realized.

The general conclusion from the data presented in Table 1 is that for 16 counters each containing 1 mol of gas the tolerable background is somewhere in between R and $10R$. The notable point is that if we take argon from atmosphere the background from ^{39}Ar will be just in between these marks if to take the results of measurements presented in [11]. The use of argon from underground sources depleted by ^{39}Ar may turn out to be a very useful approach. The background from neutrons generated in the surrounding materials by cosmic rays was calculated as it was described in [12]. It is presented in Figure 2 for different gases and also for germanium just for comparison. One can see that it is quite tolerable to conduct the experiment and it can be efficiently suppressed by an active shield.

3. Results and Discussions

The measurements were performed on argon proportional counter at pressure from 0.1 till 0.3 MPa using ^{55}Fe calibration sources to record the shapes of the pulses from ionization with amplitudes from a few eV till a few keV. It was shown that the use of gaseous proportional counters with gas amplification of about 10^5 and low noise electronics enable the reliable registration of the ionizing eradiation with the energy threshold as low as 5 eV. The pulse shape discrimination in the energy interval from 5 eV till 100 eV enables substantially reduce noise from electromagnetic interferences and microphonics. The critical point to conduct the experiment is the background. The one from neutrons generated in

(a)

(b)

(c)

(d)

(e)

(f)
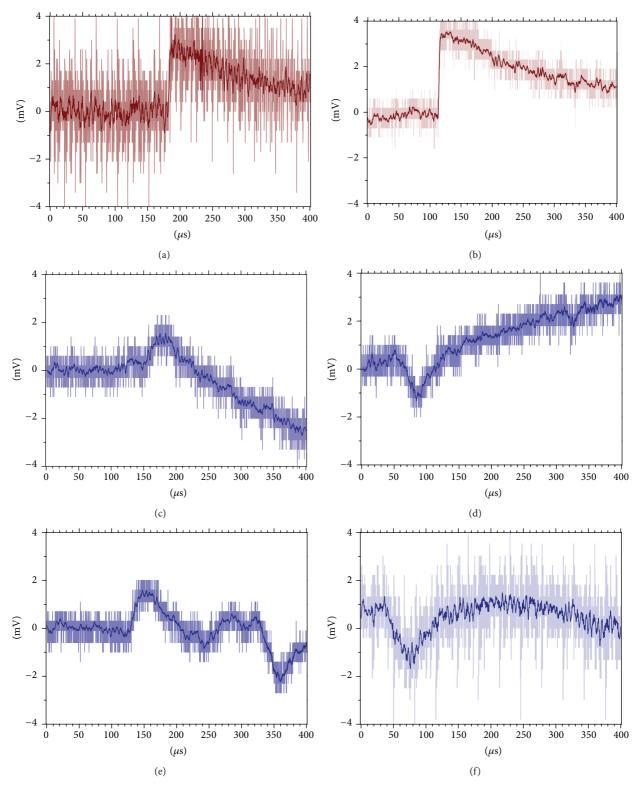
FIGURE 8: The shapes of the pulses in the time interval 400 μs.

the surrounding materials by cosmic rays was calculated for different working mediums. The detector should be placed as close as possible to the core of the reactor to get high flux of antineutrinos. So the overburden in the experiment is determined by the construction of the reactor and cannot be changed. The calculation shows (see Figure 2) that the background level from neutrons is quite satisfactory and can be tolerated. The total background from all sources, internal

TABLE 1: The times of measurements in years at reactor on and reactor off to get a relative uncertainty δ at $B = R$ and $B = 10R$.

Gas	$B = R$			$B = 10R$		
	$\delta = 10\%$	$\delta = 5\%$	$\delta = 2\%$	$\delta = 10\%$	$\delta = 5\%$	$\delta = 2\%$
^{40}Ar	0.037	0.141	0.889	0.248	0.996	6.219
^{132}Xe	0.019	0.081	0.507	0.141	0.567	3.541
^{74}Ge	0.022	0.085	0.533	0.148	0.596	3.726
CO_2	0.052	0.215	1.341	0.374	1.504	9.396
CF_4	0.022	0.089	0.548	0.152	0.615	3.841
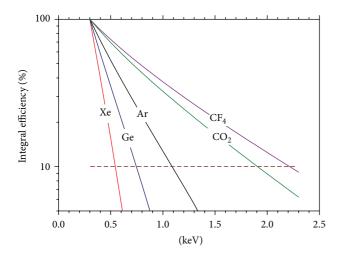
FIGURE 9: The integral efficiency of counting as a function of a threshold.

and external, can be tolerated if it is somewhere in between two marks: $B = R$ and $B = 10R$, and it determines the time of measurements needed to get the definite uncertainty. One can see from Table 1 that it is quite appropriate from experimental point of view. However it demands that very clean materials be used for the fabrication of the detector and in case of argon it would be helpful to use an underground argon depleted by ^{39}Ar. The important point for verification of the discovery of CNNS would be to make experiment with different gases, say, argon and xenon, to compare the results obtained and to prove that the spectral data are in agreement with the predicted ones for CNNS.

4. Conclusions

The gaseous proportional counter with a threshold 5 eV is a very perspective tool to study neutrino scattering on electrons and nuclei at small recoil energies. It has a potential of making discovery of still unobserved effect from coherent scattering of neutrinos on nuclei and may measure the magnetic moment of neutrinos, if it is higher than $5 \cdot 10^{-12} \mu_B$. To have a mass adequate to obtain the accuracy of measurements of a few percent the detector should be composed of several counters. We are planning to use an array of 16 counters arranged in 4 planes. The main limiting factor is the background so the detector should be constructed from very pure materials, well shielded from external radiation and

neutrons and equipped with an electronics system with pulse shape discrimination. At the present time the work is focused on the development of the prototype module. The next step will be the construction of the array from 16 modules and placing the full assembly with active and passive shielding at the reactor.

Conflict of Interests

The authors declare that there is no conflict of interests regarding the publication of this paper.

Acknowledgment

References

[1] A. G. Beda, V. B. Brudanin, V. G. Egorov et al., "Gemma experiment: the results of neutrino magnetic moment search," *Physics of Particles and Nuclei Letters*, vol. 10, no. 2, pp. 139–143, 2013.

[2] A. Aboubrahim, T. Ibrahim, A. Itani, and P. Nath, "Large neutrino magnetic dipole moments in MSSM extensions," *Physical Review D*, vol. 89, Article ID 055009, 2014.

[3] C. E. Aalseth, P. S. Barbeau, J. Colaresi et al., "CoGeNT: a search for low-mass dark matter using p-type point contact germanium detectors," *Physical Review D: Particles, Fields, Gravitation and Cosmology*, vol. 88, no. 1, Article ID 012002, 2013.

[4] D. Z. Freedman, "Coherent effects of a weak neutral current," *Physical Review D*, vol. 9, no. 5, pp. 1389–1392, 1974.

[5] D. Z. Freedman, D. N. Schramm, and D. L. Tubbs, "The weak neutral current and its effects in stellar collapse," *Annual Review of Nuclear and Particle Science*, vol. 27, pp. 167–207, 1977.

[6] P. S. Amanik and G. C. McLaughlin, "Neutron form factor from neutrino-nucleus coherent elastic scattering," *Journal of Physics G*, vol. 36, Article ID 015105, 2009.

[7] A. J. Anderson, J. M. Conrad, E. Figueroa-Feliciano, K. Scholberg, and J. Spitz, "Coherent neutrino scattering in dark matter detectors," *Physical Review D*, vol. 84, no. 1, Article ID 013008, 2011.

[8] P. Vogel and J. Engel, "Neutrino electromagnetic form factors," *Physical Review D*, vol. 39, no. 11, pp. 3378–3383, 1989.

[9] V. N. Gavrin, S. N. Danshin, A. V. Kopylov, and V. I. Cherekhovsky, "Low-background semiconductor gamma-spectrometer for measurements of ultralow concentrations of ^{238}U, ^{226}Ra, ^{232}Th," Preprint P-0494, INR, Moscow, Russia, 1986.

[10] M. Galeazzi, G. Gallinaro, F. Gatti et al., "Lithium versus chlorine: for the solution of the solar neutrino problem," *Physics Letters B: Nuclear, Elementary Particle and High-Energy Physics*, vol. 398, no. 1-2, pp. 187–193, 1997.

[11] J. Xu, F. Calaprice, and C. Galbiati, "A Study of the Residual 39Ar Content in Argon from Underground Sources," 2012, http://arxiv.org/abs/1204.6011.

[12] A. V. Kopylov, I. V. Orekhov, V. V. Petukhov, and A. E. Solomatin, "Gaseous detector of ionizing radiation for registration of coherent neutrino scattering on nuclei," *Technical Physics Letters*, vol. 40, no. 3, p. 185, 2014.

Review Article

Theory of Neutrino-Atom Collisions: The History, Present Status, and BSM Physics

Konstantin A. Kouzakov[1] and Alexander I. Studenikin[2,3]

[1] *Department of Nuclear Physics and Quantum Theory of Collisions, Faculty of Physics, Lomonosov Moscow State University, Moscow 119991, Russia*
[2] *Department of Theoretical Physics, Faculty of Physics, Lomonosov Moscow State University, Moscow 119991, Russia*
[3] *Joint Institute for Nuclear Research, Dubna 141980, Russia*

Correspondence should be addressed to Konstantin A. Kouzakov; kouzakov@srd.sinp.msu.ru

An overview of the current theoretical studies on neutrino-atom scattering processes is presented. The ionization channel of these processes, which is studied in experiments searching for neutrino magnetic moments, is brought into focus. Recent developments in the theory of atomic ionization by impact of reactor antineutrinos are discussed. It is shown that the stepping approximation is well applicable for the data analysis practically down to the ionization threshold.

1. Introduction

In particle physics, the neutrino plays a remarkable role of a "tiny" particle. The scale of neutrino mass m_ν is much lower than that of the charged fermions ($m_{\nu_f} \ll m_f$, $f = e, \mu, \tau$). Interaction of neutrinos with matter is extremely weak as compared to that in the case of other known elementary fermions. According to the Standard Model (SM), it can be mediated only via exchange of the $W^\pm$ and Z^0 bosons. However, the recent development of our knowledge of neutrino mixing and oscillations, supported by the discovery of flavor conversions of neutrinos from different sources (see [1–4]), substantiates the assumption that neutrinos can possess electromagnetic properties and, hence, take part in electromagnetic interactions (see, e.g., the review articles [5–7]). These properties include, in particular, the electric charge, the charge radius, the anapole moment, and the dipole electric and magnetic moments. Such nontypical neutrino features are of particular interest, because they open a door to "new physics" beyond the SM (BSM). In spite of appreciable efforts in searches for neutrino electromagnetic characteristics, up to now there is no experimental evidence favoring their nonvanishing values.

Among the electromagnetic properties of neutrinos, the most studied and well understood theoretically are neutrino magnetic moments (NMM), along with electric dipole moments. For the most recent and complete review on theoretical and experimental aspects of NMM, as well as for the corresponding references, see [7]. The effective Lagrangian, which describes the coupling of NMM to the electromagnetic field $F^{\alpha\beta}$, can be written in the form

$$L_{\text{int}} = \frac{1}{2}\overline{\psi}_i \sigma_{\alpha\beta} \left(\mu_{ij} + \epsilon_{ij}\gamma_5 \right) \psi_j F^{\alpha\beta} + \text{h.c.}, \tag{1}$$

where the magnetic moments μ_{ij}, in the presence of mixing between different neutrino states, are associated with the neutrino mass eigenstates ν_i. The interplay between the magnetic moment and neutrino mixing effects is important. Note that the electric (transition) moments ϵ_{ij} do also contribute to the coupling. A Dirac neutrino may have nonzero diagonal electric moments in models where CP invariance is violated. For a Majorana neutrino the diagonal magnetic and electric moments are zero. Therefore, NMM can be used to distinguish between Dirac and Majorana neutrinos [8–10].

In the Standard Model the magnetic moment of a massless neutrino is zero. In the minimal extension of the SM,

the explicit evaluation of the one-loop contributions to the Dirac NMM in the leading approximation over small parameters $b_i = m_i^2/M_W^2$ (m_i are the neutrino masses, $i = 1, 2, 3$) that however exactly accounts for the parameters $a_l = m_l^2/M_W^2$ ($l = e, \mu, \tau$) yields the following result [11–14]:

$$\mu_{ij}^D = \frac{eG_F m_i}{8\sqrt{2}\pi^2} \left(1 + \frac{m_j}{m_i}\right) \sum_{l=e,\mu,\tau} f(a_l) U_{lj} U_{li}^*, \qquad (2)$$

where U_{li} is the neutrino mixing matrix, and

$$f(a_l) = \frac{3}{4} \left[1 + \frac{1}{1-a_l} - \frac{2a_l}{(1-a_l)^2} - \frac{2a_l^2 \ln a_l}{(1-a_l)^3}\right]. \qquad (3)$$

A Majorana neutrino can also have nondiagonal (transition) magnetic moments $\mu_{ij}^M = 2\mu_{ij}^D$ ($i \neq j$). The obtained value for NMM is proportional to the neutrino mass and is, in general, of the order $\sim 10^{-21}$–$10^{-19} \mu_B$.

Much larger values for NMM can be obtained in different other SM extensions (see [6, 7] for the detailed discussion). However, there is a problem [15] for any BSM theory of how to get a large NMM value and simultaneously to avoid an unacceptable large contribution to the neutrino mass. Recently, this problem has been reconsidered for a class of BSM theories and it has been shown in a model-independent way that in principle it is possible to avoid the above mentioned contradiction in the case of Dirac [16] and Majorana [17] neutrinos. It has been shown that in this kind of theoretical models the NMM can naturally reach values of $\sim 10^{-15}$–$10^{-14} \mu_B$. These values are at least two orders of magnitude smaller than the present laboratory experimental limits (see below). There is also a huge gap of many orders of magnitude between these values and the prediction of the minimal extension of the SM. Therefore, if any direct experimental confirmation of nonzero NMM is obtained in the laboratory experiments, it will open a window to "new physics."

The neutrino magnetic moments are being searched in reactor [18, 19], accelerator [20, 21], and solar [22, 23] experiments on low-energy elastic neutrino-electron scattering (for more details see the review articles [6, 7] and references therein). The current best upper limit on the NMM value obtained in such direct laboratory measurements is

$$\mu_\nu \leq 2.9 \times 10^{-11} \mu_B, \qquad (4)$$

where $\mu_B = e/(2m_e)$ is a Bohr magneton. This bound, which is due to the GEMMA experiment [19] with a HPGe detector at Kalinin nuclear power station, is by an order of magnitude larger than the tightest constraint obtained in astrophysics [24]:

$$\mu_\nu \leq 3 \times 10^{-12} \mu_B. \qquad (5)$$

And it by many orders of magnitude exceeds the value derived in the minimally extended SM that includes right-handed neutrinos [12, 14]:

$$\mu_\nu \leq 3 \times 10^{-19} \mu_B \left(\frac{m_\nu}{1\,\text{eV}}\right), \qquad (6)$$

where m_ν is a neutrino mass. At the same time, there are different theoretical BSM scenarios that predict much higher μ_ν values. For example, the effective NMM value in a class of extra-dimension models can be as large as about $10^{-10} \mu_B$ [25]. Future higher precision reactor experiments can therefore be used to provide new constraints on large extra-dimensions.

The paper is organized as follows. Section 2 outlines the current status of searches for NMM and the problem of atomic-ionization effects in reactor experiments. Section 3 is devoted to the theoretical background for neutrino scattering on atomic electrons. In Section 4, we discuss the case of neutrino scattering on one bound electron. Hydrogen-like states and a semiclassical limit are considered. Section 5 focuses on ionization of many-electron atoms by neutrino impact. The case of a helium atomic target and the Thomas-Fermi and *ab initio* approaches are discussed. Finally, Section 6 summarizes this review.

2. Searches for Neutrino Magnetic Moments of Reactor Antineutrinos

The strategy of experiments searching for NMM is as follows. One studies an inclusive cross section for elastic (anti)neutrino-electron scattering which is differential in the energy transfer T. In the ultrarelativistic limit $m_\nu \to 0$, it is given by an incoherent sum of the SM contribution $d\sigma_{\text{SM}}/dT$, which is due to weak interaction that conserves the neutrino helicity, and the helicity-flipping contribution $d\sigma_{(\mu)}/dT$, which is due to μ_ν,

$$\frac{d\sigma}{dT} = \frac{d\sigma_{\text{SM}}}{dT} + \frac{d\sigma_{(\mu)}}{dT}. \qquad (7)$$

The SM term is well documented and is given by [26]

$$\frac{d\sigma_{\text{SM}}}{dT} = \frac{G_F^2 m_e}{2\pi}$$
$$\times \left[(g_V + g_A)^2 + (g_V - g_A)^2 \left(1 - \frac{T}{E_\nu}\right)^2 \qquad (8)\right.$$
$$\left. + (g_A^2 - g_V^2) \frac{m_e T}{E_\nu^2}\right],$$

where E_ν is the incident antineutrino energy, $g_A = 1/2$ and $g_V = (4\sin^2\theta_W + 1)/2$ for ν_e, and $g_A = -1/2$ and $g_V = (4\sin^2\theta_W - 1)/2$ for ν_μ and ν_τ, with θ_W being the Weinberg angle. For antineutrinos one must substitute $g_A \to -g_A$.

The possibility for neutrino-electron elastic scattering due to NMM was first considered in [27], and the cross section of this process was calculated in [28] (the related brief historical notes can be found in [29]). Here we would like to recall the paper by Domogatsky and Nadezhin [30], where the cross section of [28] was corrected and the antineutrino-electron cross section was considered in the context of the earlier experiments with reactor antineutrinos of Cowan and Reines [31] and Cowan et al. [32], which were aimed to reveal the NMM effects. Discussions on the derivation of the cross section and on the optimal conditions for bounding

the NMM value, as well as a collection of the cross section formulas for elastic scattering of neutrinos (antineutrinos) on electrons, nucleons, and nuclei, can be found in [29, 33]. The result relevant to the μ_ν component in (7) reads [29, 30, 33]

$$\frac{d\sigma_{(\mu)}}{dT} = 4\pi\alpha\mu_\nu^2 \left(\frac{1}{T} - \frac{1}{E_\nu} \right), \tag{9}$$

where α is the fine-structure constant. Thus, the two components of the cross section (7) exhibit qualitatively different dependencies on the recoil-electron kinetic energy T. Namely, at low T values the SM cross section is practically constant in T, while that due to μ_ν behaves as $1/T$. This means that the experimental sensitivity to NMM value critically depends on lowering the energy threshold of the detector employed for measurement of the recoil-electron spectrum.

The current reactor experiments with germanium detectors [18, 19] have reached threshold values of T as low as few keV and are to further improve the sensitivity to low-energy deposition in the detector [34–36]. At low energies, however, one can expect a modification of the free-electron formulas due to the binding of electrons in the germanium atoms, where, for example, the energy of the K_α line, 9.89 keV, indicates that at least some of the atomic binding energies are comparable to the already relevant to the experiment values of T. Thus a proper treatment of the atomic effects in neutrino scattering is necessary and important for the analysis of the current and, even more, of the future data with a still lower threshold. Furthermore, there is no known means of independently calibrating experimentally the response of atomic systems, such as the germanium, to the scattering due to the interactions relevant for the neutrino experiments. Therefore, one has to rely on a pure theoretical analysis in interpreting the neutrino data. For the first time this problem was addressed in [37], where a 2-3-time enhancement of the electroweak cross section in the case of ionization from a $1s$ state of a hydrogen-like atom with nuclear charge Z had been numerically determined at neutrino energies $E_\nu \sim \alpha Z m_e c^2$. Subsequent numerical calculations within the relativistic Hartree-Fock method for ionization from inner shells of various atoms showed much lower enhancement ($\sim$5–10%) of the electroweak contribution [38–43]. It was found that in the scattering on realistic atoms, such as germanium, the so-called stepping approximation works with a very good accuracy. The stepping approach, introduced in [40] from an interpretation of numerical data, treats the process as scattering on individual independent electrons occupying atomic orbitals and suggests that the cross section follows the free-electron behavior in (8) and (9) down to T equal to the ionization threshold for the orbital and that below that energy the electron on the corresponding orbital is "deactivated" thus producing a sharp "step" in the dependence of the cross section on T.

The interest in the role of atomic effects was renewed in several more recent papers. The early claim [44] of a significant enhancement of the NMM contribution in the case of germanium due to the atomic effects has been later disproved [45, 46] and it was argued [47–50] that the modification of the free-electron formulas (8) and (9) by the atomic-binding effects is insignificant down to very low values of T. This conclusion appeared to be also in contradiction to the results of [51], where it was deduced by means of numerical calculations that the μ_ν contribution to ionization of the helium atomic target by impact of electron antineutrinos strongly enhances relative to the free-electron approximation. However, from calculations performed in [52] it follows that the stepping approximation is well applicable practically down to the ionization threshold for helium.

3. General Theoretical Framework

As indicated in the introduction, the most sensitive and widely used method for the experimental investigation of the neutrino electromagnetic properties is provided by direct laboratory measurements of low-energy elastic scattering of neutrinos and antineutrinos with electrons in reactor, accelerator, and solar experiments. In this section, we deliver a theoretical background for such studies.

3.1. Neutrino-Electron Interactions. Let us consider the elastic-scattering process

$$\nu + e^- \longrightarrow \nu + e^-, \tag{10}$$

where an incident neutrino with energy E_ν transfers to a free electron, which is initially at rest in the laboratory frame, the energy-momentum q. There are two recoil-electron observables: the kinetic energy T, which amounts to the energy transfer, and the outgoing angle χ measured with respect to the incident neutrino direction. In the ultrarelativistic limit $m_\nu = 0$, these kinematical variables are related by

$$\cos\chi = \frac{E_\nu + m_e}{E_\nu} \sqrt{\frac{T}{T + 2m_e}}. \tag{11}$$

The maximal value of the kinetic electron energy is thus realized when $\chi = 0°$ and is given by

$$T_{\max} = \frac{2E_\nu^2}{2E_\nu + m_e}. \tag{12}$$

Within the SM, the scattering process (10) takes place due to exchange of the weak bosons, as shown in Figure 1. The W-boson channel corresponds to the charged current interaction and is absent in the cases of the muon and tau neutrinos. If $|q^2| \ll m_W^2$, where m_W is the W-boson mass, the scattering amplitude is given by [26]

$$M_W = \frac{G_F}{\sqrt{2}} \bar{u}_{\nu_2} \gamma_\alpha \left(1 - \gamma_5\right) u_{\nu_1} \bar{u}_{e_2} \gamma^\alpha \left(1 - \gamma_5\right) u_{e_1}, \tag{13}$$

where u_{ν_1} (u_{e_1}) and u_{ν_2} (u_{e_2}) are initial and final neutrino (electron) spinors. The Z^0 boson mediates the neutral current interaction. The corresponding scattering amplitude in the case $|q^2| \ll m_Z^2$, where m_Z is the Z^0-boson mass, reads [26]

$$M_Z = \frac{G_F}{\sqrt{2}} \bar{u}_{\nu_2} \gamma_\alpha \left(1 - \gamma_5\right) u_{\nu_1} \bar{u}_{e_2} \gamma^\alpha \left(g_V - g_A\gamma_5\right) u_{e_1}. \tag{14}$$

(a)   (b)
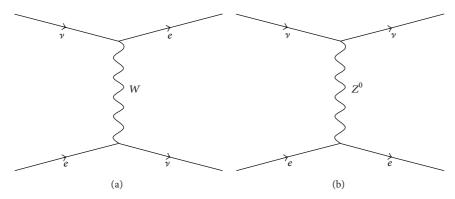
FIGURE 1: Elastic neutrino-electron scattering due to the weak interaction. Exchange by the W (a) and Z^0 (b) bosons is shown.
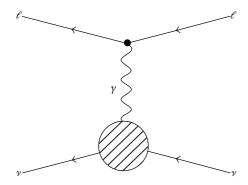
FIGURE 2: Contribution of the neutrino electromagnetic vertex function to neutrino elastic scattering on a charged lepton [5].

Using the matrix elements (13) and (14), one arrives, after averaging over the initial and summing over the final electron spins, at the SM single-differential cross section (8).

Figure 2 shows the electromagnetic channel of the scattering process (10). In general, the matrix element of the neutrino electromagnetic current J_μ can be considered between different neutrino initial $\psi_i(p)$ and final $\psi_j(p')$ states of different masses, $p^2 = m_i^2$ and $p'^2 = m_j^2$,

$$\left\langle \psi_j\left(p'\right) \left| J_\mu \right| \psi_i\left(p\right) \right\rangle = \bar{u}_j\left(p'\right) \Lambda_\mu\left(q\right) u_i\left(p\right). \quad (15)$$

In the most general case consistent with Lorentz and electromagnetic gauge invariance, the vertex function is defined as (see [5, 6] and references therein)

$$\Lambda_\mu\left(q\right) = \left[f_Q\left(q^2\right)_{ij} + f_A\left(q^2\right)_{ij}\gamma_5 \right]\left(q^2\gamma_\mu - \gamma_\mu\slashed{q}\right) \\ + f_M\left(q^2\right)_{ij}i\sigma_{\mu\nu}q^\nu + f_E\left(q^2\right)_{ij}i\sigma_{\mu\nu}q^\nu\gamma_5, \quad (16)$$

where $f_Q(q^2)$, $f_A(q^2)$, $f_M(q^2)$, and $f_E(q^2)$ are, respectively, the charge, anapole, dipole magnetic, and dipole electric neutrino form factors, which are matrices in the space of neutrino mass eigenstates [14].

Consider the diagonal case $i = j$. The hermiticity of the electromagnetic current and the assumption of its invariance under discrete symmetries' transformations put certain constraints on the form factors, which are in general different for the Dirac and Majorana neutrinos. In the case of Dirac neutrinos, the assumption of CP invariance combined with the hermiticity of the electromagnetic current J_μ implies that the electric dipole form factor vanishes, $f_E = 0$. At zero momentum transfer only $f_Q(0)$ and $f_M(0)$, which are called the electric charge and the magnetic moment, respectively, contribute to the Hamiltonian $H_{int} \sim J_\mu A^\mu$ that describes the neutrino interaction with the external electromagnetic field A^μ. The hermiticity also implies that f_Q, f_A, and f_M are real. In contrast, in the case of Majorana neutrinos, regardless of whether CP invariance is violated or not, the charge, dipole magnetic, and electric moments vanish, $f_Q = f_M = f_E = 0$, so that only the anapole moment can be nonvanishing among the electromagnetic moments. Note that it is possible to prove [8–10] that the existence of a nonvanishing magnetic moment for a Majorana neutrino would bring about a clear evidence for CPT violation.

In the off-diagonal case $i \neq j$, the hermiticity by itself does not imply restrictions on the form factors of Dirac neutrinos. It is possible to show [8] that if the assumption of the CP invariance is added, the form factors f_Q, f_M, f_E, and f_A should have the same complex phase. For the Majorana neutrino, if CP invariance holds, there could be either a transition magnetic or a transition electric moment. Finally, as in the diagonal case, the anapole form factor of a Majorana neutrino can be nonzero.

The neutrino dipole magnetic and electric form factors (and the corresponding magnetic and electric dipole moments) are theoretically the most well-understood among the form factors. The value of the magnetic form factor $f_M(q^2)$ at $q^2 = 0$ defines the NMM, $\mu_\nu = f_M(0)$. In the low-energy limit, the NMM contribution to the effective electromagnetic vertex can be expressed in the following form:

$$\Lambda_\alpha = \frac{\mu_\nu}{2m_e}\sigma_{\alpha\beta}q^\beta. \quad (17)$$

Thus, the corresponding scattering amplitude is

$$M_{(\mu)} = \frac{4\pi\mu_\nu\sqrt{\alpha}}{2m_e q^2}\bar{u}_{\nu_2}\sigma^{\alpha\beta}q_\beta u_{\nu_1}\bar{u}_{e_2}\gamma_\alpha u_{e_1}. \quad (18)$$

This leads to the NMM single-differential cross section given by (9).

3.2. Neutrino Scattering on Atomic Electrons. Consider the process where a neutrino with energy-momentum $p_\nu = (E_\nu, \mathbf{p}_\nu)$ scatters on an atom at energy-momentum transfer $q = (T, \mathbf{q})$. In what follows the recoil of the atomic nucleus is neglected because of the typical of current experiments situation $T \gg 2E_\nu^2/M_N$, where M_N is the nuclear mass. The atomic target is supposed to be unpolarized and in its ground state $|0\rangle$ with the corresponding energy E_0. It is also supposed that $T \ll m_e$ and $\alpha Z \ll 1$, where Z is the nuclear charge and α is the fine-structure constant, so that the initial and final electronic systems can be treated nonrelativistically. The neutrino states are described by the Dirac spinors assuming $m_\nu = 0$.

Thus, the magnetic moment interaction of the neutrino field ψ with the atomic electrons is described by the Lagrangian

$$L_{\text{int}} = \frac{\mu_\nu}{2m_e} \overline{\psi}\left(p_\nu'\right) \sigma_{\alpha\beta} \psi\left(p_\nu\right) q^\alpha A^\beta, \tag{19}$$

where p_ν' is the final neutrino four-momentum. The electromagnetic field $A = (A_0, \mathbf{A})$ of the atomic electrons is $A_0(\mathbf{q}) = \sqrt{4\pi\alpha}\, \rho(\mathbf{q})/q^2$, $\mathbf{A}(\mathbf{q}) = \sqrt{4\pi\alpha}\mathbf{j}(\mathbf{q})/q^2$ (hereafter we use the notation $q = |\mathbf{q}|$), where $\rho(\mathbf{q})$ and $\mathbf{j}(\mathbf{q})$ are the Fourier transforms of the electron number density and current density operators, respectively,

$$\rho(\mathbf{q}) = \sum_{a=1}^{Z} \exp\left(i\mathbf{q}\cdot\mathbf{r}_a\right), \tag{20}$$

$$\mathbf{j}(\mathbf{q}) = -\frac{i}{2m}\sum_{a=1}^{Z}\left[\exp\left(i\mathbf{q}\cdot\mathbf{r}_a\right)\frac{\partial}{\partial\mathbf{r}_a} + \frac{\partial}{\partial\mathbf{r}_a}\exp\left(i\mathbf{q}\cdot\mathbf{r}_a\right)\right], \tag{21}$$

and the sums run over the positions $\mathbf{r}_a$ of all the Z electrons in the atom. The double-differential cross section can be presented as

$$\frac{d^2\sigma_{(\mu)}}{dTdq^2} = \left(\frac{d^2\sigma_{(\mu)}}{dTdq^2}\right)_\parallel + \left(\frac{d^2\sigma_{(\mu)}}{dTdq^2}\right)_\perp, \tag{22}$$

where

$$\left(\frac{d^2\sigma_{(\mu)}}{dTdq^2}\right)_\parallel = 4\pi\alpha\frac{\mu_\nu^2}{q^2}\left(1 - \frac{T^2}{q^2}\right)S\left(T, q^2\right), \tag{23}$$

$$\left(\frac{d^2\sigma_{(\mu)}}{dTdq^2}\right)_\perp = 4\pi\alpha\frac{\mu_\nu^2}{q^2}\left(1 - \frac{q^2}{4E_\nu^2}\right)R\left(T, q^2\right), \tag{24}$$

where $S(T, q^2)$, also known as the dynamical structure factor [53], and $R(T, q^2)$ are

$$S\left(T, q^2\right) = \sum_n \delta\left(T - E_n + E_0\right)\left|\langle n|\rho(\mathbf{q})|0\rangle\right|^2, \tag{25}$$

$$R\left(T, q^2\right) = \sum_n \delta\left(T - E_n + E_0\right)\left|\langle n|j_\perp(\mathbf{q})|0\rangle\right|^2, \tag{26}$$

with $j_\perp$ being the $\mathbf{j}$ component perpendicular to $\mathbf{q}$ and parallel to the scattering plane, which is formed by the incident and

final neutrino momenta. The sums in (25) and (26) run over all the atomic states $|n\rangle$ with energies E_n of the electron system, with $|0\rangle$ being the initial state.

The longitudinal term (23) is associated with atomic excitations induced by the force that the neutrino magnetic moment exerts on electrons in the direction parallel to $\mathbf{q}$. The transverse term (24) corresponds to the exchange of a virtual photon which is polarized as a real one, that is, perpendicular to $\mathbf{q}$. It resembles a photoabsorption process when $q \to T$ and the virtual-photon four-momentum thus approaches a real-photon value. Due to selections rules, the longitudinal and transverse excitations do not interfere (see [54] for detail).

The factors $S(T, q^2)$ and $R(T, q^2)$ are related to, respectively, the density-density (or polarization) and current-current Green's functions

$$S\left(T, q^2\right) = \frac{1}{\pi}\operatorname{Im}F\left(T, q^2\right),$$
$$R\left(T, q^2\right) = \frac{1}{\pi}\operatorname{Im}L\left(T, q^2\right), \tag{27}$$

where

$$F\left(T, q^2\right) = \sum_n \frac{\left|\langle n|\rho(\mathbf{q})|0\rangle\right|^2}{T - E_n + E_0 - i\epsilon}$$
$$= \left\langle 0\left|\rho(-\mathbf{q})\frac{1}{T - H + E_0 - i\epsilon}\rho(\mathbf{q})\right|0\right\rangle, \tag{28}$$

$$L\left(T, q^2\right) = \sum_n \frac{\left|\langle n|j_\perp(\mathbf{q})|0\rangle\right|^2}{T - E_n + E_0 - i\epsilon}$$
$$= \left\langle 0\left|j_\perp(-\mathbf{q})\frac{1}{T - H + E_0 - i\epsilon}j_\perp(\mathbf{q})\right|0\right\rangle, \tag{29}$$

H being the Hamiltonian for the system of electrons. From these relations it follows that, due to the parity selection rule, the functions $S(T, q^2)$ and $R(T, q^2)$ are even with respect to q.

For small q values, in particular, such that $q \sim T$, only the lowest-order nonzero terms of the expansion of (27) in powers of q^2 are of relevance (the so-called dipole approximation). In this case, one has [45, 47]

$$R\left(T, q^2\right) = \frac{T^2}{q^2}S\left(T, q^2\right). \tag{30}$$

Taking into account (30), the experimentally measured singe-differential inclusive cross section is, to a good approximation, given by (see, e.g., [47, 49, 50])

$$\frac{d\sigma_{(\mu)}}{dT} = 4\pi\alpha\mu_\nu^2 \int_{T^2}^{(2E_\nu - T)^2} S\left(T, q^2\right)\frac{dq^2}{q^2}. \tag{31}$$

The standard electroweak contribution to the cross section can be similarly expressed in terms of the same factor $S(T, q^2)$ [45, 50] as

$$\frac{d\sigma_{\text{SM}}}{dT} = \frac{G_F^2}{4\pi}\left(1 + 4\sin^2\theta_W + 8\sin^4\theta_W\right)$$
$$\times \int_{T^2}^{(2E_\nu - T)^2} S\left(T, q^2\right)dq^2, \tag{32}$$

where the factor $S(T, q^2)$ is integrated over q^2 with a unit weight, rather than q^{-2} as in (31).

The kinematical limits for q^2 in an actual neutrino scattering are explicitly indicated in (31) and (32). At large E_ν, typical for the reactor neutrinos, the upper limit can in fact be extended to infinity, since in the discussed here nonrelativistic case the range of momenta $q \sim E_\nu$ is indistinguishable from infinity on an atomic scale. The lower limit can be shifted to $q^2 = 0$, since the contribution of the region of $q^2 < T^2$ can be expressed in terms of the photoelectric cross section [45] and is negligibly small (at the level of below one percent in the considered range of T). For this reason one can discuss the momentum-transfer integrals in (31) and (32) running from $q^2 = 0$ to $q^2 = \infty$:

$$I_1(T) = \int_0^\infty S(T, q^2) \frac{dq^2}{q^2},$$
$$I_2(T) = \int_0^\infty S(T, q^2) dq^2. \tag{33}$$

For a free electron, which is initially at rest, the density-density correlator is the free particle Green's function

$$F_{(\text{FE})}(T, q^2) = \left(T - \frac{q^2}{2m_e} - i\epsilon\right)^{-1}, \tag{34}$$

so that the dynamical structure factor is given by

$$S_{(\text{FE})}(T, q^2) = \delta\left(T - \frac{q^2}{2m_e}\right), \tag{35}$$

and the discussed here integrals are in the free-electron limit as follows:

$$I_1^{(\text{FE})} = \int_0^\infty S_{(\text{FE})}(T, q^2) \frac{dq^2}{q^2} = \frac{1}{T},$$
$$I_2^{(\text{FE})} = \int_0^\infty S_{(\text{FE})}(T, q^2) dq^2 = 2m_e. \tag{36}$$

Clearly, these expressions, when used in the formulas (31) and (32), result in the free-electron cross sections for the case $T \ll E_\nu$,

$$\frac{d\sigma_{(\mu)}}{dT} = \frac{4\pi\alpha\mu_\nu^2}{T},$$
$$\frac{d\sigma_{\text{SM}}}{dT} = \frac{G_F^2 m_e}{2\pi}\left(1 + 4\sin^2\theta_W + 8\sin^4\theta_W\right), \tag{37}$$

correspondingly.

4. Scattering on One Bound Electron

In this section, we consider neutrino scattering on an electron bound in an atom following consideration of [47, 49, 50]. The binding effects generally deform the density-density Green's function, so that both the integrals (33) are somewhat modified. Namely, the binding effects spread the free-electron δ-peak in the dynamical structure function (35) at $q^2 = 2m_e T$ and also shift it by the scale of characteristic electron momenta in the bound state.

4.1. Ionization from a Hydrogen-Like Orbital. Consider the situation when the initial electron occupies the discrete nl orbital in a Coulomb potential $V(\mathbf{r}) = -\alpha Z/r$. The dynamical structure factor for this hydrogen-like system is given by

$$S_{(nl)}(T, q^2) = \frac{m_e k}{(2\pi)^3} \frac{1}{2l+1} \sum_{m=-l}^{l} \int d\Omega_k |\langle \varphi_{\mathbf{k}}^- | \rho(\mathbf{q}) | \varphi_{nlm} \rangle|^2, \tag{38}$$

where φ_{nlm} is the bound-state wave function, $\varphi_{\mathbf{k}}^-$ is the outgoing Coulomb wave for the ejected electron with momentum $\mathbf{k}$, and $k = |\mathbf{k}| = \sqrt{2m_e T - p_n^2}$, with $p_n = \alpha Z m_e / n$ being the electron momentum in the nth Bohr orbit. The closed-form expressions for the bound-free transition matrix elements in (38) can be found, for instance, in [55]. In principle, they allow for performing angular integrations in (38) analytically. This task, however, turns out to be formidable for large values of n. Therefore, below we restrict our consideration to the $n = 1, 2$ states only, which nevertheless is enough for demonstrating the validity of the semiclassical approach described in Section 4.2.

Using results of [56], we can present the function (38) when $n = 1, 2$ as

$$S_{(nl)}(T, q^2) = \frac{2^8 m_e p_n^6}{3\left[1 - \exp\left(-2\pi\eta\right)\right]}$$
$$\times \frac{q^2 f_{nl}(q^2)}{\left[(q^2 - k^2 + p_n^2)^2 + 4p_n^2 k^2\right]^{2n+1}} \tag{39}$$
$$\times \exp\left[-2\eta \arctan\left(\frac{2p_n k}{q^2 - k^2 + p_n^2}\right)\right],$$

where the branch of the arctangent function that lies between 0 and π should be used, $\eta = \alpha Z m_e / k$ is the Sommerfeld parameter, and

$$f_{1s}(q^2) = 3q^2 + k^2 + p_1^2, \tag{40}$$

$$f_{2s}(q^2) = 8\left[3q^{10} - (32p_2^2 + 11k^2)q^8\right.$$
$$+ (82p_2^4 + 72p_2^2 k^2 + 14k^2)q^6$$
$$+ (20p_2^6 - 62p_2^4 k^2 - 20p_2^2 k^4 - 6k^6)q^4$$
$$+ (p_2^2 + k^2) \tag{41}$$
$$\times \left(\frac{47}{5}p_2^6 - \frac{47}{5}p_2^4 k^2 - 7p_2^2 k^4 - k^6\right)q^2$$
$$\left. + (4p_2^2 + k^2)(p_2^2 + k^2)^4\right],$$
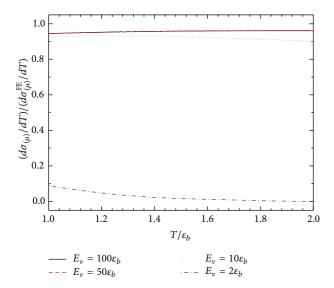
FIGURE 3: The ratio of single-differential cross sections for magnetic neutrino scattering from the $1s$ hydrogen-like and free-electron states, respectively, versus T/ε_b at different values of E_ν. The $E_\nu = 50\varepsilon_b$ and $E_\nu = 100\varepsilon_b$ curves are practically indistinguishable.

$$f_{2p}\left(q^2\right) = 2p_2^2 \left[36q^8 - 48\left(p_2^2 + k^2\right)q^6 \right.$$
$$+ \left(152p_2^4 - 48p_2^2 k^2 - 8k^4\right)q^4$$
$$+ \left(p_2^2 + k^2\right) \qquad (42)$$
$$\times \left(\frac{1712}{15}p_2^4 + \frac{1568}{15}p_2^2 k^2 + 16k^4\right)q^2$$
$$\left. + \left(\frac{44}{3}p_2^4 + 4k^2\right)\left(p_2^2 + k^2\right)^3 \right].$$

Figure 3 shows the magnetic single-differential cross section (31) for ionization from the $1s$ orbital, which is normalized to the free-electron value (9), as a function of T/ε_b, with the electron binding energy given by $\varepsilon_b = \alpha^2 Z^2 m_e/2$. As can be seen, the numerical results for $E_\nu \gg \varepsilon_b$ are close to the free-electron ones in magnitude. This can be qualitatively explained by noticing the following facts. First, in an attractive Coulomb potential there is an infinite set of bound states, with the discrete spectrum smoothly transforming into the continuum at the ionization threshold. Second, the average value of the $1s$ electron momentum is $p_e = p_1$ and the average change in the electron momentum after ejection, Δp_e, is such that $\Delta p_e^2 = 2m_e T$, which is analogous to the free-electron case.

Thus, taking into account the results in Figure 3, one might expect the atomic-binding effects to play a subsidiary role when $E_\nu \gg \varepsilon_b$. The authors of [44], however, came to the contrary conclusion that the single-differential cross section dramatically enhances due to atomic ionization when $T \sim \varepsilon_b$. The enhancement mechanism proposed in [44] is based on an analogy with the photoionization process. As mentioned above, when $q \to T$ the virtual-photon momentum approaches the physical regime $T^2 - q^2 = 0$.

In this limit, we have for the transverse component of the double-differential cross section (24)

$$\left(\frac{d^2\sigma_{(\mu)}}{dT dq^2}\right)_\perp = \frac{\mu_\nu^2}{\pi} \frac{\sigma_\gamma(T)}{T}, \qquad (43)$$

where $\sigma_\gamma(T)$ is the photoionization cross section at the photon energy T [57]. The limiting form (43) was used in [44] in the whole integration interval, when deriving the single-differential cross section. Such procedure is obviously incorrect, for the integrand rapidly falls down as q^2 ranges from T^2 up to $(2E_\nu - T)^2$, especially when $q^2 \gtrsim r_a^{-2}$, where r_a is a characteristic atomic size (within the Thomas-Fermi model $r_a^{-1} = Z^{1/3}\alpha m_e$ [58]). This fact reflects a strong departure from the real-photon regime. For this reason we can classify the enhancement of the differential cross section determined in [44] as spurious.

Insertion of (39) into the integrals (33) and integration over q^2, using the change of variable

$$\frac{2p_n k}{q^2 - k^2 + p_n^2} = \tan x \qquad (44)$$

and the standard integrals involving the products of the exponential function and the powers of sine and cosine functions, yield [50]

$$I_1^{(1s)}(T) = \frac{I_2^{(1s)}(T)}{2m_e T}$$
$$= \frac{T^{-1}}{1 - \exp\left(-2\pi/\sqrt{y_1 - 1}\right)}$$
$$\times \left\{ 1 - \exp\left(-\frac{\pi}{\sqrt{y_1 - 1}}\right) \right. \qquad (45)$$
$$\times \exp\left[\frac{-2}{\sqrt{y_1 - 1}} \arctan\left(\frac{y_1 - 2}{2\sqrt{y_1 - 1}}\right)\right]$$
$$\left. \times \left(1 - \frac{4}{y_1} + \frac{16}{3y_1^2}\right) \right\},$$

$$I_1^{(2s)}(T) = \frac{T^{-1}}{1 - \exp\left(-4\pi/\sqrt{y_2 - 1}\right)}$$
$$\times \left\{ 1 - \exp\left(-\frac{2\pi}{\sqrt{y_2 - 1}}\right) \right.$$
$$\times \exp\left[\frac{-4}{\sqrt{y_2 - 1}} \arctan\left(\frac{y_2 - 2}{2\sqrt{y_2 - 1}}\right)\right] \qquad (46)$$
$$\left. \times \left(1 - \frac{8}{y_2} + \frac{80}{3y_2^2} - \frac{448}{15y_2^3} + \frac{1792}{15y_2^4}\right) \right\},$$

$$I_2^{(2s)}(T) = \frac{2m_e}{1 - \exp\left(-4\pi/\sqrt{y_2 - 1}\right)}$$
$$\times \left\{1 - \exp\left(-\frac{2\pi}{\sqrt{y_2 - 1}}\right)\right.$$
$$\times \exp\left[\frac{-4}{\sqrt{y_2 - 1}} \arctan\left(\frac{y_2 - 2}{2\sqrt{y_2 - 1}}\right)\right] \tag{47}$$
$$\left.\times \left(1 - \frac{8}{y_2} + \frac{80}{3y_2^2} - \frac{448}{15y_2^3} + \frac{1024}{15y_2^4}\right)\right\},$$

$$I_1^{(2p)}(T) = \frac{T^{-1}}{1 - \exp\left(-4\pi/\sqrt{y_2 - 1}\right)}$$
$$\times \left\{1 - \exp\left(-\frac{2\pi}{\sqrt{y_2 - 1}}\right)\right.$$
$$\times \exp\left[\frac{-4}{\sqrt{y_2 - 1}} \arctan\left(\frac{y_2 - 2}{2\sqrt{y_2 - 1}}\right)\right] \tag{48}$$
$$\left.\times \left(1 - \frac{8}{y_2} + \frac{80}{3y_2^2} - \frac{704}{15y_2^3} + \frac{3328}{45y_2^4}\right)\right\},$$

$$I_2^{(2p)}(T) = \frac{2m_e}{1 - \exp\left(-4\pi/\sqrt{y_2 - 1}\right)}$$
$$\times \left\{1 - \exp\left(-\frac{2\pi}{\sqrt{y_2 - 1}}\right)\right.$$
$$\times \exp\left[\frac{-4}{\sqrt{y_2 - 1}} \arctan\left(\frac{y_2 - 2}{2\sqrt{y_2 - 1}}\right)\right] \tag{49}$$
$$\left.\times \left(1 - \frac{8}{y_2} + \frac{80}{3y_2^2} - \frac{704}{15y_2^3} + \frac{512}{15y_2^4}\right)\right\},$$

where $y_n = 2m_e T/p_n^2 \equiv T/|E_n|$. The largest deviations of these integrals from the free-electron analogs (36) occur at the ionization threshold $T = |E_n|$. The corresponding relative values in this specific case are [50]

$$\frac{I_1^{(1s)}}{I_1^{(FE)}} = \frac{I_2^{(1s)}}{I_2^{(FE)}} = 1 - \frac{7}{3}e^{-4} = 0.9572635093, \tag{50}$$

$$\frac{I_1^{(2s)}}{I_1^{(FE)}} = 1 - \frac{1639}{15}e^{-8} = 0.9633451168,$$

$$\frac{I_2^{(2s)}}{I_2^{(FE)}} = 1 - \frac{871}{15}e^{-8} = 0.9805208034,$$

$$\frac{I_1^{(2p)}}{I_1^{(FE)}} = 1 - \frac{2101}{45}e^{-8} = 0.9843376226, \tag{51}$$

$$\frac{I_2^{(2p)}}{I_2^{(FE)}} = 1 - \frac{103}{15}e^{-8} = 0.9976964900.$$

The above results indicate a clear tendency: the larger the n and l are, the closer the $I_1^{(nl)}$ and $I_2^{(nl)}$ are to the free-electron values. The departure from the free-electron behavior does not exceed several percent at most. These observations provide a solid base for the semiclassical approach described below.

4.2. Semiclassical Approach. In the one-electron approximation, the Hamiltonian has the form $H = p^2/2m_e + V(r)$, and the density-density Green's function from (28) can be written as

$$F\left(T, q^2\right)$$
$$= \left\langle 0 \left| e^{-i\mathbf{q}\cdot\mathbf{r}} \left[T - H(\mathbf{p}, \mathbf{r}) + E_0\right]^{-1} e^{i\mathbf{q}\cdot\mathbf{r}} \right| 0 \right\rangle$$
$$= \left\langle 0 \left| \left[T - H(\mathbf{p} + \mathbf{q}, \mathbf{r}) + E_0\right]^{-1} \right| 0 \right\rangle \tag{52}$$
$$= \left\langle 0 \left| \left[T - \frac{q^2}{2m_e} - \frac{\mathbf{p}\cdot\mathbf{q}}{m_e} - H(\mathbf{p}, \mathbf{r}) + E_0\right]^{-1} \right| 0 \right\rangle,$$

where the infinitesimal shift $T \to T - i\epsilon$ is implied.

Clearly, a nontrivial behavior of the latter expression in (53) is generated by the presence of the operator $(\mathbf{p} \cdot \mathbf{q})$ in the denominator and the fact that it does not commute with the Hamiltonian H. Thus an analytical calculation of the Green's function as well as the dynamical structure factor is feasible in only few specific problems. In Section 4.1 such calculation has been presented for ionization from the $1s$, $2s$, and $2p$ hydrogen-like states. In particular, we have seen that the deviations of the discussed integrals (33) from their free values are very small: the largest deviation is exactly at the ionization threshold, where, for instance, each of the $1s$ integrals is equal to the free-electron value multiplied by the factor $(1 - 7\,e^{-4}/3) \approx 0.957$ (see (50)). It can be also noted from (45) that both integrals are modified in exactly the same proportion, so that their ratio is not affected at any T: $I_2(T)/I_1(T) = 2m_e T$. We find, however, that this exact proportionality is specific for the ionization from the ground state in the Coulomb potential.

The problem of calculating the integrals (33), however, can be solved in the semiclassical limit, where one can neglect the noncommutativity of the momentum $\mathbf{p}$ with the Hamiltonian and rather treat this operator as a number vector. Taking also into account that $(H - E_0)|0\rangle = 0$, one can then readily average the latter expression in (53) over the directions of $\mathbf{q}$ and find the formula for the dynamical structure factor:

$$S\left(T, q^2\right)$$
$$= \frac{m_e}{2pq} \left[\theta\left(T - \frac{q^2}{2m_e} + \frac{pq}{m_e}\right) - \theta\left(T - \frac{q^2}{2m_e} - \frac{pq}{m_e}\right)\right], \tag{53}$$

where θ is the standard Heaviside step function. The expression in (53) is nonzero only in the range of q satisfying the condition $-pq/m_e < T - q^2/2m_e < pq/m_e$, that is, between the (positive) roots of the binomials in the arguments of the step functions: $q_{min}^2 = \sqrt{2m_e T + p^2} - p$ and $q_{max}^2 = \sqrt{2m_e T + p^2} + p$. One can notice that the previously mentioned "spread and shift" of the peak in the dynamical structure function in this limit corresponds to a flat pedestal between q_{min}^2 and q_{max}^2. The calculation of the integrals (33)

with the expression (53) is straightforward and yields the free-electron expressions (36) for the discussed here integrals in the semiclassical (WKB) limit:

$$I_1^{(\mathrm{WKB})} = \frac{1}{T}, \qquad I_2^{(\mathrm{WKB})} = 2m_e. \qquad (54)$$

The appearance of the free-electron expressions here is not surprising, since (53) can be also viewed as the one for scattering on an electron boosted to the momentum p. The difference from the pure free-electron case however is in the range of the energy transfer T. Namely, the expressions (54) are applicable in this case only above the ionization threshold, that is, at $T \geq |E_0|$. Below the threshold the electron becomes "inactive."

We believe that the latter conclusion explains the so-called stepping behavior observed empirically [40] in the results of numerical calculations. Namely, the calculated cross section $d\sigma/dT$ for ionization of an electron from an atomic orbital follows the free-electron dependence on T all the way down to the threshold for the corresponding orbital with a very small, at most a few percent, deviation. This observation led the authors of [40] to suggest the stepping approximation for the ratio of the atomic cross section (per target electron) to the free-electron one:

$$f(T) \equiv \frac{d\sigma/dT}{(d\sigma/dT)_{\mathrm{FE}}} = \frac{1}{Z} \sum_i n_i \theta \left(T - |E_i| \right), \qquad (55)$$

where the sum runs over the atomic orbitals with the binding energies E_i and the filling numbers n_i. Clearly, the factor $f(T)$ simply counts the fraction of "active" atomic electrons at the energy T, that is, those for which the ionization is kinematically possible. For this reason we refer to $f(T)$ as an *atomic factor*. We conclude here that the stepping approximation is indeed justified with a high accuracy in the approximation of the scattering on independent electrons, that is, if one neglects the two-electron correlations induced by the interference of terms in the operator $\rho(\mathbf{q})$ in (20) corresponding to different electrons. The effects of such interference will be discussed in the next section.

5. Scattering on Many-Electron Atoms

In considering the neutrino scattering on actual many-electron atoms one needs to evaluate the dependence of the number of active electrons on T and generally also evaluate the effect of the two-electron correlations. The latter can be studied, for example, in the case of a helium atom, where the electron-electron correlations are known to play a very significant role.

5.1. Helium. Recently, the authors of [51] deduced by means of numerical calculations that the μ_ν contribution to ionization of the He atomic target by impact of electron antineutrinos from reactor and tritium sources strongly departures from the stepping approximation, exhibiting large enhancement relative to the free-electron case. According to [51], the effect is maximal when the T value approaches the ionization threshold in helium, $T_I = 24.5874\,\mathrm{eV}$, where

the relative enhancement is as large as almost eight orders of magnitude. It was thus suggested that this finding might have an impact on searches for μ_ν, provided that its value falls within the range 10^{-13}-$10^{-12}\mu_B$. In this section, following consideration of [52], we show that (i) the result of [51] is erroneous and (ii) the stepping approximation for helium is well applicable, except the energy region $T \sim T_I$ where the differential cross section substantially decreases relative to the free-electron case.

We consider the process where an electron antineutrino with energy E_ν scatters on a He atom at energy and spatial-momentum transfers T and $\mathbf{q}$, respectively. In what follows we focus on the ionization channel of this process in the kinematical regime $T \ll E_\nu$, which mimics a typical situation with reactor ($E_\nu \sim 1\,\mathrm{MeV}$) and tritium ($E_\nu \sim 10\,\mathrm{keV}$) antineutrinos when the case $T \to T_I$ is concerned. The He target is assumed to be in its ground state $|\Phi_i\rangle$ with the corresponding energy E_i. Since for helium one has $\alpha Z \ll 1$, where $Z = 2$ is the nuclear charge, the state $|\Phi_i\rangle$ can be treated nonrelativistically. As we are interested in the energy region $T \sim T_I$, the final He state $|\Phi_f\rangle$ (with one electron in continuum) can also be treated in the nonrelativistic approximation.

Under the above assumptions, the dynamical structure factor (25) is given by

$$S\left(T, q^2\right) = \sum_f \left| \left\langle \Phi_f \left(\mathbf{r}_1, \mathbf{r}_2 \right) \right| e^{i\mathbf{q}\cdot\mathbf{r}_1} + e^{i\mathbf{q}\cdot\mathbf{r}_2} \left| \Phi_i \left(\mathbf{r}_1, \mathbf{r}_2 \right) \right\rangle \right|^2 \qquad (56)$$

$$\times \delta \left(T - E_f + E_i \right).$$

Here the f sum runs over all final He states having one electron ejected in continuum, with E_f being their energies.

For evaluation of the dynamical structure factor (56) we employ the same models of the initial and final He states as in [51]. The initial state is given by a product of two $1s$ hydrogen-like wave functions with an effective charge Z_i,

$$\Phi_i \left(\mathbf{r}_1, \mathbf{r}_2 \right) = \varphi_{1s} \left(Z_i, \mathbf{r}_1 \right) \varphi_{1s} \left(Z_i, \mathbf{r}_2 \right),$$

$$\varphi_{1s} \left(Z_i, \mathbf{r} \right) = \sqrt{\frac{Z_i^3}{\pi a_0^3}} e^{-Z_i r/a_0}, \qquad (57)$$

where $a_0 = 1/(\alpha m_e)$ is the Bohr radius. The final state has the form

$$\Phi_f \left(\mathbf{r}_1, \mathbf{r}_2 \right)$$

$$= \frac{1}{\sqrt{2}} \left[\varphi_{\mathbf{k}}^- \left(Z_f, \mathbf{r}_1 \right) \varphi_{1s} \left(Z, \mathbf{r}_2 \right) + \varphi_{\mathbf{k}}^- \left(Z_f, \mathbf{r}_2 \right) \varphi_{1s} \left(Z, \mathbf{r}_1 \right) \right],$$

$$(58)$$

where $\varphi_{\mathbf{k}}^-(Z_f, \mathbf{r})$ is an outgoing Coulomb wave for the ejected electron with spatial momentum $\mathbf{k}$. Z_f is the effective charge experienced by the ejected electron in the field of the final He$^+$ ion. Contributions to the dynamical structure factor from excited He$^+$ states are neglected due to their very small overlap with the K-electron state in the He atom.

To avoid nonphysical effects connected with nonorthogonality of states (57) and (58), we use the Gram-Schmidt orthogonalization

$$\left| \Phi_f \right\rangle \longrightarrow \left| \Phi_f \right\rangle - \left\langle \Phi_i \mid \Phi_f \right\rangle \left| \Phi_i \right\rangle. \tag{59}$$

Substitution of (57) and (58) into (56) thus yields

$$S\left(T, q^2\right) = \int \frac{d\mathbf{k}}{(2\pi)^3} |F(\mathbf{k}, \mathbf{q})|^2 \tag{60}$$
$$\times \delta \left(T - \frac{k^2}{2m_e} + 2\alpha^2 m_e - Z_i^2 \alpha^2 m_e \right),$$

where $k = \sqrt{2m_e(T + 2\alpha^2 m_e - Z_i^2 \alpha^2 m_e)}$, and

$$F(\mathbf{k}, \mathbf{q}) = \sqrt{2} \left\langle \varphi_{\mathbf{k}}^- \left(Z_f, \mathbf{r}_1\right) \varphi_{1s} \left(Z, \mathbf{r}_2\right) \right| e^{i\mathbf{q}\cdot\mathbf{r}_1} + e^{i\mathbf{q}\cdot\mathbf{r}_2}$$
$$- 2\rho_{1s}(\mathbf{q}) \left| \varphi_{1s} \left(Z_i, \mathbf{r}_1\right) \varphi_{1s} \left(Z_i, \mathbf{r}_2\right) \right\rangle \tag{61}$$

is the inelastic form factor, with

$$\rho_{1s}(\mathbf{q}) = \int \varphi_{1s}(Z_i, \mathbf{r}) e^{i\mathbf{q}\cdot\mathbf{r}} \varphi_{1s}(Z_i, \mathbf{r}) \, d\mathbf{r}. \tag{62}$$

It is straightforward to perform the further calculation of the dynamical structure factor analytically (see, e.g., the textbook [58]). The resulting expression is

$$S\left(T, q^2\right) = \frac{2^{16} \alpha^4 m_e^5 Z_f Z_i^6}{\left(1 - e^{2\pi\eta}\right)\left(2 + Z_i\right)^6}$$
$$\times \left[A_1(k, q) + B(k, q) A_2(k, q) + B^2(k, q) \right], \tag{63}$$

where $\eta = -\alpha Z_f m_e / k$ and (introducing $p_i = \alpha Z_i m_e$)

$$A_1(k, q)$$
$$= \left(\left(\exp\left(2\eta \arccos \frac{p_i^2 + q^2 - k^2}{\sqrt{\left(p_i^2 + q^2 + k^2\right)^2 - 4k^2 q^2}}\right)\right)\right.$$
$$\times \left(\left[\left(p_i^2 + q^2 + k^2\right)^2 - 4k^2 q^2\right]^3\right)^{-1}\right)$$
$$\times \left\{ \left(p_i + \eta k\right)^2 \left(p_i^2 + q^2 + k^2\right)^2 \right.$$
$$+ 4kq^2 \left[\frac{1}{3} k p_i^2 - \frac{2}{3} \eta^2 k p_i^2 - \eta^2 k^3 \right.$$
$$\left. \left. - \eta p_i \left(p_i^2 + q^2 + k^2\right) \right] \right\},$$

$$A_2(k, q)$$
$$= \left(\left(2 \exp\left(\eta \arccos \frac{p_i^2 + q^2 - k^2}{\sqrt{\left(p_i^2 + q^2 + k^2\right)^2 - 4k^2 q^2}}\right)\right)\right.$$
$$\times \left(\left(p_i^2 + q^2 + k^2\right)^2 - 4k^2 q^2\right)^{-1}\right)$$
$$\times \left[p_i \cos\left(\frac{\eta}{2} \ln \frac{(k+q)^2 + p_i^2}{(k-q)^2 + p_i^2}\right) \right.$$
$$+ \frac{p_i^2 - q^2 + k^2}{2q}$$
$$\left. \times \sin\left(\frac{\eta}{2} \ln \frac{(k+q)^2 + p_i^2}{(k-q)^2 + p_i^2}\right) \right],$$

$$B(k, q) = e^{2\eta \operatorname{arctg}(k/p_i)} \frac{\left(Z_i - Z_f\right) \alpha m_e}{\left(k^2 + p_i^2\right)^2}$$
$$\times \left\{ \frac{\left(2 + Z_i\right)^4 \alpha^4 m_e^4}{\left[\left(2 + Z_i\right)^2 \alpha^2 m_e^2 + q^2\right]^2} - \frac{32 p_i^4}{\left(4p_i^2 + q^2\right)^2} \right\}. \tag{64}$$

Finally, the usual choice of the effective charges is $Z_i = 27/16 \approx 1.69$ and $Z_f = 1$ (see, e.g., [59] and references therein). The value $Z_i = 27/16$ follows from the variational procedure that minimizes the ground-state energy E_i, while the value $Z_f = 1$ ensures the correct asymptotic behavior of the final state. However, the authors of [51] utilized in their calculations the values $Z_i = 1.79$ and $Z_f = 1.1$ derived from fitting the photoionization cross section data on helium with the present model of the He states.

The departures of the differential cross sections (31) and (32) from the free-electron approximation are characterized by the respective atomic factors

$$f_{\text{SM}} = \frac{d\sigma_{\text{SM}}/dT}{d\sigma_{\text{SM}}^{\text{FE}}/dT}, \qquad f_{\text{NMM}} = \frac{d\sigma_{(\mu)}/dT}{d\sigma_{(\mu)}^{\text{FE}}/dT}, \tag{65}$$

where $d\sigma_{\text{SM}}^{\text{FE}}/dT$ and $d\sigma_{(\mu)}^{\text{FE}}/dT$ are the SM and μ_ν contributions to the differential cross section for scattering of an electron antineutrino on two free electrons. Let us recall that following [51] one should expect the f_{NMM} value to be of about 10^8 at $T \to T_I$.

Numerical results for atomic factors (65) are shown in Figure 4. They correspond to the kinematical regime $T \ll \alpha m_e \ll 2E_\nu$, which is typically realized both for reactor and for tritium antineutrinos when $T < 200$ eV. Note that in such case one can safely set the upper limit of integrals in (31) and (32) to infinity, as the dynamical structure factor $S(T, q^2)$ rapidly falls down when $q \gtrsim \alpha m_e$ and practically vanishes in the region $q \gg \alpha m_e$. It can be seen from Figure 4 that atomic factors exhibit similar behaviors for both sets of the Z_i and Z_f parameters discussed in the previous section.
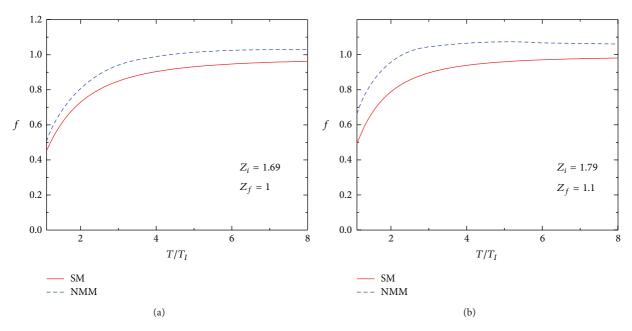
FIGURE 4: Atomic factors (65) as functions of the energy transfer [52].

Namely, their values are minimal (~0.5) at the ionization threshold, $T = T_I$, and tend to unity with increasing T. The latter tendency is readily explained by approaching the free-electron limit. It can be also seen that a more or less serious deviation (>10%) of the present results from the stepping approximation is observed only in the low-energy region $T <$ 100 eV. This deviation can be attributed to the effect of the electron-electron correlation in a helium atom. Indeed, if the electrons do not interact with each other, then they occupy two $1s$ hydrogen-like states (with opposite spins), in which case the departure of the atomic-factor values from unity is, according to the results of Section 4.1, less than 5%.

Thus, the calculations presented in Figure 4 do not confirm the huge enhancement of the μ_ν contribution with respect to the free-electron approximation. Moreover, in accord with various calculations for other atomic targets [38–41, 43, 47, 49, 50], we find that at small energy-transfer values the electron binding in helium leads to the appreciable reduction of the differential cross section relative to the free-electron case. We attribute the erroneous prediction of [51] to the incorrect dynamical model that draws an analogy between the NMM-induced ionization and photoionization. Indeed, as discussed in Section 3.2, the virtual photon in the NMM-induced ionization process can be treated as real only when $q \to T$. However, the integration in (31) involves the q values ranging from T up to $2E_\nu - T$. Since $E_\nu \gg T$, the real-photon picture appears to be applicable only in the vicinity of the lower integration limit. When moving away from that momentum region, one encounters a strong departure from the real-photon approximation which treats the integrand as a constant in the whole integration range, assuming it to be equal to its value at $q = T$; that is,

$$\frac{1}{q^2}\, S\left(T, q^2\right) = \frac{1}{T^2}\, S\left(T, T^2\right). \tag{66}$$

Such an approach is manifestly unjustified, and it gives rise to the spurious enhancement of the μ_ν contribution to the differential cross section.

5.2. Thomas-Fermi Model. In the Thomas-Fermi model (see, e.g., [58]) the atomic electrons are described as a degenerate free-electron gas in a master potential $\phi(r)$ filling the momentum space up to the zero Fermi energy, namely, up to the momentum $p_0(r)$ such that $p_0^2/2m_e - e\phi = 0$. The electron density $n(r) = p_0^3/(3\pi^2)$ then determines the potential $\phi(r)$ from the usual Poisson's equation. In the discussed picture at an energy transfer T the ionization is possible only for the electrons whose energies in the potential are above $-T$, that is, with momenta above $p_T(r)$ with $p_T^2/2m_e - e\phi = -T$. The electrons with lower energy are inactive. Calculating the density of the inactive electrons as $p_T^3/(3\pi^2)$ and subtracting their total number from Z, one readily arrives at the formula for the atomic factor, that is, the effective fraction of the active electrons Z_{eff}/Z as a function of T,

$$f\left(T\right) = \frac{Z_{\text{eff}}\left(T\right)}{Z}$$
$$= 1 - \int_0^{x_0(T)} \left[\frac{\chi\left(x\right)}{x} - \frac{T}{T_0}\right]^{3/2} x^2 dx, \tag{67}$$

where $\chi(x)$ is the Thomas-Fermi function, well known and tabulated, of the scaling variable $x = 2(4/3\pi)^{2/3} m_e \alpha Z^{1/3}$, the energy scale T_0 is given by

$$T_0 = 2\left(\frac{4}{3\pi}\right)^{2/3} m_e \alpha^2 Z^{4/3} \approx 30.8 Z^{4/3} \text{ eV}, \tag{68}$$

and, finally, $x_0(T)$ is the point where the integrand becomes zero, namely, corresponding to the radius beyond which all
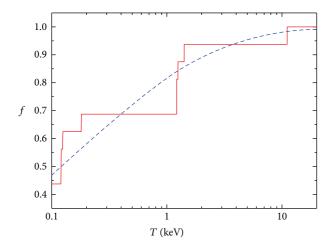
FIGURE 5: The atomic factor f for germanium in the stepping approximation with the actual energies of the orbitals (solid line) and its interpolation in the Thomas-Fermi model (dashed line) [49].

the electrons are active at the given energy T. The energy scale T_0 in germanium ($Z = 32$) evaluates to $T_0 \approx 3.1$ keV. The Thomas-Fermi atomic factor for germanium calculated from the formula (67) is shown by the dashed line in the plot of Figure 5. The discussed statistical model is known to approximate the average bulk properties of the atomic electrons with a relative accuracy $O(Z^{-2/3})$ and as long as the essential distances r satisfy the condition $Z^{-1} \ll m_e \alpha r \ll 1$, which condition in terms of the scaling variable x reads as $Z^{-2/3} \ll x \ll Z^{1/3}$. In terms of the formula (67) for the number of active electrons, the lower bound on the applicability of the model is formally broken at $T \sim Z^{2/3}T_0$, that is, at the energy scale of the inner atomic shells. However, the effect of the deactivation of the inner electrons is small, of order Z^{-1} in comparison with the total number Z of the electrons. On the other hand, at low T, including the most interesting region of $T \sim T_0$, the integral in (67) is determined by the range of x of order one, where the model treatment is reasonably justified.

The energies of the inner K, L, and M orbitals in the germanium atom are well known (see, e.g., [61]) and provide the necessary data for a description of the neutrino scattering by the stepping formula (55) down to the values of the energy transfer T in the range of the binding of the M electrons, that is, at $T > |E_M| \approx 0.18$ keV. The corresponding steps in the atomic factor are shown in Figure 5. One can see that the stepping atomic factor (55) mimics upon average over the energy intervals between the electron shells in germanium the Thomas-Fermi result. Thus, it can be considered as refinement of the latter due to accounting for the quantization of the electron binding energies. It can be mentioned that if one applies formulas of Section 4.1 to the onset of the K shell step, namely, just above 10.9 keV, the difference from the shown in the plot step function would be practically invisible in the scale of Figure 5.

5.3. Ab Initio Approaches. While the treatments based on a generic model of many-electron atomic targets allow

determining characteristic features and behaviors of the differential cross sections (31) and (32), to obtain accurate numerical results one needs to resort to *ab initio* calculations. Such calculations can be realized using the Hartree-Fock (HF) method (see, e.g., [58]) and its modifications. In the HF approximation, atomic electrons occupy one-electron states in a spherically-symmetric mean-field potential which is derived self-consistently from the solution of the HF equations. Accordingly, each one-electron state independently contributes to the atomic-ionization process. For the first time this approach was formulated in [38, 39], where it was illustrated with numerical calculations of neutrino-impact ionization of the F and Mo atomic targets. The wave functions and energies of atomic bound states were calculated within the relativistic HF method [62, 63] with local exchange-correlation potential [64]. The wave functions of outgoing electrons were obtained by a numerical solution of the Dirac equation in the same mean-field potential as for the wave functions of discrete states. Performed in [40] numerical calculations for ionization of the iodine atoms by impact of reactor antineutrinos led the authors to suggest the stepping approximation (55).

In a very recent theoretical study [60], the authors adopted the multiconfiguration relativistic random-phase approximation (MCRRPA) [65, 66] to evaluate the germanium atomic factors. This particular method is based on the time-dependent HF approximation [67]; however, several important features make it a better tool beyond the usual HF approximation to describe transitions of open-shell atoms of high atomic number Z. First, for open-shell atoms, typically there is more than one configuration which has the desired ground-state properties. Therefore, a proper HF reference state should be formed by a linear combination of these allowed configurations, that is, a multiconfiguration reference state. Second, for atoms of high Z, the relativistic corrections can no longer be ignored. By using a Dirac equation, instead of a Schrödinger one, the leading relativistic terms in the atomic Hamiltonian are treated nonperturbatively from the onset. Third, two-body correlations in addition to the HF approximation are generally important for excited states and transition matrix elements. The random-phase approximation (RPA) is devised to account for part of the additional two-body correlations (particles can be in the valence or core states) not only for the excited but also for the reference state, and in a lot of cases, it gives good agreement with experiment [68]. Furthermore, it has been shown that RPA equations preserve gauge invariance [69]; this provides a measure of stability of their solutions.

The MCRRPA has been applied successfully to photoexcitation and photoionization of divalent atoms such as Be, Mg, Zn, and Sr (some of the results are summarized in [70]). Following similar treatments, the authors of [60] treated the electronic configuration of germanium as a core filled up to the $4s$ orbits, with two valence electrons in the $4p$ orbits. As the Ge ground state is a $^3P_0$ state, it is a linear combination of two configurations, namely, [Zn] $4p_{1/2}^2$ and [Zn] $4p_{3/2}^2$. The wave function was calculated using the multiconfiguration Dirac-Fock package [71]. The atomic excitations due to
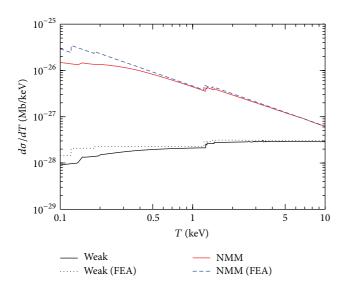
FIGURE 6: The SM (weak) and NMM contributions to the differential cross section of $\bar{\nu}_e$-Ge ionization at $E_\nu = 1$ MeV [60] in comparison with the corresponding stepping-approximation results (FEA). The NMM value is set to be the current upper limit $\mu_\nu = 2.9 \times 10^{-11} \mu_B$ [19].

weak and magnetic scattering were solved by the MCRRPA equation, and consequently transition matrix elements were yielded. In that calculation, all the current operators were expanded by spherical multipoles, and the resulting final scattering states were represented in the spherical wave basis and subject to the incoming-wave boundary condition.

Compared with the previous works on the same subject [38–41, 43] which are also in the similar spirit of the relativistic HF method, the MCRRPA approach differs in several respects. First, due to the near degeneracy of the $N_{II}(4p_{3/2})$ and $N_{III}(4p_{1/2})$ levels, using a multiconfiguration reference state is necessary. Second, the nonlocal Fock term is treated exactly, without resorting to the local exchange potentials. Third, the excited states are calculated with two-body correlation built in by MCRRPA, not simply by solving a Coulomb wave function with a static one-hole mean field.

Figure 6 shows numerical results from [60] for ionization of germanium by impact of an electron antineutrino. As can be seen, in the energy region $T \gtrsim 1$ keV the results are very well explained by the stepping-approximation formula (55). At the same time, in the sub-keV region, that is, where the electrons from the K and L shells in germanium stay "inactive," both the SM and NMM contributions appear to be significantly suppressed as compared to the stepping approximation. The latter finding seems to disagree with the semiclassical approach discussed in Section 4.2, according to which the ionization involving more loosely-bound electron states, such as those belonging to the M and N shells, is expected to follow more closely the free-electron scenario. Notice that a similar suppression of the atomic-factor values close to the ionization threshold was observed in the case of helium (see Figure 4), and it was attributed to the two-electron correlation effect. Thus, we can suggest that the correlation effects beyond the approximation of independent

electrons lead to the suppression of atomic factors in the low-energy region. This feature will be important for the next-generation experiments with Ge detectors having energy thresholds in the sub-keV region [34–36].

6. Summary and Perspectives

In this review, we have considered the neutrino-atom ionizing collisions with focus on the most important theoretical issues related to the problem. The main results discussed in the paper can be summed up as follows.

The differential over the energy transfer cross section given by the free-electron formulas (8) and (9) and the stepping behavior of the atomic factor given by (55) provide a reasonable description of the neutrino-impact ionization of a complex atom, such as germanium, down to quite low-energy transfer. The deviation from this approximation due to the onset of the ionization near the threshold is less than 5% (of the height of the step) for the K electrons, if one applies the analytical behavior of this onset that one finds for the ground state of a hydrogen-like ion. It is also found that the free-electron expressions for the differential cross section are not affected by the atomic binding effects in the semiclassical limit and for independent electrons. These analytical results can support the numerically determined behaviors of the electroweak and magnetic contributions to the neutrino-impact ionization of various atomic targets within the mean-field model [38–41]. At the same time, very recent numerical calculations of the $\bar{\nu}_e$-impact ionization processes of helium [52] and germanium [60] exhibit suppression of the SM and NMM differential cross sections relative to the stepping approximation with lowering the energy-transfer value. This suppression can be assigned to the electron-electron correlation effects.

A theoretical analysis [52] of ionization of helium by electron-antineutrino impact shows no evidence of the recently predicted enhancement [51] of the electromagnetic contribution as compared with the free-electron case. In contrast, in line with previous studies on other atomic targets, it is found that the magnitudes of the differential cross sections decrease relative to the free-electron approximation when the energy transfer is close to the ionization threshold. Thus, no sensitivity enhancement can be expected when using the He atomic target in searches for NMM. And the stepping approximation appears to be valid, within a few-percent accuracy, down to the energy-transfer values as low as almost 100 eV. We thus conclude that for practical applications, that is, for the analysis of data of the searches for NMM, one can safely apply the free-electron formulas and the stepping approximation at the energy transfer down to this range.

When analyzing the low-T data of the current high-sensitivity experiments searching for neutrino electromagnetic properties, one must go beyond the free-electron approximation for the elastic neutrino-electron scattering and take into account the atomic-ionization effects, at least, in the case of K electrons. At the present time, the experiment GEMMA-II with reactor antineutrinos is in preparation [19]. Its sensitivity to the NMM value is expected to be at the level

of $1 \times 10^{-11} \mu_B$. To achieve such a sensitivity level, which is the region of astrophysical interest [24], it is planned to reduce the effective energy threshold of a Ge detector from 2.8 to 1.5 keV. This threshold value will be very close to the binding energies of the L electrons in germanium (1.2–1.4 keV [61]). Recently, a p-type point-contact Ge detector [34–36] has been implemented in the TEXONO experiment with reactor antineutrinos. The energy threshold of this detector is about 0.3 keV, whose value is comparable to the binding energies of the $M_{\text{I–III}}$ electrons in germanium (0.12–0.18 keV [61]). This means that an accurate analysis of the corresponding data will require numerical calculations based on the *ab initio* methods.

With lowering the T value down to $T = 2E_\nu^2/(E_\nu + M_N)$, an additional collision channel apart from ionization opens up, namely, the coherent elastic neutrino-nucleus scattering [72], which has not been observed experimentally so far. The early treatments of the atomic effects in the coherent elastic neutrino-nucleus scattering within SM can be found in [37, 73, 74]. It should be noted that any deviation of the measured cross section of the coherent elastic neutrino-nucleus scattering from the very precisely known SM value [75] will provide a signature of the BSM physics (see [76–79]). In this context, the accurate calculations of the NMM-induced contribution to the cross section of the coherent elastic neutrino-nucleus scattering appear to be of particular importance. The NMM-induced coherent neutrino scattering by single atoms as well as by crystals was discussed theoretically only in [80]. However, further studies are necessary for the correct interpretation of future measurements at low T values [81].

Conflict of Interests

The authors declare that there is no conflict of interests regarding the publication of this paper.

Acknowledgment

References

[1] C. Giunti and C. W. Kim, *Fundamentals of Neutrino Physics and Astrophysics*, Oxford University Press, Oxford, UK, 2007.

[2] M. C. Gonzalez-Garcia and M. Maltoni, "Phenomenology with massive neutrinos," *Physics Reports*, vol. 460, no. 1–3, pp. 1–129, 2008.

[3] S. Bilenky, *Introduction to the Physics of Massive and Mixed Neutrinos*, vol. 817 of *Lecture Notes in Physics*, Springer, New York, NY, USA, 2010.

[4] Z. Z. Xing and S. Zhou, *Neutrinos in Particle Physics, Astronomy and Cosmology*, Zhejiang University Press, 2011.

[5] C. Giunti and A. Studenikin, "Neutrino electromagnetic properties," *Physics of Atomic Nuclei*, vol. 72, no. 12, pp. 2089–2125, 2009.

[6] C. Broggini, C. Giunti, and A. Studenikin, "Electromagnetic properties of neutrinos," *Advances in High Energy Physics*, vol. 2012, Article ID 459526, 47 pages, 2012.

[7] C. Giunti and A. Studenikin, "Neutrino electromagnetic interactions: a window to new physics," http://arxiv.org/abs/1403.6344.

[8] J. F. Nieves, "Electromagnetic properties of Majorana neutrinos," *Physical Review D*, vol. 26, no. 11, pp. 3152–3158, 1982.

[9] B. Kayser, "Majorana neutrinos and their electromagnetic properties," *Physical Review D*, vol. 26, no. 7, pp. 1662–1670, 1982.

[10] B. Kayser, "CPT, CP, and C phases, and their effects, in Majorana-particle processes," *Physical Review D*, vol. 30, no. 5, pp. 1023–1033, 1984.

[11] S. T. Petcov, "The processes $\mu \to e + \gamma, \mu \to e + e + \bar{e}, \nu' \to \nu + \gamma$ in the Weinberg-Salam model with neutrino mixing," *Soviet Journal of Nuclear Physics*, vol. 25, p. 340, 1977.

[12] K. Fujikawa and R. E. Shrock, "Magnetic moment of a massive neutrino and neutrino-spin rotation," *Physical Review Letters*, vol. 45, no. 12, pp. 963–966, 1980.

[13] P. B. Pal and L. Wolfenstein, "Radiative decays of massive neutrinos," *Physical Review D*, vol. 25, no. 3, pp. 766–773, 1982.

[14] R. E. Shrock, "Electromagnetic properties and decays of Dirac and Majorana neutrinos in a general class of gauge theories," *Nuclear Physics B*, vol. 206, no. 3, pp. 359–379, 1982.

[15] J. F. Beacom and P. Vogel, "Neutrino magnetic moments, flavor mixing, and the super-kamiokande solar data," *Physical Review Letters*, vol. 83, no. 25, pp. 5222–5225, 1999.

[16] N. F. Bell, V. Cirigliano, M. J. Ramsey-Musolf, P. Vogel, and M. B. Wise, "How magnetic is the dirac neutrino?" *Physical Review Letters*, vol. 95, no. 15, Article ID 151802, 4 pages, 2005.

[17] N. F. Bell, M. Gorchtein, M. J. Ramsey-Musolf, P. Vogel, and P. Wang, "Model independent bounds on magnetic moments of Majorana neutrinos," *Physics Letters B: Nuclear, Elementary Particle and High-Energy Physics*, vol. 642, no. 4, pp. 377–383, 2006.

[18] H. T. Wong, H. B. Li, S. T. Lin et al., "Search of neutrino magnetic moments with a high-purity germanium detector at the Kuo-Sheng nuclear power station," *Physical Review D*, vol. 75, no. 1, Article ID 012001, 16 pages, 2007.

[19] A. G. Beda, V. B. Brudanin, V. G. Egorov et al., "The results of search for the neutrino magnetic moment in GEMMA experiment," *Advances in High Energy Physics*, vol. 2012, Article ID 350150, 12 pages, 2012.

[20] L. B. Auerbach, R. L. Burman, D. O. Caldwell et al., "Measurement of electron-neutrino electron elastic scattering," *Physical Review D*, vol. 63, no. 11, Article ID 112001, 2001.

[21] R. Schwienhorst, D. Ciampa, C. Erickson et al., "A new upper limit for the tau-neutrino magnetic moment," *Physics Letters B*, vol. 513, no. 1-2, pp. 23–29, 2001.

[22] D. W. Liu, Y. Ashie, S. Fukuda et al., "Limits on the neutrino magnetic moment using 1496 days of Super-Kamiokande-I solar neutrino data," *Physical Review Letters*, vol. 93, no. 2, Article ID 021802, 5 pages, 2004.

[23] C. Arpesella, H. O. Back, and M. Balata, "Direct measurement of the 7Be solar neutrino flux with 192 days of Borexino data," *Physical Review Letters*, vol. 101, no. 9, Article ID 091302, 6 pages, 2008.

[24] G. G. Raffelt, "New bound on neutrino dipole moments from globular-cluster stars," *Physical Review Letters*, vol. 64, no. 24, pp. 2856–2858, 1990.

[25] R. N. Mohapatra and P. B. Pal, *Massive Neutrinos in Physics and Astrophysics*, vol. 72 of *Lecture Notes in Physics*, World Scientific, River Edge, NJ, USA, 3rd edition, 2004.

[26] E. D. Commins and P. H. Bucksbaum, *Weak Interactions of Leptons and Quarks*, Cambridge University Press, Cambridge, UK, 3rd edition, 1983.

[27] J. F. Carlson and J. R. Oppenheimer, "The impacts of fast electrons and magnetic neutrons," *Physical Review*, vol. 41, no. 6, pp. 763–792, 1932.

[28] H. Bethe, "Ionization power of a neutrino with magnetic moment," *Mathematical Proceedings of the Cambridge Philosophical Society*, vol. 31, no. 1, pp. 108–115, 1935.

[29] A. V. Kyuldjiev, "Searching for effects of neutrino magnetic moments at reactors and accelerators," *Nuclear Physics, Section B*, vol. 243, no. 3, pp. 387–397, 1984.

[30] G. Domogatsky and D. Nadezhin, "Modern theory of star evolution and experiments of F. Reines on anti ν e-scattering detection," *Soviet Journal of Nuclear Physics*, vol. 12, p. 678, 1971.

[31] C. L. Cowan and F. Reines, "Neutrino magnetic moment upper limit," *Physical Review*, vol. 107, no. 2, pp. 528–530, 1957.

[32] C. L. Cowan Jr., F. Reines, and F. B. Harrison, "Upper limit on the neutrino magnetic moment," *Physical Review*, vol. 96, no. 5, article 1294, 1954.

[33] P. Vogel and J. Engel, "Neutrino electromagnetic form factors," *Physical Review D*, vol. 39, no. 11, pp. 3378–3383, 1989.

[34] H. T. Wong, "Low energy neutrino and dark matter physics with sub-kev germanium detectors," *International Journal of Modern Physics D*, vol. 20, no. 8, pp. 1463–1470, 2011.

[35] H. B. Li, H. Y. Liao, S. T. Lin et al., "Limits on spin-independent couplings of wimp dark matter with a p-type point-contact germanium detector," *Physical Review Letters*, vol. 110, no. 26, Article ID 261301, 5 pages, 2013.

[36] H. B. Li, L. Singh, M. K. Singh et al., "Differentiation of bulk and surface events in *p*-type point-contact germanium detectors for light WIMP searches," *Astroparticle Physics*, vol. 56, pp. 1–8, 2014.

[37] Y. V. Gaponov, Y. L. Dobrynin, and V. N. Tikhonov, "Neutrino and antineutrino scattering on hydrogen-like atom," *Soviet Journal of Nuclear Physics*, vol. 22, no. 2, pp. 328–334, 1975.

[38] V. Y. Dobretsov, A. B. Dobrotsvetov, and S. A. Fayans, "Inelastic neutrino scattering by atomic electrons," *Soviet Journal of Nuclear Physics*, vol. 55, p. 1180, 1992.

[39] S. A. Fayans, V. Y. Dobretsov, and A. B. Dobrotsvetov, "Effect of atomic binding on inelastic ve scattering," *Physics Letters, Section B: Nuclear, Elementary Particle and High-Energy Physics*, vol. 291, no. 1-2, pp. 1–6, 1992.

[40] V. I. Kopeikin, L. A. Mikaelyan, V. V. Sinev, and S. A. Fayans, "Scattering of reactor antineutrinos by electrons," *Physics of Atomic Nuclei*, vol. 60, no. 11, pp. 1859–1864, 1997.

[41] S. A. Fayans, L. A. Mikaelyan, and V. V. Sinev, "Weak and magnetic inelastic scattering of antineutrinos on atomic electrons," *Physics of Atomic Nuclei*, vol. 64, no. 8, pp. 1475–1480, 2001.

[42] G. J. Gounaris, E. A. Paschos, and P. I. Porfyriadis, "The ionization of H, He or Ne atoms using neutrinos or antineutrinos at keV energies," *Physics Letters B*, vol. 525, no. 1-2, pp. 63–70, 2002.

[43] V. I. Kopeikin, L. A. Mikaelyan, and V. V. Sinev, "Inelastic scattering of tritium-source antineutrinos on electrons of germanium atoms," *Physics of Atomic Nuclei*, vol. 66, no. 4, pp. 707–711, 2003.

[44] H. T. Wong, H. Li, and S. Lin, "Enhanced sensitivities for the searches of neutrino magnetic moments through atomic ionization," *Physical Review Letters*, vol. 105, no. 6, Article ID 061801, 2010.

[45] M. Voloshin, "Neutrino scattering on atomic electrons in searches for the neutrino magnetic moment," *Physical Review Letters*, vol. 105, no. 20, Article ID 201801, 4 pages, 2010.

[46] H. T. Wong, H.-B. Li, and S.-T. Lin, "Enhanced sensitivities for the searches of neutrino magnetic moments through atomic ionization," *Physical Review Letters*, vol. 105, Article ID 061801, 2074.

[47] K. A. Kouzakov and A. I. Studenikin, "Magnetic neutrino scattering on atomic electrons revisited," *Physics Letters B: Nuclear, Elementary Particle and High-Energy Physics*, vol. 696, no. 3, pp. 252–256, 2011.

[48] K. A. Kouzakov and A. I. Studenikin, "Electromagnetic neutrino-atom collisions: the role of electron binding," *Nuclear Physics B: Proceedings Supplements*, vol. 217, no. 1, pp. 353–356, 2011.

[49] K. A. Kouzakov, A. I. Studenikin, and M. B. Voloshin, "Testing neutrino magnetic moment in ionization of atoms by neutrino impact," *JETP Letters*, vol. 93, no. 11, pp. 623–627, 2011.

[50] K. A. Kouzakov, A. I. Studenikin, and M. B. Voloshin, "Neutrino-impact ionization of atoms in searches for neutrino magnetic moment," *Physical Review D*, vol. 83, no. 11, Article ID 113001, 11 pages, 2011.

[51] V. P. Martemyanov and V. G. Tsinoev, "Ionization of helium atoms under the effect of the antineutrino magnetic moment," *Physics of Atomic Nuclei*, vol. 74, no. 12, pp. 1671–1675, 2011.

[52] K. A. Kouzakov and A. I. Studenikin, "On sensitivity of neutrino-helium ionizing collisions to neutrino magnetic moments," *Physics of Particles and Nuclei Letters*, vol. 11, no. 4, pp. 458–461, 2014.

[53] L. van Hove, "Correlations in space and time and born approximation scattering in systems of interacting particles," *Physical Review*, vol. 95, pp. 249–262, 1954.

[54] U. Fano, "Penetration of protons, alpha particles, and mesons," *Annual Review of Nucler Science*, vol. 13, pp. 1–66, 1963.

[55] D. Belkic, "Bound-free non-relativistic transition form factors in atomic hydrogen," *Journal of Physics B: Atomic and Molecular Physics*, vol. 14, no. 12, article 005, pp. 1907–1914, 1981.

[56] A. R. Holt, "Matrix elements for bound-free transitions in atomic hydrogen," *Journal of Physics B: Atomic and Molecular Physics*, vol. 2, no. 11, article 311, pp. 1209–1213, 1969.

[57] A. I. Akhiezer and V. B. Berestetskii, *Quantum Electrodynamics*, Wiley, New York, 2nd edition, 1965.

[58] L. D. Landau and E. M. Lifshits, *Quantum Mechanics: Non-Relativistic Theory*, Pergamon, Oxford, UK, 3rd edition, 1977.

[59] K. A. Kouzakov, S. A. Zaytsev, Y. V. Popov, and M. Takahashi, "Singly ionizing 100-MeV/amu C^6 + He collisions with small momentum transfer," *Physical Review A: Atomic, Molecular, and Optical Physics*, vol. 86, no. 3, Article ID 032710, 8 pages, 2012.

[60] J.-W. Chen, H.-C. Chi, K.-N. Huang et al., "Atomic ionization of germanium by neutrinos from an ab initio approach," *Physics Letters B*, vol. 731, pp. 159–162, 2014.

[61] B. L. Henke, E. M. Gullikson, and J. C. Davis, "X-ray interactions: photoabsorption, scattering, transmission, and reflection at E = 50–30,000 eV, Z = 1–92," *Atomic Data and Nuclear Data Tables*, vol. 54, no. 2, pp. 181–342, 1993.

[62] I. P. Grant, "Relativistic self-consistent fields," *Proceedings of the Royal Society A*, vol. 262, pp. 555–576, 1961.

[63] I. P. Grant, "Relativistic self-consistent fields," *Proceedings of the Physical Society*, vol. 86, pp. 523–527, 1965.

[64] V. L. Moruzzi, J. F. Janak, and A. R. Williams, *Calculated Electronic Properties of Metals*, Pergamon, Oxford, UK, 1978.

[65] K.-N. Huang and W. R. Johnson, "Multiconfiguration relativistic random-phase approximation: theory," *Physical Review A*, vol. 25, no. 2, pp. 634–649, 1982.

[66] K.-N. Huang, "Relativistic many-body theory of atomic transitions. The relativistic equation-of-motion approach," *Physical Review A*, vol. 26, no. 2, pp. 734–739, 1982.

[67] P. Jorgensen, "Molecular and atomic applications of time-dependent Hartree-Fock theory," *Annual Review of Physical Chemistry*, vol. 26, pp. 359–380, 1975.

[68] M. Ya. Amusia and N. A. Cherepkov, "Many-body electron correlations in scattering processes," *Case Studies in Atomic Physics*, vol. 5, pp. 47–179, 1975.

[69] D. L. Lin, "Gauge properties of the Hartree-Fock and random-phase approximations," *Physical Review A*, vol. 16, no. 2, pp. 600–605, 1977.

[70] K.-N. Huang, H.-C. Chi, and H.-S. Chou, "The MCRRPA theory and its applications to photoexcitation and photoionization," *Chinese Journal of Physics*, vol. 33, no. 6, pp. 565–644, 1995.

[71] J. P. Desclaux, "A multiconfiguration relativistic DIRAC-FOCK program," *Computer Physics Communications*, vol. 9, no. 1, pp. 31–45, 1975.

[72] D. Z. Freedman, "Coherent effects of a weak neutral current," *Physical Review D*, vol. 9, no. 5, pp. 1389–1392, 1974.

[73] Yu. V. Gaponov and V. N. Tikhonov, "Elastic scattering of low-energy neutrinos by atomic systems," *Soviet Journal of Nuclear Physics*, vol. 26, p. 314, 1977.

[74] L. M. Sehgal and M. Wanninger, "Atomic effects in coherent neutrino scattering," *Physics Letters B*, vol. 171, no. 1, pp. 107–112, 1986.

[75] A. Drukier and L. Stodolsky, "Principles and applications of a neutral-current detector for neutrino physics and astronomy," *Physical Review D*, vol. 30, no. 11, pp. 2295–2309, 1984.

[76] K. Scholberg, "Prospects for measuring coherent neutrino-nucleus elastic scattering at a stopped-pion neutrino source," *Physical Review D*, vol. 73, no. 3, Article ID 033005, 9 pages, 2006.

[77] J. Barranco, O. G. Miranda, and T. I. Rashba, "Probing new physics with coherent neutrino scattering off nuclei," *Journal of High Energy Physics*, vol. 2005, article 021, 14 pages, 2005.

[78] J. Barranco, O. G. Miranda, and T. I. Rashba, "Sensitivity of low energy neutrino experiments to physics beyond the standard model," *Physical Review D*, vol. 76, Article ID 073008, 9 pages, 2007.

[79] S. Davidson, C. Peña-Garay, N. Rius, and A. Santamaria, "Present and future bounds on non-standard neutrino interactions," *Journal of High Energy Physics*, vol. 3, no. 3, article 011, 2003.

[80] J. Augustin, B. Müller, and W. Greiner, "Magnetic neutrino scattering by crystals," *Physical Review D*, vol. 41, no. 5, pp. 1683–1686, 1990.

[81] J. A. Formaggio, E. Figueroa-Feliciano, and A. J. Anderson, "Sterile neutrinos, coherent scattering, and oscillometry measurements with low-temperature bolometers," *Physical Review D*, vol. 85, no. 1, Article ID 013009, 2012.

Review Article

Neutrinos as Probes of Lorentz Invariance

Jorge S. Díaz[1,2]

[1] *Institute for Theoretical Physics, Karlsruhe Institute of Technology, 76128 Karlsruhe, Germany*
[2] *Physics Department, Indiana University, Bloomington, IN 47405, USA*

Correspondence should be addressed to Jorge S. Díaz; jorge.diaz@kit.edu

Neutrinos can be used to search for deviations from exact Lorentz invariance. The worldwide experimental program in neutrino physics makes these particles a remarkable tool to search for a variety of signals that could reveal minute relativity violations. This paper reviews the generic experimental signatures of the breakdown of Lorentz symmetry in the neutrino sector.

1. Introduction

In 1930, Pauli postulated the neutrino as a *desperate remedy* to save one of the sacred principles of physics, the conservation of energy, which appeared to be violated in beta decays [1]. Today, neutrinos remain as some of the less understood particles of the standard model (SM) and their mysteries are still fascinating. Their ghostly nature makes them barely interact with matter and their interferometric behavior makes them oscillate between different flavors. Neutrino oscillations have led to the remarkable conclusion of massive neutrinos, presenting an established evidence of physics beyond the SM.

In the search for new physics, different candidate theories for quantum gravity involve mechanisms that could trigger the breakdown of one of the most fundamental symmetries in modern physics, Lorentz invariance. In the theoretical front, Lorentz-violating descriptions of neutrino behavior have shown that these fundamental particles can serve as powerful probes of new physics. Experimentally, neutrino oscillations have been used to perform several searches for Lorentz violation. The development of techniques to perform systematic searches for Lorentz violation in many other experimental setups shows a rich phenomenology to be studied, with a large variety of experimental effects that remain unexplored.

This paper summarizes the main experimental signatures of deviations from exact Lorentz invariance in the neutrino sector. The experimental searches for Lorentz violation performed in recent years are presented and future tests of Lorentz symmetry are discussed, ranging from precision measurements of beta decay and double beta decay at low energies to the high energy of astrophysical neutrinos and oscillation experiments using accelerator, atmospheric, and reactor neutrinos.

2. Lorentz Invariance Violation

Deviations from exact Lorentz symmetry have been shown to be possible at very high energies in candidate descriptions of gravity at the quantum level. For instance, mechanisms for the spontaneous breaking of this fundamental symmetry have been identified in string-theory scenarios [2]. Interactions could generate Lorentz-violating terms if a tensor field acquires a nonzero vacuum expectation value $\langle T_{\alpha\beta\gamma\cdots}\rangle = t_{\alpha\beta\gamma\cdots} \neq 0$, which acts as a background field. In the same fashion as the nonzero vacuum expectation value of the dynamical Higgs field generates mass terms for other fields via interactions, background tensor fields that couple to conventional particles in the SM will generate new terms that break Lorentz invariance. These new terms are Lorentz scalars under coordinate transformations; in fact, the spacetime indices of the background field are all contracted with the indices of the SM operator in the form $t_{\alpha\beta\gamma\cdots}\mathcal{O}^{\alpha\beta\gamma\cdots}$. This structure guarantees that there is no privileged reference frame because the theory is observer invariant. For instance, consider the case of Lorentz violation generated by a 2-tensor

$t_{\alpha\beta}$, which will be coupled to some SM operator with the same number of spacetime indices in the form $\mathscr{L} = t_{\alpha\beta}\mathscr{O}^{\alpha\beta}$. Under a coordinate transformation both the operator and the tensor background field transform to a new set of coordinates as follows:

$$
\begin{aligned}
\mathscr{O}^{\alpha\beta} &\longrightarrow \mathscr{O}^{\alpha'\beta'} = \Lambda^{\alpha'}_{\alpha}\Lambda^{\beta'}_{\beta}\mathscr{O}^{\alpha\beta}, \\
t_{\alpha\beta} &\longrightarrow t_{\alpha'\beta'} = \left(\Lambda^{-1}\right)^{\lambda}_{\alpha'}\left(\Lambda^{-1}\right)^{\rho}_{\beta'}t_{\lambda\rho},
\end{aligned}
\tag{1}
$$

so that the terms in the Lagrangian $\mathscr{L} = t \cdot \mathscr{O}$ remain invariant $\mathscr{L}' = t' \cdot \mathscr{O}' = t \cdot \mathscr{O} = \mathscr{L}$. The same construction can be applied for a general tensor.

On the other hand, when a Lorentz transformation is performed over the physical system, this is when the experimental apparatus is rotated or boosted rather than the coordinates used to describe it, then the SM operator transforms as shown in (1) but any background field remains unchanged $\mathscr{L}' = t \cdot \mathscr{O}' \neq \mathscr{L}$. This so-called particle Lorentz transformation changes the coupling between the background fields and the SM operators, resulting in a physically observable anisotropy of spacetime; this is a violation of Lorentz invariance [3].

Phenomenological approaches to parameterize and experimentally search for particular types of Lorentz violation have been considered since several decades [4–7]. However, effective field theory can be used to incorporate generic operators that break Lorentz invariance for all the particles in the SM. This general framework is known as the standard-model extension (SME) [3, 8, 9], whose action includes general coordinate-invariant terms by contracting operators of conventional fields with controlling coefficients for Lorentz violation and reduces to the SM if all these coefficients vanish. Gravity can also be incorporated by writing the SM in a curved background [9]. The development of the SME has led to a worldwide experimental program searching for violations of Lorentz invariance, whose results are summarized in [10].

Flat spacetime is considered for experiments in particle physics, in which case the coefficients for Lorentz violation that act as background fields can be chosen to be constant and uniform, which guarantees conservation of energy and linear momentum. In this limit, these coefficients represent the vacuum expectation value of the tensor fields of the underlying theory. Excitations of these fields lead to a rich phenomenology; for instance, Nambu-Goldstone modes could play fundamental roles when gravity is included, such as the graviton, the photon in Einstein-Maxwell theory [11–14], and spin-dependent [15] and spin-independent [16] forces.

It should be noted that a subset of operators in the SME also break CPT symmetry. In fact, all the Lorentz-violating terms in the action involving operators with an odd number of spacetime indices are odd under a CPT transformation. In realistic field theories, CPT violation always appears with Lorentz violation [17]. Nonetheless, alternative approaches exist in which CPT violation is implemented with and without Lorentz invariance [18–25].

3. Neutrinos

The general description of three left-handed neutrinos and three right-handed antineutrinos in the presence of Lorentz-violating background fields is given by a 6×6 effective Hamiltonian of form [28]

$$
H = \begin{pmatrix} (h_0)_{ab} & 0 \\ 0 & (h_0)^*_{ab} \end{pmatrix} + \begin{pmatrix} \delta h_{ab} & \delta h_{a\bar{b}} \\ \delta h^*_{a\bar{b}} & \delta h_{\bar{a}\bar{b}} \end{pmatrix},
\tag{2}
$$

where the indices indicate the flavors of active neutrinos $a, b = e, \mu, \tau$ and antineutrinos $\bar{a}, \bar{b} = \bar{e}, \bar{\mu}, \bar{\tau}$. The Lorentz-preserving component is explicitly given by the following:

$$
(h_0)_{ab} = |\mathbf{p}| \, \delta_{ab} + \frac{m^2_{ab}}{2 \, |\mathbf{p}|},
\tag{3}
$$

where at leading order the neutrino momentum is given by the energy $|\mathbf{p}| \approx E$ and the mass-squared matrix is commonly written in terms of the Pontecorvo-Maki-Nakagawa-Sakata (PMNS) matrix [29–31] as $m^2 = U_{\mathrm{PMNS}}(m^2_D)U^{\dagger}_{\mathrm{PMNS}}$, with $m^2_D = \mathrm{diag}(m^2_1, m^2_2, m^2_3)$.

The Lorentz-violating block describing neutrinos in the Hamiltonian (2) is given by the following:

$$
\delta h_{ab} = (a_L)^{\alpha}_{ab}\hat{p}_{\alpha} + (c_L)^{\alpha\beta}_{ab}\hat{p}_{\alpha}\hat{p}_{\beta} \, |\mathbf{p}| \, .
\tag{4}
$$

The components of the 3×3 complex matrices $(a_L)^{\alpha}_{ab}$ and $(c_L)^{\alpha\beta}_{ab}$ are called coefficients for CPT-odd and CPT-even Lorentz violation, respectively. The spacetime indices α, β encode the nature of the broken symmetry; for instance, isotropic (direction-independent) Lorentz violation appears when only the time components of the coefficients are nonzero; while space anisotropy appears when any of the other components is nonzero, generating direction-dependent effects in the neutrino behavior. The breakdown of invariance under rotations is evident due to the presence of the four-vector $\hat{p}^{\alpha} = (1; \hat{p})$ that depends on the neutrino direction of propagation $\hat{p}$.

The block Hamiltonian describing right-handed antineutrinos is obtained as the CP conjugate of the neutrino Hamiltonian $\delta h_{\bar{a}\bar{b}} = \mathrm{CP}(\delta h_{ab})$, which has the same form as the neutrino Hamiltonian (4) with $(a_R)^{\alpha}_{\bar{a}\bar{b}} = -(a_L)^{\alpha*}_{ab}$ and $(c_R)^{\alpha\beta}_{\bar{a}\bar{b}} = (c_L)^{\alpha\beta*}_{ab}$. Given the structure of these coefficients in flavor space, it is expected that they will affect neutrino mixing and oscillations. Notice, however, that there exist coefficients that modify the three flavors in the same way, producing no effects on neutrino oscillations because they are proportional to the identity in flavor space. These *oscillation-free* coefficients and their observable effects are discussed in Sections 5 and 6.

Signals of the breakdown of Lorentz invariance correspond to the anisotropy of spacetime due to preferred directions set by the coefficients for Lorentz violation that act as fixed background fields. Taking advantage of the coupling of these background fields with the neutrino direction of propagation $\hat{p}$, we can search for violations of Lorentz invariance by making measurements with neutrino beams

with different orientations, which would reveal the presence of the SME coefficients $(a_L)_{ab}^{\alpha}$ and $(c_L)_{ab}^{\alpha\beta}$. For Earth-based experiments, detectors and source rotate with a well-defined angular frequency $\omega_{\oplus} \simeq 2\pi/(23\,\text{h}\,56\,\text{min})$ due to Earth's rotation, which makes the neutrino direction vary with respect to the fixed background fields. This time dependence will explicitly appear in the relevant observable quantities and it can be parameterized as harmonics of the sidereal angle $\omega_{\oplus}T_{\oplus}$. Due to the invariance of the theory under coordinate transformations, there is no preferred reference frame to make the measurements. In order to establish a consistent and systematic search for Lorentz-violating effects, experimental results are conventionally reported in the Sun-centered equatorial frame described in [10, 32]. In this frame, the sidereal variation of the coupling between the neutrino direction $\widehat{p}$ and the background fields that break Lorentz symmetry can be explicitly written in the form

$$
\begin{aligned}
\delta h_{ab} = (\mathscr{C})_{ab} &+ (\mathscr{A}_s)_{ab} \sin \omega_{\oplus} T_{\oplus} \\
&+ (\mathscr{A}_c)_{ab} \cos \omega_{\oplus} T_{\oplus} \\
&+ (\mathscr{B}_s)_{ab} \sin 2\omega_{\oplus} T_{\oplus} + (\mathscr{B}_c)_{ab} \cos 2\omega_{\oplus} T_{\oplus},
\end{aligned}
\tag{5}
$$

where the amplitude of each sidereal harmonic is a function of the coefficients for Lorentz violation and experimental parameters including neutrino energy, location of the experiment, and relative orientation between source and detector [33, 34].

The coefficients $(a_L)_{ab}^{\alpha}$ and $(c_L)_{ab}^{\alpha\beta}$ arise from operators of dimension three and four, respectively. Operators of arbitrary dimension d can be incorporated in the theory, in which case the coefficients for Lorentz violation in the Hamiltonian (4) appear as momentum-dependent quantities of the form [35, 36]

$$
\begin{aligned}
(a_L)_{ab}^{\alpha} &\longrightarrow (\widehat{a}_L)_{ab}^{\alpha\lambda_1\cdots\lambda_{d-3}} p_{\lambda_1} \cdots p_{\lambda_{d-3}}, \quad d \text{ odd,} \\
(c_L)_{ab}^{\alpha\beta} &\longrightarrow (\widehat{c}_L)_{ab}^{\alpha\beta\lambda_1\cdots\lambda_{d-3}} p_{\lambda_1} \cdots p_{\lambda_{d-3}}, \quad d \text{ even.}
\end{aligned}
\tag{6}
$$

The extra derivatives in the Lagrangian appear in the neutrino Hamiltonian as higher powers of the neutrino energy. Although the conventional massive-neutrino description of oscillations accommodates all the established experimental results, nonnegative powers of the neutrino energy could help to elegantly solve some anomalous results obtained in recent years in beam experiments [37–39]. In fact, interesting attempts to describe the global data using the SME have led to the construction of alternative models for neutrino oscillations that can accommodate the results reported by different experiments [40–46].

In the following sections we discuss the observable signatures of these coefficients for Lorentz violation in different types of neutrino experiments including oscillations, neutrino velocity, and beta decays.

4. Neutrino Oscillations

The interferometric nature of neutrino oscillations has been widely identified as an ideal experimental setup to search for new physics in the form of deviations from the conventional description of neutrinos. The mixing and oscillation between neutrino flavors occur in general due to off-diagonal entries in the neutrino Hamiltonian leading to eigenstates with different energy.

4.1. Oscillation of Neutrinos and Antineutrinos. Neutrino oscillations are well described by a model of three massive neutrinos, which depends on two mass-squared differences Δm_{21}^2 and Δm_{31}^2 controlling the oscillation lengths and three mixing angles θ_{12}, θ_{13}, and θ_{23} that govern the amplitude of the oscillation [47]. According to this massive-neutrino model, the oscillation probabilities are proportional to the factor $\sin^2(\Delta m_{ij}^2 L/4E)$. Tests of Lorentz invariance using neutrino oscillations can be performed by searching for deviations from the conventional behavior. For some experiments studying neutrinos over a large range of energies and baselines, such as Super-Kamiokande [48], an exact treatment of the diagonalization of the Hamiltonian is necessary [49]. In most cases, the experimental features allow the implementation of approximation methods for determining the oscillation probabilities, as discussed in the following sections.

4.1.1. Short-Baseline Approximation. According to the massive-neutrino model, for experiments using neutrinos of energy E and baseline L that satisfy $\Delta m_{ij}^2 L/4E \ll \pi/2$, the oscillation phase would be too small to impact the neutrino propagation and no neutrino oscillations should be observed. The effects of the mass terms in the conventional Hamiltonian h_0 (3) become negligible and the effective Hamiltonian can be approximated by $h \approx \delta h$. Direct calculation of the oscillation probabilities shows that in this approximation we can write the appearance probability [33]

$$
P_{\nu_b \to \nu_a} \simeq L^2 |\delta h_{ab}|^2, \quad a \neq b,
\tag{7}
$$

with a similar expression for antineutrinos using $\delta h_{\overline{ab}}$ instead. The sidereal decomposition of the Hamiltonian (5) can be used to show that the probability will also exhibit sidereal variations, one of the key signatures of Lorentz violation. The Hamiltonian contains also a time-independent component $(\mathscr{C})_{ab}$, which can lead to both isotropic and direction-dependent effects. In all cases, the energy dependence is different with respect to the conventional case, so spectral studies can be used to study these particular coefficients.

Experimental studies using the probability (7) have been performed by Double Chooz [50], IceCube [51], LSND [52], MiniBooNE [53, 54], and MINOS using its near detector [55, 56]. The absence of a positive signal in all these experiments has been used to set tight constraints on several coefficients for Lorentz violation, which are summarized in [10]. It is important to emphasize that, since all these searches use different oscillation channels, they are complementary, accessing similar coefficients but with different flavor indices.

4.1.2. Perturbative Approximation. Since the phase of the oscillation is given by $\Delta m_{ij}^2 L/4E$, the oscillation probability can be enhanced by placing a detector at a distance $L =$
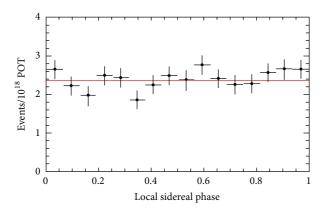
FIGURE 1: Number of events normalized by protons on target (POT) in the MINOS far detector as a function of the sidereal phase. The flat distribution of events is interpreted as the absence of sidereal variations in the oscillation probability. Figure adapted from [26].

$2\pi E/\Delta m_{ij}^2$ from the neutrino source. For experiments satisfying this condition, mass-driven oscillations h_0 dominate in the Hamiltonian and we can consider the effects of Lorentz violation δh as a small perturbation [34]. In this case, the oscillation probability appears as a power series of the form

$$P_{\nu_b \to \nu_a} = P_{\nu_b \to \nu_a}^{(0)} + P_{\nu_b \to \nu_a}^{(1)} + \cdots, \qquad (8)$$

where $P_{\nu_b \to \nu_a}^{(0)}$ is the conventional probability given by the massive-neutrino model and the following terms are given in powers of the coefficients for Lorentz violation, whose explicit form is given in [34]. Once again, the sidereal variation of the oscillation probability appears as a key signal to search by experiments. For instance, the leading-order term $P_{\nu_b \to \nu_a}^{(1)}$ can be generically written as follows:

$$\begin{aligned}
\frac{P_{\nu_b \to \nu_a}^{(1)}}{2L} &= \left(P_{\mathcal{C}}^{(1)}\right)_{ab} \\
&+ \left(P_{\mathcal{A}_s}^{(1)}\right)_{ab} \sin \omega_\oplus T_\oplus + \left(P_{\mathcal{A}_c}^{(1)}\right)_{ab} \cos \omega_\oplus T_\oplus \\
&+ \left(P_{\mathcal{B}_s}^{(1)}\right)_{ab} \sin 2\omega_\oplus T_\oplus + \left(P_{\mathcal{B}_c}^{(1)}\right)_{ab} \cos 2\omega_\oplus T_\oplus.
\end{aligned} \qquad (9)$$

This is the dominating probability for neutrino mixing as well as antineutrino oscillations.

Since the first-order correction (9) to the oscillation probability arises from the interference between the conventional and the Lorentz-violating effects, the sensitivity to the coefficients in $P_{\nu_b \to \nu_a}^{(1)}$ is greater than in the short-baseline approximation presented in the previous section. Figure 1 shows part of the study performed by the MINOS experiment, which used the expression (9) to search for sidereal variations in the event rate measured at the far detector. The sensitivity to different coefficients was improved by a factor 20–510 compared to the previous constraints using the near detector [26].

The mixing between neutrinos and antineutrinos is also possible due to the block $\delta h_{a\bar{b}}$ in the Hamiltonian (2), which is discussed in the following section.

4.2. Neutrino-Antineutrino Mixing. The off-diagonal block $\delta h_{a\bar{b}}$ in the Hamiltonian (2) can produce the mixing between neutrinos and antineutrinos. This 3×3 matrix is given by [28]

$$\delta h_{a\bar{b}} = i\sqrt{2}(\epsilon_+)_\alpha \widetilde{H}_{a\bar{b}}^\alpha - i\sqrt{2}(\epsilon_+)_\alpha \hat{p}_\beta \widetilde{g}_{a\bar{b}}^{\alpha\beta} |\mathbf{p}|, \qquad (10)$$

where the complex 4-vector $(\epsilon_+)_\alpha$ is the neutrino polarization that can be directly written in terms of the location of the experiment and the orientation of the neutrino beam [34]. Two sets of coefficients for Lorentz violation denoted by $\widetilde{H}_{a\bar{b}}^\alpha$ and $\widetilde{g}_{a\bar{b}}^{\alpha\beta}$ control CPT-even and CPT-odd effects, respectively. This Hamiltonian can also be decomposed in form (5), with harmonic amplitudes given in terms of the coefficients $\widetilde{H}_{a\bar{b}}^\alpha$ and $\widetilde{g}_{a\bar{b}}^{\alpha\beta}$ [34].

Contrary to the neutrino Hamiltonian (4), the neutrino-antineutrino block always appears with direction-dependent effects, for this reason the search of sidereal variations is an ideal setup to search for these coefficients. Following the perturbative description presented in Section 4.1.2, it has been shown that at first order the oscillation probability vanishes, in other words, neutrino-antineutrino oscillations appear as a second order effect [34]. For this reason, the second-order probability $P_{\nu_a \to \bar{\nu}_b}^{(2)}$ can be decomposed in form (9), although involving up to four harmonics.

The possible oscillation of neutrinos into antineutrinos modifies, for instance, the survival probability of muon neutrinos in a beam experiment because now some ν_μ could disappear into antineutrino states. A systematic search of the 66 coefficients $\widetilde{H}_{a\bar{b}}^\alpha$ and $\widetilde{g}_{a\bar{b}}^{\alpha\beta}$ producing sidereal variations was performed using data from the MINOS experiment [57]. The remaining 15 coefficients producing time-independent effects could only be explored by a spectral study in a disappearance experiment. Figure 2 shows a fit to the data from the Double Chooz experiment, searching for the spectral modification that could arise in the disappearance of electron antineutrinos [27].

A total of 81 coefficients $\widetilde{H}_{a\bar{b}}^\alpha$ and $\widetilde{g}_{a\bar{b}}^{\alpha\beta}$ has been tightly constrained by these two experimental searches, whose results are summarized in [10].

5. Neutrino Kinematics

Oscillations are very sensitive to unconventional effects producing neutrino mixing due to their interferometric nature. There are, however, terms in the Hamiltonian (2) that are unobservable in oscillations. Neutrino oscillations only allow us to measure energy differences between different neutrino states; for this reason, the absolute scale of neutrino masses cannot be determined from oscillations. Similarly, some coefficients for Lorentz violation modify the energy of all flavors in the same way producing no effects in oscillations. Neglecting mixing effects results in a decoupling of the three-flavor system into three copies of a single state. One of the observable effects of these *oscillation-free* coefficients is the modification of the neutrino velocity, which produces measurable effects in the neutrino time of flight. Moreover, as a consequence of the unconventional dispersion relations,
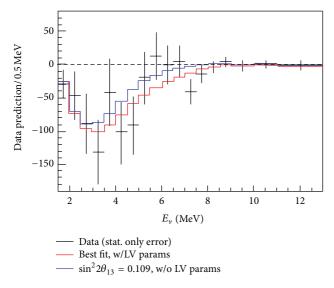
FIGURE 2: Fit to the disappearance of reactor antineutrinos in the form $\bar{\nu}_e \rightarrow \nu_e$ due to neutrino-antineutrino mixing (red line) and the conventional oscillation in the absence of Lorentz violation (blue line) in the Double Chooz experiment. Figure adapted from [27].

the neutrino phase space and energy-conservation condition relevant for decay processes are modified as well.

5.1. Neutrino Velocity. The neutrino velocity can be obtained from the Hamiltonian (2). For completeness, operators of arbitrary dimension d can be incorporated, in which case the neutrino velocity takes the form [35]

$$v_\nu = 1 - \frac{|m|^2}{2|\mathbf{p}|^2} + \sum_{djm} (d-3) |\mathbf{p}|^{d-4} e^{im\omega_\oplus T_\oplus} {}_0\mathcal{N}_{jm}$$

$$\times \left(\left(a_{\text{of}}^{(d)} \right)_{jm} - \left(c_{\text{of}}^{(d)} \right)_{jm} \right),$$

(11)

where the factor $|m|^2$ is a real mass parameter that does not participate in oscillations, and the Lorentz-violating component has been written in spherical form. The index d denotes the effective dimension of the operator and the pair jm corresponds to angular momentum indices that label the rotational properties of the oscillation-free spherical coefficients $(a_{\text{of}}^{(d)})_{jm}$ and $(c_{\text{of}}^{(d)})_{jm}$, controlling CPT-odd (for odd d) and CPT-even (for even d) effects, respectively. These spherical coefficients can be identified with coefficients in Cartesian coordinates used in the previous sections [35]. The expression for the neutrino velocity (11) has been written in the Sun-centered frame [10, 32], where all the directional information is contained in the angular factors ${}_0\mathcal{N}_{jm}$ and the sidereal time dependence appears as harmonics functions controlled by the index m.

The neutrino velocity (11) exhibits a rich phenomenology in the form of many physical effects that can affect neutrino propagation if deviations from Lorentz symmetry are present. Depending on the dimension d of the operator in the theory, neutrino velocity can be energy dependent; for $j \neq 0$, anisotropic effects appear and the velocity becomes

a function of the direction of propagation; for $m \neq 0$, time dependence arises, in which case the neutrino velocity varies with sidereal time $T_\oplus$; and for odd d, CPT violation makes neutrinos and antineutrinos move at different speed.

Beam experiments are suitable setups to compare the speed of neutrinos with respect to the speed of photons. From the neutrino velocity (11), we clearly find that the mass term makes neutrinos travel slower than light, whereas the coefficients for Lorentz violation can generate subluminal or superluminal velocities depending on the sign of each coefficient. Different beam experiments have measured the time for neutrinos to travel a distance L [58–64], which will experience a delay with respect to photons given by the following:

$$\Delta t \approx L \left(1 - v_\nu \right), \tag{12}$$

which can be used to set limits in the oscillation-free coefficients for Lorentz violation that modify the neutrino velocity in (11). Since the minute effects of Lorentz violation can be enhanced by neutrinos travelling a long distance, a precise constraint on the isotropic dimension-four coefficient was obtained using the few antineutrino events from the supernova SN1987A [65].

For the particular case of Lorentz invariance violation generated by a dimension-four operator, the modification to the neutrino velocity (11) is simply a constant factor. For operators of dimension $d \geq 5$, low- and high-energy neutrinos will move at different velocity. If a burst of neutrinos of different energies is created at the same time, this velocity difference will generate a spread of neutrinos, observable as a delay between high- and low-energy neutrinos at the detector [35]. A similar effect has been widely studied for Lorentz-violating photons [66–69].

5.2. Threshold Effects. The modified dispersion relations that neutrinos satisfy in the presence of Lorentz violation alter the energy-momentum conservation relation, which plays an important role in meson-decay processes of the form $M^+ \rightarrow l^+ + \nu_l$. It can be shown that above some threshold energy E_{th} these relations can completely block the phase space available for the decay [35, 70–78]. The observation of atmospheric and accelerator neutrinos ν_l with energy E_0 produced by the decay of a meson of mass M_M implies that $E_{\text{th}} > E_0$, which can be used to write the condition

$$\sum_{djm} E_0^{d-2} Y_{jm} (\hat{\mathbf{p}}) \left[\pm \left(a_{\text{of}}^{(d)} \right)_{jm} - \left(c_{\text{of}}^{(d)} \right)_{jm} \right] \lesssim \frac{1}{2} \left(M_M - m_{l^\pm} \right)^2,$$

(13)

where the $+$ $(-)$ sign is for neutrinos (antineutrinos) and $m_{l^\pm}$ is the mass of the accompanying charged lepton. This formula has been used in [35] to constrain several coefficients for Lorentz violation, including many associated to nonrenormalizable operators.

The sensitivity to the effects of Lorentz violation increases with the energy of neutrinos observed as well as the distance that they travel. The observation of very-high-energy neutrinos reported by the IceCube collaboration [79, 80] offers
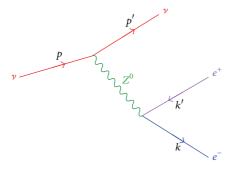
FIGURE 3: Electron-positron pair emission as neutrino Čerenkov radiation.

a great sensitivity to the effects described in this section. The small number of neutrinos observed with energies at the PeV level [79] allows the study of isotropic effects ($j = 0$); nevertheless, a full study of direction-dependent effects would require several events spread in the sky. Although the IceCube results suggest an astrophysical origin for these energetic neutrinos, tight constraints on different coefficients for Lorentz violation can be obtained even in the conservative interpretation of these neutrino events having atmospheric origin [81]. The observation of PeV neutrinos created by the decay of heavy mesons in the upper atmosphere has been used to implement the threshold condition (13), leading to sensitive limits in several isotropic coefficients of dimension $d = 4, 6, 8$ and 10 [81].

5.3. Čerenkov Radiation. In same way as some processes can be forbidden above certain energies, the effects of Lorentz violation can also open particular decay channels that would be otherwise forbidden. In particular, coefficients leading to $v_\nu > 1$ in (11) can produce Čerenkov emission of one or more particles [35, 82–92]. Čerenkov radiation makes neutrinos lose energy, which distorts the spectrum in long-baseline experiments using accelerator and atmospheric neutrinos. This feature provides another method to search for Lorentz violation. The observation of high-energy neutrinos after propagating a distance L sets a lower value for the characteristic distortion distance $D(E) = -E/(dE/dx)$ in the form $L < D(E)$. The determination of the characteristic distance for the spectral distortion caused by the isotropic Lorentz-violating operator of dimension four $(c_{of}^{(4)})_{00}$ is described in [82–92]. The general calculation including direction-dependent effects for operators of arbitrary dimension can be found in [35].

Using the PeV neutrinos observed by IceCube [79], the limits obtained using threshold conditions can be improved by one order of magnitude by determining spectral distortion produced by Čerenkov radiation [81]. For instance, the emission of electron-positron pairs in the form $\nu \rightarrow \nu + e^- + e^+$ is characterized by a rate of energy loss given by [35, 81]

$$\frac{dE}{dx} = -\frac{C}{8} \int \frac{\kappa^0 \boldsymbol{\kappa'}^2}{\left(\kappa^2 - M_Z^2\right)^2} \frac{\partial \left|\boldsymbol{\kappa'}\right|}{\partial \kappa_0} \frac{q \cdot k q' \cdot k'}{q_0 k_0 q_0' k_0'} d^3 p' d\Omega_{\kappa'}, \quad (14)$$

where C is a constant, the auxiliary 4 vectors $\kappa = k + k'$ and $\kappa' = k - k'$ have been defined in terms of the momentum of the electron and the positron, and $q/q_0 = (1, \hat{\mathbf{p}})$, $q'/q_0' = (1, \hat{\mathbf{p}}')$, following the conventions in Figure 3. Several orders of magnitude in sensitivity can be gained when using an astrophysical interpretation for the PeV neutrinos in IceCube. After travelling astrophysical distances these neutrinos would rapidly fall below the threshold energy for Čerenkov emission. The observation of these neutrinos with PeV energies implies that this threshold energy lies above 1 PeV, leading to stringent limits on isotropic Lorentz violation of dimension $d = 4, 6, 8$, and 10 [81]. Similar studies for the case $d = 4$ can be found in [93, 94].

Direction-dependent effects using high-energy neutrinos require several events. The recent observation of 26 new energetic events in IceCube [80] distributed in the sky allows the search of space anisotropy for operators of dimension $d = 4, 6$ [81]. The simultaneous study of several coefficients producing direction-dependent effects allows two-sided bounds, more restrictive than the very particular case of isotropic Lorentz violation considering superluminal velocity that allows one-sided limits only. In the future, the observation of more events should allow a detailed study of operators of higher dimension.

6. Beta Decay

The interferometric nature of neutrino oscillations makes them an ideal type of experiment to search for minute deviations from exact Lorentz symmetry. Nonetheless, the effects that modify the kinematics of all neutrino flavors in the same manner are unobservable in oscillation experiments, which makes the studies described in Section 5 an important complement to oscillation searches. The enhancement of Lorentz-violating effects with the neutrino energy makes also the study of neutrino velocity and Čerenkov radiation a sensitive probe of Lorentz invariance with high-energy neutrinos. Nevertheless, it has been shown that low-energy experiments can also play a key role in the study of Lorentz invariance. In particular, signals of oscillation-free operators of dimension three $(a_{of}^{(3)})_{jm}$ are not only unobservable in oscillations but also produce no effects in the neutrino velocity (11).

The experimental signatures of the coefficients associated with these so-called *countershaded* operators [16, 95, 96] motivate the study of weak decays. The effects of these operators are unaffected by the neutrino energy, giving low-energy experiments a competitive sensitivity to signals of Lorentz violation. It is important to emphasize that Lorentz-violating effects appear as kinematical effects modifying the neutrino phase space; nevertheless, modifications of the spinor solutions must also be taken into account. Beta decay in the context of Lorentz violation in sectors other than neutrinos has recently been studied theoretically [97, 98] and experimentally [99].

6.1. Tritium Decay. The absolute mass scale of neutrinos cannot be studied in oscillation experiments, which only offer

access to mass-squared differences. The direct measurement of neutrino masses can be made by searching for a distortion of the electron energy spectrum in tritium decay. The measurement of beta electrons near the endpoint of the spectrum

$$\frac{d\Gamma}{dT} = C\left[(\Delta T)^2 - \frac{1}{2}m_\nu^2\right], \tag{15}$$

allows the study of the effective mass m_ν^2 of electron antineutrinos, where C is approximately constant and $\Delta T = T - T_0$ denotes the kinetic energy of the electron T measured from the endpoint energy T_0. This type of experimental measurements has been made by Troitsk [100] and Mainz [101], and high precision will be achieved by KATRIN [102].

In these experiments the antineutrino escapes undetected; however, magnetic fields select the beta electrons emitted in a particular direction to be studied. This feature permits the study of anisotropic effects. In the presence of Lorentz-violating neutrinos, the spectrum (15) gets corrected by the replacement

$$\Delta T \longrightarrow \Delta T + \left(k_{\mathscr{C}}^{(3)}\right) + \left(k_{\mathscr{A}_s}^{(3)}\right)\sin\omega_\oplus T_\oplus$$
$$+ \left(k_{\mathscr{A}_c}^{(3)}\right)\cos\omega_\oplus T_\oplus, \tag{16}$$

which shows that the distortion near the endpoint can be shifted and also exhibits a sidereal-time dependence. The amplitudes in the modification (16) depend on the four independent coefficients $(a_{of}^{(3)})_{00}$, $(a_{of}^{(3)})_{10}$, $(a_{of}^{(3)})_{11}$, and $(a_{of}^{(3)})_{1-1}$ and experimental quantities such as location of the laboratory, orientation of the apparatus, and intensity of the magnetic fields used to select the beta electrons for their analysis [96].

An interesting feature appears when the effective coefficients $(c_{of}^{(2)})_{1m}$ are considered, which arise as a consequence of neutrino mass and CPT-even Lorenz violation [35]. These coefficients can mimic the effects of a mass parameter, in which case the spectrum (15) gets modified in the form

$$m_\nu^2 \longrightarrow m^2 = m_\nu^2 + \left(k_{\mathscr{C}}^{(2)}\right) + \left(k_{\mathscr{A}_s}^{(2)}\right)\sin\omega_\oplus T_\oplus$$
$$+ \left(k_{\mathscr{A}_c}^{(2)}\right)\cos\omega_\oplus T_\oplus. \tag{17}$$

We find that the experimental mass-squared parameter m^2 involves the actual neutrino mass m_ν; however, the mass can be screened by the effects of the three coefficients $(c_{of}^{(2)})_{1m}$ ($m = 0, \pm 1$), varying with sidereal time and depending on the orientation of the apparatus. Notice also that the sign of the experimental mass-squared parameter m^2 is not restricted to be positive, so the coefficients $(c_{of}^{(2)})_{1m}$ could even mimic a tachyonic neutrino [103].

Alternative approaches have been considered to search for isotropic Lorentz violation in tritium decay for other operators in [104, 105].

6.2. Neutron Decay. Neutrons are fascinating laboratories to study the validity of fundamental symmetries. The effects of deviations from exact Lorentz invariance would affect the

spectrum of the beta electrons as well as the measurements of particular experimental asymmetries. Contrary to tritium decay experiments, the study of neutron decay covers the whole energy spectrum, which takes the form of the spectrum (15) neglecting the neutrino mass that plays no role far from the endpoint and the factor C can no longer be approximated by a constant so it becomes a function of the electron energy. For experiments only counting the number of beta electrons per energy range, all the anisotropic effects disappear after integrating over all the neutrino orientations. The net effect is a distortion of the whole spectrum that can be studied by searching for deviations from the conventional spectrum. The residual spectrum is proportional to the coefficient $(a_{of}^{(3)})_{00}$ [96].

Anisotropic effects can be studied by constructing asymmetries $\mathbf{A}_{exp}$ in experiments that can determine the directionality of some of the decay products. For experiments using unpolarized neutrons, an asymmetry counting electrons emitted in the same direction as the antineutrino N_+ compared to events in which the two leptons are emitted in opposite directions N_- can be constructed for the measurement of the electron-antineutrino correlation a in the form of

$$a_{exp} = \frac{N_+ - N_-}{N_+ + N_-}. \tag{18}$$

Similarly, experiments using polarized neutrons that are able to measure the electron and the recoiling proton can be used to search for electron-proton coincidence events, useful for the measurement of the neutrino asymmetry B. As shown in Figure 4, the experimental asymmetry counts events in which proton and electron are emitted against N_{--} or along N_{++}; the direction of the neutron polarization $\hat{\mathbf{n}}$ can be written in the form

$$B_{exp} = \frac{N_{--} - N_{++}}{N_{--} + N_{++}}. \tag{19}$$

Effects of Lorentz violation arise from the modified spinor solutions that affect the matrix element of the decay as well as the unconventional form of the neutrino phase space due to the modified dispersion relations, making the asymmetries (18) and (19) have the general form [96]

$$\mathbf{A}_{exp} = \left(\mathbf{A}_{\mathscr{C}}\right) + \left(\mathbf{A}_{\mathscr{A}_s}\right)\sin\omega_\oplus T_\oplus + \left(\mathbf{A}_{\mathscr{A}_c}\right)\cos\omega_\oplus T_\oplus, \tag{20}$$

where the amplitudes depend on the coefficients for Lorentz violation $(a_{of}^{(3)})_{10}$, $(a_{of}^{(3)})_{11}$, and $(a_{of}^{(3)})_{1-1}$ and experimental quantities including the orientation and location of the apparatus.

6.3. Double Beta Decay. The same coefficients modifying the spectrum for beta decay can also introduce observable effects in double beta decay experiments. Since the antineutrinos escape unobserved, the simplest test of Lorentz invariance is an alteration of the two-electron spectrum for the two-neutrino mode of double beta decay produced by the coefficient $(a_{of}^{(3)})_{00}$ [96, 106]. Similar to the neutron-decay
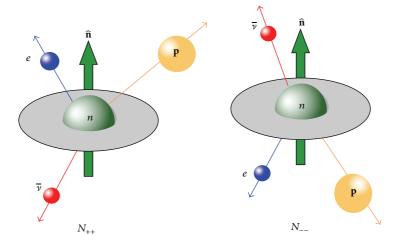
FIGURE 4: Electron-proton coincidence events for the asymmetry B_{exp}. The polarization of the neutron is denoted by $\hat{\mathbf{n}}$.

spectrum, the resulting effect is a distortion of the whole spectrum that can be studied by searching for deviations from the conventional spectrum. The energy at which this effect is maximal has been identified for several isotopes, which will guide these types of studies [106].

The neutrinoless mode of double beta decay offers access to other type of coefficient, one that modifies the neutrino propagator. This Majorana coupling in the SME denoted $|g_{\beta\beta}^{\lambda\rho}|$ is a combination of other coefficients in the SME that can trigger neutrinoless double beta decay even if the Majorana mass is negligible. In terms of this effective coefficient for CPT-odd Lorentz violation, the half-life of an isotope of radius R is given by [106]

$$\left(T_{1/2}^{0\nu}\right)^{-1} = G^{0\nu}\left|M^{0\nu}\right|^2 \frac{\left|g_{\beta\beta}^{\lambda\rho}\right|^2}{4R^2}, \tag{21}$$

where $G^{0\nu}$ is the phase-space factor regarding the two emitted electrons and $M^{0\nu}$ is the relevant nuclear matrix element. Limits on the Majorana mass parameter $|m_{\beta\beta}|$ can be used to constrain the coefficient $|g_{\beta\beta}^{\lambda\rho}|$. Since the Lorentz-violating neutrinoless double beta decay depends on the nuclear size R of the isotope used, a future observation of this decay mode can be distinguished because the Majorana-mass mechanism depends on the isotope only through the nuclear matrix elements.

7. Conclusions

In this paper we have presented a general overview of the effects of deviations from exact Lorentz invariance in neutrinos in the context of the Standard-Model Extension. In general, the signatures of the breakdown of Lorentz symmetry are direction and time dependence of the relevant observables for Earth-based experiments as well as unconventional dependence on the neutrino energy. Neutrino oscillations are

sensitive probes of new physics, which makes this type of experiment an ideal setup to search for violations of Lorentz invariance. In oscillations, some effects of Lorentz violation include direction and time dependence of the oscillation probability, oscillation phases that grow with the neutrino energy, CPT violation, and mixing between neutrinos and antineutrinos.

Some effects are unobservable in neutrino oscillations, in which case kinematical effects become a complementary technique. Effects of Lorentz violation appear as modifications to the neutrino velocity as well as unconventional behavior in decay processes. In particular, some decays with neutrinos in the final state can become forbidden above certain threshold energy; similarly, some forbidden processes can become allowed, including Čerenkov radiation of one or more particles. Most of these effects are enhanced by the neutrino energy, which makes high-energy neutrinos of particular interest for future tests of Lorentz invariance.

Finally, there are operators in the theory whose experimental signatures are independent of the neutrino energy. In this case, the high precision of low-energy experiments can play a fundamental role in the test of Lorentz symmetry for some particular operators that are unobservable in oscillations and that leave the neutrino velocity unchanged. For these countershaded operators, beta decay is the ideal experimental setup. Depending on the properties of the experiment, the main features have been identified for studies of tritium decay, neutron decay, and double beta decay.

To date, there is no compelling evidence of Lorentz violation; nevertheless, only a few of the experimental signatures have been studied [10]. Neutrinos offer great sensitivity and numerous ways to test the validity of the cornerstone of modern physics. Many of the different techniques presented in this review are currently being implemented by a variety of experimental collaborations. Interesting new tests of Lorentz symmetry will be performed in the near future, in which low- and high-energy neutrinos will play a key role in our understanding of the nature of spacetime.

Conflict of Interests

The author declares that there is no conflict of interests regarding the publication of this paper.

Acknowledgments

References

[1] W. Pauli, Offener Brief an die Gruppe der Radioaktiven bei der Gauvereins-Tagung zu Tübingen, 1930.

[2] V. A. Kostelecký and S. Samuel, "Spontaneous breaking of Lorentz symmetry in string theory," *Physical Review D*, vol. 39, article 683, 1989.

[3] D. Colladay and V. A. Kostelecký, "CPT violation and the standard model," *Physical Review D*, vol. 55, no. 11, pp. 6760–6774, 1997.

[4] H. B. Nielsen and I. Picek, "The Rédei-like model and testing Lorentz invariance," *Physics Letters B*, vol. 114, no. 2-3, pp. 141–146, 1982.

[5] H. B. Nielsen and I. Picek, "Lorentz non-invariance," *Nuclear Physics B*, vol. 211, no. 2, pp. 269–296, 1983.

[6] R. Huerta and J. L. Lucio M., "Testing Lorentz invariance in baryon decay," *Physics Letters B*, vol. 131, no. 4–6, pp. 471–473, 1983.

[7] R. Huerta-Quintanilla and J. L. Lucio M., "Constraint on Lorentz non-invariance from the Michel parameter," *Physics Letters B*, vol. 124, no. 5, pp. 369–370, 1983.

[8] D. Colladay and V. A. Kostelecký, "Lorentz-violating extension of the standard model," *Physical Review D*, vol. 58, no. 11, Article ID 116002, 1998.

[9] V. A. Kostelecký, "Gravity, Lorentz violation, and the standard model," *Physical Review D*, vol. 69, Article ID 105009, 2004.

[10] V. A. Kostelecký and N. Russell, "Data tables for Lorentz and CPT violation," *Reviews of Modern Physics*, vol. 83, article 11, 2011.

[11] V. A. Kostelecký and S. Samuel, "Phenomenological gravitational constraints on strings and higher-dimensional theories," *Physical Review Letters*, vol. 63, article 224, 1989.

[12] V. A. Kostelecký and R. Potting, "Gravity from local Lorentz violation," *General Relativity and Gravitation*, vol. 37, no. 10, pp. 1675–1679, 2005.

[13] R. Bluhm and V. A. Kostelecký, "Spontaneous Lorentz violation, Nambu-Goldstone modes, and gravity," *Physical Review D*, vol. 71, Article ID 065008, 2005.

[14] O. Bertolami and J. Páramos, "Vacuum solutions of a gravity model with vector-induced spontaneous Lorentz symmetry breaking," *Physical Review D*, vol. 72, no. 4, Article ID 044001, 2005.

[15] N. Arkani-Hamed, H. C. Cheng, M. Luty, and J. Thaler, "Universal dynamics of spontaneous Lorentz violation and a new spin-dependent inverse-square law force," *Journal of High Energy Physics*, vol. 7, article 029, 2005.

[16] V. A. Kostelecký and J. D. Tasson, "Prospects for large relativity violations in matter-gravity couplings," *Physical Review Letters*, vol. 102, no. 1, Article ID 010402, 2009.

[17] O. W. Greenberg, "CPT violation implies violation of Lorentz invariance," *Physical Review Letters*, vol. 89, no. 23, Article ID 231602, 2002.

[18] J. Ellis and N. E. Mavromatos, "Comments on CP, T and CPT violation in neutral kaon decays," *Physics Report*, vol. 320, no. 1–6, pp. 341–354, 1999.

[19] F. R. Klinkhamer, "A CPT anomaly," *Nuclear Physics B*, vol. 578, no. 1-2, pp. 277–289, 2000.

[20] C. Adam and F. R. Klinkhamer, "Causality and CPT violation from an Abelian Chern-Simons-like term," *Nuclear Physics B*, vol. 607, no. 1-2, pp. 247–267, 2001.

[21] G. Barenboim, L. Borissov, J. Lykken, and A. Y. Smirnov, "Neutrinos as the messengers of CPT violation," *Journal of High Energy Physics*, vol. 10, article 001, 2002.

[22] G. Barenboim, J. F. Beacom, L. Borissov, and B. Kayser, "CPT violation and the nature of neutrinos," *Physics Letters B*, vol. 537, no. 3-4, pp. 227–232, 2002.

[23] F. R. Klinkhamer and C. Rupp, "Spacetime foam, CPT anomaly, and photon propagation," *Physical Review D*, vol. 70, no. 4, Article ID 045020, 2004.

[24] N. E. Mavromatos, "CPT violation and decoherence in quantum gravity," in *Planck Scale Effects in Astrophysics and Cosmology*, vol. 669 of *Planck Scale Effects in Astrophysics and Cosmology*, pp. 245–320, 2005.

[25] M. Chaichian, A. D. Dolgov, V. A. Novikov, and A. Tureanu, "CPT violation does not lead to violation of Lorentz invariance and vice versa," *Physics Letters B*, vol. 699, no. 3, pp. 177–180, 2011.

[26] P. Adamson, D. J. Auty, MINOS Collaboration et al., "Search for Lorentz invariance and CPT violation with the MINOS far detector," *Physical Review Letters*, vol. 105, Article ID 151601, 2010.

[27] J. S. Díaz, T. Katori, J. Spitz, and J. M. Conrad, "Search for neutrino–antineutrino oscillations with a reactor experiment," *Physics Letters B*, vol. 727, no. 4-5, pp. 412–416, 2013.

[28] V. A. Kostelecký and M. Mewes, "Lorentz and CPT violation in neutrinos," *Physical Review D*, vol. 69, Article ID 016005, 2004.

[29] Z. Maki, M. Nakagawa, and S. Sakata, "Remarks on the unified model of elementary particles," *Progress of Theoretical Physics*, vol. 28, no. 5, pp. 870–880, 1962.

[30] B. Pontecorvo, "Neutrino experiments and the problem of conservation of leptonic charge," *Journal of Experimental and Theoretical Physics*, vol. 53, pp. 1717–1725, 1967.

[31] B. Pontecorvo, "Neutrino experiments and the question of leptonic-charge conservation," *Soviet Physics—JETP*, vol. 26, pp. 984–988, 1968.

[32] R. Bluhm, V. A. Kostelecký, C. D. Lane, and N. Russell, "Clock-comparison tests of Lorentz and CPT symmetry in space," *Physical Review Letters*, vol. 88, Article ID 090801, 2002.

[33] V. A. Kostelecký and M. Mewes, "Lorentz violation and short-baseline neutrino experiments," *Physical Review D*, vol. 70, Article ID 076002, 2004.

[34] J. S. Díaz, V. A. Kostelecký, and M. Mewes, "Perturbative Lorentz and CPT violation for neutrino and antineutrino oscillations," *Physical Review D*, vol. 80, Article ID 076007, 2009.

[35] V. A. Kostelecký and M. Mewes, "Neutrinos with Lorentz-violating operators of arbitrary dimension," *Physical Review D*, vol. 85, Article ID 096005, 2012.

[36] V. A. Kostelecký and M. Mewes, "Fermions with Lorentz-violating operators of arbitrary dimension," *Physical Review D*, vol. 88, Article ID 096006, 2013.

[37] A. Aguilar-Arevalo, L. B. Auerbach, and LSND Collaboration, "Evidence for neutrino oscillations from the observation of $\overline{\nu}_e$ appearance in a $\overline{\nu}_\mu$ beam," *Physical Review D*, vol. 64, Article ID 112007, 2001.

[38] A. A. Aguilar-Arevalo, A. O. Bazarko, MiniBooNE Collaboration et al., "Search for Electron Neutrino Appearance at the $\triangle m^2 \sim 1eV^2$ Scale," *Physical Review Letters*, vol. 98, Article ID 231801, 2007.

[39] A. A. Aguilar-Arevalo, C. E. Anderson, MiniBooNE Collaboration et al., "Unexplained excess of electronlike events from a 1-GeV neutrino beam," *Physical Review Letters*, vol. 102, Article ID 101802, 2009.

[40] V. A. Kostelecký and M. Mewes, "Lorentz and CPT violation in the neutrino sector," *Physical Review D*, vol. 70, Article ID 031902, 2004.

[41] T. Katori, V. A. Kostelecký, and R. Tayloe, "Global three-parameter model for neutrino oscillations using Lorentz violation," *Physical Review D*, vol. 74, Article ID 105009, 2006.

[42] V. Barger, D. Marfatia, and K. Whisnant, "Challenging Lorentz noninvariant neutrino oscillations without neutrino masses," *Physics Letters B*, vol. 653, no. 2–4, pp. 267–277, 2007.

[43] V. Barger, J. Liao, D. Marfatia, and K. Whisnant, "Lorentz noninvariant oscillations of massless neutrinos are excluded," *Physical Review D*, vol. 84, no. 5, Article ID 056014, 2011.

[44] J. S. Díaz and V. A. Kostelecký, "Three-parameter Lorentz-violating texture for neutrino mixing," *Physics Letters B*, vol. 700, no. 1, pp. 25–28, 2011.

[45] J. S. Díaz and V. A. Kostelecký, "Lorentz- and CPT-violating models for neutrino oscillations," *Physical Review D*, vol. 85, Article ID 016013, 2012.

[46] S. J. Rong and Q. Y. Liu, "The perturbed puma model," *Chinese Physics Letters*, vol. 29, no. 4, Article ID 041402, 2012.

[47] J. Beringer, J. F. Arguin, Particle Data Group et al., "Review of Particle Physics," *Physical Review D*, vol. 86, Article ID 010001, 2012.

[48] T. Akiri and Super-Kamiokande Collaboration, "Sensitivity of atmospheric neutrinos in Super-Kamiokande to Lorentz violation," *High Energy Physics-Phenomenology*, http://arxiv.org/abs/1308.2210.

[49] J. S. Díaz, IUHET-585.

[50] Y. Abe, C. Aberle, Double Chooz Collaboration et al., "First test of Lorentz violation with a reactor-based antineutrino experiment," *Physical Review D*, vol. 86, Article ID 112009, 2012.

[51] R. Abbasi, Y. Abdou, IceCube Collaboration et al., "Search for a Lorentz-violating sidereal signal with atmospheric neutrinos in IceCube," *Physical Review D*, vol. 82, Article ID 112003, 2010.

[52] L. B. Auerbach, R. L. Burman, LSND Collaboration et al., "Tests of Lorentz violation in $\overline{\nu}_\mu \rightarrow \overline{\nu}_e$ oscillations," *Physical Review D*, vol. 72, Article ID 076004, 2005.

[53] A. A. Aguilar-Arevalo, C. E. Anderson, MiniBooNE Collaboration et al., "Test of Lorentz and CPT violation with short baseline neutrino oscillation excesses," *Physics Letters B*, vol. 718, no. 4–5, pp. 1303–1308, 2013.

[54] T. Katori, "Tests of lorentz and cpt violation with MiniBooNE neutrino oscillation excesses," *Modern Physics Letters A*, vol. 27, no. 25, Article ID 1230024, 2012.

[55] P. Adamson et al., "Testing Lorentz invariance and CPT conservation with NuMI neutrinos in the MINOS near detector," *Physical Review Letters*, vol. 101, Article ID 151601, 2008.

[56] P. Adamson, D. S. Ayres, The MINOS Collaboration et al., "Search for Lorentz invariance and CPT violation with muon antineutrinos in the MINOS near detector," *Physical Review D*, vol. 85, Article ID 031101, 2012.

[57] B. Rebel and S. Mufson, "The search for neutrino–antineutrino mixing resulting from Lorentz invariance violation using neutrino interactions in MINOS," *Astroparticle Physics*, vol. 48, pp. 78–81, 2013.

[58] J. Alspector, G. R. Kalbfleisch, N. Baggett et al., "Experimental comparison of neutrino and muon velocities," *Physical Review Letters*, vol. 36, no. 15, pp. 837–840, 1976.

[59] G. R. Kalbfleisch, N. Baggett, E. C. Fowler, and J. Alspector, "Experimental comparison of neutrino, antineutrino, and muon velocities," *Physical Review Letters*, vol. 43, no. 19, pp. 1361–1364, 1979.

[60] P. Adamson, C. Andreopoulos, MINOS Collaboration et al., "Measurement of neutrino velocity with the MINOS detectors and NuMI neutrino beam," *Physical Review D*, vol. 76, Article ID 072005, 2007.

[61] T. Adam, N. Agafonova, OPERA Collaboration et al., "Measurement of the neutrino velocity with the OPERA detector in the CNGS beam," *Journal of High Energy Physics*, vol. 2012, p. 93, 2012.

[62] M. Antonello, P. Aprili, ICARUS Collaboration et al., "Measurement of the neutrino velocity with the ICARUS detector at the CNGS beam," *Physics Letters B*, vol. 713, no. 1, pp. 17–22, 2012.

[63] P. Alvarez Sanchez, R. Barzaghi, Borexino Collaboration et al., "Measurement of CNGS muon neutrino speed with Borexino," *Physics Letters B*, vol. 716, pp. 401–405, 2012.

[64] N. Y. Agafonova, M. Aglietta, LVD Collaboration et al., "Measurement of the velocity of neutrinos from the CNGS beam with the large volume detector," *Physical Review Letters*, vol. 109, Article ID 070801, 2012.

[65] M. J. Longo, "Tests of relativity from SN1987A," *Physical Review D*, vol. 36, no. 10, pp. 3276–3277, 1987.

[66] V. A. Kostelecký and M. Mewes, "Lorentz-violating electrodynamics and the cosmic microwave background," *Physical Review Letters*, vol. 99, Article ID 011601, 2007.

[67] V. A. Kostelecký and M. Mewes, "Astrophysical tests of Lorentz and CPT violation with photons," *The Astrophysical Journal Letters*, vol. 689, no. 1, article L1, 2008.

[68] V. A. Kostelecký and M. Mewes, "Electrodynamics with Lorentz-violating operators of arbitrary dimension ," *Physical Review D*, vol. 80, Article ID 015020, 2009.

[69] V. Vasileiou, A. Jacholkowska, F. Piron et al., "Constraints on Lorentz invariance violation from Fermi-Large Area Telescope observations of gamma-ray bursts," *Physical Review D*, vol. 87, no. 12, Article ID 122001, 2013.

[70] B. Altschul, "Consequences of neutrino Lorentz violation for leptonic meson decays," *Physical Review D*, vol. 84, Article ID 091902, 2011.

[71] A. Chodos, V. A. Kostelecký, R. Potting, and E. Gates, "Null experiments for neutrino masses," *Modern Physics Letters A*, vol. 7, no. 6, article 467, 1992.

[72] A. Chodos and V. A. Kostelecký, "Nuclear null tests for spacelike neutrinos," *Physics Letters B*, vol. 336, no. 3-4, pp. 295–302, 1994.

[73] V. A. Kostelecký, "Mass bounds for spacelike neutrinos," in *Topics in Quantum Gravity and Beyond: Essays in Honor of Louis Witten*, F. Mansouri and J. J. Scanio, Eds., p. 369, World Scientific, Singapore, 1993.

[74] L. Gonzalez-Mestres, "Astrophysical consequences of the OPERA superluminal neutrino," *General Physics*, http://arxiv.org/abs/1109.6630.

[75] X. J. Bi, P. F. Yin, Z. H. Yu, and Q. Yuan, "Constraints and tests of the OPERA superluminal neutrinos," *Physical Review Letters*, vol. 107, Article ID 241802, 2011.

[76] R. Cowsik, S. Nussinov, and U. Sarkar, "Superluminal nutrinos at OPERA confront pion decay kinematics," *Physical Review Letters*, vol. 107, no. 25, Article ID 251801, 2011.

[77] M. Mannarelli, M. Mitra, F. L. Villante, and F. Vissani, "Non-standard neutrino propagation and pion decay," *Journal of High Energy Physics*, vol. 2012, no. 1, article 136, 2012.

[78] V. Baccetti, K. Tate, and M. Visser, "Lorentz violating kinematics: threshold theorems," *Journal of High Energy Physics* , vol. 2012, article 87, 2012.

[79] M. G. Aartsen et al., "First observation of PeV-energy neutrinos with iceCube," *Physical Review Letters*, vol. 111, Article ID 021103, 2013.

[80] M. G. Aartsen et al., "Evidence for high-energy extraterrestrial neutrinos at the icecube detector," *Science*, vol. 342, no. 6161, Article ID 1242856, 2013.

[81] J. S. Díaz, V. A. Kostelecký, and M. Mewes, "Testing relativity with high-energy astrophysical neutrinos," *Physical Review D*, vol. 89, Article ID 043005, 2014.

[82] S. R. Coleman and S. L. Glashow, "High-energy tests of Lorentz invariance," *Physical Review D*, vol. 59, Article ID 116008, 1999.

[83] D. Mattingly, T. Jacobson, and S. Liberati, "Threshold configurations in the presence of Lorentz violating dispersion relations," *Physical Review D*, vol. 67, no. 12, Article ID 124012, 2003.

[84] D. M. Mattingly, L. MacCione, M. Galaverni, S. Liberati, and G. Sigl, "Possible cosmogenic neutrino constraints on Planck-scale Lorentz violation," *Journal of Cosmology and Astroparticle Physics*, vol. 2010, no. 2, article 007, 2010.

[85] J. Alexandre, J. Ellis, and N. E. Mavromatos, "On the possibility of superluminal neutrino propagation," *Physics Letters B*, vol. 706, no. 4-5, pp. 456–461, 2012.

[86] A. G. Cohen and S. L. Glashow, "Pair creation constrains superluminal neutrino propagation," *Physical Review Letters*, vol. 107, no. 18, Article ID 181803, 2011.

[87] J. M. Carmona and J. L. Cortes, "Constraints from neutrino decay on superluminal velocities," *High Energy Physics*, http://arxiv.org/abs/1110.0430.

[88] L. Maccione, S. Liberati, and D. M. Mattingly, "Violations of Lorentz invariance in the neutrino sector: an improved analysis of anomalous threshold constraints," *Journal of Cosmology and Astroparticle Physics*, vol. 2013, no. 3, article 039, 2013.

[89] S. Mohanty and S. Rao, "Constraint on super-luminal neutrinos from vacuum Cerenkov processes," *High Energy Physics*, http://arxiv.org/abs/1111.2725.

[90] M. Li, D. Liu, J. Meng, T. Wang, and L. Zhou, "Replaying neutrino bremsstrahlung with general dispersion relations," *High Energy Physics*, http://arxiv.org/abs/1111.3294.

[91] Y. Huo, T. Li, Y. Liao, D. V. Nanopoulos, and Y. Qi, "Constraints on neutrino velocities revisited," *Physical Review D*, vol. 85, no. 3, Article ID 034022, 2012.

[92] S. J. Brodsky and S. Gardner, "Pair production constraints on superluminal neutrinos revisited," *High Energy Physics*, http://arxiv.org/abs/1112.1090.

[93] E. Borriello, S. Chakraborty, A. Mirizzi, and P. D. Serpico, "Stringent constraint on neutrino Lorentz invariance violation from the two IceCube PeV neutrinos," *Physical Review D*, vol. 87, no. 11, Article ID 116009, 2013.

[94] F. W. Stecker, "Constraining superluminal electron and neutrino velocities using the 2010 Crab nebula flare and the iceCube PeV neutrino events," *High Energy Physics*, http://arxiv.org/abs/1306.6095.

[95] V. A. Kostelecký and J. D. Tasson, "Matter-gravity couplings and Lorentz violation," *Physical Review D*, vol. 83, Article ID 016013, 2011.

[96] J. S. Díaz et al., "Relativity violations and beta decay," *Physical Review D*, vol. 88, Article ID 071902, 2013.

[97] J. P. Noordmans, H. W. Wilschut, and R. G. E. Timmermans, "Lorentz violation in neutron decay and allowed nuclear beta decay," *Physical Review C*, vol. 87, Article ID 055502, 2013.

[98] B. Altschul, "Contributions to pion decay from Lorentz violation in the weak sector," *Physical Review D*, vol. 88, Article ID 076015, 2013.

[99] S. E. M. Müller, E. A. Dijck, H. Bekker et al., "First test of Lorentz invariance in the weak decay of polarized nuclei," *Physical Review D*, vol. 88, Article ID 071901, 2013.

[100] V. N. Aseev, A. I. Belesev, A. I. Berlev et al., "Upper limit on the electron antineutrino mass from the Troitsk experiment," *Physical Review D*, vol. 84, Article ID 112003, 2011.

[101] C. Kraus, B. Bornschein, L. Bornschein et al., "Final results from phase II of the Mainz neutrino mass searchin tritium β decay," *The European Physical Journal C*, vol. 40, no. 4, pp. 447–468, 2005.

[102] J. Angrik and KATRIN Collaboration, KATRIN design report, FZKA Scientific Report 7090, 2005.

[103] A. Chodos, A. I. Hauser, and V. A. Kostelecký, "The neutrino as a tachyon," *Physics Letters B*, vol. 150, no. 6, pp. 431–435, 1985.

[104] J. M. Carmona and J. L. Cortes, "Testing Lorentz invariance violations in the tritium beta-decay anomaly," *Physics Letters B*, vol. 494, no. 1-2, pp. 75–80, 2000.

[105] A. E. Bernardini and O. Bertolami, "Lorentz violating extension of the standard model and the β-decay endpoint," *Physical Review D*, vol. 77, Article ID 085032, 2008.

[106] J. S. Díaz, "Limits on Lorentz and CPT violation from double beta decay," *Physical Review D*, vol. 89, Article ID 036002, 2014.

Research Article

Constraints on Light Neutrino Parameters Derived from the Study of Neutrinoless Double Beta Decay

Sabin Stoica[1,2] and Andrei Neacsu[1,2]

[1] *Horia Hulubei Foundation, P.O. Box MG-12, Romania*
[2] *Horia Hulubei National Institute of Physics and Nuclear Engineering, P.O. Box MG-6, 077125 Magurele, Bucharest, Romania*

Correspondence should be addressed to Sabin Stoica; stoica@theory.nipne.ro

The study of the neutrinoless double beta ($0\nu\beta\beta$) decay mode can provide us with important information on the neutrino properties, particularly on the electron neutrino absolute mass. In this work we revise the present constraints on the neutrino mass parameters derived from the $0\nu\beta\beta$ decay analysis of the experimentally interesting nuclei. We use the latest results for the phase space factors (PSFs) and nuclear matrix elements (NMEs), as well as for the experimental lifetime limits. For the PSFs we use values computed with an improved method reported very recently. For the NMEs we use values chosen from the literature on a case-by-case basis, taking advantage of the consensus reached by the community on several nuclear ingredients used in their calculation. Thus, we try to restrict the range of spread of the NME values calculated with different methods and, hence, to reduce the uncertainty in deriving limits for the Majorana neutrino mass parameter. Our results may be useful to have an updated image on the present neutrino mass sensitivities associated with $0\nu\beta\beta$ measurements for different isotopes and to better estimate the range of values of the neutrino masses that can be explored in the future double beta decay (DBD) experiments.

1. Introduction

Neutrinoless double beta decay is a beyond standard model (BSM) process by which an even-even nucleus transforms into another even-even nucleus with the emission of two electrons/positrons but no antineutrinos/neutrinos in the final states. Its study is very attractive because it would clarify the question about the lepton number conservation, decide on the neutrinos character (are they Dirac or Majorana particles?), and give a hint on the scale of their absolute masses. Moreover, the study of the $0\nu\beta\beta$ decay has a broader potential to search for other BSM phenomena. The reader can find up-to-date information on these studies from several recent reviews [1–6], which also contain therein a comprehensive list of references in the domain.

The scale of the absolute mass of neutrinos is a key issue for understanding the neutrino properties. It cannot be derived from neutrino oscillation experiments which can only measure the square of the neutrino mass differences between different flavors [7–12]. Analysis of $0\nu\beta\beta$ decay and cosmological data are at present the most sensitive ways to investigate this issue.

The lifetime of the $0\nu\beta\beta$ decay modes can be expressed, in a good approximation, as a product of a phase space factor (depending on the atomic charge and energy released in the decay, $Q_{\beta\beta}$), a nuclear matrix element (related to the nuclear structure of the parent and daughter nuclei), and a lepton number violation (LNV) parameter (related to the BSM mechanism considered). Thus, to extract reliable limits for the LNV parameters we need accurate calculations of both PSFs and NMEs, as well as reliable measurements of the lifetime.

The largest uncertainties in theoretical calculations for DBD are related to the NMEs values. That is why there is a continuous effort in the literature to develop improved nuclear structure methods for their computation. At present, the NMEs are computed by several methods which differ conceptually, the most employed being the proton-neutron quasi-random phase approximation (pnQRPA) [13–20], interacting shell model (ISM) [21–25], interacting

boson approximation (IBA) [26–28], projected Hartree-Fock-Bogoliubov (PHFB) [29, 30], and energy density functional (EDS) method [31]. There are still large differences between the NMEs values computed with different methods and by different groups, and these have been largely discussed in the literature (see, e.g., [2, 3]). On the other side, there is a consensus in the community on the way that several nuclear effects and nuclear parameters should be used in calculations. In this work, we take advantage of this consensus when we chose the NMEs values, trying to restrict their range of spread and, consequently, to reduce the uncertainty in deriving the neutrino Majorana mass parameters.

Unlike the NMEs, the PSFs have been calculated a long time ago [32–39] and were considered to be computed with enough precision. However, recently, they were recalculated within an improved approach, by using exact electron Dirac wave functions (w.f.) taking into account the finite nuclear size and electron screening effects [40]. The authors found differences between their results and those calculated previously with approximate electron w.f., especially for heavier nuclei. We have also independently recalculated the PSFs by developing new routines for computing the relativistic (Dirac) electron w.f. by taking into account the nuclear finite size and screening effects. In addition, we use a Coulomb potential derived from a realistic proton density distribution in the daughter nucleus [41, 42]. In this work we use new PSFs values obtained by improving the numerical precision of our routines as compared with our previous works. The obtained values are very close to those reported in [40, 41].

Finally, for the lifetime limits, we take the most recent results found in the literature.

The paper is organized as follows. In the next section we shortly recall the general formalism for the derivation of the neutrino mass parameters from $0\nu\beta\beta$ decay analysis, highlighting the nuclear ingredients involved in calculations. In Section 3 we discuss the way of choosing the NME values and report our results for the light neutrino Majorana mass parameters, while in Section 4 we formulate the conclusions of our work.

2. Formalism

We shortly present the general formalism for the derivation of neutrino mass parameters from $0\nu\beta\beta$ decay analysis. We start with the lifetime formula and then describe the main steps and ingredients used in the theoretical calculation of their components, that is, PSFs and NMEs.

Assuming that the dominant mechanism of occurrence for the $0\nu\beta\beta$ decay mode is the exchange of Majorana left-handed light neutrinos between two nucleons from the parent nucleus, the lifetime reads

$$\left(T_{1/2}^{0\nu}\right)^{-1} = G^{0\nu}\left(Q_{\beta\beta}, Z\right)\left|M^{0\nu}\right|^2\left(\frac{\langle m_\nu \rangle}{m_e}\right)^2, \quad (1)$$

where $G^{0\nu}$ are the PSFs for this decay mode, depending on the energy decay $Q_{\beta\beta}$ and nuclear charge Z, $M^{0\nu}$ are the corresponding NMEs, depending on the nuclear structure of the parent and daughter nuclei involved in the decay, m_e is

electron mass, and $\langle m_\nu \rangle$ is the light neutrino Majorana mass parameter. This parameter can be expressed as a (coherent) linear combination of the light neutrino masses:

$$\langle m_\nu \rangle = \left|\sum_{k=1}^{3} U_{ek}^2 m_k\right|, \quad (2)$$

where U_{ek} are the elements of the first row in the PMNS (Pontecorvo-Maki-Nakagawa-Sakata) neutrino matrix and m_k are the light neutrino masses [56]. From (1) the expression of m_ν reads

$$\langle m_\nu \rangle = \frac{m_e}{\left|M^{0\nu}\right|\sqrt{T^{0\nu} \cdot G^{0\nu}}}. \quad (3)$$

For deriving $\langle m_\nu \rangle$ we need accurate calculations of both PSFs and NMEs for each isotope for which there are experimental lifetime limits. The PSFs have been calculated a long time ago in some approximations [32–39] and were considered, until recently, to be computed with enough precision. However, they were recalculated recently in [40–42] using more advanced approaches for the numerical evaluation of the Dirac wave functions with the inclusion of nuclear finite size and screening effects. In addition, in [41] the usual Coulomb spherical potential was replaced by another one, derived from a more realistic proton density distribution in the daughter nucleus. These recent PSF calculations led to significant differences in comparison to the older calculations, especially for the heavier isotopes, that should be taken into account for a precise derivation of the neutrino mass parameters.

The computation of the NMEs is a subject of debate in the literature for long time, because they bring the large uncertainties in the theoretical calculations for DBD. Different groups have developed several conceptually different nuclear structure methods [13–31], as we have mentioned in the previous section. The expression of the NMEs can be written, in general, as a sum of three components:

$$M^{0\nu} = M_{GT}^{0\nu} - \left(\frac{g_V}{g_A}\right)^2 \cdot M_F^{0\nu} - M_T^{0\nu}, \quad (4)$$

where $M_{GT}^{0\nu}$, $M_F^{0\nu}$, and $M_T^{0\nu}$ are the Gamow-Teller (GT), Fermi (F), and Tensor (T) components, respectively. These are defined as follows:

$$M_\alpha^{0\nu} = \sum_{m,n} \left\langle 0_f^+ \left\| \tau_{-m}\tau_{-n}O_{mn}^\alpha \right\| 0_i^+ \right\rangle, \quad (5)$$

where O_{mn}^α are transition operators ($\alpha = $ GT, F, T) and the summation is performed over all the nucleon states. An important part of the NME calculation is the computation of the reduced matrix elements of the two-body transition operators O^α. Their calculation can be decomposed into products of reduced matrix elements within the spin and relative coordinate spaces. Their explicit expressions are [4, 23]

$$O_{12}^{GT} = \sigma_1 \cdot \sigma_2 H(r), \qquad O_{12}^F = H(r),$$

$$O_{12}^T = \sqrt{\frac{2}{3}}[\sigma_1 \times \sigma_2]^2 \cdot \frac{r}{R}H(r)C^{(2)}(\hat{r}). \quad (6)$$

The most difficult is the computation of the radial part of the two-body transition operators, which contains the neutrino potentials. These potentials depend weakly on the intermediate states and are defined by integrals of momentum carried by the virtual neutrino exchanged between the two nucleons [16]:

$$
\begin{aligned}
H_\alpha(r) &= \frac{2R}{\pi} \int_0^\infty j_i(qr) \frac{h_\alpha(q)}{\omega} \frac{1}{\omega + \langle E \rangle} q^2 dq \\
&\equiv \int_0^\infty j_i(qr) V_\alpha(q) q^2 dq,
\end{aligned}
\tag{7}
$$

where $R = r_0 A^{1/3}$ fm ($r_0 = 1.2$ fm), $\omega = \sqrt{q^2 + m_\nu^2}$ is the neutrino energy, and $j_i(qr)$ is the spherical Bessel function ($i = 0, 0,$ and 2 for GT, F, and T, resp.). Usually, in calculations one uses the closure approximation which consists of a replacement of the excitation energies of the states in the intermediate odd-odd nucleus contributing to the decay, by an average expression $\langle E \rangle$. This approximation works well in the case of $0\nu\beta\beta$ decay modes and simplifies much the calculations. The expressions of h_α ($\alpha = $ GT, F, T) are

$$
h_F = G_V^2\left(q^2\right),
\tag{8}
$$

$$
h_{GT}\left(q^2\right) = \frac{G_A^2\left(q^2\right)}{g_A^2}\left[1 - \frac{2}{3}\frac{q^2}{q^2 + m_\pi^2} + \frac{1}{3}\left(\frac{q^2}{q^2 + m_\pi^2}\right)^2\right]
$$
$$
+ \frac{2}{3}\frac{G_M^2\left(q^2\right)}{g_A^2}\frac{q^2}{4m_p^2},
\tag{9}
$$

$$
h_T\left(q^2\right) = \frac{G_A^2\left(q^2\right)}{g_A^2}\left[\frac{2}{3}\frac{q^2}{q^2 + m_\pi^2} - \frac{1}{3}\left(\frac{q^2}{q^2 + m_\pi^2}\right)^2\right]
$$
$$
+ \frac{1}{3}\frac{G_M^2\left(q^2\right)}{g_A^2}\frac{q^2}{4m_p^2},
\tag{10}
$$

where m_π is the pion mass, m_p is the proton mass, and

$$
G_M\left(q^2\right) = \left(\mu_p - \mu_n\right) G_V\left(q^2\right),
\tag{11}
$$

with $(\mu_p - \mu_n) = 4.71$.

The expressions (9)-(10) include important nuclear ingredients that should be taken into account for a precise computation of the NMEs, such as the higher order currents in the nuclear interaction (HOC) and finite nucleon size effect (FNS). Inclusion of HOC brings additional terms in the H_{GT} component and leads to the appearance of the H_T component in the expressions of the neutrino potentials. FNS effect is taken into account through G_V and G_A form factors:

$$
G_A\left(q^2\right) = g_A\left(\frac{\Lambda_A^2}{\Lambda_A^2 + q^2}\right)^2,
$$
$$
G_V\left(q^2\right) = g_V\left(\frac{\Lambda_V^2}{\Lambda_V^2 + q^2}\right)^2.
\tag{12}
$$

For the vector and axial coupling constants, the majority of the calculations take either the quenched value, $g_V = 1$, or the unquenched one, $g_A = 1.25$, while the values of the vector and axial vector form factors are $\Lambda_V = 850$ MeV and $\Lambda_A = 1086$ MeV [1], respectively. As one can see, when HOC and FNS corrections are included in the calculations, the dependence of NMEs expression on g_A is not trivial and the NMEs values obtained with the quenched or the unquenched value of this parameter cannot be obtained by simply rescaling.

To compute the radial matrix elements $\langle nl|H_\alpha|n'l'\rangle$ an important ingredient is the adequate inclusion of SRCs, induced by the nuclear interaction. The way of introducing the SRC effects has also been subject of debate ([16–18, 20]). The SRC effects are included by correcting the single particle w.f. as follows:

$$
\psi_{nl}(r) \longrightarrow \left[1 + f(r)\right] \psi_{nl}(r).
\tag{13}
$$

The correlation function $f(r)$ can be parametrized in several ways. There are three parameterizations which are used, Miller-Spencer (MS), UCOM, and CCM (with CD-Bonn and AV18 potentials). The Jastrow prescription [34] for the correlation function is

$$
f(r) = -c \cdot e^{-ar^2}\left(1 - br^2\right)
\tag{14}
$$

and includes all these parameterizations, depending on values of the a, b, c parameters.

Including HOC and FNS effects, the radial matrix elements of the neutrino potentials become

$$
\begin{aligned}
\left\langle nl \left| H_\alpha(r) \right| n'l' \right\rangle &= \int_0^\infty r^2 dr \psi_{nl}(r) \psi_{n'l'}(r) \left[1 + f(r)\right]^2 \\
&\times \int_0^\infty q^2 dq V_\alpha(q) j_n(qr),
\end{aligned}
\tag{15}
$$

where ν is the oscillator constant and $V_\alpha(q)$ is an expression containing the q dependence of the neutrino potentials.

From (4)–(15) one can see that a set of approximations and parameters are involved in the NMEs expressions, as the HOC, FNS, and SRC effects and g_A, r_0, (Λ_A, Λ_B), $\langle E \rangle$ parameters. Are there any recommendations on how should they be included in the calculations? At present there is a general consensus in the community in this respect that will be discussed in the next section.

3. Numerical Results and Discussions

The neutrino mass parameters are derived from (3). To get $\langle m_\nu \rangle$ in the same units as m_e we take the NMEs dimensionless and the PSFs ($G^{0\nu}$) in units of $[\text{yr}]^{-1}$.

The PSF values were obtained by recalculating them with our code, developed in [41], but with improved numerical precision. At this point we mention that the improved PSF values come, on the one hand, by the use of a Coulomb potential describing a more realistic proton charge density in the daughter nucleus instead of the (usual) constant charge density one, to solve the Dirac equations for obtaining the

electron w.f. On the other hand, we got better precision of our numerical routines that compute the PSFs by enhancing the number of the interpolation points on a case-to-case basis until the results become stationary. The obtained values are very close to both those reported previously in [40, 41]. This gives us confidence on their reliability. We mention that these PSFs values differ from older calculations as, for example, those reported in [33, 35–37] by up to 28%. Such differences are important for precise estimations and justify the reactualization of the PSFs values in extracting Majorana neutrino mass parameters.

For the experimental lifetime we took the most recent results reported in the literature. In particular, we remark the newest results for ^{76}Ge from GERDA [49] and for ^{136}Xe from KamLAND-Zen [54].

The largest uncertainty in the derivation of $\langle m_\nu \rangle$ comes from the values of the NMEs. Fortunately, at present there is a general consensus in the community on the employment of the different nuclear effects (approximations) and parameters which appear in the NMEs expressions (see (4)–(15)) [57]. Thus, one can restrict the range of spread of the NMEs values for a particular nucleus, if one takes into account some recommendations resulting from the analysis of many NMEs calculations. For example, one recommends the inclusion in calculation of the HOC, FNS, and SRC effects (although their effects can partially compensate each other [43]). For SRCs, softer parametrizations like UCOM [17, 18, 20] and CCM [58–60] are recommended, while the MS produces a too severe cut of the w.f. for very short internucleon distances, which reflects into smaller NMEs values. Concerning the nuclear parameters, one recommends the use of an unquenched value for the g_A axial vector constant, the values specified above for the vector and axial vector form factors (Λ_V, Λ_A), and a value of $r_0 = 1.2$ fm for the nuclear radius constant. The value for the average energy ($\langle E \rangle$), used in the closure approximation, is a function of atomic mass A, but the results are less sensitive to changes within a few MeV. The use in different ways of these ingredients can result in significant differences between the NMEs values. Hence, a consensus is useful to approach the results obtained by different groups. Having agreement on these nuclear ingredients, the differences in the NMEs values should be searched in the features of the different nuclear structure methods. These methods use different ways of building the wave functions and different specific model spaces and type of nucleon-nucleon correlations and use some specific parameters [3, 24, 43]. Unfortunately, the uncertainties in the NMEs calculation associated with a particular nuclear structure method cannot be easily fixed and they are still a subject of debate. As a general feature, ShM calculations underestimate the NMEs values (due to the limitations of the model spaces used), while the other methods overestimate them. There are, however, a few hints on how to understand/bring closer the NMEs results obtained with different methods. One idea would be to analyze the structure of the wave functions used in terms of the seniority scheme [57]. Another one is to (re)calculate the NME values as to reproduce s.p. occupancies numbers measured recently for ^{76}Ge and ^{82}Se nuclei [61, 62]. For example, when the

QRPA calculations have been modified with the s.p. energies that reproduce the experimental occupancies, the new QRPA NMEs values are much closer to the ShM ones.

In Table 1 we display the NMEs values obtained with different nuclear methods. For uniformity and in agreement with the consensus discussed above, we chose those results that were performed with the inclusion of HOC, FNS, and SRC (UCOM and CD-Bonn) effects and with unquenched $g_A = 1.25$, as nuclear ingredients. We mention that the newest experimental determinations of this parameter report values even larger (1.269, 1.273) [63]. However, the differences between NMEs values obtained with $g_A = 1.25$–1.273 are not significant [43]. The NMEs values for ^{76}Ge and ^{82}Se written in parenthesis represent the adjusted NMEs values obtained with QRPA method by the Tuebingen and Jyvaskyla groups, when the s.p. energies were adjusted to the occupancy numbers reported in [61, 62]. One remarks that the QRPA calculations with s.p. occupancies in accordance with experiment get significantly close to the ShM results, which is remarkable. In the future, one expects measurements of the occupancy numbers for other nuclei, as well. Also, it would be interesting if other methods, besides QRPA, would try to recalculate the NMEs by adjusting s.p. energies to experimental occupancy numbers.

We also make some remarks about the NMEs values on a case-by-case basis. For ^{48}Ca we appreciate that ShM calculations give more realistic results than the other methods. In support of this claim we mention that, in the case of this isotope, ShM calculations are performed within the full pf shell and using good effective NN interactions, checked experimentally on other spectroscopic quantities [43, 44, 64]. Also, we remark that NMEs values obtained with ShM for this isotope were used to correctly predict $T_{1/2}^{2\nu}$, before its experimental measurement [65]. For the isotopes with $A = 96$–130 there is a larger spread of the NMEs values calculated with different methods and, consequently, a larger uncertainty in predicting the $\langle m_\nu \rangle$ parameters. For ^{136}Xe there are new ShM large-scale calculations with inclusion of a larger model space than the older calculations [45]. For this isotope the NMEs values are more grouped. Corroborated with a quite good experimental lifetime, from this isotope one gets the most stringent constraint for the $\langle m_\nu \rangle$ parameter.

In Table 2 we present our results for the Majorana neutrino mass parameters ($\langle m_\nu \rangle$) together with the values of $Q_{\beta\beta}$, the PSFs ($G^{0\nu}$), NMEs ($M^{0\nu}$), and experimental lifetime ($T_{1/2}^{0\nu}$) for all the isotopes for which data exists. Making a sort of the NMEs values from the literature according to the considerations presented, we reduce the interval of their spread to about a factor of 2, even less (with one exception). This results in reducing the uncertainty in deriving the constraints on the light neutrino Majorana mass parameters, while taking into account NME values obtained with all the main nuclear methods existent on the market. One observes that the stringent constraints are obtained from the ^{136}Xe isotope, followed by the ^{76}Ge one. This is due to both the experimental sensitivity of the experiments measuring these isotopes and the reliability of the PSFs and NMEs theoretical calculations. The experiments measuring these

TABLE 1: The NMEs obtained with different methods. The values are obtained using an unquenched value for g_A and softer SRC parametrizations, which are specified in the second column.

Method	SRC	^{48}Ca	^{76}Ge	^{82}Se	^{96}Zr	^{100}Mo	^{116}Cd	^{130}Te	^{136}Xe	^{150}Nd
[43] ShM	CD-BONN	0.81	3.13	2.88						
[44] ShM	CD-BONN	0.90							2.21 [45]	
[24] ShM	UCOM	0.85	2.81–3.52	2.64				2.65	2.19	
[27] IBM-2	CD-BONN	2.38	6.16	4.99	3.00	4.50	3.29	4.61	3.79	2.88
[3] QRPA	CD-BONN		5.93 (3.27)	5.30 (4.54)	2.19	4.67	3.72	4.80	3.00	3.16 [46]
[47] QRPA	UCOM		5.36 (4.11)	3.72	3.12	3.93	4.79	4.22	2.80	
[31] GCM	CD-BONN	2.37	4.60	4.22	5.65	5.08	4.72	5.13	4.20	1.71
[29, 30] PHFB	CD-BONN				2.98	6.07		3.98		2.68

TABLE 2: Majorana neutrino mass parameters together with the other components of the $0\nu\beta\beta$ decay halftimes: the $Q_{\beta\beta}$ values, the experimental lifetime limits, the phase space factors, and the nuclear matrix elements.

	$Q_{\beta\beta}$ [MeV]	$T^{0\nu\beta\beta}_{\exp}$ [yr]	$G^{0\nu\beta\beta}$ [yr^{-1}]	$M^{0\nu\beta\beta}$	$\langle m_\nu \rangle$ [eV]
^{48}Ca	4.272	>5.8 10^{22} [48]	$2.46E-14$	0.81–0.90	<[15.0–16.7]
^{76}Ge	2.039	>2.1 10^{25} [49]	$2.37E-15$	2.81–6.16	<[0.37–0.82]
^{82}Se	2.995	>3.6 10^{23} [50]	$1.01E-14$	2.64–4.99	<[1.70–3.21]
^{96}Zr	3.350	>9.2 10^{21} [51]	$2.05E-14$	2.19–5.65	<[6.59–17.0]
^{100}Mo	3.034	>1.1 10^{24} [50]	$1.57E-14$	3.93–6.07	<[0.64–0.99]
^{116}Cd	2.814	>1.7 10^{23} [52]	$1.66E-14$	3.29–4.79	<[2.00–2.92]
^{130}Te	2.527	>2.8 10^{24} [53]	$1.41E-14$	2.65–5.13	<[0.50–0.97]
^{136}Xe	2.458	>1.6 10^{25} [54]	$1.45E-14$	2.19–4.20	<[0.25–0.48]
^{150}Nd	3.371	>1.8 10^{22} [55]	$6.19E-14$	1.71–3.16	<[4.84–8.95]

isotopes are already exploring the quasi-degenerate scenarios for the neutrino mass hierarchy (which is around 0.5 eV). With the ingredients presented in Table 2 (PSFs and NMEs) one can appreciate, as well, the sensitivities, translated into neutrino mass parameters, of the future generation of DBD experiments.

4. Conclusions

We report new values of light Majorana neutrino mass parameters from a $0\nu\beta\beta$ decay analysis extended to all the isotopes for which theoretical and experimental data exists. We used the most recent results for the experimental lifetime $T^{0\nu}_{1/2}$ as well as for the theoretical quantities $G^{0\nu}$ and $M^{0\nu}$. For the PSFs we use newly obtained values, recalculated with an approach described in [41] but with improved numerical accuracy. We use exact electron w.f. obtained by solving a Dirac equation when finite nuclear size and screening effects are included and, in addition, a Coulomb potential derived from a realistic proton distribution in the daughter nucleus has been employed. For choosing the NMEs we take advantage of the general consensus in the community on several nuclear ingredients involved in the calculations (HOC, FHS, and SRCs effects, values of several nuclear input parameters) and restrict the range of spread of the NMEs values, reported in the literature. This, in turn, reduces the uncertainty in deriving constraints on the light Majorana neutrino mass

parameters, while taking into account NME values obtained with all the main nuclear methods. The stringent constraints are obtained from the ^{136}Xe and ^{76}Ge isotopes, due to both the experimental sensitivity and the reliability of the PSFs and NMEs calculations. The experiments measuring these isotopes are already exploring the quasi-degenerate scenarios for the neutrino mass hierarchy which is around 0.5 eV. Our results may be useful for having an up-to-date image on the current neutrino mass sensitivities associated with $0\nu\beta\beta$ measurements for different isotopes and to better estimate the range of the neutrino masses that can be explored in the future DBD experiments.

Note. After the submission of this paper Exo-2000 published their 2-year new limits for the neutrinoless double beta decay of ^{136}Xe, which is less than the value that we used for deriving the neutrino mass parameter in this case. For this isotope, the presently stringent limit for the lifetime is 1.9×10^{25} y, from KamLand-Zen experiment [33]. Hence, we use this value, which shifts the interval of the neutrino mass parameter to [0.23–0.44], which represents a small change in our results for this isotope.

Conflict of Interests

The authors declare that there is no conflict of interests regarding the publication of this paper.

Acknowledgments

References

[1] F. T. Avignone, S. R. Elliott, and J. Engel, "Double beta decay, Majorana neutrinos, and neutrino mass," *Reviews of Modern Physics*, vol. 80, no. 2, pp. 481–516, 2008.

[2] P. Vogel, "Nuclear structure and double beta decay," *Journal of Physics G: Nuclear and Particle Physics*, vol. 39, no. 12, Article ID 124002, 2012.

[3] A. Faessler, V. Rodin, and F. Simkovic, "Nuclear matrix elements for neutrinoless double-beta decay and double-electron capture," *Journal of Physics G: Nuclear and Particle Physics*, vol. 39, no. 12, Article ID 124006, 2012.

[4] J. Vergados, H. Ejiri, and F. Simkovic, "Theory of neutrinoless double-beta decay," *Reports on Progress in Physics*, vol. 75, no. 10, Article ID 106301, 2012.

[5] H. Ejiri, "Double beta decays and neutrino nuclear responses," *Progress in Particle and Nuclear Physics*, vol. 4, no. 2, pp. 249–257, 2010.

[6] W. Rodejohann, "Neutrinoless double-beta decay and neutrino physics," *Journal of Physics G: Nuclear and Particle Physics*, vol. 39, no. 12, Article ID 124008, 2012.

[7] F. Kaether, W. Hampel, G. Heusser, J. Kiko, and T. Kirsten, "Reanalysis of the Gallex solar neutrino flux and source experiments," *Physics Letters B*, vol. 685, no. 1, pp. 47–54, 2010.

[8] A. Gando, Y. Gando, K. Ichimura et al., "Constraints on θ_{13} from a three-flavor oscillation analysis of reactor antineutrinos at KamLAND," *Physical Review D*, vol. 83, Article ID 052002, 2011.

[9] K. Abe, Y. Hayato, T. Iida et al., "Solar neutrino results in Super-Kamiokande-III," *Physical Review D*, vol. 83, Article ID 052010, 2010.

[10] Y. Abe, C. Aberle, T. Akiri et al., "Indication of reactor $\bar{\nu}_e$ disappearance in the double chooz experiment," *Physical Review Letters*, vol. 108, Article ID 131801, 2012.

[11] F. P. An, J. Z. Bai, A. B. Balantekin et al., "Observation of electron-antineutrino disappearance at daya bay," *Physical Review Letters*, vol. 108, Article ID 171803, 2012.

[12] B. Aharmim, S. N. Ahmed, A. E. Anthony et al., "Low-energy-threshold analysis of the phase I and phase II data sets of the Sudbury Neutrino Observatory," vol. 81, Article ID 055504, 2010.

[13] V. A. Rodin, A. Faessler, F. Simkovic, and P. Vogel, "Uncertainty in the $0\nu\beta\beta$ decay nuclear matrix elements," *Physical Review C*, vol. 68, Article ID 044302, 2003.

[14] V. A. Rodin, A. Faessler, F. Simkovic, and P. Vogel, "Erratum to: "Assessment of uncertainties in QRPA $0\nu\beta\beta$-decay nuclear matrix elements" [Nucl. Phys. A 766 (2006) 107]," *Nuclear Physics A*, vol. 793, no. 1–4, pp. 213–215, 2007.

[15] S. Stoica and H. V. Klapdor-Kleingrothaus, "Critical view on double-beta decay matrix elements within Quasi Random Phase Approximation-based methods," *Nuclear Physics A*, vol. 694, no. 1-2, pp. 269–294, 2001.

[16] F. Simkovic, A. Faessler, H. Muther, V. Rodin, and M. Stauf, "$0\nu\beta\beta$-decay nuclear matrix elements with self-consistent short-range correlations," *Physical Review C*, vol. 79, Article ID 055501, 2009.

[17] M. Kortelainen, O. Civitarese, J. Suhonen, and J. Toivanen, "Short-range correlations and neutrinoless double beta decay," *Physics Letters B*, vol. 647, no. 2-3, pp. 128–132, 2007.

[18] M. Kortelainen and J. Suhonen, "Improved short-range correlations and $0\nu\beta\beta$ nuclear matrix elements of ^{76}Ge and ^{82}Se," *Physical Review C*, vol. 75, Article ID 051303, 2007.

[19] F. Simkovic, A. Faessler, V. Rodin, P. Vogel, and J. Engel, "Anatomy of the $0\nu\beta\beta$ nuclear matrix elements," *Physical Review C*, vol. 77, Article ID 045503, 2008.

[20] M. Kortelainen and J. Suhonen (Jyvaskyla U.), "Nuclear matrix elements of neutrinoless double beta decay with improved short-range correlations," *Physical Review C*, vol. 76, Article ID 024315, 2007.

[21] E. Caurier, A. P. Zuker, A. Poves, and G. Martinez-Pinedo, "Full pf shell model study of $A = 48$ nuclei," *Physical Review C*, vol. 50, p. 225, 1994.

[22] J. Retamosa, E. Caurier, and F. Nowacki, "Neutrinoless double beta decay of ^{48}Ca," *Physical Review C*, vol. 51, p. 371, 1995.

[23] M. Horoi and S. Stoica, "Shell model analysis of the neutrinoless double-β decay of ^{48}Ca," *Physical Review C*, vol. 81, Article ID 024321, 2010.

[24] J. Menéndez, A. Poves, E. Caurier, and F. Nowacki, "Disassembling the nuclear matrix elements of the neutrinoless $\beta\beta$ decay," *Nuclear Physics A*, vol. 818, no. 3-4, pp. 139–151, 2009.

[25] E. Caurier, J. Menendez, F. Nowacki, and A. Poves, "Influence of pairing on the nuclear matrix elements of the neutrinoless $\beta\beta$ decays," *Physical Review Letters*, vol. 100, Article ID 052503, 2008.

[26] J. Barea and F. Iachello, "Neutrinoless double-β decay in the microscopic interacting boson model," *Physical Review C*, vol. 79, Article ID 044301, 2009.

[27] J. Barea, J. Kotila, and F. Iachello, "Nuclear matrix elements for double-β decay," *Physical Review C*, vol. 87, Article ID 014315, 2013.

[28] J. Barea, J. Kotila, and F. Iachello, "Limits on neutrino masses from neutrinoless double-β decay," *Physical Review Letters*, vol. 109, Article ID 042501, 2012.

[29] P. K. Rath, R. Chandra, K. Chaturvedi, P. K. Raina, and J. G. Hirsch, "Uncertainties in nuclear transition matrix elements for neutrinoless $\beta\beta$ decay within the projected-Hartree-Fock-Bogoliubov model," *Physical Review C*, vol. 82, Article ID 064310, 2010.

[30] P. K. Rath, R. Chandra, K. Chaturvedi, P. Lohani, P. K. Raina, and J. G. Hirsch, "Neutrinoless $\beta\beta$ decay transition matrix elements within mechanisms involving light Majorana neutrinos, classical Majorons, and sterile neutrinos," *Physical Review C*, vol. 88, Article ID 064322, 2013.

[31] T. R. Rodriguez and G. Martinez-Pinedo, "Energy density functional study of nuclear matrix elements for neutrinoless $\beta\beta$ decay," *Physical Review Letters*, vol. 105, Article ID 252503, 2010.

[32] H. Primakov and S. P. Rosen, "Double beta decay," *Reports on Progress in Physics*, vol. 22, p. 121, 1959.

[33] J. Suhonen and O. Civitarese, "Weak-interaction and nuclear-structure aspects of nuclear double beta decay," *Physics Report*, vol. 300, no. 3-4, pp. 123–214, 1998.

[34] T. Tomoda, "Double beta decay," *Reports on Progress in Physics*, vol. 54, no. 1, p. 53, 1991.

[35] M. Doi, T. Kotani, H. Nishiura, and E. Takasugi, "Double beta decay," *Progress of Theoretical Physics*, vol. 69, no. 2, pp. 602–635, 1983.

[36] M. Doi and T. Kotani, "Neutrino emitting modes of double beta decay," *Progress of Theoretical Physics*, vol. 87, no. 5, pp. 1207–1231, 1992.

[37] M. Doi and T. Kotani, "Neutrinoless modes of double beta decay," *Progress of Theoretical Physics*, vol. 89, no. 1, pp. 139–159, 1993.

[38] W. C. Haxton and G. J. Stephenson Jr., "Double beta decay," *Progress in Particle and Nuclear Physics*, vol. 12, pp. 409–479, 1984.

[39] M. Doi, T. Kotani, and E. Takasugi, "Double beta decay and majorana neutrino," *Progress of Theoretical Physics Supplements*, vol. 83, pp. 1–175, 1985.

[40] J. Kotila and F. Iachello, "Phase-space factors for double-β decay," *Physical Review C*, vol. 85, Article ID 034316, 2012.

[41] S. Stoica and M. Mirea, "New calculations for phase space factors involved in double-β decay," *Physical Review C*, vol. 88, Article ID 037303, 2013.

[42] T. E. Pahomi, A. Neacsu, M. Mirea, and S. Stoica, "Phase space calculations for beta- beta- decays to final excited 2 + 1 states," *Romanian Reports in Physics*, vol. 66, 2, p. 370, 2014.

[43] A. Neacsu and S. Stoica, "Study of nuclear effects in the computation of the $0\nu\beta\beta$ decay matrix elements," *Journal of Physics G: Nuclear and Particle Physics*, vol. 41, no. 1, Article ID 015201, 2014.

[44] M. Horoi, "Shell model analysis of competing contributions to the double-β decay of ^{48}Ca," *Physical Review C*, vol. 87, Article ID 014320, 2013.

[45] M. Horoi and B. A. Brown, "Shell-model analysis of the ^{136}Xe double beta decay nuclear matrix elements," *Physical Review Letters*, vol. 110, Article ID 222502, 2013.

[46] D. L. Fang A Faessler, V. Rodin, and F. Šimkovic, "Neutrinoless double-β decay of ^{150}Nd accounting for deformation," *Physical Review C*, vol. 82, Article ID 051301(R), 2010.

[47] O. Civitarese and J. Suhonen, "Nuclear matrix elements for double beta decay in the QRPA approach: a critical review," *Journal of Physics: Conference Series*, vol. 173, no. 1, Article ID 012012, 2009.

[48] S. Umehara, T. Kishimoto, I. Ogawa et al., "Neutrino-less double-β decay of ^{48}Ca studied by CaF$_2$(Eu) scintillators," *Physical Review C*, vol. 78, Article ID 058501, 2008.

[49] C. Macolino and GERDA Collaboration, "Results on neutrinoless double-beta decay from GERDA phase I," *Modern Physics Letters A*, vol. 29, no. 1, Article ID 1430001, 20 pages, 2014.

[50] A. S. Barabash and V. B. Brudanin, "Investigation of double-beta decay with the NEMO-3 detector," *Physics of Atomic Nuclei*, vol. 74, no. 2, pp. 312–317, 2011.

[51] J. Argyriades, R. Arnold, C. Augier et al., "Measurement of the two neutrino double beta decay half-life of Zr-96 with the NEMO-3 detector," *Nuclear Physics A*, vol. 847, no. 3-4, pp. 168–179, 2010.

[52] F. A. Danevich, A. S. Georgadze, V. V. Kobychev et al., "Search for 2β decay of cadmium and tungsten isotopes: final results of the Solotvina experiment," *Physical Review C*, vol. 68, Article ID 035501, 2003.

[53] E. Andreotti, C. Arnaboldi, and F.T. Avignone III, "^{130}Te neutrinoless double-beta decay with CUORICINO," *Astroparticle Physics*, vol. 34, no. 11, pp. 822–831, 2011.

[54] A. Gando, Y. Gando, H. Hanakago et al., "Limit on neutrinoless $\beta\beta$ decay of ^{136}Xe from the first phase of KamLAND-Zen and comparison with the positive claim in ^{76}Ge," *Physical Review Letters*, vol. 110, Article ID 062502, 2013.

[55] J. Argyriades, R. Arnold, C. Augier et al., "Measurement of the double-β decay half-life of Nd150 and search for neutrinoless decay modes with the NEMO-3 detector," *Physical Review C*, vol. 80, Article ID 032501(R), 2009.

[56] S. F. King and C. Luhn, "Neutrino mass and mixing with discrete symmetry," *Reports on Progress in Physics*, vol. 76, no. 5, Article ID 056201, 2013.

[57] A. Giuliani and A. Poves, "Neutrinoless double-beta decay," *Advances in High Energy Physics*, vol. 2012, Article ID 857016, 38 pages, 2012.

[58] C. Giusti, H. Muther, F. D. Pacati, and M. Stauf, "Short-range and tensor correlations in the ^{16}O(e,e′pn) reaction," *Physical Review C*, vol. 60, Article ID 054608, 1999.

[59] H. Muther A Polls, "Correlations derived from modern nucleon-nucleon potentials," *Physical Review C*, vol. 61, Article ID 014304, 1999.

[60] H. Müther, "Two-body correlations in nuclear systems," *Progress in Particle and Nuclear Physics*, vol. 45, no. 1, pp. 243–334, 2000.

[61] J. P. Schiffer, S. J. Freeman, J. A. Clark et al., "Nuclear structure relevant to neutrinoless double β decay: ^{76}Ge and ^{76}Se," *Physical Review Letters*, vol. 100, Article ID 112501, 2008.

[62] B. P. Kay, J. P. Schiffer, S. J. Freeman et al., "Nuclear structure relevant to neutrinoless double β decay: the valence protons in ^{76}Ge and ^{76}Se," *Physical Review C*, vol. 79, Article ID 021301(R), 2009.

[63] J. Liu, M. P. Mendenhall, A. T. Holley et al., "Determination of the axial-vector weak coupling constant with ultracold neutrons," *Physical Review Letters*, vol. 105, Article ID 181803, 2010.

[64] J. Menendez, A. Poves, E. Caurier, and F. Nowacki, "Occupancies of individual orbits, and the nuclear matrix element of the ^{76}Ge neutrinoless $\beta\beta$ decay," *Physical Review C*, vol. 80, Article ID 048501, 2009.

[65] E. Caurier, A. Poves, and A. P. Zuker, "A full View 0 hω description of the 2$\nu\beta\beta$ decay of ^{48}Ca," *Physics Letters B*, vol. 252, no. 1, pp. 13–17, 1990.

Research Article

Entanglement in a QFT Model of Neutrino Oscillations

M. Blasone,[1,2] F. Dell'Anno,[2,3,4] S. De Siena,[2,4,5] and F. Illuminati[2,4,5]

[1] *Dipartimento di Fisica, Università degli Studi di Salerno, Via Giovanni Paolo II 132, 84084 Fisciano, Italy*

[2] *INFN Sezione di Napoli, Gruppo Collegato di Salerno, Italy*

[3] *Liceo Statale P.E. Imbriani, Via Pescatori 155, 83100 Avellino, Italy*

[4] *Dipartimento di Ingegneria Industriale, Università degli Studi di Salerno, Via Giovanni Paolo II 132, 84084 Fisciano, Italy*

[5] *Consorzio Nazionale Interuniversitario per le Scienze Fisiche della Materia (CNISM), Unità di Salerno, 84084 Fisciano, Italy*

Correspondence should be addressed to M. Blasone; mblasone@unisa.it

Tools of quantum information theory can be exploited to provide a convenient description of the phenomena of particle mixing and flavor oscillations in terms of entanglement, a fundamental quantum resource. We extend such a picture to the domain of quantum field theory where, due to the nontrivial nature of flavor neutrino states, the presence of antiparticles provides additional contributions to flavor entanglement. We use a suitable entanglement measure, the concurrence, that allows extracting the two-mode (flavor) entanglement from the full multimode, multiparticle flavor neutrino states.

1. Introduction

In the last years, many efforts have been dedicated to the investigation of entanglement in the domain of elementary particle physics and quantum field theory [1–11]. The understanding of the role of nonlocal quantum correlations in infinite-dimensional systems of fields and particles, as well as the underlying mechanism governing their aggregation, represents a main goal. For systems composed by identical particles and/or sets of in general distinguishable field modes (either discrete or continuous, finite or infinite), the characterization and quantification of entanglement are achieved unambiguously only by properly taking into account the algebra of observables besides the tensor product structure of the individual state spaces. In the case of quantum fields, a further extension of such a framework is needed to take into account the correlations among distinguishable physical field modes rather than among indistinguishable particles and excitations [12–27].

For instance, the single-particle Bell superposition state $|0, 1\rangle + |1, 0\rangle$ between any two modes of the electromagnetic field is a well-known example of a maximally (bipartite) entangled quantum state (i.e., with maximal von Neumann entropy of the reduced single-mode density matrices), despite the fact that it involves only one excitation of the field (a single photon) [26]. In this case, the entanglement is between two different field modes with occupation numbers ranging between 0 and 1. Considering single-particle or multiparticle (e.g., multiphoton) states of many modes leads to straightforward generalizations that allow considering the bipartite and multipartite multimode field entanglement of single-particle and multiparticle states. In the same way, it is possible to make precise sense of Bell nonlocality in the context of single-particle, multimode states [28–30].

In this context, it has been recently recognized that the phenomena of particle mixing and flavor oscillations can be understood in terms of quantum entanglement [4, 5]. In particular, a connection has been established among the flavor transition probabilities and the multimode, single-particle entanglement for oscillating neutrinos [5]. Such a connection allows in principle engineering experimental protocols for the transfer of the quantum information encoded in neutrino states to spatially delocalized two-flavor charged lepton states [4, 5]. The above analysis has been carried out in the context of quantum mechanics (QM), using the well-known Pontecorvo formalism for neutrino oscillations. On the other hand, it has been shown that flavor mixing in the context of quantum field theory (QFT) is associated with a highly

nontrivial nature of the vacuum for the mixed fields [31–34]. As a consequence, neutrino states turn out to be multimode, multiparticle states, with a very rich structure of quantum correlations. In [6, 7], we studied the entanglement in such a system by means of entropic measures and found a relation with experimentally measurable quantities, like the variances of the lepton numbers and charges.

In the present work, we further investigate along this direction by adopting an alternative operational viewpoint on the entanglement associated with the system of oscillating neutrinos. Indeed, entanglement is an observable-induced, relative physical quantity [15–22], endowed with a specific operational meaning according to the selected reference quantum observables and quantum subsystems. By assuming the particle-antiparticle species as further quantum modes, we investigate the entanglement content of the neutrino system in the state obtained by tracing out the antiparticle species. Since such a state turns out to be a mixed one, we adopt the concurrence as a measure for the quantification of its entanglement content. Our results are in line with those of [6, 7] and naturally generalize the QM ones presented in [5].

The paper is organized as follows. In Section 2 we review the quantum information tools exploited in the paper and some results corresponding to the QM framework. In Section 3 we investigate the entanglement phenomenology of neutrino mixing and flavor oscillations adopting a QFT framework, and we discuss the nontrivial structure of flavor entanglement that emerges in the QFT framework.

2. Entanglement and Flavor Oscillations: Quantum Mechanics

In this section, we briefly review the background of the present analysis, that is, the formalism developed and the results obtained within the quantum mechanical framework [4, 5]. Flavor mixing of neutrinos for two generations is described by the 2×2 rotation matrix $\mathbf{U}(\theta)$ [35]

$$\mathbf{U}(\theta) = \begin{pmatrix} \cos\theta & \sin\theta \\ -\sin\theta & \cos\theta \end{pmatrix}, \qquad (1)$$

where θ is the mixing angle. The two-flavor neutrino states are defined as

$$\left| \underline{\nu}^{(f)} \right\rangle = \mathbf{U}(\theta) \left| \underline{\nu}^{(m)} \right\rangle, \qquad (2)$$

where $\left| \underline{\nu}^{(f)} \right\rangle = (|\nu_e\rangle, |\nu_\mu\rangle)^T$ are the states with definite flavors e, μ and $\left| \underline{\nu}^{(m)} \right\rangle = (|\nu_1\rangle, |\nu_2\rangle)^T$ those with definite masses m_1, m_2. Both $|\nu_\alpha\rangle$ ($\alpha = e, \mu$) and $|\nu_j\rangle$ ($j = 1, 2$) are orthonormal. By describing the free propagation of the neutrino mass eigenstates with plane waves of the form $|\nu_j(t)\rangle = e^{-i\omega_j t}|\nu_j\rangle$, ω_j denoting the frequency associated with the mass eigenstate $|\nu_j\rangle$, the time evolution of the flavor states is given by

$$\left| \underline{\nu}^{(f)}(t) \right\rangle = \mathbf{U}(t) \left| \underline{\nu}^{(f)} \right\rangle \equiv \mathbf{U}(\theta) \mathbf{U}_0(t) \mathbf{U}^{-1}(\theta) \left| \underline{\nu}^{(f)} \right\rangle, \quad (3)$$

where $\left| \underline{\nu}^{(f)} \right\rangle$ are the flavor states at $t = 0$, and $\mathbf{U}_0(t) = \mathrm{diag}(e^{-i\omega_1 t}, e^{-i\omega_2 t})$. By assuming the neutrino occupation

number associated with a given flavor (mode) as reference quantum number, one can establish the following correspondences with two-qubit states:

$$|\nu_e\rangle \equiv |1\rangle_{\nu_e} |0\rangle_{\nu_\mu} \equiv |10\rangle_{e\mu},$$
$$|\nu_\mu\rangle \equiv |0\rangle_{\nu_e} |1\rangle_{\nu_\mu} \equiv |01\rangle_{e\mu}, \qquad (4)$$

where $|j\rangle_{\nu_\alpha}$ stands for a j-occupation number state of a neutrino in mode α. Entanglement is thus established among flavor modes, in a single-particle setting. For instance, the free evolution of the electron-neutrino state $|\nu_e(t)\rangle$ can be written in the form

$$\left| \nu_e(t) \right\rangle = \mathbf{U}_{ee}(t) |10\rangle_{e\mu} + \mathbf{U}_{e\mu}(t) |01\rangle_{e\mu}, \qquad (5)$$

where $|\mathbf{U}_{ee}(t)|^2 + |\mathbf{U}_{e\mu}(t)|^2 = 1$ due to normalization. Thus, the time-evolved states $\left| \underline{\nu}^{(f)}(t) \right\rangle$ are entangled Bell-like superpositions of the two masses with time-independent coefficients or flavor eigenstates with time-dependent coefficients. It is worth remarking that the entanglement of (5) is in principle experimentally accessible, throughout a scheme for its transfer from single-neutrino states to two-flavor charged lepton states [5].

The entanglement content of the pure two-qubit state equation (5) is quantified by the von Neumann entropy of the reduced density matrix (or any other monotonic function of it), which is the widely accepted measure of the bipartite entanglement of pure states [36]. For other measures of entanglement (bipartite and multipartite systems), see [37–42]. In the instance of mixed states, a particularly convenient measure for two-qubit systems is the concurrence $C(\rho)$ [43, 44]. For the particular case of a pair of qubits, such a measure is closely related to the entanglement of formation $E_F(\rho)$, which is the prototype of the convex-roof-based measures. The entanglement of formation has a simple physical interpretation: it is the minimal amount of entanglement needed for the production of a mixed state described by a given density matrix.

We briefly recall the definition of the concurrence, which will be used in this work. Let ρ be the density operator corresponding to an arbitrary N-qubit state and describing a system partitioned into N parties. The reduced density operator $\rho^{(\alpha;\beta)}$ associated with ρ is defined as

$$\rho^{(\alpha;\beta)} = \mathrm{Tr}_{\gamma \neq \alpha, \beta} [\rho], \qquad (6)$$

where the trace operation is made over all the parties different from α and β. Next, the spin-flipped state $\tilde{\rho}^{(\alpha;\beta)}$ reads

$$\tilde{\rho}^{(\alpha;\beta)} = (\sigma_y \otimes \sigma_y) \rho^{(\alpha;\beta)*} (\sigma_y \otimes \sigma_y), \qquad (7)$$

where the complex conjugate is taken in the standard basis $\{|00\rangle, |01\rangle, |10\rangle, |11\rangle\}$. Then the concurrence is expressed in terms of square roots λ_i of the eigenvalues of the non-Hermitian matrix $\rho^{(\alpha;\beta)} \tilde{\rho}^{(\alpha;\beta)}$:

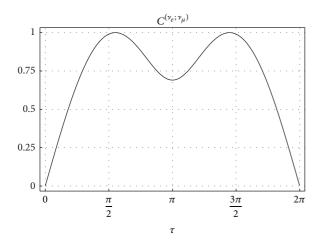$$C\left(\rho^{(\alpha;\beta)}\right) = \max\{0, \lambda_1 - \lambda_2 - \lambda_3 - \lambda_4\}, \qquad (8)$$

FIGURE 1: QM instance. The concurrence $C^{(\nu_e;\nu_\mu)}$ as function of the scaled time $\tau = (\omega_2 - \omega_1)t$. The mixing angle θ is fixed at the experimental value $\sin^2\theta = 0.314$.

where the λ_is are nonnegative real numbers taken in decreasing order with respect to the index i. The concurrence equation (8) can be easily computed for the pure two-qubit Bell state $|\nu_e(t)\rangle$, that is, (5), with density matrix $\rho_e = |\nu_e(t)\rangle\langle\nu_e(t)|$. The concurrence $C^{(\nu_e;\nu_\mu)} \equiv C(\rho^{(\nu_e;\nu_\mu)})$ writes

$$C^{(\nu_e;\nu_\mu)} = 2\left|\mathbf{U}_{ee}(t)\right|\left|\mathbf{U}_{e\mu}(t)\right|. \qquad (9)$$

It is worth noticing that, in the instance of pure states, the concurrence coincides with the square root of the linear entropy. In Figure 1, we show the behavior of $C^{(\nu_e;\nu_\mu)}$ as functions of the scaled, dimensionless time $\tau = (\omega_2 - \omega_1)t$. At time $\tau = 0$, the two flavors are not mixed, the entanglement is zero, and the global state of the system is factorized. For $\tau > 0$, flavor oscillations occur, and the linear entropy exhibits a typical oscillatory behavior; the entanglement is maximal at largest mixing.

3. Entanglement and Flavor Oscillations: Quantum Field Theory

In this section, first we review the essential features of a specific QFT model of particle mixing describing the phenomena of neutrino oscillations [31, 32]. For a general theory of mixing for an arbitrary number of fields see also [45].

Then, by using such a model, we present a generalization of the above analysis to the QFT framework. The neutrino Dirac fields $\nu_e(x)$ and $\nu_\mu(x)$ are defined through the mixing relations

$$\nu_e(x) = \cos\theta\nu_1(x) + \sin\theta\nu_2(x),$$
$$\nu_\mu(x) = -\sin\theta\nu_1(x) + \cos\theta\nu_2(x), \qquad (10)$$

where, in standard notation, x stands for the four-vector $x \equiv (t, \mathbf{x})$ and the free fields $\nu_1(x)$ and $\nu_2(x)$ with definite masses

m_1 and m_2. The generator of the mixing transformations is given by

$$G_\theta(t) = \exp\left[\theta\int d^3\mathbf{x}\left(\nu_1^\dagger(x)\nu_2(x) - \nu_2^\dagger(x)\nu_1(x)\right)\right] \quad (11)$$

so that

$$\nu_\sigma^\alpha(x) = G_\theta^{-1}(t)\nu_i^\alpha(x)G_\theta(t), \qquad (12)$$

where $(\sigma, i) = (e, 1), (\mu, 2)$, and the superscript $\alpha = 1, \dots, 4$ denotes the spinorial component. At finite volume, $G_\theta(t)$ is a unitary operator, that is, $G_\theta^{-1}(t) = G_{-\theta}(t) = G_\theta^\dagger(t)$, preserving the canonical anticommutation relations. The generator $G_\theta^{-1}(t)$ maps the Hilbert space for free fields $\mathscr{H}_{1,2}$ to the Hilbert space for mixed fields $\mathscr{H}_{e,\mu}$; that is, $G_\theta^{-1}(t) : \mathscr{H}_{1,2} \mapsto \mathscr{H}_{e,\mu}$. In particular, the flavor vacuum is given by $|0(t)\rangle_{e,\mu} = G_\theta^{-1}(t)\ |0\rangle_{1,2}$ at finite volume V. We denote by $|0\rangle_{e,\mu}$ the flavor vacuum at $t = 0$. It is worth noticing that, in the infinite volume limit, the flavor and the mass vacua are unitarily inequivalent. The free fields $\nu_i(x)$ $(i = 1, 2)$ are given by the following expansions:

$$\nu_i(x) = \frac{1}{\sqrt{V}}\sum_{\mathbf{k},r}\left[u_{\mathbf{k},i}^r\alpha_{\mathbf{k},i}^r(t) + v_{-\mathbf{k},i}^r\beta_{-\mathbf{k},i}^{r\dagger}(t)\right]e^{i\mathbf{k}\cdot\mathbf{x}}, \qquad (13)$$

where $\mathbf{k}$ is the momentum vector, $r = 1, 2$ denotes the helicity, $\alpha_{\mathbf{k},i}^r(t) = \alpha_{\mathbf{k},i}^r e^{-i\omega_{k,i}t}$, $\beta_{\mathbf{k},i}^{r\dagger}(t) = \beta_{\mathbf{k},i}^{r\dagger}e^{i\omega_{k,i}t}$, and $\omega_{k,i} = \sqrt{\mathbf{k}^2 + m_i^2}$. The operators $\alpha_{\mathbf{k},i}^r$ and $\beta_{\mathbf{k},i}^r$ are the annihilation operators for the vacuum state $|0\rangle_m \equiv |0\rangle_1 \otimes |0\rangle_2$; that is, $\alpha_{\mathbf{k},i}^r|0\rangle_m = \beta_{\mathbf{k},i}^r|0\rangle_m = 0$. The anticommutation relations are the usual ones; extended details, for example, on the orthonormality and completeness relations are presented in our previous works [31, 32]. By use of $G_\theta(t)$, the flavor fields can be expanded as

$$\nu_\sigma(\mathbf{x}) = \frac{1}{\sqrt{V}}\sum_{\mathbf{k},r}\left[u_{\mathbf{k},i}^r\alpha_{\mathbf{k},\sigma}^r(t) + v_{-\mathbf{k},i}^r\beta_{-\mathbf{k},\sigma}^{r\dagger}(t)\right]e^{i\mathbf{k}\cdot\mathbf{x}}. \qquad (14)$$

The flavor annihilation operators are defined as $\alpha_{\mathbf{k},\sigma}^r(t) \equiv G_\theta^{-1}(t)\alpha_{\mathbf{k},i}^r G_\theta(t)$ and $\beta_{\mathbf{k},\sigma}^{r\dagger}(t) \equiv G_\theta^{-1}(t)\beta_{\mathbf{k},\sigma}^{r\dagger}G_\theta(t)$. Without any loss of generality, let us choose the reference frame such that $\mathbf{k} = (0, 0, |\mathbf{k}|)$; we have

$$\alpha_{\mathbf{k},e}^r(t) = \cos\theta\alpha_{\mathbf{k},1}^r(t) \\ + \sin\theta\left(|U_\mathbf{k}|\alpha_{\mathbf{k},2}^r(t) + \epsilon^r|V_\mathbf{k}|\beta_{-\mathbf{k},2}^{r\dagger}(t)\right), \qquad (15)$$

where $\epsilon^r = (-1)^r$ and

$$|U_\mathbf{k}| \equiv u_{\mathbf{k},i}^{r\dagger}u_{\mathbf{k},j}^r = v_{-\mathbf{k},j}^{r\dagger}v_{-\mathbf{k},j}^r$$

$$= \frac{|\mathbf{k}|^2 + (\omega_{k,1} + m_1)(\omega_{k,2} + m_2)}{2\sqrt{\omega_{k,1}\omega_{k,2}(\omega_{k,1} + m_1)(\omega_{k,2} + m_2)}},$$

$$|V_\mathbf{k}| \equiv \epsilon^r u_{\mathbf{k},1}^{r\dagger}v_{-\mathbf{k},2}^r = -\epsilon^r u_{\mathbf{k},2}^{r\dagger}v_{-\mathbf{k},1}^r \qquad (16)$$

$$= \frac{(\omega_{k,1} + m_1) - (\omega_{k,2} + m_2)}{2\sqrt{\omega_{k,1}\omega_{k,2}(\omega_{k,1} + m_1)(\omega_{k,2} + m_2)}}|\mathbf{k}|,$$

with $i, j = 1, 2$, $i \neq j$, and $|U_\mathbf{k}|^2 + |V_\mathbf{k}|^2 = 1$. The explicit expression for the flavor states $|\nu^r_{\mathbf{k},e}\rangle$ at time $t = 0$ is

$$
\begin{aligned}
\left|\nu^r_{\mathbf{k},e}\right\rangle &\equiv \alpha^{r\dagger}_{\mathbf{k},e}(0)\,|0\rangle_{e,\mu} \\
&= \left[\cos\theta\,\alpha^{r\dagger}_{\mathbf{k},1} + |U_\mathbf{k}|\sin\theta\,\alpha^{r\dagger}_{\mathbf{k},2} \right. \\
&\qquad \left. - \epsilon^r\,|V_\mathbf{k}|\sin\theta\,\alpha^{r\dagger}_{\mathbf{k},1}\alpha^{r\dagger}_{\mathbf{k},2}\beta^{r\dagger}_{-\mathbf{k},1}\right] \\
&\quad \times G^{-1}_{\theta,\mathbf{k},r}(t)\prod_{\mathbf{p}\neq\mathbf{k}}G^{-1}_{\theta,\mathbf{p},s}(t)\,|0\rangle_{1,2},
\end{aligned}
\tag{17}
$$

where $G_\theta(t) = \prod_\mathbf{p}\prod_{s=1}^{2}G_{\theta,\mathbf{p},s}(t)$. In the state (17), a multiparticle component is present, disappearing in the relativistic limit $|\mathbf{k}| \gg \sqrt{m_1 m_2}$: indeed, for large $|\mathbf{k}|$, since one gets $|U_\mathbf{k}|^2 \to 1$ and $|V_\mathbf{k}|^2 \to 0$, the (quantum-mechanical) Pontecorvo states are recovered. In order to simplify the notation, we omit the superscript r (by fixing $r = 2$) and the subscript $\mathbf{k}$, thus restricting the analysis to the flavor neutrino state $|\nu_e\rangle$ of fixed momentum and helicity. Let us consider again the free evolution of the electron-neutrino state (17):

$$
\left|\nu_e(t)\right\rangle = e^{-iH_0 t}\left|\nu_e\right\rangle,
\tag{18}
$$

where H_0 is the standard QFT free Hamiltonian. Finally, in the Hilbert space $\mathcal{H}_{e,\mu}$, (18) can be written in the form

$$
\begin{aligned}
\left|\nu_e(t)\right\rangle &= \left[\mathbf{U}_{ee}(t)\,\alpha^\dagger_e + \mathbf{U}_{e\mu}(t)\,\alpha^\dagger_\mu + \mathbf{U}^{e\bar{e}}_{e\mu}(t)\,\alpha^\dagger_e\alpha^\dagger_\mu\beta^\dagger_e \right. \\
&\quad \left. + \mathbf{U}^{\mu\bar{\mu}}_{ee}(t)\,\alpha^\dagger_e\alpha^\dagger_\mu\beta^\dagger_\mu\right]|0\rangle_{e,\mu},
\end{aligned}
\tag{19}
$$

where the time-dependent coefficients are given by

$$
\begin{aligned}
\mathbf{U}_{ee}(t) &= e^{-i\omega_1 t}\left[\cos^2\theta + \sin^2\theta\left(e^{-i(\omega_2-\omega_1)t}|U|^2 \right.\right. \\
&\qquad\qquad\qquad \left.\left. + e^{-i(\omega_2+\omega_1)t}|V|^2\right)\right], \\
\mathbf{U}_{e\mu}(t) &= e^{-i\omega_1 t}U\cos\theta\sin\theta\left(e^{-i(\omega_2-\omega_1)t}-1\right), \\
\mathbf{U}^{e\bar{e}}_{e\mu}(t) &= e^{-i\omega_1 t}V\cos\theta\sin\theta\left(1-e^{-i(\omega_2+\omega_1)t}\right), \\
\mathbf{U}^{\mu\bar{\mu}}_{ee}(t) &= e^{-i\omega_1 t}UV\sin^2\theta\left(e^{-i(\omega_2+\omega_1)t}-e^{-i(\omega_2-\omega_1)t}\right), \\
\left|\mathbf{U}_{ee}(t)\right|^2 &+ \left|\mathbf{U}_{e\mu}(t)\right|^2 + \left|\mathbf{U}^{e\bar{e}}_{e\mu}(t)\right|^2 + \left|\mathbf{U}^{\mu\bar{\mu}}_{ee}(t)\right|^2 = 1.
\end{aligned}
\tag{20}
$$

In the following, in order to conveniently parameterize the neutrino masses m_1 and m_2, momentum $|\mathbf{k}|$, and the evolution time t, we use the real parameters $x = m_2/m_1$, $p = |\mathbf{k}|/\sqrt{m_1 m_2}$, and $\tau = (\omega_2 - \omega_1)t$. Therefore, x represents the ratio between the two masses eigenvalues; p expresses the ratio between the momentum and the masses geometrical mean and corresponds to the relativistic limit for $p \gg 1$.

Evidently, the time-evolved state $|\nu_e(t)\rangle$ in the flavor eigenstates Hilbert space, that is, (19), is a multiparticle entangled state. Analogously with the Pontecorvo states (5), we assume the neutrino occupation number as reference quantum number. However, with respect to (5), we have still two flavors, but we have a further degree of freedom, that
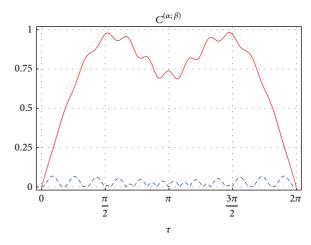

FIGURE 2: QFT instance (color online). The concurrences $C^{(\nu_e;\nu_\mu)}$ (full line) and $C^{(\bar{\nu}_e;\bar{\nu}_\mu)}$ (dashed line) as functions of the scaled time $\tau = (\omega_2 - \omega_1)t$. The mixing angle θ is fixed at the experimental value $\sin^2\theta = 0.314$; the parameters x and p are fixed as $x = 10$ and $p = 5$. The concurrence associated with the quantum-mechanical Pontecorvo states (dotted line), that is, Figure 1, is also reported for comparison.

is, the neutrino species, that is, particles and antiparticles. Therefore, we obtain multipartite entanglement in a four-qubit state. In the instance $\mathcal{H}_{e,\mu}$, (19) can be written in the form

$$
\begin{aligned}
\left|\nu_e(t)\right\rangle &= \mathbf{U}_{ee}(t)\,|1000\rangle_{e\mu\bar{e}\bar{\mu}} + \mathbf{U}_{e\mu}(t)\,|0100\rangle_{e\mu\bar{e}\bar{\mu}} \\
&\quad + \mathbf{U}^{e\bar{e}}_{e\mu}(t)\,|1110\rangle_{e\mu\bar{e}\bar{\mu}} + \mathbf{U}^{\mu\bar{\mu}}_{ee}(t)\,|1101\rangle_{e\mu\bar{e}\bar{\mu}},
\end{aligned}
\tag{21}
$$

where $|ijkh\rangle_{e\mu\bar{e}\bar{\mu}}$ denotes the four-qubit vector $|i\rangle_{\nu_e}|j\rangle_{\nu_\mu}|k\rangle_{\bar{\nu}_e}|h\rangle_{\bar{\nu}_\mu}$ with $i, j, k, h = 0, 1$. Let us analyze the entanglement content possessed by a given pair of modes of $|\nu_e\rangle$, that is, (21), by using the concurrence, that is, by (8). Specifically, we compute the quantity $C^{(\alpha;\beta)}$ associated with the two modes $\alpha \neq \beta = \nu_e, \nu_\mu, \bar{\nu}_e, \bar{\nu}_\mu$. We do not report the analytical expressions for the concurrences, as they are long and unwieldy and provide no further significant physical insight.

In Figure 2, we plot the quantities $C^{(\nu_e;\nu_\mu)}$ and $C^{(\bar{\nu}_e;\bar{\nu}_\mu)}$ as functions of the scaled time τ for $x = 10$ and $p = 5$; it is worth noticing that such a choice of the parameters corresponds to the following assumptions: mass m_2 greater than mass m_1 of one order of magnitude and momentum of the same order of magnitude as the masses geometrical mean. We observe that the particle-mode entanglement $(\nu_e; \nu_\mu)$ is predominant; thus, most entanglement is shared between the two particle modes. Notwithstanding, a nonvanishing (although suppressed), nontrivial, oscillating contribution originates from the antiparticle-mode pair $(\bar{\nu}_e, \bar{\nu}_\mu)$.

For completeness, in Figure 3 we also plot the concurrences $C^{(\nu_e;\bar{\nu}_e)}$ and $C^{(\nu_\mu;\bar{\nu}_e)}$, panel (a), and $C^{(\nu_e;\bar{\nu}_\mu)}$ and $C^{(\nu_\mu;\bar{\nu}_\mu)}$, panel (b). Specifically, plots in Figure 3 represent the concurrences associated with the pairs particle-antiparticle $(\nu_\alpha; \bar{\nu}_\beta)$. We observe that there exists strong entanglement content in these pairs; this fact is due to the Bogoliubov contribution in (15). Let us notice that the curves $C^{(\nu_e;\bar{\nu}_\beta)}$ and $C^{(\nu_\mu;\bar{\nu}_\beta)}$ (with
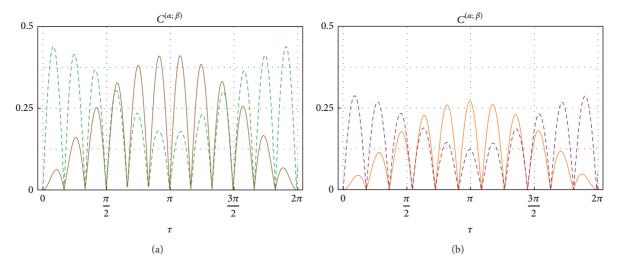
FIGURE 3: QFT instance (color online). In (a) the concurrences $C^{(\nu_e;\bar{\nu}_e)}$ (full line) and $C^{(\nu_\mu;\bar{\nu}_e)}$ (dashed line), in (b) the concurrences $C^{(\nu_e;\bar{\nu}_\mu)}$ (full line) and $C^{(\nu_\mu;\bar{\nu}_\mu)}$ (dashed line), as functions of the scaled time $\tau = (\omega_2 - \omega_1)t$. The mixing angle θ and the parameters x and p are fixed as in Figure 2.

$\beta = e, \mu$) exhibit an opposite behavior; on average, when the former increases (decreases), the latter decreases (increases).

4. Conclusions

In this paper, we analyzed a paradigmatic phenomenon of particle physics, that is, neutrino oscillations, from the point of view of entanglement, one of the fundamental aspects of quantum theory. More specifically, we studied the entanglement associated with a QFT model of neutrino oscillations, generalizing our previous results derived in the context of QM. The two-mode state, obtained by tracing out two modes, is a mixed one, and we characterized the entanglement of such a state by means of the concurrence.

We showed that such a phenomenon, described in a QFT framework, exhibits significantly more complex effects with respect to that found in a QM setting. This procedure is applicable as well to other multiparticle QFT systems, beyond the model considered here.

The present analysis has been carried out for the case of two generations. A further extension can be carried out by considering the case of three flavors, including CP violation, for which the structure of QFT flavor states is considerably more involved [34].

Moreover, the entanglement dynamics has been studied in the time domain; an analogous study can be carried out in the space domain, by considering the spatial distribution of entanglement.

At last, it is also worth remarking that the (exact) results obtained in our paper represent a canonical example of evaluation of entanglement for a relativistic system.

Conflict of Interests

The authors declare that there is no conflict of interests regarding the publication of this paper.

References

[1] R. A. Bertlmann and W. Grimus, "Quantum-mechanical interference over macroscopic distances in the $B^0\overline{B}^0$ system," *Physics Letters B*, vol. 392, no. 3-4, pp. 426–432, 1997.

[2] R. A. Bertlmann, W. Grimus, and B. C. Hiesmayr, "Bell inequality and CP violation in the neutral kaon system," *Physics Letters A*, vol. 289, no. 1-2, pp. 21–26, 2001.

[3] A. Di Domenico, A. Gabriel, B. C. Hiesmayr et al., "Heisenberg's uncertainty relation and bell inequalities in high energy physics: an effective formalism for unstable two-state systems," *Foundations of Physics*, vol. 42, no. 6, pp. 778–802, 2012.

[4] M. Blasone, F. Dell'Anno, S. De Siena, M. Di Mauro, and F. Illuminati, "Multipartite entangled states in particle mixing," *Physical Review D*, vol. 77, Article ID 096002, 2008.

[5] M. Blasone, F. Dell'Anno, S. De Siena, and F. Illuminati, "Entanglement in neutrino oscillations," *Europhysics Letters*, vol. 85, no. 5, Article ID 50002, 2009.

[6] M. Blasone, F. Dell'Anno, S. De Siena, and F. Illuminati, "Entanglement in quantum field theory: particle mixing and oscillations," *Journal of Physics: Conference Series*, vol. 442, no. 1, Article ID 012070, 2013.

[7] M. Blasone, F. Dell'Anno, S. De Siena, and F. Illuminati, "A field-theoretical approach to entanglement in neutrino mixing and oscillations," In press, http://arxiv.org/abs/1401.7793.

[8] B. Kayser, J. Kopp, R. G. H. Robertson, and P. Vogel, "Theory of neutrino oscillations with entanglement," *Physical Review D*, vol. 82, Article ID 093003, 2010.

[9] E. K. Akhmedov and A. Y. Smirnov, "Neutrino oscillations: entanglement, energy-momentum conservation and QFT," *Foundations of Physics*, vol. 41, no. 8, pp. 1279–1306, 2011.

[10] D. Boyanovsky, "Short baseline neutrino oscillations: when entanglement suppresses coherence," *Physical Review D*, vol. 84, Article ID 065001, 2011.

[11] L. Lello, D. Boyanovsky, and R. Holman, "Entanglement entropy in particle decay," *Journal of High Energy Physics*, vol. 2013, article 116, 2013.

[12] G. Ghirardi and L. Marinatto, "Criteria for the entanglement of composite systems with identical particles," *Fortschritte der Physik*, vol. 52, no. 11-12, pp. 1045–1051, 2004.

[13] F. Benatti, R. Floreanini, and U. Marzolino, "Bipartite entanglement in systems of identical particles: the partial transposition criterion," *Annals of Physics*, vol. 327, no. 5, pp. 1304–1319, 2012.

[14] F. Benatti, R. Floreanini, and U. Marzolino, "Sub-shot-noise quantum metrology with entangled identical particles," *Annals of Physics*, vol. 325, no. 4, pp. 924–935, 2010.

[15] P. Zanardi, "Quantum entanglement in fermionic lattices," *Physical Review A*, vol. 65, Article ID 042101, 2002.

[16] P. Zanardi and X. Wang, "Fermionic entanglement in itinerant systems," *Journal of Physics A: Mathematical and General*, vol. 35, no. 37, article 7947, 2002.

[17] P. Zanardi, "Bipartite mode entanglement of bosonic condensates on tunneling graphs," *Physical Review A*, vol. 67, Article ID 054301, 2003.

[18] P. Giorda and P. Zanardi, "Mode entanglement and entangling power in bosonic graphs," *Physical Review A*, vol. 68, Article ID 062108, 2003.

[19] E. Ciancio, P. Giorda, and P. Zanardi, "Mode transformations and entanglement relativity in bipartite Gaussian states," *Physics Letters A*, vol. 354, no. 4, pp. 274–280, 2006.

[20] P. Zanardi, D. A. Lidar, and S. Lloyd, "Quantum tensor product structures are observable induced," *Physical Review Letters*, vol. 92, Article ID 060402, 2004.

[21] H. M. Wiseman and J. A. Vaccaro, "Entanglement of indistinguishable particles shared between two parties," *Physical Review Letters*, vol. 91, Article ID 097902, 2003.

[22] M. R. Dowling, A. C. Doherty, and H. M. Wiseman, "Entanglement of indistinguishable particles in condensed-matter physics," *Physical Review A*, vol. 79, Article ID 052323, 2006.

[23] H. Barnum, E. Knill, G. Ortiz, R. Somma, and L. Viola, "A subsystem-independent generalization of entanglement," *Physical Review Letters*, vol. 92, Article ID 107902, 2004.

[24] H. Barnum, G. Ortiz, R. Somma, and L. Viola, "A generalization of entanglement to convex operational theories: entanglement relative to a subspace of observables," *International Journal of Theoretical Physics*, vol. 44, no. 12, pp. 2127–2145, 2005.

[25] M.-C. Banuls, J. I. Cirac, and M. M. Wolf, "Entanglement in fermionic systems," *Physical Review A*, vol. 76, Article ID 022311, 2006.

[26] S. J. van Enk, "Single-particle entanglement," *Physical Review A*, vol. 72, Article ID 064306, 2005.

[27] M. O. T. Cunha, J. A. Dunningham, and V. Vedral, "Entanglement in single-particle systems," *Proceedings of the Royal Society A: Mathematical, Physical and Engineering Sciences*, vol. 463, no. 2085, pp. 2277–2286, 2007.

[28] J. Dunningham and V. Vedral, "Nonlocality of a single particle," *Physical Review Letters*, vol. 99, Article ID 180404, 2007.

[29] J. Dunningham, V. Palge, and V. Vedral, "Entanglement and nonlocality of a single relativistic particle," *Physical Review A*, vol. 80, Article ID 044302, 2009.

[30] L. Heaney, A. Cabello, M. F. Santos, and V. Vedral, "Extreme nonlocality with one photon," *New Journal of Physics*, vol. 13, Article ID 053054, 2011.

[31] M. Blasone and G. Vitiello, "Quantum field theory of fermion mixing," *Annals of Physics*, vol. 244, no. 2, pp. 283–311, 1995.

[32] M. Blasone, P. A. Henning, and G. Vitiello, "The exact formula for neutrino oscillations," *Physics Letters B: Nuclear, Elementary Particle and High-Energy Physics*, vol. 451, no. 1-2, pp. 140–145, 1999.

[33] M. Blasone, P. Jizba, and G. Vitiello, "Currents and charges for mixed fields," *Physics Letters B: Nuclear, Elementary Particle and High-Energy Physics*, vol. 517, no. 3-4, pp. 471–475, 2001.

[34] M. Blasone, A. Capolupo, and G. Vitiello, "Quantum field theory of three flavor neutrino mixing and oscillations with CP violation," *Physical Review D*, vol. 66, no. 2, Article ID 025033, 2002.

[35] C. Giunti and C. W. Kim, *Fundamentals of Neutrino Physics and Astrophysics*, Oxford University Press, Oxford, UK, 2007.

[36] R. Horodecki, P. Horodecki, M. Horodecki, and K. Horodecki, "Quantum entanglement," *Reviews of Modern Physics*, vol. 81, no. 2, pp. 865–942, 2009.

[37] H. Barnum and N. Linden, "Monotones and invariants for multi-particle quantum states," *Journal of Physics A: Mathematical and General*, vol. 34, no. 35, pp. 6787–6805, 2001.

[38] D. A. Meyer and N. R. Wallach, "Global entanglement in multiparticle systems," *Journal of Mathematical Physics*, vol. 43, no. 9, pp. 4273–4278, 2002.

[39] G. K. Brennen, "An observable measure of entanglement for pure states of multi-qubit systems," *Quantum Information & Computation*, vol. 3, no. 6, pp. 619–626, 2003.

[40] T.-C. Wei and P. M. Goldbart, "Geometric measure of entanglement and applications to bipartite and multipartite quantum states," *Physical Review A*, vol. 68, Article ID 042307, 2003.

[41] T. R. de Oliveira, G. Rigolin, and M. C. de Oliveira, "Genuine multipartite entanglement in quantum phase transitions," *Physical Review A*, vol. 73, Article ID 010305(R), 2006.

[42] M. Blasone, F. Dell'Anno, S. de Siena, and F. Illuminati, "Hierarchies of geometric entanglement," *Physical Review A*, vol. 77, no. 6, Article ID 062304, 2008.

[43] W. K. Wootters, "Entanglement of formation of an arbitrary state of two qubits," *Physical Review Letters*, vol. 80, no. 10, pp. 2245–2248, 1998.

[44] S. Hill and W. K. Wootters, "Entanglement of a pair of quantum bits," *Physical Review Letters*, vol. 78, no. 26, pp. 5022–5025, 1997.

[45] C. -R. Ji and Y. Mishchenko, "General theory of quantum field mixing," *Physical Review D*, vol. 65, Article ID 096015, 2002.